Design strategies for carbon nanotube-based biosensors

DISSERTATION

for the award of the degree
"Doctor rerum naturalium"
of the Georg-August-Universität Göttingen

within the doctoral program
"IMPRS Physics of Biological and Complex Systems"
of the Georg-August University School of Science (GAUSS)

submitted by

Florian Alexander Mann

from Göttingen, Germany

Göttingen, 2020

Thesis Advisory Committee & Members of the Examination Board

Dr. Sebastian Kruss (1st Referee)
Institute for Physical Chemistry
Georg-August-University Göttingen

Prof. Dr. Martin Suhm (2nd Referee)
Institute for Physical Chemistry
Georg-August-University Göttingen

Prof. Dr. Claudia Steinem
Institute for Organic and Biomolecular Chemistry
Georg-August-University Göttingen

Further members of the Examination Board

Prof. Dr. Michael Meinecke, Department of Cellular Biochemistry, University Medical Center Göttingen

Prof. Dr. Jörg Großhans, Institute of Developmental Biochemistry, University Medical Center Göttingen/Georg-August Universität Göttingen

Prof. Dr. Silvio O. Rizzoli, Department of Neuro- and Sensory Physiology, University Medical Center Göttingen

Date of oral examination: 24.06.2020

Table of Contents

1 | Abstract

1.1 English

Global health crises such as the COVID-19 pandemic clearly show the need for novel and better diagnostic and therapeutic tools. Additionally, understanding underlying molecular processes is crucial. However, current methods face several problems including e.g. the specificity and spatiotemporal resolution of biomarker detection or *in vivo* targeting of drug delivery vehicles.

Single-walled carbon nanotubes (SWCNTs) are all-carbon nanoparticles with the potential to tackle these challenges. They emit near-infrared (NIR) light ($>$ 900 nm), which leads to three distinct advantages. First, NIR light can be used for enhanced *in vivo* fluorescence imaging with reduced background and deeper tissue penetration. Second, their NIR fluorescence does not bleach or blink enabling continuous monitoring over long time scales (hours to days). Third, the light emission is responsive to its chemical environment, which in combination with the SWCNT's large surface area promises high-sensitivity optical sensors for e.g. disease biomarkers. However, these beneficial optical properties can only be utilized when the all-carbon surface is chemically modified to generate selectivity either for biomarker detection or for targeting the SWCNTs to the desired place of action (e.g. cellular receptors).

This thesis provides new design strategies for SWCNT-based fluorescent biosensors and is organized according to the nature of conjugation (covalent/non-covalent) and the type of the conjugated biomolecule (DNA, peptide, protein).

In the first part, the SWCNTs were non-covalently functionalized with different DNA sequences. It has been known that such SWCNT/DNA hybrids show a fluorescence increase in the presence of the important neurotransmitter dopamine. Here, the correlation between sequence and sensitivity/selectivity was quantified leading to dissociation constants (K_d = 2.3 nM - 9.4 μM) and allowing the detection of dopamine in the presence of structurally similar neurotransmitters such as norepinephrine.

In the second part, such SWCNT/DNA-based dopamine sensors were modified with small antibody fragments (nanobodies) lending the required specificity to create tar-

geted dopamine sensors. These targeted sensors were not only fully characterized *in vitro*, but also applied *in vivo* in embryos of *Drosophila melanogaster* for deep-tissue NIR immunofluorescence imaging of the spindle apparatus. Furthermore, this new tool allowed for the first time tracking of a single Kinesin motor protein inside a living organism giving rise to deeper understanding of important intracellular processes as e.g. the velocity a motor protein is moving at *in vivo* ($\overline{v}$ = 610 $\pm$ 330 nm s^{-1}).
To expand the structural possibilities for SWCNT modification, peptidic barrels were introduced as a new molecular entity encapsulating SWCNTs with matching diameter. This new strategy, where *de novo* designed peptide barrels can be chosen to cover the corresponding SWCNT species, allows not only for chirality enrichment, but also for the subsequent attachment of functional units with applications in targeting or fluorescence microscopy.
In the last part, two new so-called quantum defects were introduced into SWCNTs generating an anchor site for subsequent covalent functionalization. In contrast to other covalent functionalization approaches, quantum defects create red-shifted emission features corresponding to exciton traps, but do not quench the SWCNT's NIR fluorescence. By combining this photophysical advantage with anchor groups for protein attachment and peptide growth, it was possible to generate functional, NIR-fluorescent and covalent SWCNT-Nanobody conjugates, multi-color SWCNTs as well as SWCNT-Peptide hybrids. With the superior stability of covalent chemistry, these anchor-quantum-defects can now be used as a platform technology for the generation of NIR-fluorescent tools for biosensing or immunofluorescence microscopy.
In summary, these four different parts report fundamental insights into SWCNT surface chemistry and its impact on the photophysical properties. Furthermore, it shows the potential of SWCNTs as building blocks for the generation of new SWCNT-based optical sensors, NIR-tools for fluorescence microscopy or vehicles for targeted delivery under continuous NIR optical monitoring ultimately generating new options for detection and/or treatment of diseases.

1.2 Deutsch

Globale Gesundheitskrisen wie die COVID-19-Pandemie zeigen deutlich den Bedarf an neuartigen und besseren diagnostischen und therapeutischen Instrumenten. Darüber hinaus ist das Verständnis der zugrunde liegenden molekularen Prozesse von entschei-

dender Bedeutung. Existierende Methoden haben jedoch in einigen Bereichen Defizite, insbesondere im Hinblick auf die Spezifität und das Auflösungsvermögen der Detektion sowie den zielgerichteten Transport von Medikamenten.
Einwandige Kohlenstoffnanoröhren (*single-walled carbon nanotubes*, SWCNTs) sind reine Kohlenstoff-Nanopartikel, die das Potenzial haben, diese Herausforderungen zu bewältigen. Sie emittieren Licht im nahen Infrarot (NIR, $>$ 900 nm), was zu drei deutlichen Vorteilen führt. Erstens kann NIR-Strahlung für verbesserte *in vivo*-Fluoreszenz-Bildgebung mit reduziertem Hintergrund und tieferer Gewebepenetration verwendet werden. Zweitens ist die NIR-Fluoreszenz der SWCNTs nicht-bleichender sowie nicht-blinkender Natur, welches wiederum längere Beobachtungsdauern von mehreren Stunden oder Tagen erlaubt. Drittens ist die NIR-Fluoreszenz von SWCNTs abhängig von ihrer chemischen Umgebung. Dies führt in Zusammenhang mit der großen Oberfläche dazu, dass Kohlenstoffnanoröhren als hochsensitive optische Sensoren zum Beispiel für die Biomarkerdetektion verwendet werden können. Diese vorteilhaften Eigenschaften können jedoch nur ihre Anwendung finden, wenn es gelingt, die einzig aus Kohlenstoffatomen bestehende Oberfläche so weit chemisch zu verändern, dass sie die selektive Erkennung z.B. von Biomarkern oder das Anvisieren von z.B. zellulären Rezeptoren ermöglicht.
Zu diesem Zweck stellt diese Arbeit neue Strategien vor, mit denen kohlenstoffnanoröhrenbasierte Biosensoren generiert werden können. In einem ersten Schritt wurden Sensoren für den Neurotransmitter Dopamin hinsichtlich ihrer Sensitivität und Selektivität charakterisiert und optimiert. Ein *Screening* von unterschiedlichen DNA-Sequenzen, welche auf der Nanoröhrenoberfläche adsorbieren, führte zu unterschiedlichen K_{d}-Werten (2.3 nM - 9.4 µM) sowie zu speziellen DNA-Sequenzen, welche es erlauben, Dopamin in Gegenwart des strukturell ähnlichen Neurotransmitters Noradrenalin zu detektieren.
In einem nächsten Schritt wurde nun dieser Dopaminsensor mit kleinen Antikörperfragmenten (*Nanobodies*) dekoriert, welche es vermögen, ihr Antigen mit hoher Spezifität zu binden. Diese neuen zielgerichteten Sensoren wurden nicht nur umfassend *in vitro* charakterisiert, sondern auch *in vivo* in Drosophilaembryonen angewandt, um dort den Spindelapparat mittels NIR-Immunfluoreszenzmikroskopie in tiefen Gewebeschichten untersuchen zu können. Ferner erlaubte es diese neue Technik, zum ersten Mal ein sich bewegendes Kinesin-Motorprotein in einem lebenden Organismus zu verfolgen und somit ein vertieftes Verständnis wichtiger intrazellulärer Prozesse zu erlangen (wie z.B. die Geschwindigkeit, mit der sich ein Motorprotein *in vivo* bewegt, $\overline{v} = 610 \pm 330$ nm s^{-1}).
Darüber hinaus wurden neben DNA-Oligonukleotiden auch Peptidfässer als neuartige

1. Abstract

Oberflächenmodifikation von SWCNTs eingeführt. Diese *de novo* erstellten Peptidfässer bieten nicht nur eine höhere Sequenzvariabilität im Vergleich zu Nukleinsäuren, sondern ebenfalls die Möglichkeit, bestimmte SWCNT-Chiralitäten anzureichern. Außerdem haben sie das Potenzial zur Anwendung als Funktionalisierungsplattform mit der Möglichkeit, funktionale Einheiten wie Fluorophore, Medikamente oder Antikörper anzubringen.
Zu guter Letzt wurden zwei neue so genannte Quantendefekte in SWCNTs eingebaut, welche zusätzlich eine Ankereinheit tragen, die nachfolgende kovalente Funktionalisierung ermöglicht. Im Gegensatz zu anderen Ansätzen der kovalenten SWCNT-Funktionalisierung führen Quantendefekte zu einer Rotverschiebung, nicht jedoch zu einer Löschung der NIR-Fluoreszenz. Durch Kombination dieser photophysikalischen Vorzüge mit den Ankereinheiten war es möglich, kovalente, funktionale und NIR-fluoreszente SWCNT-Nanobody-Konjugate, mehrfarbige SWCNTs sowie SWCNT-Peptid-Hybride herzustellen. Mit der erhöhten Stabilität durch die kovalente Verknüpfung können diese Ankerquantendefekte nun als eine Plattformtechnologie dienen, um neue NIR-fluoreszente Werkzeuge für Biosensoren oder die Immunfluoreszenzmikroskopie herzustellen.
Zusammengefasst stellen diese vier Technologien (DNA-basierte Dopaminsensoren, zielgerichtete Sensoren mit Nanobodies, die Peptidfass-Ummantelung sowie die Quantendefekt-Funktionalisierung) wertvolle neue Bausteine für die Herstellung von SWCNT-basierten optischen Sensoren, NIR-Werkzeugen für die Fluoreszenzmikroskopie oder Vehikeln für den zielgerichteten Transport von Medikamenten unter kontinuierlicher NIR-Observation dar. In Zukunft könnten somit neue Optionen für die Erkennung und Behandlung von Krankheiten generiert werden.

2 Introduction

2.1 Motivation

The COVID-19 pandemic, which is currently spreading, has already cost the lives of more than 200,000 people at the time this work was completed.[1] Together with other societal developments such as demographic change, which is resulting in an ever-increasing number and diversity of especially age-related diseases, these developments are placing an increasing burden on health systems. In order to counteract these developments, not only are functioning health care systems needed, but in particular suitable tools for a better understanding of diseases and their rapid and reliable detection. Over the last two decades, several novel diagnostic and therapeutic tools have been developed for the detection and treatment of cancer and other diseases, including cancer immunotherapy[2], CAR T cell therapy[3] or antibody/aptamer-based diagnostic devices. However, a large part of clinical diagnostics is still based on large and expensive equipment, which requires not only high acquisition costs but also trained personnel. In addition, many of these laboratory analyses are very time-consuming, which can lead to dramatic developments and e.g. undiscovered infections during a pandemic. With respect to age-related neurodegenerative diseases such as Parkinson's or Alzheimer's, the tools to gain fundamental understanding are especially limited regarding their ability to resolve small, yet important events in intercellular communication and the malfunction thereof. To address these problems and develop new, better and faster diagnostic tools, more research is needed in the life sciences. This will allow new relationships to be uncovered, biomarkers for the early detection of diseases to be found and, ultimately, new devices to be developed. These, in turn, will enable earlier diagnoses, leading to improved prognosis for patients and possibly lower costs for the health system.

In the last decade, nanotechnology has been demonstrated to be a great resource for building blocks of both diagnostic and therapeutic devices. Nanosized objects have the distinct advantage of being on the same length scale as the systems they are used to investigate. In addition, they can function as a scaffold for the attachment of multiple functional units responsible for different tasks such as targeting (e.g. antibody), report-

ing (e.g. fluorophore) and therapy (e.g. drug). In the future, these multifunctional devices could then potentially be injected, targeted to the desired site in the body, report on the disease status and directly release an appropriate drug in a targeted and thus less harmful fashion.

Carbon nanotubes are very promising candidates to fulfill these tasks. Compared to other nanomaterials, they provide the decisive advantage of having a valuable property for diagnostic or therapeutic devices already integrated - fluorescence. The near-infrared fluorescence of carbon nanotubes is even particularly suitable for *in vivo* imaging due to its enhanced tissue penetration properties compared to visible light. Furthermore, this fluorescence was shown to be dependent on the nanotube's surrounding and can thus not only be used for static tracking *in vivo*, but also to report on changing environments

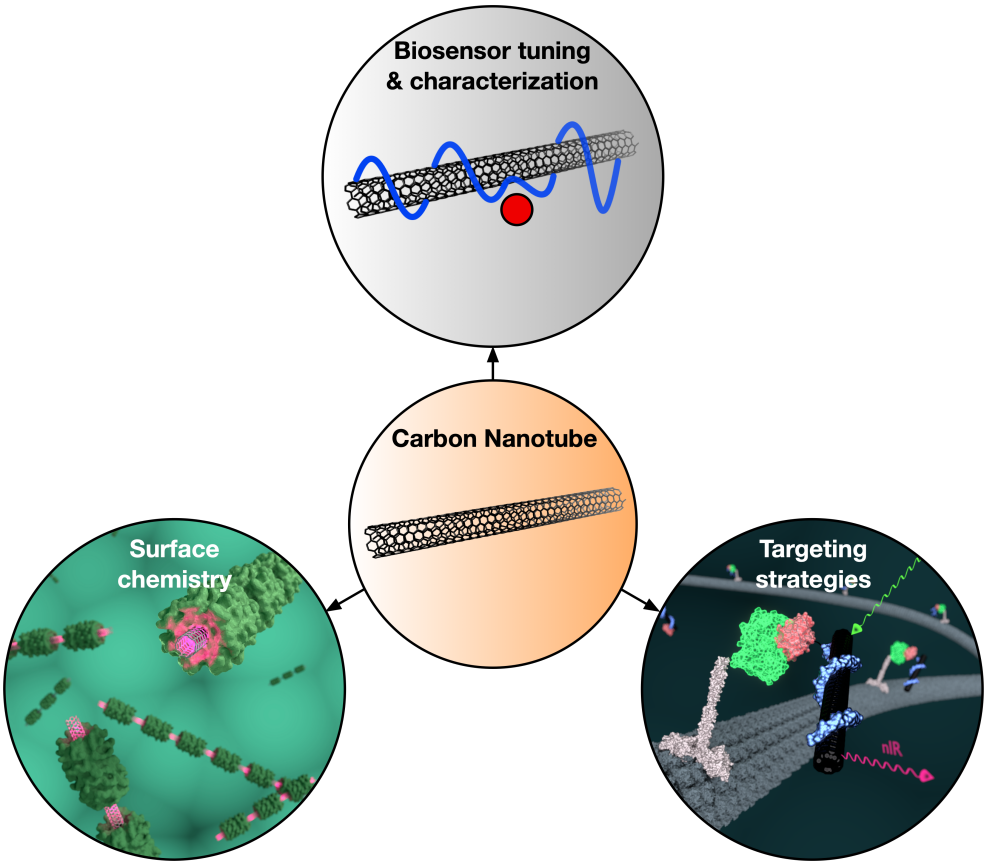

Figure 2.1.: **Design strategies for carbon nanotube based biosensors.** The goal of this work is the covalent and non-covalent functionalization of carbon nanotubes for the generation of novel optical biosensors as well as their targeted delivery to desired sites of action.

such as different pH[4] in cancer tissue or even small signaling molecules.[5]
The goal of this work is on the one hand to develop new methods for expanding the reporting/sensor capabilities of this carbon-based nanomaterial and on the other hand to combine these readout properties with targeting approaches based on small antibody fragments - termed nanobodies. By combining these two key properties we can get another step closer to advanced diagnostic and therapeutic devices, which could ultimately help to provide a better and more affordable health-care for an aging society.

2.2 Single-walled carbon nanotubes

Nanoparticles or in general nano-sized objects are defined in such a way, that at least one dimension needs to be within 1-100 nm.[6] Single-walled carbon nanotubes (SWCNTs) fall into that category with their almost one-dimensional structure showing lengths up to the mm-range with diameters between 0.4-2.5 nm.[7] This extraordinary high aspect ratio is not only interesting from a chemical standpoint, but also leads to highly unique photophysical properties and resulting applications, as will be discussed in the following sections.

2.2.1. Structure and Synthesis

Carbon is one of the elements central to all life on earth with a vast variety of compounds formed in conjunction with other elements such as hydrogen, nitrogen, oxygen, sulfur etc. But there is also carbon in pure elementary form. At ambient pressure, it exists mostly in the form of graphite, while at highly elevated pressures above several GPa diamond is formed. Whereas these 'classical' allotropes are known since a long time and very well characterized, the fields studying other, smaller carbon allotropes are still comparably young. It started with the discovery of the so-called 'Buckminsterfullerene' (C_{60}) by Kroto et al. in 1985[8], followed by the discovery of carbon nanotubes by Iijima in 1991[9] and graphene by Novoselov et al. in 2004.[10] Among these nanosized allotropes of carbon, carbon nanotubes have attracted particular attention due to their unique, tunable properties and possible applications in the field of biomedical sciences.[11]
Carbon nanotubes can be subdivided into two distinct species: Single-walled carbon nanotubes (SWCNTs) and multi-walled carbon nanotubes (MWCNTs). Structurally, they can be imagined as a rolled-up sheet of graphene (see Fig. 2.2a), i.e. a monolayer of graphitic, sp^2-hybridized carbon. But of course, this imaginary roll-up process does not leave the graphene sheet unaltered. Carbon nanotubes are energetically favored compared to graphene with respect to less edge atoms and corresponding dangling bonds at the expense of a high(er) curvature and ring strain. This ring strain is compensated to a certain extent by admixed sp^3-bonds in a carbon nanotube causing not only a different structure, but, resulting from that, also different physical and chemical properties.[12,13]
In addition, about 2% of the carbon atoms occur in non-hexagonal rings or pentagon-heptagon pairs (Stone-Wales defects) leading to locally enhanced reactivity, which will be discussed in further detail in section 2.2.3.[14]

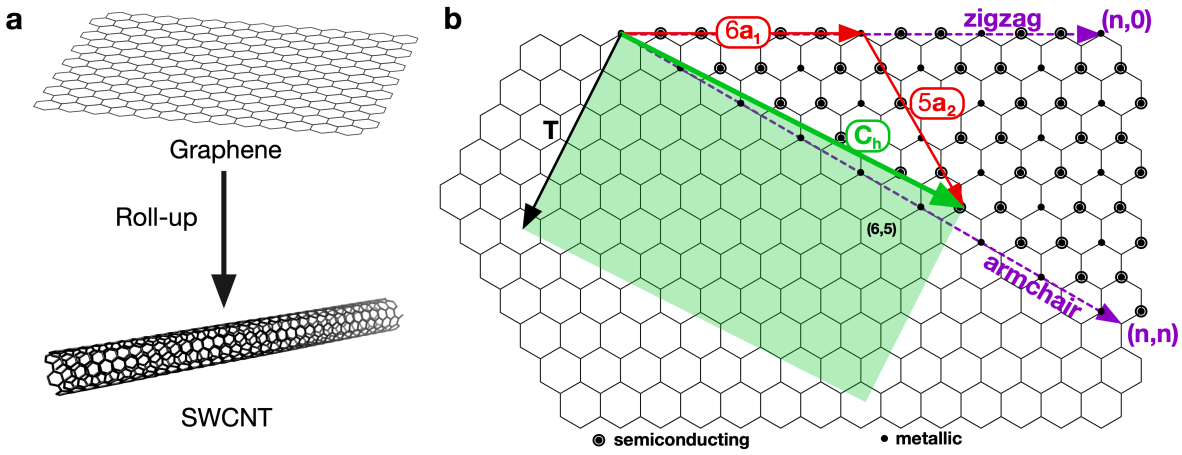

Figure 2.2.: **Structure and nomenclature of single-walled carbon nanotubes (SWCNT).** a) Imaginary roll-up of a graphene-sheet yielding a SWCNT. Based on Kruss et al.[11] b) Graphene lattice showing the different possibilities of SWCNT formation. The tube's chirality is defined by a linear combination of the vectors $\mathbf{a}_1$ and $\mathbf{a}_2$. In this example, the chiral vector $\mathbf{C}_h$ of a (6,5)-SWCNT and the corresponding unit-cell (green) is shown. Based on Dresselhaus et al.[12]

Depending on the direction of (imaginary) roll-up, SWCNTs with a large variety of different diameters and chiralities are formed. As shown in Fig. 2.2b, the chiral vector $\mathbf{C}_h$ defines - together with the lattice vector $\mathbf{T}$ - the 1D-unit cell of a SWCNT.[12] The structure space of SWCNTs is defined by the two unit vectors of the hexagonal graphene lattice $\mathbf{a}_1$ and $\mathbf{a}_2$, which upon linear combination yield the chiral vector $\mathbf{C}_h$, that describes the direction of roll-up or the circumference of a carbon nanotube. Correspondingly, the tubular axis is defined by the vector $\mathbf{T} \perp \mathbf{C}_h$.[12] These two vectors span up the SWCNT unit cell (shown in green in Fig. 2.2b). Linear combinations of the (n,0)-type are called zigzag-SWCNTs (chiral angle $\Theta = 0°$), whereas (n,n)-combinations are called armchair-carbon nanotubes ($\Theta = 30°$). All other (n,m) combinations are referred to as chiral SWCNTs with $0° \leq \Theta \leq 30°$. But the chiral vector $\mathbf{C}_h$ not only contains the information on the nanotube's chirality, but its length also corresponds to the SWCNT's circumference. The diameter of a (n,m)-nanotube can be calculated by the formula

$$d = \frac{|\mathbf{C}_h|}{\pi} = \frac{a_0}{\pi}\sqrt{n^2 + nm + m^2} \tag{2.1}$$

with $\mathbf{a}_0$ being the lattice constant of graphene (2.46 Å).[11] Different combinations of $\mathbf{a}_1$ and $\mathbf{a}_2$ thus lead to different chiralities and different diameters. Furthermore, these structural parameters also predetermine the SWCNT's properties. As shown in Fig. 2.2b,

all armchair SWCNTs are metallic, whereas certain zigzag and chiral species show semiconducting behavior. This outstanding physicochemical property will be discussed in further detail in section 2.2.2.

In 1991, Sumio Iijima found the first (multi-walled) carbon nanotubes using transmission electron microscopy (TEM) following the process used already earlier for the mass-production of fullerene C_{60} by Krätschmer et al.[15] (see. Fig. 2.3a). He reported on the growth of "graphitic carbon needles, ranging from 4 to 30 nm in diameter and up to 1 μm in length" on the negative end of the carbon electrode in an argon-filled vessel

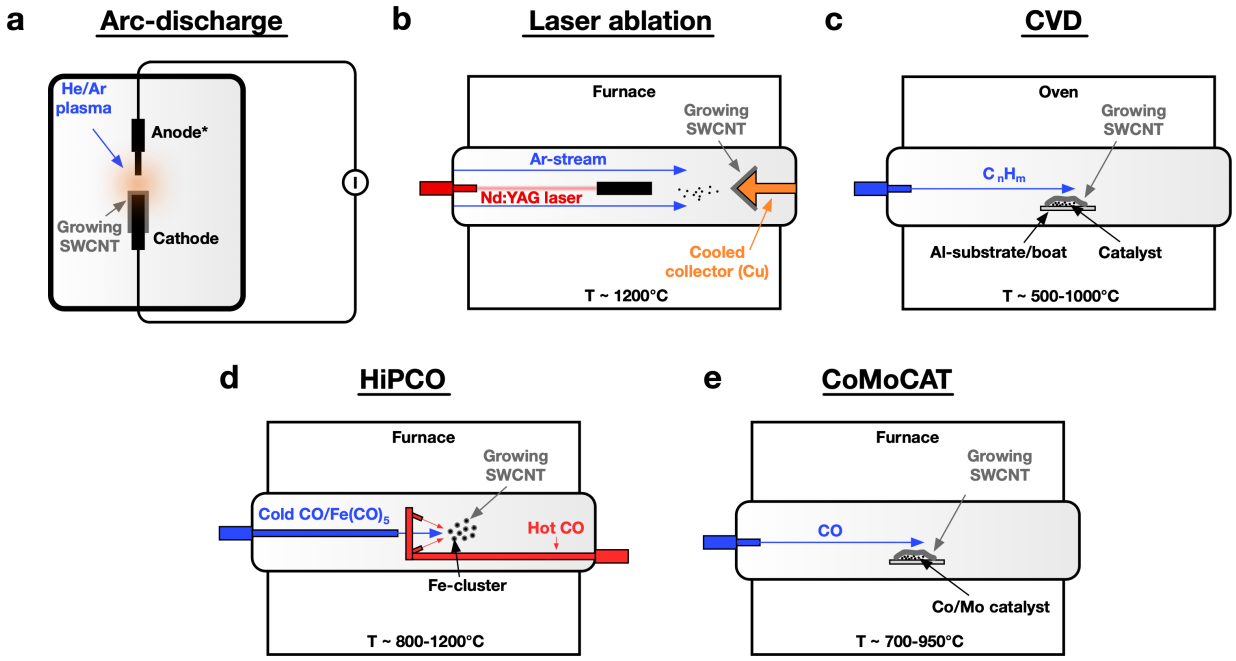

Figure 2.3.: **Different processes for the synthesis of SWCNTs.** a) The arc-discharge process utilizes two (transition metal modified) carbon electrodes to ignite an inert gas plasma used for the evaporation of carbon atoms. Depending on the metal catalyst, the inert gas pressure as well as the arcing current, the process yields fullerenes, MWCNTs or SWCNTs. b) The laser-ablation method involves a graphite-target (0.5 % Co/Ni), which is placed in a furnace at 1200 °C and vaporized using high-energy laser pulses. The vaporized carbonaceous material is then transported by an Ar-stream and deposited on a Cu-collector. c) Chemical vapor deposition can be used to grow high-purity SWCNTs from different gaseous (organic) carbon precursors in an oven on metal catalyst (Fe, Ni, Co). d) The HiPCO®, process is a modified CVD process with $Fe(CO)_5$ as a gaseous catalyst precursor yielding SWCNTs after CO disproportionation. e) In the CoMoCAT®, process, a cobalt/molybdenum catalyst is used as a template for SWCNT growth, which can be tuned in its particle size by different reaction parameters. This, in turn, not only allows preferential SWCNT synthesis, but also tuning of the resulting SWCNT's diameter.

(133 mbar).[9] In 1993, Iijima as well as Bethune et al.[16] used only a slightly modified variant of this technique for the first observations of SWCNTs.[16,17] Whereas Iijima used a iron-modified carbon cathode and a methane/Argon mixture as a chamber gas, Bethune et al. used a cobalt-filled anode and a Helium-filled chamber. Both groups found the addition of Fe or Co to the electrode crucial for single- instead of multi-walled carbon nanotube formation. In general, this arc-discharge method works via the evaporation of carbon atoms aided by a He/Ar-plasma ignited by high currents (see Fig. 2.3a).[12] Aspects such as the inert gas pressure or the arcing current can be modified to direct the synthesis either towards MWCNTs, fullerenes or SWCNTs (with Fe/Co addition).
In 1995, Smalley and coworkers achieved the synthesis of high-quality SWCNT on the gram scale using laser ablation (see Fig. 2.3b).[18] Here, a carbon-target containing 0.5 % Co/Ni is placed in a furnace and heated at 1200 °C under a constant stream of Argon. High-energy laser pulses are used for ablation of carbonaceous material, which is then transported outside the furnace by the Ar-stream and deposited on a water-cooled copper-collector. Side-products are, as also for the arc-discharge method, fullerenes, graphitic polyhedrons as well as amorphous carbon. The SWCNTs produced via both methods also contain a lot of metal catalyst impurities, which need to be removed for downstream and especially biological applications.[12]
Fig. 2.3c schematically shows the process of chemical vapor deposition (CVD). Here, different gaseous carbon species (e.g. hydrocarbons CH_4, C_2H_4, C_2H_6 etc.) are submitted to a CVD oven containing certain (transition) metal catalysts. These catalysts are mostly iron, nickel or cobalt nanoparticles formed on an aluminium substrate. Upon catalytic dissociation of the hydrocarbon, carbon dissolves and saturates in the metal nanoparticle leading to carbon "precipitation" and formation of a carbon hemisphere followed by tubular carbon growth ultimately leading to end-capped carbon nanotubes. Depending on the diameter of the metal catalyst, carbon nanotubes of different diameter are formed giving the possibility of control over the chirality distribution. Iron, nickel and cobalt are chosen in all of these methods as catalysts due to their phase diagram with carbon, where carbon shows a finite solubility in these metals at high temperatures giving rise to the possibility of carbon precipitation/growth.[12] Due to the lower process temperatures compared to the arc-discharge and laser ablation method, CVD-produced carbon nanotubes display a higher density of structural defects and thus also weaker electrical and mechanical properties. On the other hand, the CVD process is advantageous with respect to upscaling and mass production.[19]

This potential for upscaling also led to the two processes which are most widely used nowadays for the production of commercially available carbon nanotubes: the HiPCO®,[20] (see Fig. 2.3d) and the CoMoCAT®,[21] (see Fig. 2.3e) process. Both processes are advanced and refined versions of the CVD process leading to higher selectivity for SWCNT production on larger scales. The HiPCO process operates with $Fe(CO)_5$ as a gaseous catalyst precursor, which, upon *in situ* thermal decomposition and iron cluster formation, provides the possibility for catalytic carbon monoxide disproportionation. This CO disproportionation follows the Boudouard mechanism/equilibrium:

$$CO_{(g)} + CO_{(g)} \rightleftharpoons CO_{2(g)} + C_{(SWCNT)}$$

Via filtration/separation of the formed SWCNTs from the unreacted CO it is also possible to drive this process continuously instead of batch operation.[19]
The CoMoCAT process was developed shortly after the HiPCO process by Resasco et al. in 2000.[21] Again, SWCNTs are produced by CO disproportionation over a solid supported cobalt/molybdenum catalyst. At low Co:Mo ratios, carbon nanotubes are formed with a high selectivity (approx. 80 %).[19] By precisely controlling the different reaction parameters such as CO partial pressure, the amount of catalyst (precursor), temperature and others, it is possible to change the size of the catalytic particles. This in turn allows to drive the synthesis towards favoring certain SWCNT diameters and thus yielding narrower diameter/chirality distributions compared to the other methods. In the last two decades, a whole research field evolved investigating the SWCNT growth mechanisms depending on different catalysts, SWCNT precursor caps, growth conditions etc.[22] In this work, mostly SWCNTs produced by the CoMoCAT process and enriched in the (6,5) chirality are used, further modified and brought to different applications.

2.2.2. Optoelectronic properties

SWCNTs possess many outstanding properties as e.g. an extraordinarily high electrical and thermal conductivity as well as tensile strength.[12,23,24] In addition, depending on the direction of an imaginary roll-up from a sheet of graphene, SWCNTs can be either metallic or semiconducting. But what makes the properties of SWCNTs so fundamentally different from those of graphene and why are the electronic properties so sensitive to structural changes? This difference can be understood using the band-folding picture.

2.2.2.1. Zone-folding and density of states

Graphene already has a unique electronic structure near the *Fermi* energy with an occupied π- and an unoccupied π* band. These two bands show a linear dispersion and cross each other at the Fermi-energy at the K- and the K'-point of the Brillouin zone (see Fig. 2.4a).[12] These properties render graphene a so-called zero-bandgap semiconductor or semi-metal.

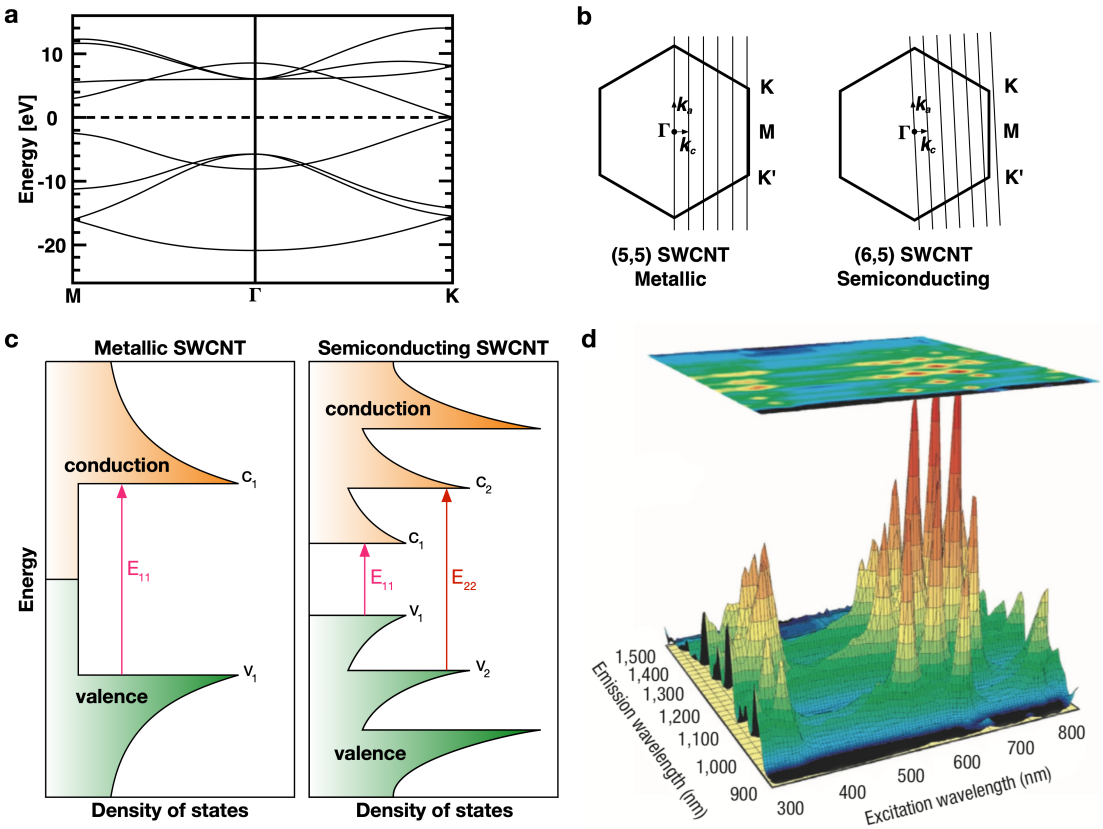

Figure 2.4.: **Carbon nanotube electronic structure and excited states.** a) Band structure of graphene as derived from the tight-binding model showing the valence and the conduction band overlapping only at the K-point at the Fermi-level. Modified from Dresselhaus et al.[12] b) Depending on the direction of roll-up to a SWCNT, discreet wave vectors are obtained leading to either metallic (wave vector crossing the K-point as e.g. (5,5) tubes) or semiconducting (wave vector not crossing the K-point as e.g. (6,5) tubes) SWCNTs. Modified from Graf (2019)[25] c) Density of states (DOS) diagram showing van-Hove singularities and a non-zero DOS for metallic SWCNTs as opposed to zero DOS for semiconducting SWCNTs. The size of the bandgap depends on the nanotube's chirality leading to different excitation/emission properties for each SWCNT chirality (d). Reproduced with permission from Avouris et al.[26].

When the graphene sheet is now rolled up to form a cylinder, the band structure gets altered by periodic boundary conditions in the circumferential direction. This in turn results in only a set of allowed wave vectors the electrons can exhibit following

$$1 = \exp[i\ (\mathbf{k}_a + \mathbf{k}_c)(\mathbf{C}_h + \mathbf{T})] \tag{2.2}$$

and

$$|\mathbf{k}_c| = j\frac{2\pi}{\mathbf{C}_h}\text{ , with j = 0, 1, ..., j}_{\text{max}} \tag{2.3}$$

with $\mathbf{k}_a$ being the reciprocal lattice vector along the SWCNT-axis and $\mathbf{k}_c$ the portion along the nanotube's circumference.[27] The circumferential boundary condition (eqn 2.3) leads to discreetly spaced wave vectors and a series of lines crossing the band structure of graphene (zone-folding, see Fig. 2.4b) depending on the direction of roll-up and thus the SWCNT's chirality.[12,25,27] If these lines cross the K-point, the SWCNT is metallic with a non-zero density of states (DOS) at the Fermi-level, whereas if the K-point is not included, the SWCNT is a semiconductor with differently sized band-gaps depending on $\mathbf{C}_h$ ($DOS_{Fermi} = 0$).[12] In line with theoretical calculations for a 1D quantum system, van-Hove singularities can be observed as sharp peaks/spikes within the DOS (see Fig. 2.4c).[25,27] Dipolar optical transitions with an electrical field polarized along the tube axis are only allowed between two symmetrical sub-bands giving rise to S_{11}, S_{22}, S_{ii} transitions for semiconducting and M_{ii} transitions for metallic SWCNTs.[24,28] These transitions then give rise to the excitation/emission maps as shown in Fig. 2.4d. Depending on the SWCNT's chirality, the emitted light with the energy E_{11} is in the near-infrared region of the spectrum rendering SWCNTs a promising "fluorophore" for biomedical imaging, which profits from enhanced tissue penetration when compared with visible light (due to reduced absorbance and scattering in biological tissue).[11] For semiconducting SWCNTs, the energy difference between the first van Hove singularity of electrons and holes corresponds to the bandgap energy E_{11}, which can be approximated by

$$E_{11} = \frac{2a_{C-C}\ \gamma_0}{d_t} \tag{2.4}$$

with a_{C-C} being the nearest-neighbor carbon-carbon distance (1.44 Å in a SWCNT), γ_0 the nearest-neighbor carbon-carbon interaction energy and d_t the tube's diameter.[29] In a first approximation it can thus be concluded, that the bandgap energy of semiconducting SWCNTs is inversely dependent on the tube diameter, which was later also confirmed

by experiments, although showing deviations in absolute bandgap energies (see Fig. 2.5a).[28,30,31]

2.2.2.2. Electrons, holes and excitons

These deviations not only result from tube curvature effects, but especially from the low dimensionality of SWCNTs causing one-dimensional confinement of electrons and holes generated upon excitation. In addition, the substantial coulombic attraction leads to strongly bound electron-hole pairs, also called excitons.[24,32] This exciton binding energy E_b (defined to be positive) is cancelled out to a large extent by the so-called self-energy E_{self} resulting from repulsion of both the excited electron and hole by conduction band electrons and valence band holes.[32] The bandgap energy can thus be determined as

$$E_{11,exc.} = E_{11} + E_{self} - E_b. \tag{2.5}$$

For many SWCNTs, the E_{self} is larger than E_b leading to an effectively increased bandgap (see Fig. 2.5a). However, Maultzsch et al., using two-photon luminescence spectroscopy, reported an increasing exciton binding energy for small-diameter SWCNTs leading to exciton stability even at room temperature.[25,33] The excitonic energy levels are strongly dependent on graphene's band structure, altered by the additional 1D confinement. The K- and K'-point in graphene's unit cell are degenerate (see Fig. 2.4b). Together with the possible spins of both electron and hole this leads to 16 possible excitonic states for each band index j with 12 triplet states and four singlet states.[34] While only the latter are accessible in dipolar optical transitions[28] (weak spin-orbit coupling and low intersystem crossing yield), their degeneracy is lifted by electron-hole interactions giving rise to the energy levels shown in Fig. 2.5b.[35] Both excitons with electron and hole not from the same valley (KK'-exciton and K'K-exciton) carry momentum and can thus not be excited by light (dark excitons).[25] In contrast, the two excitons arising from the same valley electron/hole (KK and K'K') do not carry momentum perpendicular to the tube axis and are generally energetically favored. The lowest energy exciton has a spatially even wave function (even parity) and can thus not couple to the ground state radiatively. Therefore, this exciton is referred to as a dark exciton. Around 55 meV higher in energy (Δ_-, for (6,5)-SWCNTs) is the only bright excitonic state out of the sixteen possible states due to its odd-symmetry and zero center-of-mass momentum.[34] The interplay of these two excitonic S_{11} states is crucial for the photophysical properties of SWCNTs

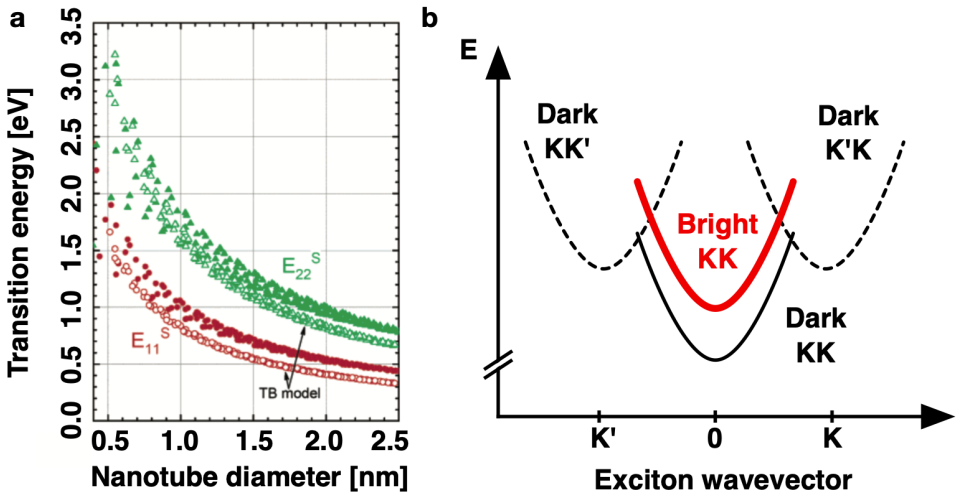

Figure 2.5.: **Excitons in single-walled carbon nanotubes.** a) Difference between experimentally derived values (solid symbols) for the bandgap energy and those derived by the tight-binding model (open symbols) depending on the tube diameter represented in a Kataura plot. Adapted and modified with permission from Weisman et al.[31] b) Energy diagram showing the four different singlet excitonic states. The two excitons with electron and hole from different valleys carry momentum and can thus not be excited by light (dark), whereas the KK excitons do not carry momentum. The energetically lowest state, however, has even parity and thus can not relax to the ground state radiatively. Modified from Graf (2019)[25]

and is also, amongst others, one explanation for their relatively low photoluminescence (PL) quantum yield (PLQY, typically 1%[36]) due to non-radiative decay into the dark KK excitonic state after excitation of the bright exciton.[26,34] This in turn also explains the strong dependency of PL efficiency and exciton lifetime on temperature.[37] Furthermore, Perebeinos et al.[38] and Mortimer et al.[37] found out, that applied magnetic fields along the tube's axis lead to enhanced PL by symmetry breaking and lifting of the degeneracy of the K and K' points.

2.2.2.3. Luminescent quantum defects

A similar and perhaps even more drastic effect was reported by Piao et al. in 2013, when they observed a new PL peak red-shifted by up to 254 meV compared to the original 'bright' S_{11}-exciton upon introduction of sp^3 'quantum defects' into the SWCNT lattice (see Fig. 2.6).[39] The authors achieved this significant but unexpected finding by stirring a dispersion of SWCNTs in D_2O with different aryl diazonium compounds for several

hours. Whereas before diazonium chemistry and sp^3-defects in general were known to quench the nanotube's PL[14,40], in this case an up to 28-fold brightening was observed. The PL increase was attributed to defect-induced symmetry breaking creating a new, optically allowed excitonic state below the dark KK-exciton leading to more efficient radiative relaxation to the ground state (see Fig. 2.6a). This new S_{11}^* state is also often referred to as a trap leading to strong exciton localization (see Fig. 2.6d/e/f) and thus prevention of diffusive quenching at e.g. SWCNT ends.[43,45] The authors found the increase in PL to be dependent on multiple factors such as defect density, the chemical nature of the defect (electron withdrawing or -donating, see Fig. 2.6c) as well as SWCNT chirality.[39] In a recent study, Berger et al. incorporated aryl defects into SWCNTs purified using the polyfluorene copolymer poly-[(9,9-dioctylfluorenyl-2,7-diyl)-alt-co-(6,6')-(2,2'-bipyridine)] (PFO-BPy), which enables a more detailed evaluation of the impact of defect introduction on the SWCNT's NIR-fluorescence. Using this method, they found the resulting NIR-fluorescence to strongly depend also on the SWCNT length (higher PLQY but lower brightening observed for longer SWCNTs) and the number of pre-existing sidewall defects (as e.g. incorporated by tip-sonication).[45]

The combination of the further red-shifted PL with the generally increased PLQY renders these defect-carrying SWCNTs (from here on referred to as SWCNT*) very promising for various applications in electronics, quantum computing but also in biomedical imaging. Here, it is now possible to excite the carbon nanotubes at their S_{11}-transition (approx. 1000 nm for (6,5)-SWCNTs) instead of the commonly used S_{22} excitation (approx. 560 nm for (6,5)-SWCNTs) leading to deeper tissue penetration of the excitation light at lower excitation doses.[46] In addition, the new defect-induced PL-peak (S_{11}^*) is, as opposed to the original S_{11} transition, not prone to reabsorption by the SWCNTs themselves, giving rise to an increased PLQY.[45] In the recent years, also other research groups followed up on this topic using different sp^3-defects for e.g. localized pH sensing[4], brightening of ultrashort SWCNTs[43] (see Fig. 2.6d/e/f) or single-photon quantum light sources.[36] An important factor is the density of sp^3-defects created in the SWCNT host. As shown in Fig. 2.6b, the E_{11} emission decreases whereas the E_{11}^* emission increases with increasing concentrations of the diazonium salt. At a ratio of 1:100 ([Dz]:[carbon]) the PL was completely diminished probably due to the loss of sufficient sp^2-based electron/exciton delocalization preventing excitation of the S_{11}-transition. This finding underlines the importance of finding the correct reaction parameters, which will also be of crucial importance for parts of this work (chapter 4.4). The reaction mechanism as

well as ways to control the defect density and thus the photophysical properties will be discussed in greater detail in chapter 2.2.3.

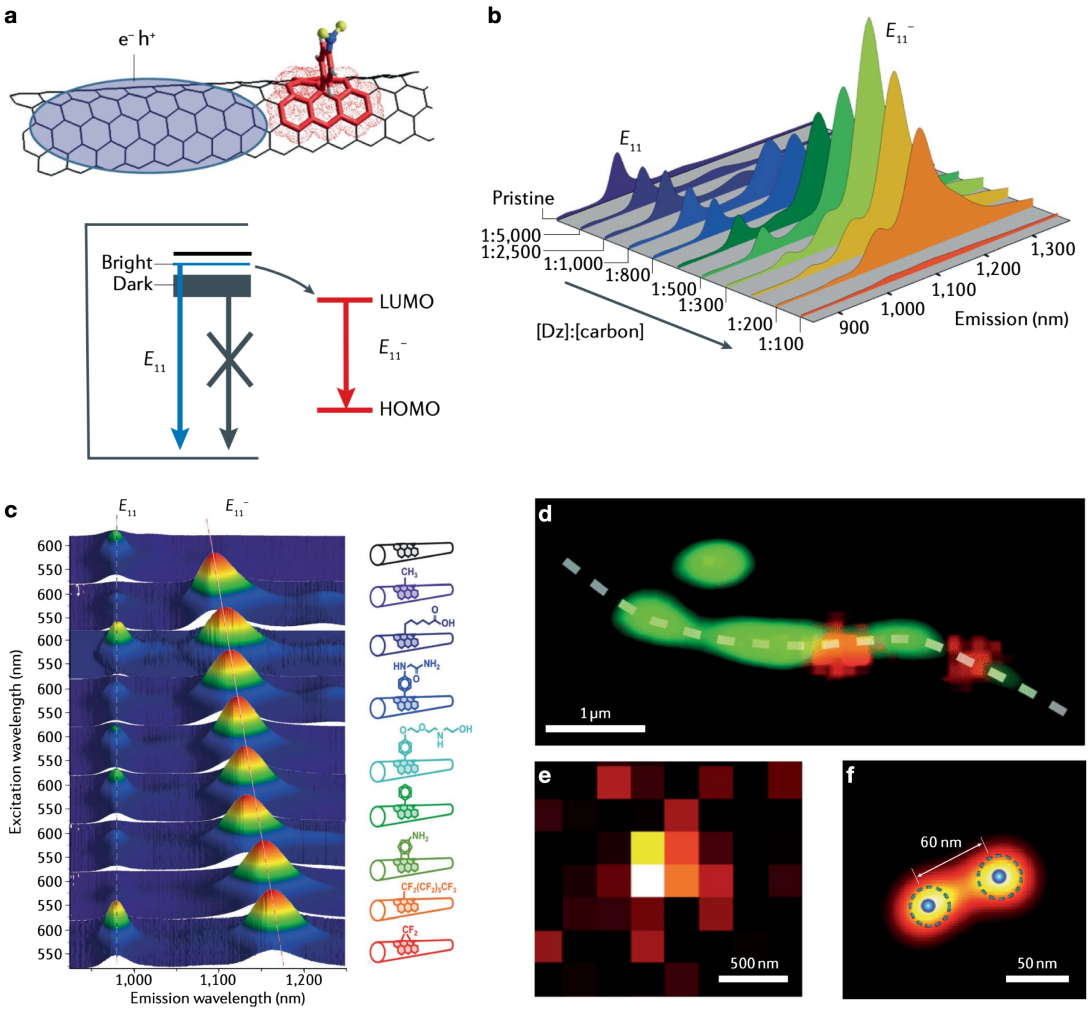

Figure 2.6.: **sp^3-defect related photoluminescence.** a) Schematic showing a sp^3 defect and its effect on the SWCNT's excitonic states. Due to symmetry-breaking, a new bright state is created below the dark KK exciton allowing for efficient radiative exciton recombination. b) Effect of reaction parameters such as the concentration of the diazonium salt (with respect to carbon atoms) on the PL of both the S_{11} and S_{11}^* exciton with their corresponding energies E_{11} and E_{11}^*. c) Tunability of the S_{11}^* excitonic state depending on the functional group attached to the defect site.[41] d) Single SWCNT (indicated by dashed line) showing both 'delocalized' E_{11} PL as well as E_{11}^*-PL 'localized' at defect sites.[42] e) Diffraction-limited as well as super-localized (f) E_{11}^* emission of ultrashort SWCNT, enabled by exciton-trapping and prevention of diffusive quenching.[43] Reproduced with permission from Brozena et al.[44]

2.2.3. Reactivity and functionalization of carbon nanotubes

As described in the chapters 2.2.1 and 2.2.2, carbon nanotubes are a highly interesting and unique material both from a chemical and photophysical perspective. However, one can also argue, that they are just a fascinating arrangement of carbon atoms and are consequently limited in terms of their chemical and biological applications due to the lack of properties such as e.g. specific binding of (bio)molecules. It is exactly this point, where (organic) chemistry comes into play to build on top of the unique (photo)physical properties and add extra 'layers' of functionality. Essentially, there are two different ways for the functionalization of single-walled carbon nanotubes - covalent (see Fig. 2.7) or non-covalent (see Fig. 2.8) chemistry. For this reason, the following section will be structured accordingly. In general, it should be noted that covalent modification of the SWCNT's ends or sidewall alters their structure and thus also their previously described properties whereas non-covalent 'wrapping' leaves the SWCNT's integrity untouched.

2.2.3.1. Non-covalent functionalization

As described in section 2.2.1, carbon nanotubes are hollow cylinders compromised of almost only carbon atoms arranged in approx. 98% hexagonal, sp^2-hybridized rings leading to large-range π-electronic delocalization. Consequently, they are highly hydrophobic in nature and tend to form large aggregates due to strong inter-nanotube van der Waals- as well as π-stacking interactions (Fig. 2.7a). As a result, SWCNTs are neither soluble in water nor in any other organic solvent[14] limiting both further processing as well as use in (biologically) relevant scenarios.
In need for better purification methods, Bonard et al. used the surfactant sodium dodecylsulfate (SDS) in combination with ultrasonic treatment to break up the SWCNT bundles and stabilize single, separated SWCNTs in aqueous solution by micelle formation.[47] This finding led to a large variety of surface-active or amphiphilic molecules to be used in the last two decades for "solubilization" of SWCNTs, as e.g. sodium dodecylbenzenesulfonate (SDBS), sodium cholate (SC) or sodium deoxycholate (DOC). Due to their dynamic/micellar dispersion mechanism, however, these surfactants require a concentration above their critical micelle concentration (CMC) to effectively stabilize SWCNT dispersions and prevent them from aggregation. While this is no problem for the means of purification, it hampers the nanotube's use in biological applications, where excess surfactant could impair biosensing of an analyte or destabilize biological membranes

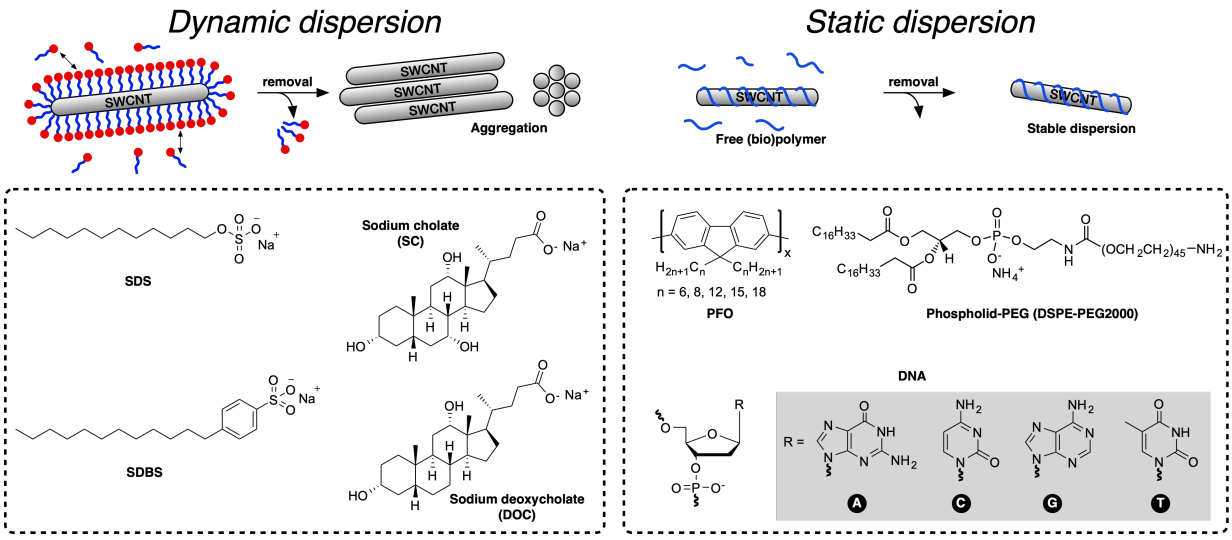

Figure 2.7.: **Non-covalent carbon nanotube functionalization.** The non-covalent functionalization of SWCNTs can - depending on the surface-active molecule employed - result in either static or dynamic dispersions. While the former leads to stable aqueous SWCNT-dispersions, dynamically dispersed SWCNTs will aggregate upon removal of excess surfactant. Examples of commonly used molecules for each type are given in the respective boxes.

causing cell toxicity.[11] On the other hand, strong π-π- or CH-π-interactions can help to overcome this problem resulting in static dispersions. The most prominent examples of this class are pyrenes, porphyrines, conjugated organic polymers such as poly[9,9-dioctylfluorenyl-2,7-diyl] (PFO), but also biopolymers such as deoxyribonucleic acid (DNA) or ribonucleic acid (RNA). While SWCNT-PFO dispersion are known to yield almost perfectly isolated SWCNTs in organic solvents (e.g. tetrahydrofuran [THF]) with high quantum yields of 1.5-3.0%[45], oligonucleotide wrappings of SWCNTs produce stable aqueous dispersions. Moreover, the DNA/RNA wrapping entails another important property - tunability. In contrast to the other classes of molecules described before, the oligonucleotide sequence can be varied (by chemical or biochemical synthesis), which was shown to have a drastic influence on SWCNT quantum yield, dispersion quality/yield and ultimately applicability in biosensing.[5,48–51] This characteristic as well as its inherent specificity for certain target analytes will be discussed further in section 2.2.4. Besides RNA and DNA, also peptides and proteins such as albumin or different enzymes were already used to disperse SWCNTs in aqueous systems. Whilst generally resulting in lower quality dispersions, in many cases the proteins were still able to carry out their native function, although being adsorbed on a hydrophobic nanotube.[52] All together,

non-covalent functionalization of SWCNTs has proven to be a highly valuable tool not only for studying their properties or for their purification, but also if proper anchors are included for the attachment of further functional units without perturbation of the nanotube's structural integrity.

2.2.3.2. Covalent functionalization

In stark contrast to non-covalent wrapping of SWCNTs, which besides ultrasonic treatment is considered a very mild procedure, covalent functionalization by design alters the nanotube's structure and with it its unique photophysical and electronic properties. As mentioned above, carbon nanotubes can be imagined as a rolled-up sheet of graphene resulting in a susceptibility towards chemical reactions borrowed from large aromatic systems influenced by a certain degree of additional curvature. This curvature results in deviations from bond angles normally found for extended π-systems as well as ring strain and structural defects compensating for that strain. These properties build the foundation for the covalent chemistry of SWCNTs. As a consequence, the large variety of reactions already known for aromatic compounds or graphite represents a toolbox for chemists and material scientists to play with in order to generate SWCNT derivatives with additional functions. In general, the covalent chemistry of carbon nanotubes can be subdivided into two fields - the modification of functional groups/defects introduced by oxidative treatments (etching) and the functionalization of pristine tubes directly via addition reactions at e.g. their sidewall (see Fig. 2.8).

The oxidative treatment of SWCNTs can be carried out either in the gas-phase by ozone/plasma treatment or in solution with oxidizing acids such as H_2SO_4/HNO_3 or mixtures of HNO_3/H_2O_2. While the latter is widely applied in the field also for the sake of catalyst-removal or shortening of nanotubes by cutting at defect sites[54], both methods yield a whole variety of oxygen-containing defects. As shown schematically in Fig. 2.8a, these include predominantly carboxylic acids, but also hydroxyl groups, aldehydes or ketones.[55] These functional groups can then be further targeted and derivatized e.g. using thionyl chloride and alcohols or amines to form the corresponding esters or amides. This route and other amidation procedures were widely applied in the last two decades leading, amongst others, to SWCNT-protein[56], -PEG[57], -sugar[58] or -oligonucleotide[59,60] conjugates with possible applications in drug delivery or immunology.[55]

Besides the derivatization of oxidized SWCNTs, there are a whole variety of other re-

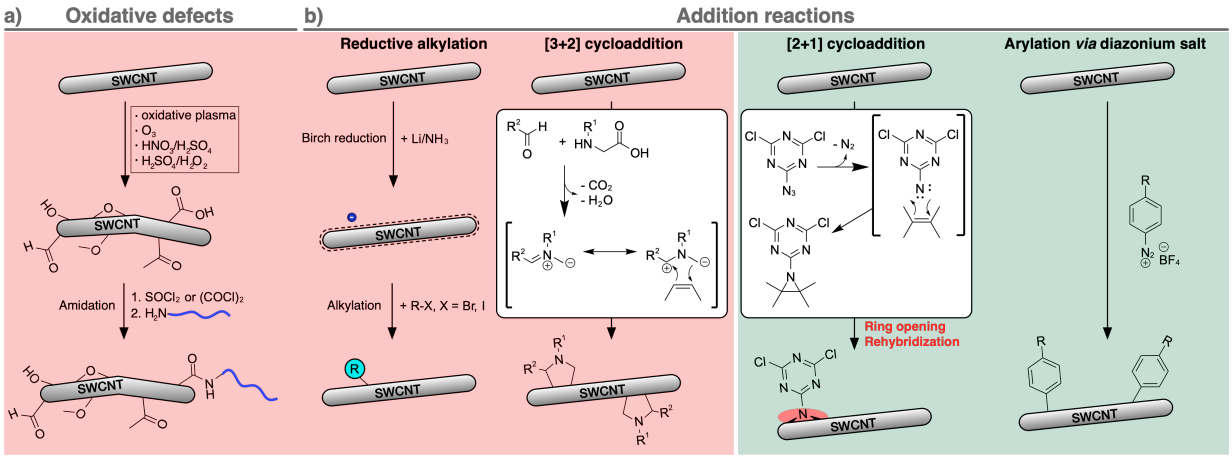

Figure 2.8.: **Covalent carbon nanotube functionalization.** a) Oxidation of SWCNTs leads to different oxygen-containing functional groups on the nanotube surface, which can subsequently be modified further by e.g. amidation reactions. b) Several examples of addition reactions leading to covalently modified SWCNTs. Whereas oxidative defects as well as reductive alkylation and [3+2] cycloadditions diminish the SWCNT's PL (red box), a [2+1] cycloaddition by Setaro et al.[53] as well as finely tuned reactions with diazonium salts[39] were shown to yield nIR-fluorescent nanotubes (green box).

actions, which were exploited in the recent years for the modification of SWCNTs. A selection of those methods is presented in Fig. 2.8b. They all share the idea of having one highly reactive species, which - when in proximity to a carbon nanotube - can undergo an addition reaction both at its tips or at its sidewall. While the tips are typically more reactive, sidewall-defects arising e.g. from the synthesis can also lead to higher susceptibility for addition reactions on the sidewall.[55] The variety of reactions include fluorination[61], carbene[62]/nitrene[63,64] addition, Diels-Alder cycloadditions[65], nucleophilic additions[66], reductive alkylations[67,68], free radical additions[69,70], 1,3-dipolar cycloadditions[71–73] or direct arylations with e.g. diazonium salts.[74,75] Whereas fluorinated nanotubes were shown to increase solubility in organic solvents and provide the possibility of further derivatization using e.g. Grignard-reagents or organolithium compounds[61,76], carbene- and nitrene additions were used e.g. to attach crown-ethers or oligoethyleneglycol units.[63] One reaction, which was exceptionally often employed, is the so-called 'Prato reaction'. It dates back to 1993, when Prato and coworkers first utilized the reactivity of azomethine ylides for the derivatization of the fullerene C_{60}.[77] In this reaction, azomethine ylides are formed *in situ* via the condensation of an α-amino acid and an aldehyde followed by a [3+2] cycloaddition to the nanotube's sidewall or end-tip. Prato's and also other groups quickly expanded the scope of this reaction uti-

lizing it not only for the synthesis of water soluble SWCNTs[78], but also for the attachment of peptides[79], fluorophores[80], cytotoxic drugs[81], antibiotics[82] or the multimodal modification of nanotubes.[83] Despite the quick adoption of this reaction, it has to be noted, that the resulting carbon nanotubes do not display their characteristic nIR photoluminescence anymore. Thus, for biological applications they lost one of their biggest advantages and consequently could only be used for imaging upon conjugation of another organic fluorophore - leaving the nanotube being no more than an attachment platform. To circumvent this problem, Setaro et al.[53] made use of a different type of reaction in 2017 - a [2+1] cycloaddition with electron-poor aromatic nitrenes (see Fig. 2.8b). In particular, they used azidodichloro-triazine as a source for the *in situ* generated nitrene. This nitrene, in turn, can then undergo a [2+1] cycloaddition with the SWCNT's sidewall as also observed earlier by the groups of Takagaki (2005)[64] and Hirsch (2001)[63] for the attachment of alkyl chains or carborane cages. In contrast to these older observations, however, Setaro et al. reported preserved nIR photoluminescence. The authors attribute this crucial difference to the electron-poor, aromatic nature of the dichloro-triazine, which together with the high strain leads to ring-opening and rehybridization. In the next step, they used this functionalization strategy for the generation of spiropyran-switchable nanotubes and conjugation of plasmonic gold nanoparticles leading to even further increased PL intensity.[53] Another alternative for SWCNT functionalization is the reaction with aryl diazonium salts. This reaction was reported already by Dyke and Tour in 2004 for the modification of carbon nanotubes (and their separation from metallic SWCNTs)[84], however, it was the laboratory of YuHuang Wang and coworkers at the University of Maryland to find the preservation and also modulation of the SWCNT's PL at certain reaction conditions. While the effect of these so-called quantum defects on the nanotube's PL was already discussed in section 2.2.2.3, the reaction mechanism leading to these defects should be discussed in the following.

As stated in section 2.2.2.3, carbon nanotubes containing quantum defects could present a highly valuable tool for biomedical imaging and diagnostics. The red-shifted PL peak, which now resides at around 1130 nm, allows SWCNT excitation at their S_{11}-transition (approx. 990 nm for (6,5)-species) instead of S_{22} excitation at approx. 560 nm allowing for greatly enhanced tissue penetration and better contrast.[46] Thus, it is highly desirable and also one of the aims of this work to use these defects not only for PL modulation, but also as an anchor for the attachment of other functional moieties such as fluorophores, peptides or proteins. The corresponding techniques for (bio)conjugation will be dis-

cussed in section 2.4.1. When Piao et al. observed the PL modulation in 2013[39], they were stirring a SDS-dispersed SWCNT sample with 4-nitrobenzenediazonium tetrafluoroborate for a prolonged time (240 h) at 25°C. Three years later, the same group published a revised procedure with drastically enhanced reaction kinetics upon SWCNT excitation (Fig. 2.9a).[85] This is due to the nature of the reaction of carbon nanotubes, dispersed in water using a surfactant as e.g. SDS or SDBS, and an aryldiazonium salt **1**, which proceeds *via* a radical mechanism with two possibilities for the initiation step. First, the cleavage of an *in situ* formed diazoanhydride (**2**, *via* a Gomberg-Bachmann reaction) can give the aryl radical **3** and second, the excitation of SWCNTs with (resonant, see Fig. 2.9b) light could lead to a single electron transfer (SET) from the nanotube **5**

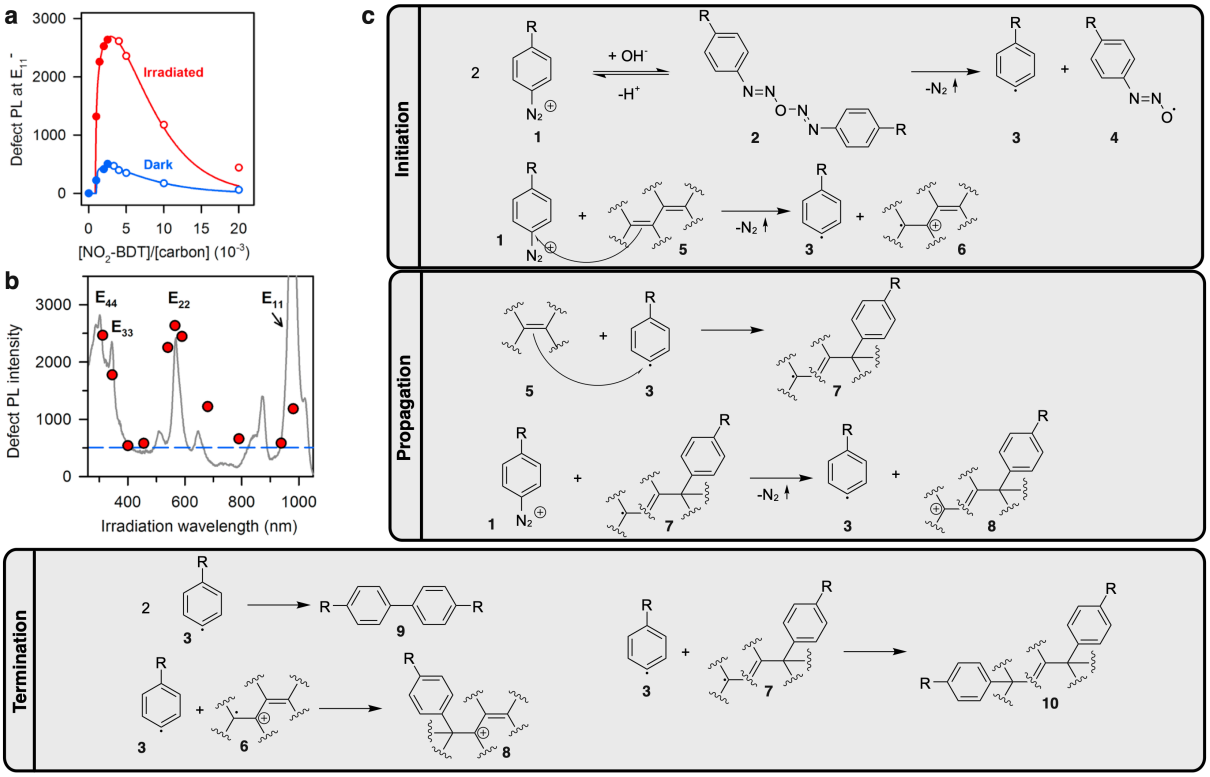

Figure 2.9.: **Mechanism of defect introduction by diazonium salts.** a) Diagram showing the difference in SWCNT-PL increase of a defect-reaction (p−NO_2-Dz) with and without excitation. b) Absorbance spectrum of a SDS-SWCNT sample and its influence on the defect PL intensity (shown as red dots at the respective excitation wavelength). c) Free radical chain mechanism for the incorporation of defects into SWCNTs using diazonium salts. Depending on the reaction conditions, there are two possibilities for initial radical formation. In **7**, the radical is formed on the α-carbon, but can migrate over the extended π-system. Parts a) and b) were reproduced with permission from Powell et al.[85]

onto the aryldiazonium salt yielding a aryl radical and a SWCNT-radical-cation **6** (with faster kinetics).[85,86] Following a radical chain propagation mechanism, the formed aryl radical **3** can now attack a SWCNT **5** resulting in a Aryl-SWCNT radical **7**, which in turn can generate another aryl radical *via* SET or recombine with an aryl radical to form a doubly substituted SWCNT (**10**, see Fig. 2.9c). It is important to note, that the radical in **7** is formed in 1,2-position with respect to the aryl substituent, but can migrate throughout the extended π-system of the SWCNT until recombination with e.g. another aryl radical or trion formation.[87]
If these quantum defects should now be utilized e.g. for the attachment of functional units to SWCNTs or to increase aqueous solubility, it is, however, very important to look at the number of defects introduced using diazonium chemistry. Whereas other techniques such as the Prato reaction, fluorination or the addition of nitrenes/carbenes (including the recent approach by Setaro et al.[53]) lead to one defect for every 2-100 carbon atoms (which roughly translates to one defects per 0.1-1 nm for (6,5)-SWCNT), the carefully adjusted conditions employed by Piao et al. for the generation of quantum defects result in approximately one functional group per 10-20 nm length of (6,5)-SWCNT. This difference is of crucial importance when it comes to sensing capabilities (e.g. sensor dynamic range, sensitivity) and also shielding of the hydrophobic SWCNT surfaces for aqueous solubility.

2.2.4. Application as optical sensors

As described in the previous sections, carbon nanotubes are special from many points of view. Their 1D tubular nature renders every (carbon) atom building up the tube a surface atom. This has one immediate consequence: The nanotube's optoelectronic properties are highly sensitive to changes in the SWCNT's surrounding. This can be observed immediately when looking at the absorption maxima of SWCNTs wrapped with different surfactants varying over approx. 20 nm.[88] This change depending on the nature, conformation and surface-coverage of the encapsulating molecule can be broken down to changes in the dielectric environment in general.[34] Here, an increasing dielectric constant is causing a red-shifted absorbance/emission as well as a decrease of exciton oscillator strength.[34] Both the redshift and the decrease of exciton oscillator strength can be attributed to dielectric screening of excitons by solvent molecules with the effect of enhanced non-radiative recombination or exciton dissociation.[89,90] However, this effect is not uniform in nature as SWCNTs were also shown to display different PLQY in solvents

of similar polarity. Larsen et al. found, that the additional important factor is solvent electrophilicity, which could lead to a shift of electron density from the tubular surface by electrophilic solvents. This, in turn, could lead to more non-radiative recombination sites and consequently reduced PLQY.[89]
This dependence on the dielectric properties as well as on the electrophilicity of the surrounding environment holds true not only for (organic) solvents, but also for surfactants, polymers or even solute molecules in general.[34] While (bio)polymers or surfactants, as described in section 2.2.3.1, can form micelles around SWCNTs or directly adsorb on their hydrophobic surface and thus directly impact the dielectric environment, solute molecules can intermittently interfere with this coating and in that way cause dielectric perturbations. Using near-infrared fluorescence spectroscopy, these dielectric perturbations can be probed either in terms of changes in PL intensity or wavelength shifts. Mechanistically, there are several approaches discussed in literature including solvatochromism, charge-transfer or doping/redox-reactions.[11] While redox reactions or doping results in increased/decreased non-radiative exciton recombination sites ($\rightarrow$ decreased/increased PLQY), charge-transfer e.g. from the SWCNT's valence band to the analytes' LUMO leads to altered population of ground/excited state and thus changed exciton relaxation kinetics ($\rightarrow$ decreased/increased PLQY).[11]
Whereas the PL of SWCNTs is highly sensitive to its environment and is able to report on changes via PL intensity- or wavelength modulation (detection unit), a sensor additionally requires both a recognition unit (e.g. antibody or aptamer) as well as a signal transduction unit (e.g. molecular linker, enzyme) for selective binding and detection of a target analyte. With respect to SWCNT-based sensors, they can roughly be sorted into two categories. First, those relying on known recognition motifs or known interactions and second, sensors found based on a screening approach making use of the unique structural confinement of biopolymers on the hydrophobic SWCNT surface leading to new recognition motifs.[91] A few examples for SWCNT-based optical sensors developed during the last 15 years are shown in Fig. 2.10. SWCNT-based optical sensors cover a wide range of analytes from reactive oxygen/nitrogen species (ROS/RNS) such as NO[98], OH radicals[99] or H_2O_2[100] over small molecules as riboflavin[48], glucose[92] or dopamine[5] to larger biomolecules (e.g. DNA[101,102], glycan-profiling[103], single nucleotide polymorphisms[104]) or even whole proteins (e.g. fibrinogen[50], HE4[96]). By comparing the sensors targeting these very different molecules, the differences in sensor readout are very much apparent comprising PL wavelength shifts or PL intensity modula-

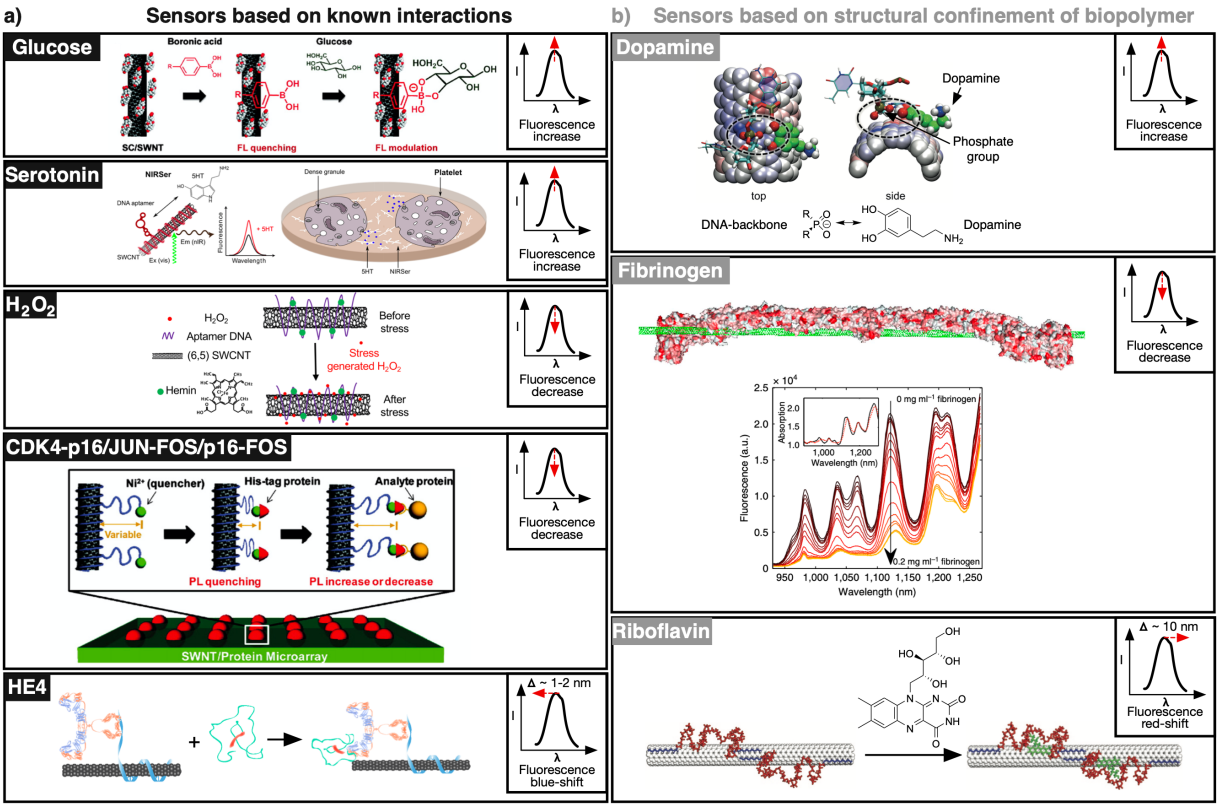

Figure 2.10.: **SWCNT-based optical sensors.** Overview on different mode of actions of several sensors and their respective sensor readout (top right boxes). a) Examples of SWCNT-based optical sensors utilizing known recognition motifs or interactions for the detection of glucose[92], the neurotransmitter serotonin[93], H_2O_2 released during plant stress[94], several proteins[95] or the ovarian cancer biomarker HE4.[96] b) SWCNT-based optical sensors based on structurally constrained (bio)polymers pinned to the SWCNT-surface detecting dopamine[97], fibrinogen[50] or riboflavin.[48] Figures adapted and modified with permission from Yum et al.[92], Dinarvand et al.[93], Wu et al.[94], Ahn et al.[95], Williams et al.[96], Kruss et al.[97], Bisker et al.[50] and Zhang et al.[48]

tion caused by the phenomena discussed above. The sensors developed for ROS/RNS respond most likely to adsorption of these redox-active molecules on the SWCNT's surface and thus show quenched PL, which was utilized e.g. for the spatiotemporal monitoring of NO-production inside macrophage cells.[105] The same readout mode (PL quenching) is observed for many protein sensors as e.g. those shown in Fig. 2.10a/b for fibrinogen or the p16-CDK4/Jun-Fos pairs. While for the latter case the PL quenching is caused by Ni^{2+}-induced proximity quenching, which is enhanced upon binding of the target protein (after a conformational change of the "bait" protein), Bisker et al. attribute the selective PL quenching to a combined effect of molecular recognition by the phospholipid-PEG

corona-phase and the unique 3D-structure of fibrinogen.[50] In contrast, glucose or the neurotransmitter dopamine are detected with an increase of PL caused by a conformational change of the wrapping $(GT)_{15}$ oligonucleotide (dopamine)[5] or boronic ester formation (glucose).[92] Besides PL quenching or enhancement, a wavelength shift can also be a tool for analyte detection. Among others, this was utilized for the optical sensing of riboflavin or the ovarian cancer biomarker HE4 (human epididymis protein 4), where Williams et al.[96] made use of a anti-HE4 antibody as a detection unit. The wavelength-shift was attributed to solvatochromism induced by polymer dielectric changes[48] or removal of water upon binding of the HE4-protein resulting in a reduction of the local dielectric constant as discussed above.[96]

While Fig. 2.10 highlights *in vitro* applications of SWCNT-based sensors, the beneficial properties of nIR-PL such as enhanced tissue penetration depth or the absence of bleaching/blinking led to quick adoption of a variety of the described sensors in *in cellulo* or even *in vivo* applications. The dopamine sensor developed by Kruss et al.[5] was later applied for the monitoring of dopamine secretion from stimulated PC12 cells allowing for a high spatiotemporal resolution surpassing existing electrochemical techniques.[97] Furthermore, several other nanotube-based sensors were even applied in live brain slices[46] or mice[96]. It is now part of this work to further enhance SWCNT-based optical sensors and to find other chemistries allowing for a more general approach of sensor generation.

2.3 Peptides and proteins as recognition elements

Peptides and proteins are molecules essential to all life on earth. They consist out of a set of 22 'proteinogenic' amino acids, linked via an amide bond to form a linear peptidic chain. If the length of this chain exceeds 100 monomers, the molecule is referred to as a protein.[106] Proteins carry out a whole variety of functions in nature and are responsible for processes crucial to life as well as for diseases in the case of malfunction. While small peptides often serve as hormones (e.g. insulin or oxytocin)[107], larger proteins e.g. catalyze biochemical reactions (enzymes), transport oxygen in hemoglobin, are responsible for movement with actin- and myosin filaments, built up skin and hair to a large extent with collagen/keratin or even synthesize other proteins in the ribosome. All of these functions described rely on a precise folding of the peptidic chain allowing for proteins to work either on their own or in large concerted protein-complexes mediated by protein-protein interactions (PPI). The folding and thus the 3D-structure of a protein is largely defined by the properties of the amino acids it consists of as well as their sequential arrangement. The latter is also defined as the protein's primary structure. Building on top of that, the secondary structure describes the local structure of a peptide, i.e. the way single amino acids are arranged with respect to one another. This is determined by intramolecular interactions such as hydrogen bonding, van der Waals forces or ionic interactions. Important secondary structures are the α-helix, the parallel or antiparallel β-sheet and the β- or γ-turn. The arrangement of these secondary structural motifs in the three-dimensional space is referred to as the tertiary structure of a protein. Like the secondary structure, the folding of the whole protein and its domains is also governed by intramolecular interactions. In this case, however, they can also be of covalent nature as in the case of disulfide bridges between two cysteines. Finally, the quaternary structure describes the arrangement of different protein strands with respect to one another which is crucial for the formation of larger protein assemblies relying on several subunits to carry out their function (e.g. hemoglobin, RNA-polymerase).
In nature, proteins are synthesized in the ribosome, a large complex comprised of protein and RNA subunits. Here, the assembly proceeds from the *N*- to the *C*-terminus with the ribosome reading the mRNA in 5'$\rightarrow$3' direction. In contrast, the chemical synthesis of peptides is carried out in the opposite direction, as described in greater detail in the following section.

2.3.1. Solid-phase peptide synthesis

The chemical synthesis of peptides is not just a trivial condensation of amino acids. Besides the fact, that the reaction of two amino acids can already form four different diastereomers, the different functional groups occurring in natural amino acids require sophisticated protecting group strategies. When synthesized in solution, the side products generated during synthesis also make an extensive purification necessary after each step and for some protected peptides also their low solubility can be an issue.[108] To overcome these problems, Bruce Merrifield developed the solid-phase peptide synthesis (SPPS) in 1963.[109] Here, the C-terminal amino acid is attached onto a solid support/resin (either as an ester or amide) followed by repetitive deprotection/coupling steps until the desired peptide sequence/length is reached. Between each deprotection and coupling step, the excess reagents can be removed easily via filtration. This one-pot approach without intermittent purification steps is not only time-saving, but also allows for the use of higher excess of deprotection/activation reagents leading to improved coupling kinetics and yields. To exclude side-reactions of side-chain functional groups such as thiols, amines or alcohols, they have to be permanently protected during the whole synthesis with a protecting group (PG) orthogonal to the temporary N^{α}-PG.

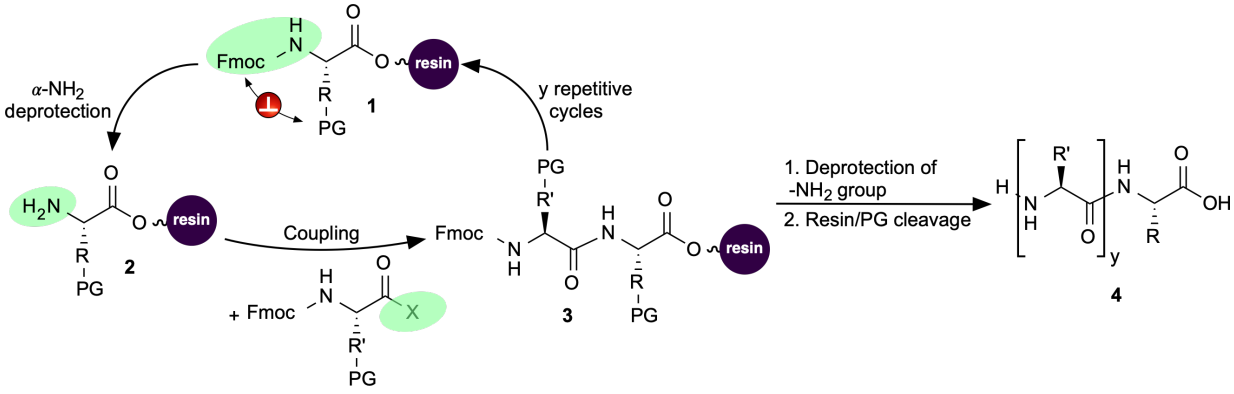

Figure 2.11.: **Solid-phase peptide synthesis.** General scheme depicting the essential steps of SPPS after immobilization of the first amino acid on the solid support (resin, **1**). In repetitive cycles the N-terminus of the growing peptide chain is deprotected under basic conditions (**2**) followed by amide-coupling to Fmoc-protected amino acids as an active ester (**3**). After the desired peptide sequence/length has been reached, the N-terminal Fmoc group is removed and the peptide cleaved off the resin under strong acidic conditions (e.g. 95% TFA). This step also cleaves the orthogonal protecting groups (PG) of the amino acid's side chain yielding the final product **4**

The most common N^{α}-PG is 9-fluorenylmethoxycarbonyl (Fmoc), which is also shown in the general SPPS-scheme in Fig. 2.11. This orthogonal protection group strategy is crucial to the success of the whole SPPS. The Fmoc-group is cleaved off under basic conditions (e.g. 20% piperidine/DMF) leaving a freely accessible amine group. This amine can now carry out a nucleophilic attack to the next amino acid's activated carboxy-group. After assembly of the complete sequence, the peptide is cleaved off the solid support under acidic conditions (e.g. 95% TFA) also cleaving the acid-labile orthogonal PG's from the AA's side chains yielding the desired peptide (**4** in Fig. 2.11). This whole process is easily automated and was consequently not only established for routine peptide synthesis, but also for the synthesis of therapeutic peptides[110], cyclic peptides[111] and peptides containing unnatural derivatives or post-translational modifications (PTM)[112], which would otherwise not be accessible using other chemical or biochemical methods.

2.3.2. α-helical coiled-coil barrels

SPPS enables the synthesis of almost any peptide sequence of choice. One exceptionally intriguing example especially when viewed besides carbon nanotubes are so-called α-helical coiled-coil barrels. In nature, α-helical coiled-coils are ubiquitous constituting approx. 3% of the protein-encoding regions of the genome. They are responsible not only for certain protein structures but also for directing protein-protein interactions in almost all intracellular and extracellular processes.[113] The α-helices are amphipathic and consist of the general sequence heptad repeat $(HPPHPPP)_n$ (also $(abcdefg)_n$), with H corresponding to hydrophobic and P to polar AA residues. In order to shield their hydrophobic a/d faces, the helices can form oligomeric assemblies (see Fig. 2.12a) with dimers, trimers and tetramers dominating in nature.[113] On average, the spacing of the hydrophobic residues in heptad-repeats is 3.5, whereas the pitch of an ideal α-helix corresponds to 3.6 residues. This (small) mismatch is the reason for two or more α-helices wrapping slowly around each other forming coiled-coil or supercoil structures. In addition to the hydrophobic seam winding around the helix, so-called knobs-into-holes interactions of adjacent helices represent a more specific type of interaction explaining also the vast heterogeneity of coiled-coils in nature. Here, the side-chain of one helix ('knob') can interact with a 'hole' structure formed by four residues of a neighboring helix (see Fig. 2.12b).[113–115] Taken together, these well-characterized sequence-to-structure relationships make α-helical coiled coils one of the best studied protein structural motif[113,115–117] and even enabled computational *de novo* design of novel coiled-coil

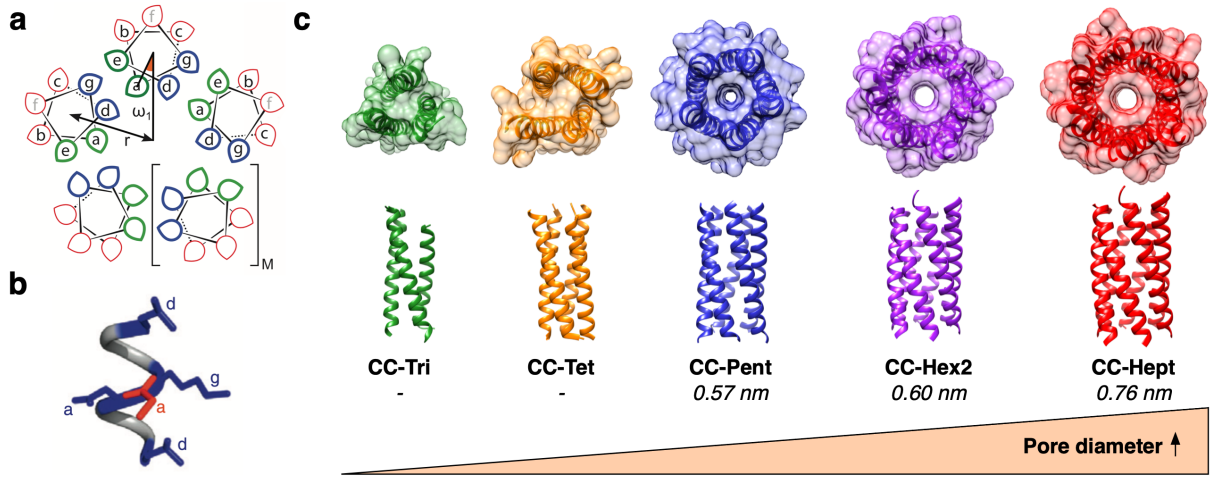

Figure 2.12.: **α-helical coiled-coil barrels.** a) Helical wheel diagram for a coiled-coil pentamer (M=1) showing the interhelical contacts, the coiled-coil radius r and the helical offset ω_1. Adapted with permission from Thomson et al.[114] b) Example of *knob-into-hole* interaction of a residue a with a ***dgad*** hole formed by another helix (from X-ray crystal structure of GCN4-p1). Adapted with permission from Woolfson et al.[113] c) Examples of α-helical coiled-coil barrels showing the increasing pore diameter with increasing oligomeric state (Structures generated from 4DZL (CC-Tri), 3R4A (CC-Tet), 4PN8 (CC-Pent), 4PN9 (CC-Hex) and 4PNA (CC-Hept)).

structures.[114,115] Here, Thomson et al. showed, that depending on the amino acid sequence of the α-helical monomer the resulting peptidic barrels can be tunable in their pore sizes with diameters between 0.5 and 0.8 nm (see Fig. 2.12c).[114]

In addition to freely-standing barrels, which could be of interest e.g. for artificial membrane channels, Burgess et al.[118] and Thomas et al.[119] also showed the possibility of self-assembly into long peptide nanotubes (PNTs). This was achieved either via end-to-end stacking of positively/negatively charged termini[118] or even covalently using native chemical ligation (NCL) to site-selectively cross-link adjacent peptide barrels and thus increase the PNT's stability.[119]

It appears, that the diameters of the larger oligomeric species CC-Hex or CC-Hept are in the same order of magnitude as common diameters of small carbon nanotubes with e.g. (6,5)-SWCNTs having a diameter of 0.76 nm. Therefore, the idea of this work is to use these larger oligomers for the dispersion of SWCNTs in aqueous environments. As opposed to commonly used surfactants or biopolymers such as DNA (see section 2.2.3.1), peptides offer a larger degree of structural variability and were up to now only rarely used for the non-covalent functionalization of SWCNTs. In 2003, Dieckmann

et al. used a peptide folding into α-helical structures in the presence of SWCNTs for their dispersion in aqueous solutions[120], whereas Ortiz-Acevedo et al. used reversible cyclic peptides (linked *via* a disulfide bridge) to achieve a selectivity for certain SWCNT diameters.[121] In 2011, Grigoryan et al. computationally designed peptides binding certain SWCNTs species preferentially upon self-assembly into antiparallel hexameric helical bundles and utilized that for the generation of a regularly spaced SWCNT-gold-NP hybrid material.[122] It is now the aim of this work to use the well-studied sequence-to-structure relationship of α-helical coiled-coil peptide barrels for the encapsulation of certain SWCNT species with *de novo* designed α-HBs.

2.3.3. Antibodies and their functional fragments

While peptides are a very important class of biomolecules and recently also gained more attention as therapeutic entities[123], by far the most widely used and powerful tool of biomedical research are antibodies.[124] Antibodies, the most important protein in our immune system, are large proteins with a size of approx. 150 kDa formed by a heterotetrameric assembly. They are composed of two identical heavy (H) and light (L) chains, each equipped with a variable domain at the respective N-terminus, which is responsible for antigen binding and specificity (termed V_H and V_L).[124] The light and heavy chains are linked together by disulfide bridges (two H-H-linkages, two L-H linkages) leading to an overall Y-shape of the molecule (see Fig. 2.13a). The disulfide-nature of these linkages is crucial for the antibodies function and specificity, however, it is also responsible for some limitations. For instance, the cytosol is a highly reducing environment[126] with excess glutathione leading to structural instability of antibodies inside cells. Consequently, in our immune system, antibodies are either displayed on the outside cellular surface or secreted by immune cells to fight pathogens. Researchers recognized the large potential of these highly specific binders already over a century ago[127,128] and antibodies became the one of the most powerful tools not only in biomedical diagnostics and imaging (with fluorescently tagged antibodies), but in the last two decades also in immune therapy or more targeted chemotherapies (with antibody-drug conjugates, ADC).[125,129] The already mentioned structural complexity and especially their susceptibility towards intracellular reduction and disassembly, however, led to the development of many other formats of specific binders, often derived from classical immunoglobulins.[125] Prominent examples are the monovalent *antigen-binding fragments* (Fab) lacking the *crystallizable*

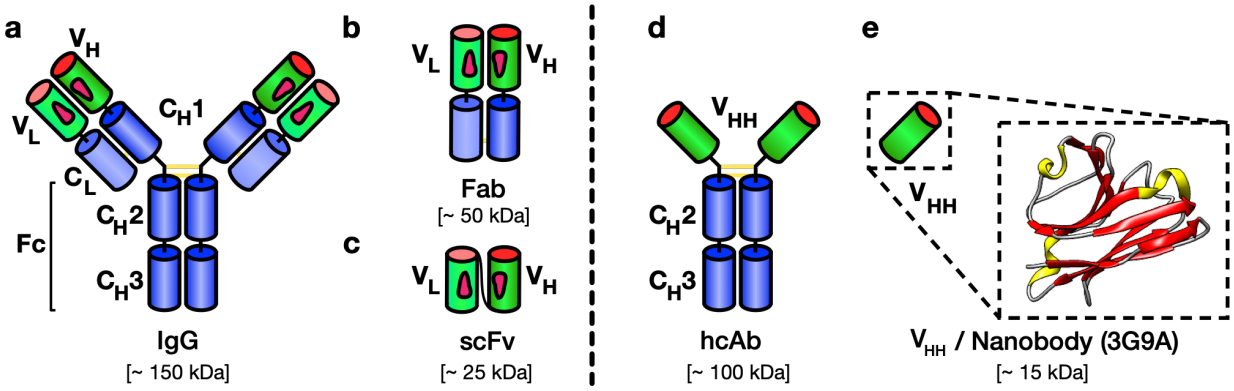

Figure 2.13.: **Schematic structure of antibodies and derived binders.** a) Schematic structure of a conventional full-length-antibody/immunoglobulin G (IgG) composed of two heavy and two light chains linked *via* four disulfide bonds (yellow). Each heavy chain contains three constant regions ($C_H1/2/3$) and one variable region. The light chain contains one constant region (C_L) and one variable region (V_L). The variable regions are responsible for antigen binding (with each three complementary determining regions [CDR], in total twelve) and associate via inter-domain interactions of hydrophobic framework residues (pink). b) Fab-fragment lacking the Fc-region of a conventional IgG. c) scFv antibody formed by covalent peptidic linkage of the V_L and the V_H domain. d) Heavy-chain antibody found e.g. in *camelidae* consisting only of the two heavy chains linked via two disulfide bonds. The V_{HH} domain does not rely on hydrophobic interdomain interactions for antigen binding making it possible to use also just the single V_{HH} domain in its isolated form as a stable and small binder (Nanobody, e)). Based on Helma et al.[125]

fragment (Fc) of a conventional IgG (50 kDa, Fig. 2.13b) or scFVs consisting a V_L and a V_H domain fused together via a peptidic linker sequence (25 kDa, Fig. 2.13c). These formats, however, suffer from thermodynamic instability as they rely on non-covalent inter-domain interactions for the correct fold and function.[125] To overcome this problem, also single-domain antibodies derived directly from IgG's were tested. Here, however, the isolated variable V_L and V_H domains showed low solubilities and thus require extensive protein engineering to drive them towards applications.[130] Consequently, the finding of naturally evolved heavy-chain antibodies (hcAb, approx. 100 kDa, Fig. 2.13d) in *camelidae* and cartilaginous fish (e.g. sharks) attracted a lot of attention as in these cases nature already carried out the mutations necessary to provide e.g. improved solubility.[124,125] HcAbs bind their antigen only *via* one variable domain (V_{HH}) and in contrast to the V_L or V_H domains of human IgG's, the V_{HH} domain is stable on its own in an aqueous environment and can thus be cloned from the cDNA (encoding the hcAb) into phage-display

vectors for selection and amplification of potent binders. These V_{HH}-binders are, due to their small size in the single-digit nanometer range, called nanobodies (approx. 15 kDa, Fig. 2.13e). The absence of interchain disulfide-bridges or the necessity of non-covalent inter-domain interactions renders nanobodies extraordinarily stable also e.g. in reducing environments such as the intracellular space. This was demonstrated by the so-called chromobody-technology, where nanobodies are expressed as fusion-proteins with fluorescent proteins (RFP/GFP) allowing labelling and tracking of antigens inside a living cell.[131] In addition, Herce and Schumacher et al. were able to modify nanobodies site-specifically with cell-penetrating peptides allowing for antigen labeling in non-genetically modified living cells. Furthermore, the special convex paratope shape of nanobodies allows binding of otherwise not reachable epitopes such as enzymes[132] while their small size (1.5 nm x 2.5 nm compared to 10 nm of an IgG) can lead to drastically reduced linkage errors in super-resolution microscopy.[133]
In this work, a GFP-binding nanobody will be used to generate nanotube-nanobody conjugates enabling the labelling and tracking of GFP-tagged antigens *in vivo* as well as targeted placement of nIR sensors. To achieve this goal and keeping the nanobody in a functional state, the attachment to the SWCNT has to be carried out in a mild and well defined fashion. In this work, this will be achieved by a single, ectopic C-terminal cysteine, that can be attached to maleimide units presented on the SWCNT-surface. This process will be explained in greater detail on the following pages.

2.4 Carbon nanotube-Protein conjugates

Both single-walled carbon nanotubes and peptides/proteins are intriguing molecules on their own and possess a whole variety of outstanding properties. This work, however, aims at a combination of both of these molecules in order to blend their most beneficial properties. While SWCNTs display stable and non-bleaching photoluminescence in the biological transparency window, peptides/proteins can be either used as a functionalization platform or directly for imparting target specificity to the molecular hybrid. In any case, novel functional groups will be introduced to the all-carbon nanotube. The ways to achieve this functionalization as well as the current status of SWCNT-protein conjugates will be explained in the following section.

2.4.1. Conjugation strategies - bioorthogonal/chemoselective reactions

As already described in section 2.2.3, carbon nanotubes can be derivatized either by covalent or non-covalent chemistries. While the covalent functionalization leads to very stable conjugates also under challenging conditions, it also disrupts the SWCNT's sp^2 network and thus diminishes its PLQY. In contrast, non-covalent functionalization leaves the carbon nanotube itself untouched, but coats its surface with e.g. amphiphilic molecules, which could carry another molecular anchor for further covalent derivatization (hybrid functionalization). Very recently, Setaro et al. also achieved covalent functionalization of SWCNTs under preservation of the nanotube's PL.[53] Within this work, all of the described ways for SWCNT functionalization will be evaluated for the use in different applications. Non-covalent modification of SWCNTs with DNA-oligonucleotides can lead to functional hybrids for sensing of important neurotransmitters, whereas further covalent derivatization of this oligonucleotide with nanobodies will be evaluated as an approach for the targeted delivery of these nIR optical sensors. Furthermore, aryl defects introduced *via* diazonium chemistry will be used for the covalent attachment nanobodies and growth of peptidic chains directly on the nanotube's sidewall under preservation of its PL with the additional red-shifted E_{11}^* emission peak. All these applications have in common, that it is highly important to generate these SWCNT-hybrid materials in a reproducible and well-defined fashion. This does not only include the number of attached units and functionalities, but also their fold and orientation on the SWCNT's surface. The latter characteristic is especially important for antigen-binding proteins to ensure that the paratope is pointing away from the SWCNT surface to allow fast and sensitive

antigen detection. The orientation of proteins, but also other functional units, can be controlled by site-specific attachment of the SWCNT to the protein.
Proteins contain a whole variety of different functional groups including amines (Lysine). guanidines (arginine), alcohols (serine, threonine) and thiols (cysteine). The most common way for protein functionalization is the targeting of lysine residues, which can be accomplished by the reaction with activated acyl groups (active esters or acyl chlorides, see Fig. 2.14a). However, lysine's high abundance leads to inhomogeneous protein mixtures, which can be especially problematic for therapeutic applications.[134] In addition, also residues essential for the protein's fold or function could be affected leading to e.g. abolished activity.[135] To circumvent these problems, a whole variety of different techniques for both chemo- and regioselective labelling/functionalization of proteins were developed. One approach used extensively in fluorescence microscopy applications is the genetic fusion to other functional proteins.[136] These can be either fluorescent themselves as the green-fluorescent protein (GFP, 27 kDa) and its differently colored derivatives (see Fig. 2.14b)[137] or so-called self-labeling protein-tags as e.g. the HALO- (33 kDa)[138] or SNAP-tag (20 kDa)[139] (see Fig. 2.14c). While the fusion of fluorescent proteins (FP) enabled direct localization or even quantification[140] of proteins in cells or in whole animals[141], self-labeling tags allow site-selective incorporation of the whole variety of organic fluorophores with superior photophysical properties compared to FPs.[142] However, both self-labeling tags and FPs are often larger than the protein-of-interest (POI) itself and several studies already reported changes in cellular localization or folding of the POI.[143,144]
One way to circumvent problems arising from large-size fusion proteins interfering with the POI's function, but still be able to site-specifically modify proteins also inside living cells, is the incorporation of unnatural amino acids (UAA) or small chemical anchors. UAAs can either be incorporated directly during expression of the POI (by auxotrophic expression[145] or amber codon suppression[146], see Fig. 2.14d) or post-translationally using chemoenzymatic approaches[147] with enzymes such as sortase[148], tubulin-tyrosine ligase[149] or the formyl glycine generating enzyme[150] (see Fig. 2.14e). While auxotrophic expression allows for the residue-specific placement of UAAs (instead of one natural residue), amber-codon suppression makes site-specific incorporation of UAAs possible. Chemoenzymatic systems can, depending on the system employed, also introduce unnatural residues both to the *C*- or *N*-terminus or sequence-internally through attachment to short peptide tags.[147] Another type of modification, that can be used

for site-specific modification of proteins is the so-called expressed protein ligation (EPL) making use of intervening proteins (inteins) and their ability to excise themselves out of an already expressed protein leaving the two flanking regions fused together by a native amide bond (Fig. 2.14f). Inteins and their self-splicing ability were already utilized as cleavable purification tags[151], for protein semisynthesis with synthetic peptides[152] or for live-cell protein labelling with so-called split-inteins.[153] While all of these approaches enable the site-specific and bioorthogonal functionalization of proteins, some of them suffer from tedious genetic engineering required and low yields (genetic code ex-

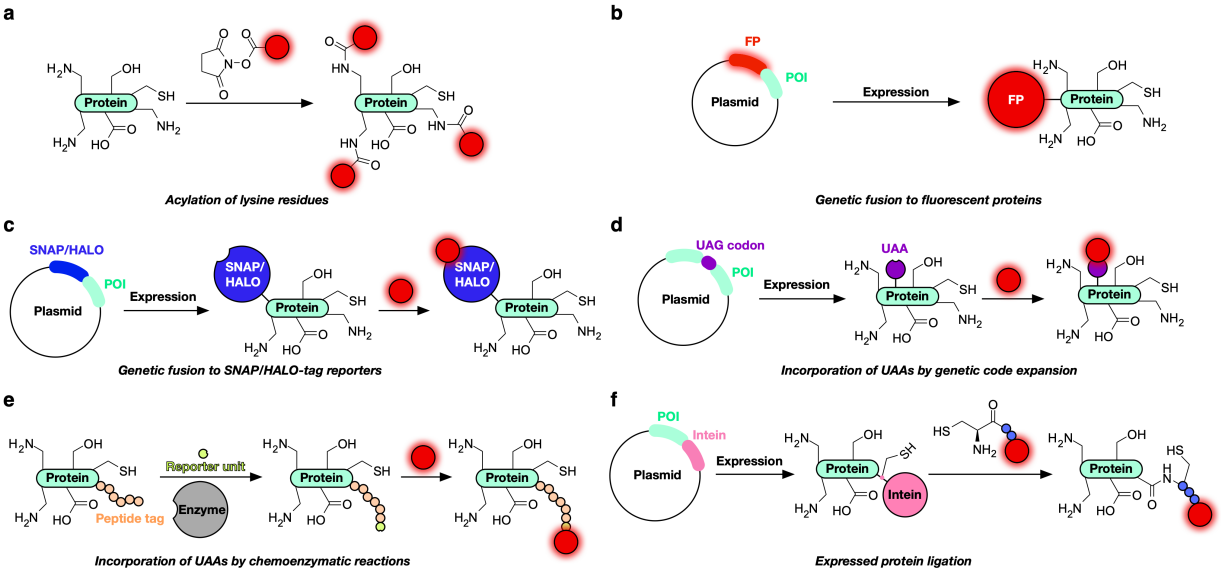

Figure 2.14.: **Protein functionalization methods.** a) Labeling of lysine residues leading to inhomogeneous product mixtures due to the high abundance of lysine. b) *In cellulo* or *in vivo* expression of the protein of interest (POI) fused to a fluorescent protein (FP) either an its *N*- or *C*-terminus. c) Expression of the POI fused to either the SNAP- or the HALO-tag allowing the functionalization with different moieties such as fluorophores, biotin or beads carrying a benzylguanine (SNAP) or haloalkane (HALO). d) Site-specific incorporation of unnatural amino acids (UAA) at the Amber Stop Codon (UAG) *via* utilization of orthogonal tRNA/aminoacyl-tRNA synthetase pairs. e) Naturally occurring enzymes or evolved variants can recognize a small peptidic tag on the POI and attach an UAA or modify one of its amino acids to install a chemical reporter. This reporter unit can now be targeted using bioorthogonal chemistry with e.g. a fluorophore or a drug molecule. f) The expression of the POI fused to an intein allows not only purification of the POI, but also the attachment of modified peptides or even proteins after an *S,N*-acyl shift. The ligation of the two fragments leaves a cysteine residue at the ligation site and the two parts are fused together by a native amide bond making protein semisynthesis possible.

pansion) or peptidic tags which need to be incorporated for successful enzymatic recognition.

This work will make use of a much more straightforward method of protein modification utilizing the high nucleophilicity and low abundance (less than 2%) of the amino acid cysteine.[134] While not being generally applicable for site-specific protein functionalization, in the right systems containing e.g. only one solvent-exposed cysteine residue, this technique can be used to generate homogeneous protein-conjugates. There is a variety of different methods available for the modification of cysteine with Fig. 2.15 showing a selection of the most widely used methods. Out of the methods shown in Fig. 2.15, the alkylation with iodoacetamide, disulfide exchange reactions with electrophilic disulfides and the Michael-addition to maleimides are the most commonly used methods.[134,154] Whereas iodoacetamide is often employed as a capping reagent e.g. before protein digestion for sequencing, disulfide exchange reactions lead to bioconjugates, that can be cleaved again under reducing conditions. This additional feature makes them interesting e.g. for targeted drug delivery and intracellular release. Apart from that also other methods have been developed for cysteine-selective protein functionalization proceeding via

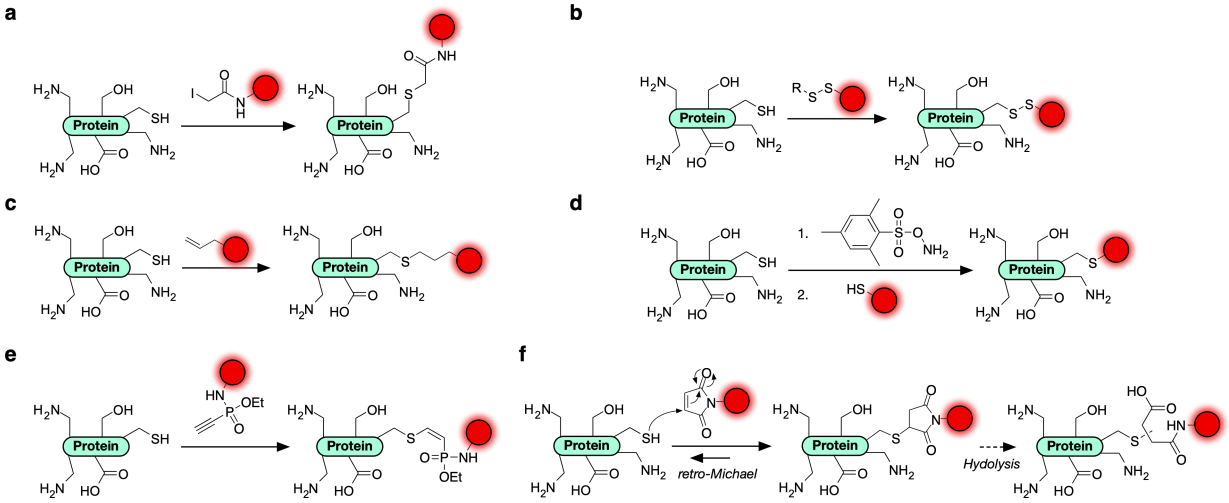

Figure 2.15.: **Methods for cysteine functionalization.** a) Alkylation of cysteine using iodoacetamide. b) Disulfide exchange with electrophilic disulfides. c) Radical-catalyzed thiol-ene chemistry. d) Conversion of a cysteine residue to dehydroalanine and subsequent Michael addition. e) Addition of the protein to electron-poor alkynephosphonamidates generated from electron-rich alkynephosphonites through Staudinger-phosphonite reaction. f) Michael addition of a protein's thiol to a maleimide resulting in a thioether-linked conjugate, which could undergo hydrolysis to the thiosuccinimide or react backwards in a retro-Michael reaction with an excess of competitive thiols.

alternative mechanisms (dehydroalanine formation and subsequent Michael-addition or radical chemistry in thiol-ene reactions, Fig. 2.15d/e) and/or offering increased stability when e.g. compared to standard maleimide chemistry such as the cysteine addition to electron-poor ethynylphosphonamidates recently introduced by Kasper et al.[155].
In the course of this work, however, standard maleimide chemistry (Fig. 2.15f) will be employed for cysteine-selective attachment to SWCNTs yielding a thioether-linked conjugate. This reaction proceeds via a Michael addition, where the cysteine's deprotonated thiol ($pK_a \sim 8$) attacks the maleimide leading to an strongly basic enolate intermediate, which, after abstraction of a proton from another thiol (cysteine), forms the thiosuccinimide (see Fig. 2.15f). Due to the high polarizability and resulting soft nucleophilicity of the thiolate, thiol-Michael-additions with maleimides proceed with fast kinetics under physiological conditions.[156] In this work, the maleimide moiety will be employed within a phenylmaleimide diazonium salt for covalent SWCNT-functionalization and the cross-linker sulfosuccinimidyl-4-(N-maleimidomethyl)cyclohexan-1-carboxylate (Sulfo-SMCC) for attachment to the DNA-polymeric phase around the SWCNTs. Sulfo-SMCC also contains an amine-reactive succinimidyl-ester and thereby enables the attachment of a protein to an amine-modified DNA-oligonucleotide wrapping a carbon nanotube. This strategy and others have already been employed successfully in the past for the generation of SWCNT-Protein conjugates and functional sensors, which will be described in the following section.

2.4.2. Functional conjugates and sensors

While in the previous section the importance of chemo- and regioselectivity was discussed, the following lines will give a selection of examples, where SWCNT/Protein-hybrids were already successfully used in *in vitro* or *in vivo* applications.
The first carbon nanotube/protein hybrids were reported by Tsang et al. in 1995[157] using metallothionein proteins non-covalently adsorbed to the inside of multi-walled carbon nanotubes (MWCNTs) followed by Balavoine et al. in 1999[158], who managed to coat the outer surface of MWCNTs with streptavidin (see Fig. 2.16a). Both of these early discoveries were proven using electron microscopy. Only shortly afterwards, in 2001, Erlanger et al. used a monoclonal IgG, originally targeted towards the C_{60} fullerene, for binding of SWCNTs, mediated by a large extent of hydrophobic residues in the antigen binding region. They were able to image the SWCNT/Antibody hybrid using atomic

force microscopy (AFM).[159] The following years saw, in addition to more non-covalent approaches, a major rise of covalent chemistry on carbon nanotubes and the attachment of peptides and proteins to covalent carboxylic acid defects or those created by the 1,3-dipolar cycloaddition with azomethine ylides. Whereas the former was pioneered by Huang et al. with the covalent immobilization of bovine serum albumine (BSA) on the sidewalls of SWCNTs and MWCNTs after carbodiimide activation[56], Pantarotto et al. used azomethine ylide defects for the attachment of a 20-mer peptide from the viral envelope protein VP1 with retained structural integrity in 2003[79]. In 2007, You et al. reported a strategy for the stimuli-sensitive covalent immobilization of proteins on SWCNTs *via* disulfide bonds cleavable under reducing conditions (see Fig. 2.16b).[160] In order to achieve functional electrical or optical sensors, non-covalent functionalization was often the method of choice as also in a few SWCNT/Enzyme hybrids[162] or SWCNT-Glucose-binding protein conjugates, which were able to detect glucose *via* a conformational shift of the protein resulting in a change of the SWCNT's dielectric environment and thus altered PL (see section 2.2.4).[161] A similar readout strategy was utilized in another striking example of nanotube/protein hybrids by Ahn et al., who generated a nanotube/protein microarray by cell-free synthesis of His-tagged proteins directly on Ni^{2+}-nitrilotriacetic acid (NTA)-modified chitosan wrapped carbon nanotubes (see Fig. 2.16d). The Ni^{2+}-ion acts as a proximity quencher for the SWCNT's PL and is, upon binding of the analyte protein to the His-tagged protein, displaced either towards or away from the nanotube's surface resulting in either increased or diminished nIR-PL.[95] In addition to the described examples, also antibodies were already immobilized on carbon nanotubes for the use in biomedical applications. In 2009, Liu et al. presented a protocol for the non-covalent immobilization of the anti-Her2 antibody Herceptin *via* a phospholipid-polyethyleneglycol(PEG)-5000-linker and used the conjugate for the *in vivo* nIR imaging of tumor vessels.[163] Williams et al. in contrast, used an antibody against the ovarian cancer biomarker human epididymis protein 4 (HE4) as a targeting unit to create a nIR-PL based sensor for this biomarker operating *via* a wavelength-shift readout model. After successful *in vitro* validation, the authors were able to apply this sensor also in mouse ovarian cancer models for the *in vivo* monitoring of HE4 (see Fig. 2.16e).[96]
The approaches presented here highlight the potential of SWCNT/Protein hybrids, however, until now only non-covalent functionalization approaches were utilized for NIR-fluorescent SWCNTs and their decoration with e.g. antibodies. In contrast, this work should also explore the potential for covalent nanotube functionalization using sp^3-

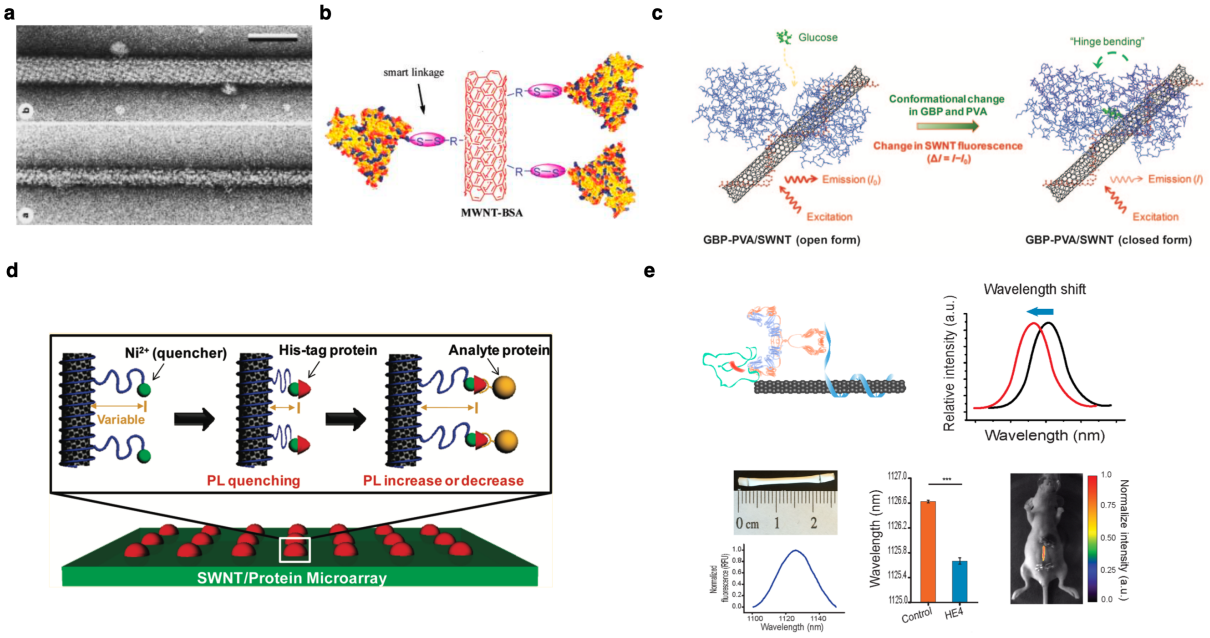

Figure 2.16.: **SWCNT-Protein conjugates and applications.** a) Multi-walled carbon nanotubes (d<15 nm) stochastically coated with the protein streptavidin *versus* helical organization of streptavidin on larger MWCNTs (d=16 nm). Reproduced with permission from Balavoine et al.[158] b) Conjugation of bovine serum albumine (BSA) to SWCNTs via a disulfide bond, which can be cleaved under the right conditions (e.g. excess thiol) and is thus termed 'smart linkage'. Reproduced with permission from You et al.[160] c) SWCNT-Glucose-binding protein (GBP) hybrid, which is able to detect glucose through a conformational change of the protein and thus altered SWCNT photoluminescence (PL). Reproduced with permission from Yoon et al.[161] d) SWCNT/Protein microarray for selective protein recognition. Upon binding of the analyte protein to the His-tag protein, the Ni^{2+}-quencher is displaced altering the SWCNT's PL. Reproduced with permission from Ahn et al.[95] e) SWCNT-antibody conjugate for the detection of an ovarian cancer biomarker (HE4) working *via* a blue-shift of the SWCNT's PL upon antigen-binding. The so created sensor was then also applied for antigen-monitoring in mice. Reproduced with permission from Williams et al.[96]

defects as described in section 2.2.3 as well as the use of smaller proteinaceous recognition units such as nanobodies to decrease the distance of the carbon nanotube and the binding event. These efforts as well as other strategies to create nIR-fluorescent SWCNT-based sensors will be described in the following chapters.

3 | Objectives

Carbon nanotubes have, since their discovery almost 30 years ago, found applications in many different fields of science owing to their unique molecular nature and the resulting properties that are interesting not only for the application in transistors, as single-photon sources, fluorophores or drug delivery vehicles, but also as optical sensors. They were used for the detection of a variety of different analytes ranging from metal ions over small molecules such as glucose to whole proteins. While a few of these sensors were fabricated through immobilization of analyte-binding proteins such as the glucose-binding protein, the larger portion was created *via* structural confinement of a (bio)polymer on the SWCNT's surface. This concept was coined Corona Phase Molecular Recognition and describes the process of the (bio)polymer adapting 3D structures on the SWCNT surface, which would be otherwise not accessible in solution. While this process has proven to yield successful sensors in many cases, the screening process remains tedious and selectivity of these sensors can be an issue. In addition, often DNA oligonucleotides or phospholipids were chosen as the corona phase to impart selectivity, however, their structural space is very limited compared to peptides and proteins, which are largely unexplored in conjunction with SWCNTs to this date.
Consequently, the aim of this work is to elucidate and test different ways for the functionalization of carbon nanotubes and their impact on their photophysical properties, their ability to act as a biosensors and the possibility of targeted placement/delivery of these fluorescent molecules.

GOAL 1 - Competitive detection of the neurotransmitter dopamine

Carbon nanotubes wrapped by the DNA oligonucleotide $(GT)_{15}$ were shown to be sensitive towards the neurotransmitter dopamine[5] and this concept has also been used recently for the spatiotemporal imaging of dopamine release from PC12 cells.[97] In this early work, however, the selectivity has not been heavily investigated especially with regard to the discrimination of other relevant catecholamines. Thus, the aim of this project is to test different DNA oligonucleotides for the PL response to dopamine, epinephrine

and norepinephrine, which are two structurally very similar neurotransmitters, that also cause cross-reactivity in other established electrochemical sensor formats.[164] Using this systematic study, the influence of the DNA sequence on the sensor response should be evaluated and eventually used to create more selective dopamine sensors.

GOAL 2 - Targeted delivery of nanosensors

Carbon nanotube based optical sensors have demonstrated their potential for the monitoring of a variety of biologically relevant analytes in the recent years. However, envisioning *in vivo* applications, the placement of these sensors will be a factor of crucial importance. If injected, the nanoscopic sensors would diffuse freely and randomly associate e.g. with blood plasma proteins or unspecifically adsorb to tissue. For this reason, the aim of this project is to use nanobodies as a targeting unit on the carbon nanotube while still preserving the sensing capabilities. This approach should be demonstrated with the SWCNT-DNA-based dopamine sensors and a nanobody capable of binding GFP, which would open up the possibility of targeting and studying a whole variety of proteins expressed as GFP-fusions already in *in vivo* settings.

GOAL 3 - Peptides as a more versatile SWCNT surface modification

SWCNT-based optical sensors are mainly composed of DNA oligonucleotide or phospholipid coatings. However, the 20 proteinogenic amino acids constituting proteins and peptides do not offer only a much larger structural variety, but also allow the introduction of residues carrying e.g. different charges. To make use of this larger structural space for the development of SWCNT-based sensors, α-helical coiled-coil peptide barrels will be evaluated for their capabilities to encapsulate SWCNTs and stabilize them in aqueous solution. Furthermore, recently discovered sp^3 defects in the nanotube's sidewall leading to red-shifted PL emission will be explored as a platform for SWCNT functionalization. To achieve this, two anchor-group bearing diazonium salts will be synthesized and tested with respect to defect incorporation and change of the nIR fluorescence. Furthermore, their phenylalanine and maleimide anchor groups will be used as a starting point for peptide growth directly on the nanotube's sidewall and nanobody attachment, respectively. If successful, this could lead to much more stable SWCNT-bioconjugates for applications in nIR-labelling and -sensing.

4 Results and Discussion

4.1 Competitive detection of the neurotransmitter dopamine

Neurotransmitters are molecules essential to cognitive processes and the function of our brain. In addition, neurotransmitters including dopamine are linked to several severe neurological disorders such as Huntington's and Parkinson's disease or schizophrenia.[165] Thus, it is essential to be able to detect neurotransmitter signaling in order to gain a better understanding of these fundamental processes. Although there are several techniques to detect neurotransmitters based e.g. on their redox potential using amperometry or fast scan cyclic voltammetry (FSCV), these techniques are not able to provide the temporal or spatial resolution necessary to resolve release events.[166] In the last years, DNA-oligonucleotide wrapped carbon nanotubes gained attention for application as optical sensors for the spatiotemporal monitoring of dopamine release events.[5,97] However, these sensors were not yet thoroughly evaluated regarding their selectivity with respect to structurally similar neurotransmitters (epinephrine, norepinephrine) and their binding characteristics (dissociation constants). Therefore, the aim of this project is to further study the relationship between the DNA oligonucleotide's sequence and the selectivity and sensitivity of the SWCNT-based dopamine sensors (K_d values, limit of detection (LOD)) in order to ultimately enable competitive detection of dopamine at equimolar concentrations of epinephrine and/or norepinephrine.

4.1.1. Tuning Selectivity of Fluorescent Carbon Nanotube-Based Neurotransmitter Sensors (Manuscript 1)

This chapter was published in the following journal:

Florian A. Mann, Niklas Herrmann, Daniel Meyer and Sebastian Kruss*

"Tuning Selectivity of Fluorescent Carbon Nanotube-Based Neurotransmitter Sensors"

Sensors **2017**, 17, 1521

The article is available at: DOI:10.3390/s17071521
* Corresponding author

Responsibility assignment: S.K. designed and conceived the project with inputs from F.A.M.. F.A.M. and N.H. performed SWCNT dispersion, absorbance/fluorescence spectroscopy as well as microscopy experiments. F.A.M. performed the data analysis. F.A.M. and S.K wrote the manuscript with input from N.H..

sensors

MDPI

Article

Tuning Selectivity of Fluorescent Carbon Nanotube-Based Neurotransmitter Sensors

Florian A. Mann [1,2], Niklas Herrmann [1], Daniel Meyer [1,2] and Sebastian Kruss [1,2,*]

[1] Institute of Physical Chemistry, Göttingen University, 37077 Göttingen, Germany; florian.mann@med.uni-goettingen.de (F.A.M.); niklas.herrmann1@stud.uni-goettingen.de (N.H.); daniel.meyer@uni-goettingen.de (D.M.)

[2] Center for Nanoscale Microscopy and Molecular Physiology of the Brain (CNMPB), 37073 Göttingen, Germany

* Correspondence: skruss@uni-goettingen.de; Tel.: +49-551-392-0936

Received: 30 April 2017; Accepted: 25 June 2017; Published: 28 June 2017

Abstract: Detection of neurotransmitters is an analytical challenge and essential to understand neuronal networks in the brain and associated diseases. However, most methods do not provide sufficient spatial, temporal, or chemical resolution. Near-infrared (NIR) fluorescent single-walled carbon nanotubes (SWCNTs) have been used as building blocks for sensors/probes that detect catecholamine neurotransmitters, including dopamine. This approach provides a high spatial and temporal resolution, but it is not understood if these sensors are able to distinguish dopamine from similar catecholamine neurotransmitters, such as epinephrine or norepinephrine. In this work, the organic phase (DNA sequence) around SWCNTs was varied to create sensors with different selectivity and sensitivity for catecholamine neurotransmitters. Most DNA-functionalized SWCNTs responded to catecholamine neurotransmitters, but both dissociation constants (K_d) and limits of detection were highly dependent on functionalization (sequence). K_d values span a range of 2.3 nM (SWCNT-$(GC)_{15}$ + norepinephrine) to 9.4 µM (SWCNT-$(AT)_{15}$ + dopamine) and limits of detection are mostly in the single-digit nM regime. Additionally, sensors of different SWCNT chirality show different fluorescence increases. Moreover, certain sensors (e.g., SWCNT-$(GT)_{10}$) distinguish between different catecholamines, such as dopamine and norepinephrine at low concentrations (50 nM). These results show that SWCNTs functionalized with certain DNA sequences are able to discriminate between catecholamine neurotransmitters or to detect them in the presence of interfering substances of similar structure. Such sensors will be useful to measure and study neurotransmitter signaling in complex biological settings.

Keywords: carbon nanotube; biosensor; fluorescence; DNA; neurotransmitter; affinity

1. Introduction

Neurotransmitters are essential for basic functions of the human body and especially for chemical signaling in neuronal circuits of the brain. However, their mode of action is widely unexplored due to a lack of tools to measure their concentration profiles in a spatiotemporal manner. In the past decades several analytical methods have been developed to measure neurotransmitter concentrations [1–5]. Those methods range from magnetic resonance imaging with contrast agents for neurotransmitters to electrochemical approaches, but most of them lack either high spatial or temporal resolution or they are not compatible with biological environments [2–4,6]. The detection of neurotransmitters is very challenging because of several limiting conditions. First, many neurotransmitters are small molecules that share structural homologies with each other and with additional interfering substances in the brain or in the cell culture. Second, during exocytotic events only 100–100,000 molecules are released within milliseconds [7]. Finally, the most prominent release sites, i.e., synapses, are very small

($300 \times 300 \times 20$ nm^3) and not easily accessible by macroscopic probes [8]. All these hallmarks of neural networks indicate that neurotransmitter sensors should be sensitive/selective (single-molecule level), label-free, small (nanoscale), fast (milliseconds), and non-invasive (e.g., optical).

Classical approaches to detect (redox-active) neurotransmitters are electrochemical methods such as amperometry or cyclic voltammetry [9,10]. Many biological studies were only possible because these methods provided quantitative information about neurotransmitter concentrations around cells, in brain slices and in vivo [2,11]. However, electrochemical methods are limited to molecules that can be oxidized at the electrode (e.g., dopamine or serotonin) or make use of enzymatic reactions [12]. Therefore, important neurotransmitters, such as glutamate or γ-aminobutyric acid (GABA), cannot be detected. Moreover, electrodes are large compared to the site of neurotransmitter release, which limits simultaneous and parallel/spatial detection. Another approach is based on modifying biological recognition units of neurotransmitters and conjugating them with fluorescent dyes. This method was used to engineer GABA sensors and glutamate sensors [13,14]. Recently, glutamate was detected by using green-fluorescent protein (GFP)-conjugated glutamate receptors that can be also transfected into cells [15]. The disadvantage of this approach is the need for cell transfection and manipulation, which is difficult in complex primary biological samples and in vivo. Additionally, sensing is restricted to the cell surface and, therefore, diffusion characteristics cannot be assessed.

Nanomaterials are promising building blocks for neurotransmitter sensors/probes [1]. Among the different materials carbon nanotubes attract a lot of interest due to their unique optoelectronic properties. Semiconducting single-walled carbon nanotubes have a bandgap that leads to near infrared (NIR) fluorescence [16]. SWCNTs can be non-covalently decorated with an organic phase generating the desired specificity for the molecular target. Examples for sensors of this class range from small molecule analytes, like neurotransmitters, sugars, and explosives, to miRNA or proteins [17–23]. These sensors combine specificity for the target generated by the organic corona-phase and the advantageous properties of SWCNTs for optical sensing and imaging [16,24–26]. These advantages are, among others, the extraordinarily high photostability compared to organic fluorophores, the absence of fluorescence blinking, as well as the large Stokes-shift of >400 nm allowing for low-background imaging in the biologically-transparent near-infrared (NIR) window [16]. Such reversible sensors have been used to detect the efflux of dopamine from cells by imaging many of them at the same time [5]. This approach enabled a spatial resolution that was not possible before with electrochemical approaches.

The organic phase (corona) around these sensors plays a central for molecular recognition and signal transduction. The mechanism and the reasons for selectivity are, however, still not completely understood. Fluorescence changes were attributed to conformational changes, redox chemistry and free surface area [5,27,28]. Another possible mechanism could be a change of exciton diffusion upon binding of an analyte [29].

Although SWCNT-based sensors have shown great potential for interesting applications, there are still several obstacles to overcome with respect to specificity, affinity, and kinetics. Especially kinetics (rate constants) and dissociation constants play decisive roles in the fast detection of neurotransmitters [30]. These issues have not yet been taken into account so far, but will be important to enable applications in chemically-complex environments.

In this work, we address remaining challenges of neurotransmitter detection with carbon nanotube-based sensors by varying the organic phase around the SWCNT scaffold and evaluating the resulting dissociation constants and limits of detection for relevant neurotransmitters. This approach (Figure 1) enables us to identify organic phases (DNA sequences) that impart the best sensor performance (selectivity, sensitivity at relevant concentrations, dynamic range, etc.).

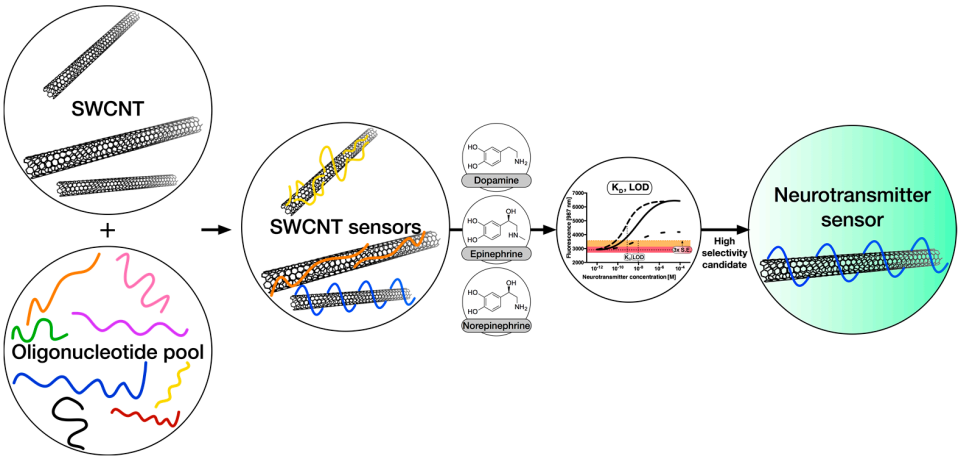

Figure 1. Strategy to measure and optimize selectivity and sensitivity of neurotransmitter sensors. Candidate sensors are synthesized from single-walled carbon nanotubes (SWCNTs) and DNA oligonucleotides and their responses to the neurotransmitters dopamine, epinephrine and norepinephrine are quantified. Crucial for the success of these sensors is the discrimination between different, but chemically very similar, neurotransmitters. In this work, a set of different DNA-oligonucleotides is tested as an organic phase and corresponding sensor properties, such as K_d-values, are evaluated to find the most selective and robust sensors.

2. Materials and Methods

Materials: Unless stated otherwise, all chemicals and oligonucleotides were purchased from Sigma Aldrich (Taufkirchen, Germany) or TCI (Eschborn, Germany). For epinephrine and norepinephrine, the racemic mixture was used.

Dispersion and functionalization of carbon nanotubes: To generate a stable single-walled carbon nanotube (SWCNT) dispersion under physiological conditions, 0.5 mg oligonucleotide was added to 0.5 mg of 6,5-chirality enriched SWCNT (Sigma Aldrich, Product No.: 773735) in 0.5 mL 1× phosphate-buffered saline (PBS). The resulting suspension was first tip sonicated for 10 min (Fisher Scientific™ Model 120 Sonic Dismembrator, 20% amplitude) and subsequently centrifuged at 16,100 g (2 × 30 min) to remove large bundles, aggregates or metal catalysts remaining from SWCNT synthesis. The supernatant containing individualized SWCNTs was used as a stock solution for downstream experiments after absorbance measurements and estimation of nanotube concentration using the molar extinction coefficient at 991 nm [31]. The solutions corresponding to the different DNA-sequences were adjusted in concentration according to the collected absorbance spectra.

Spectroscopy of SWCNT-DNA complexes: NIR absorbance spectra were measured with a UV-VIS-NIR spectrometer (JASCO V-670, Spectra Manager Software) using a 10 mm-path cuvette.

NIR fluorescence spectra were recorded on a Shamrock 193i spectrograph (Andor Technology Ltd., Belfast, Northern Ireland) coupled to an Olympus BX53 microscope using an exposure time of 10 s and a slit width of 500 µm and an Andor iDus InGaAs 491 array NIR detector. SWCNTs were excited at 560 nm.

NIR-fluorescence dose-response curves: Ten microliters of the corresponding and freshly-prepared catecholamine ·HCl solution (0, 100 pM, 1 nM, 10 nM, 100 nM, 1 µM, 10 µM, 100 µM) in 1× phosphate-buffered saline (PBS) were added to 90 µL of DNA-suspended SWCNTs (0.1 nM, in 1× PBS) in a 96-well plate format. The fluorescence counts were averaged from triplicates and plotted against the neurotransmitter concentration on a log-scale.

Extraction of dissociation constants from dose-response curves: The NIR-fluorescence dose-response curves were fitted using Equation (2). From this fit the dissociation constant and its 95% confidence interval were extracted for each combination of SWCNT-DNA sensor and catecholamine. In the case of dopamine, 100 µM values were neglected for K_d estimation, as dopamine is prone to

oxidation and polymerization at higher concentrations [32,33], which was previously shown to have an effect on SWCNT-DNA fluorescence modulation [17].

Near infrared microscopy of immobilized SWCNT-DNA sensors: Twenty microliters of the 0.1 nM SWCNT-DNA (SWCNT-$(GT)_{10}$, SWCNT-$(GA)_{15}$) solution were incubated on (3-aminopropyl)triethoxysilane (APTES)-pre-activated glass bottom Petri dishes (1 wt % APTES/H_2O in EtOH, 1 h) overnight at 4 °C. After a 1× PBS wash, NIR imaging was carried out on an Olympus BX53 microscope (Olympus K.K., Tokyo, Japan) using a 60× oil-immersion objective and a Xenics® Xeva-1.7-320 NIR camera (Xenics, Heverlee, Belgium). The frame-rate was set to 0.5 fps. After approx. 10 frames, 20 µL 100 nM norepinephrine solution was added to the adsorbed SWCNT-DNA. Dopamine was added after 50 additional frames in the same volume and concentration to yield 40 µL containing 50 nM of each neurotransmitter.

Dose-response measurements of immobilized SWCNT-DNA sensors: One-hundred microliters of a 1.1 µM SWCNT-$(GT)_{10}$ solution in 1× PBS was incubated on glass-bottom Petri dishes for one hour at 4 °C. After a 1× PBS wash, NIR imaging was carried out on an Olympus BX53 microscope using a 60× oil-immersion objective and a Xenics® Xeva-1.7-320 NIR camera. The frame-rate was set to 0.5 fps. Approx. every 30 frames, 5 µL of increasing dopamine concentrations (a = 1 nM, b = 10 nM, c = 100 nM, d = 1 µM, e = 10 µM) were added to a 50 nM norepinephrine solution (in 1× PBS, 500 µL) on top of the adsorbed SWCNT-DNA.

3. Results

3.1. Preparation and Optical Properties

(6,5)-chirality enriched SWCNTs were dispersed using tip-ultrasonication with ten different oligonucleotides in 1× PBS (pH 7.4). The corresponding absorbance and NIR-fluorescence emission spectra are shown for $(GT)_{10}$ as an example in Figure 2.

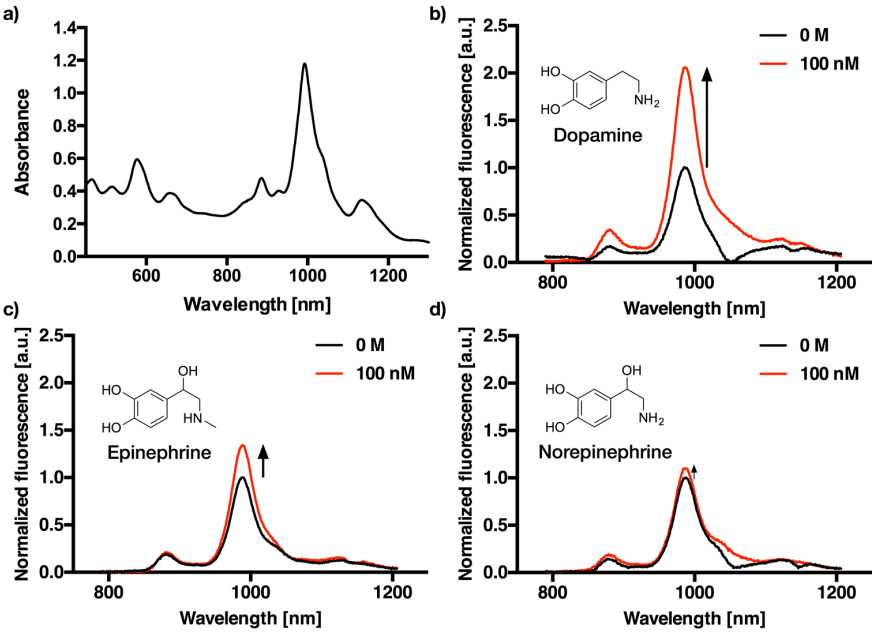

Figure 2. Absorbance and fluorescence spectra of DNA-dispersed single-walled carbon nanotubes (SWCNT). (**a**) VIS-NIR absorbance spectra of $(GT)_{10}$-dispersed SWCNT. (**b**) NIR-fluorescence emission spectra of $(GT)_{10}$-dispersed SWCNT after the addition of 0 M (black) and 100 nM dopamine (red). (**c**) NIR-fluorescence emission spectra of $(GT)_{10}$-dispersed SWCNT after the addition of 0 M (black) and 100 nM epinephrine (red). (**d**) NIR-fluorescence emission spectra of $(GT)_{10}$-dispersed SWCNT after the addition of 0 M (black) and 100 nM norepinephrine (red).

The absorbance spectra (Figures 2a and A1) clearly show that it is possible to disperse the otherwise insoluble carbon nanotubes with all tested DNA sequences. For the fluorescence measurement with an excitation wavelength of 560 nm, SWCNT-DNA conjugates were adjusted in concentration to 0.1 nM according to their absorbance at the S_{11} peak at around 991 nm [31].

Figure 2b–d shows the representative fluorescence spectra of $(GT)_{10}$-dispersed SWCNT before and after the addition of 100 nM dopamine, epinephrine, and norepinephrine. Between the three neurotransmitters, which were selected due to their structural similarity to dopamine, there is a clear difference in fluorescence intensity modulation at this concentration. Interestingly, most SWCNT-DNA conjugates responded to catecholamines by an increase of fluorescence. However, the absolute changes depend strongly on DNA sequence and structure of the analyte. This is in agreement with previous studies and indicates that these SWCNT-DNA conjugates can serve as sensors for catecholamine neurotransmitters [5,27]. However, the limits of detection and the dynamic range remained unclear, which is important if there are multiple catecholamines present in a sample.

3.2. Dose-Response Curves for Dopamine, Epinephrine, and Norepinephrine

A good sensor should not only be sensitive for its respective analyte, but also show high selectivity for its target and exclude biologically-relevant interfering molecules. To evaluate, whether the sensors for dopamine built from SWCNTs and oligomeric DNA sequences are suitable for the desired kind of discrimination between these neurotransmitters, we took the aforementioned pool of sensors and collected dose-response curves for each of them against dopamine, epinephrine, and norepinephrine. The resulting relative changes in fluorescence for each combination are depicted in Figure 3.

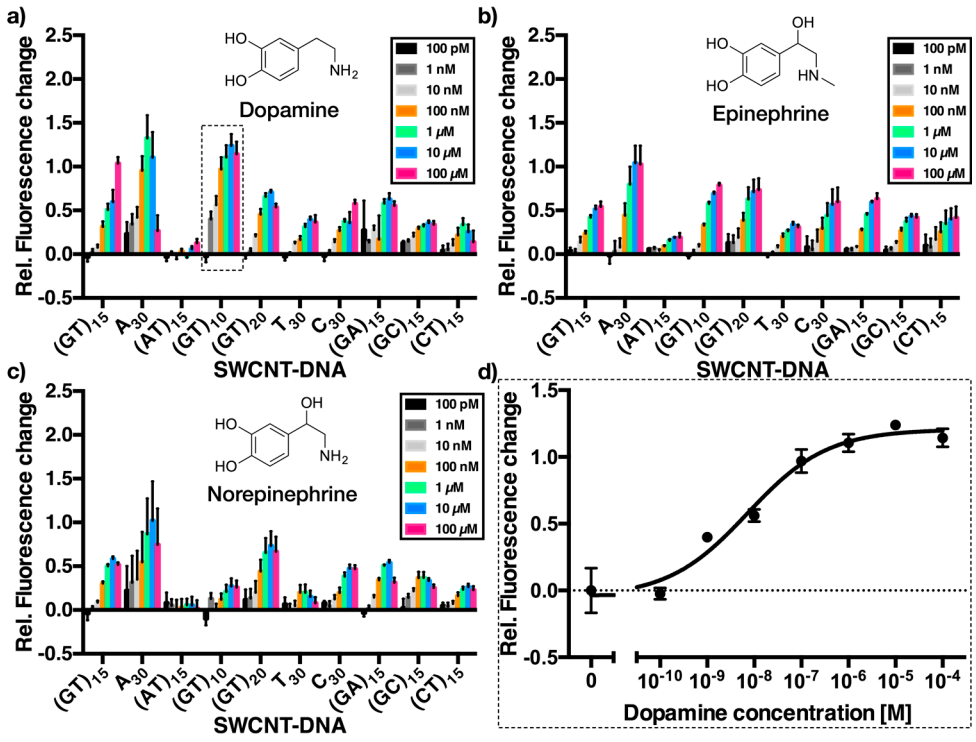

Figure 3. Dose-response curves of different catecholamine SWCNT/DNA sensors. Relative fluorescence change of the sensors upon addition of increasing concentrations (0, 100 pM, 1 nM, 10 nM, 100 nM, 1 µM, 10 µM, 100 µM) of dopamine (**a**), epinephrine (**b**), and norepinephrine (**c**). The *x*-axis shows different DNA sequences used to functionalize the SWCNTs. Here, the (6,5)-SWCNTs responses were evaluated. Errors are standard deviations (n = 3). (**d**) An example dose-response plot for dopamine recognition of SWCNT-$(GT)_{10}$. Errors are standard deviations (n = 3).

The data shown in Figure 3 contains all the information to evaluate sensor performance. The first and most obvious observation is that almost all SWCNT-DNA sensors react upon exposure to dopamine, epinephrine, and norepinephrine with an increase in NIR fluorescence. A_{30}, $(GT)_{10}$ and $(GT)_{20}$ show the largest relative fluorescence increase for dopamine and epinephrine, while $(GT)_{10}$-dispersed SWCNT only react minimally to norepinephrine. Interestingly, SWCNT-$(AT)_{15}$ does not show any change in fluorescence in case of dopamine and norepinephrine and only a small change to epinephrine. However, for most analytical tasks it is important to consider relevant concentrations. For example, the maximum concentration of 100 µM used in these assays is high and will most likely not be reached (for long periods of time) in biological scenarios [34]. All sensors respond to catecholamines with different magnitudes and they saturate at different concentrations. Therefore, it should be possible to discriminate between different neurotransmitters at concentrations << 100 µM (see Figure 3).

The heatmap in Figure 4 illustrates the relative NIR-fluorescence change of DNA-dispersed (6,5)-SWCNTs upon exposure to 100 nM and 1 µM dopamine, epinephrine and norepinephrine. Especially A_{30}, $(GT)_{10}$ and $(AT)_{15}$ exhibit a different response to the three different neurotransmitters at these concentrations. This presentation of the response data is different from Figure 3 because it sets the focus on smaller concentrations, which are most likely more relevant in many analytical scenarios. For example, the static concentration of catecholamine neurotransmitters in brain tissue is in the order of 1–50 nM [35]. In contrast, concentrations of dopamine in vesicles reach values >100 mM [11]. When they are released, dopamine levels are very high for the first few milliseconds but decline very quickly to the nM regime [30]. Therefore, the effective mean concentration that is seen by a sensor during acquisition is typically in the range depicted in Figure 4 (1 nM–1 µM). Consequently, response data in this concentration regime provide a more realistic picture than at higher concentrations, at which most sensors already saturate. The results shown in Figure 4 indicate that for example at catecholamine concentrations of 100 nM the SWCNT-$(GT)_{10}$ sensor is able to distinguish between dopamine and epinephrine/norepinephrine as the corresponding relative fluorescence intensity changes are 0.97 (±0.14) vs. 0.33 (±0.02)/0.12 (±0.07).

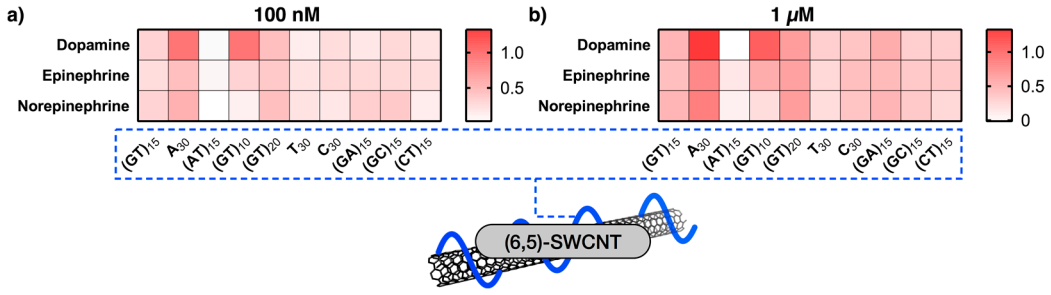

Figure 4. Sensitivity versus selectivity at low catecholamine concentrations. Relative fluorescence change of sensors upon addition of 100 nM (**a**) and 1 µM (**b**) of dopamine, epinephrine, and norepinephrine in the range from 0 (i.e., no change in fluorescence intensity) to 1.3 (equaling 130% fluorescence increase). Here, the (6,5)-SWCNTs responses at 987 nm were evaluated.

As already shown by Salem et al., the chirality of the SWCNTs has an influence on SWCNT/DNA sensors similar to those presented in this work [36]. This behavior can be expected because different chiralities/diameters should cause different macromolecule adsorption (organic phases) and, therefore, different sensor responses. The corresponding heatmaps for the (6,4)- and (8,4)-SWCNT species are provided in Figure A2. Both chiralities also show increasing fluorescence at ≈885 nm and ≈1122 nm, respectively. The relative fluorescence increase, however, differs quite significantly (Figure A2). We attribute these large differences to a chirality dependence but the spectra consist of at least three nanotube species (6,4), (6,5), and (8,4) and the absolute differences might, therefore, be convoluted. Additionally, the experiments were performed for constant (6,5)-SWCNT concentrations (0.1 nM),

adjusted via the (6,5)-S_{11} peak. The SWCNT concentration can have an influence on the absolute fluorescence values/changes and different dispersion yields by different DNA-oligonucleotides could affect it [5]. In the future, our studies could be extended to highly-purified (6,4) and (8,4) SWCNT species to study chirality dependence in greater detail.

3.3. Dissociation Constants and Limits of Detection for Different Neurotransmitter-Sensors

The recognition of catecholamines by SWCNT-DNA sensors can be seen as a bimolecular reaction:

$$S + A \rightleftharpoons SA. \tag{1}$$

Here, the sensor S reacts with an analyte A to form a sensor/analyte complex SA. To get an idea of the dynamic range and the limits of detection for the different sensor-analyte combinations, the dose-response curves (Figure 3) were fitted using Equation (2):

$$Y = y_{min} + \frac{y_{max} - y_{min}}{1 + 10^{(\log(K_D) - X) \times HillSlope}} \tag{2}$$

The obtained dissociation constants from this logistic fit are shown in Table 1 and in a heatmap (Figure A3). In addition, Table 1 also contains the limits of detection extracted from each dose-response curve for every sensor-analyte combination.

Table 1. Overview of the different dissociation constants (K_d) and limits of detection (LOD) values obtained for each SWCNT-DNA sensor-neurotransmitter combination. Both K_d and LOD are in nmol/L.

	NT	$(GT)_{15}$	$(GT)_{20}$	$(GT)_{10}$	A_{30}	C_{30}	T_{30}	$(GA)_{15}$	$(GC)_{15}$	$(CT)_{15}$	$(AT)_{15}$
K_d	D	395.2 *	42.3	9.2	28.4	499.2 *	237.2	627.8 *	0.7 *	25.8	9438
	E	159.1	112.6	178.2	171.9	177.2	51.1	234.3	49.3	47.1	241.5
	N	70.3	58	71.9	25	193.1	33.6 *	21.4	2.3	52.8	-*
LOD	D	6.4 *	0.6	0.1	3.6	2.7 *	1.2 *	507.2	28.5 *	4.4	3776.6
	E	1.4	2.2	0.7	3.2	1.4	1.0	1.8	0.5	0.8 *	23.7
	N	3.2	2.4	7.7	1.6	4.8	33.3	3.8	0.5	3.9	*

* No clear (sigmoidal) fit possible. K_d: Dissociation constant. LOD: Limit of detection definition used = 3× standard error at c = 0 nM. D: Dopamine. E: Epinephrine. N: Norepinephrine.

The results show that there are large differences even though all sensors respond to catecholamines. The K_d-values vary from 2.3 nM to 9.4 µM and the limits of detection from 0.5 to 507.2 nM. This span of six (four) orders of magnitude demonstrates the large influence of oligonucleotide sequence. K_d values give an idea of where the middle of the dynamic range of the sensor is and consequently for which analytical task it can be used.

Certain K_d values obtained for dopamine have larger confidence intervals due to poor fitting/non-sigmoidal dose-response curves. Nevertheless, the dissociation constants for epinephrine in general exceed those of dopamine and norepinephrine. In detail, especially SWCNT-$(GT)_{10}$, SWCNT-$(A)_{30}$, and SWCNT-$(AT)_{15}$ seem to be well suited for discrimination between the three catecholamines, which are structurally very similar as they share the same catechol-moiety. By using MD simulations it was previously shown that the two hydroxy groups of the catechol-moiety interact with phosphate groups of the DNA backbone on SWCNT/DNA sensors [5]. Our results show fluorescence increases for all three neurotransmitters but the magnitude and the onset of saturation varies by orders of magnitude. This observation might be explained by differences between those three neurotransmitters (e.g., primary vs. secondary amine, size, and charge).

3.4. Detection of Dopamine with Single Carbon Nanotube Sensors in the Presence of Homologues

One very important aspect of a sensor is the need to detect the analyte of interest (e.g., dopamine) in the presence of other relevant analytes, which can be very similar in structure. After having determined the dissociation constants and limits of detection for different SWCNT-DNA sensors for dopamine, epinephrine, and norepinephrine, the next step was to verify it in a realistic scenario with nM concentrations of dopamine and a homologue. SWCNT-$(GT)_{10}$ sensors were immobilized on a glass surface by physisorption and the NIR response of single sensors to dopamine (50 nM) in a background of norepinephrine (50 nM) was quantified. SWCNT-$(GT)_{10}$ sensors were used because the K_d-values and responses (Figures 3 and 4.) indicated that these sensors respond to dopamine, but not to norepinephrine, at this concentration. The results including the control using the lower-affinity sensor $(GA)_{15}$ as a control are shown in Figure 5.

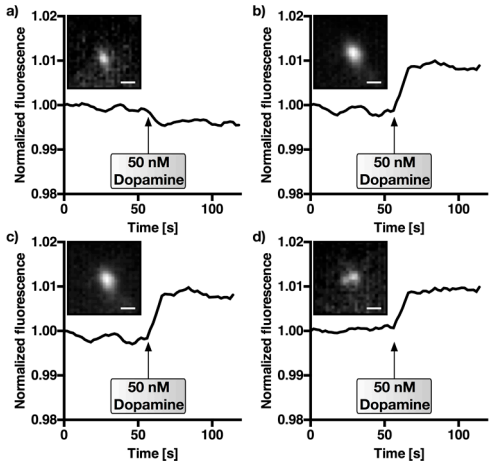

Figure 5. Detection of dopamine in the presence of norepinephrine. NIR fluorescence images of single (SWCNT)-DNA sensors. Here, 50 nM dopamine was added (t = 60 s) in the presence of 50 nM norepinephrine in phosphate-buffered saline. (**a**) Control experiment using SWCNT-$(GA)_{15}$, which showed a lower affinity/selectivity for dopamine (see Figures 3 and 4). (**b**–**d**) Three SWCNT-$(GT)_{10}$-traces showing a change in fluorescence intensity upon dopamine addition. Insets show the fluorescence images of the single sensors at t = 0. Fluorescence counts were normalized. Scale bar = 1 μm.

Single SWCNT-$(GT)_{10}$ sensor particles responded to dopamine in the presence of norepinephrine, which indicates that it is possible to discriminate those neurotransmitters, at least at 50 nM concentrations. In contrast, it was not possible to monitor the addition of dopamine after 60 s using neither the control sensor SWCNT-$(GA)_{15}$ nor SWCNT-$(AT)_{15}$ (see Figure A4) for which the results of Figures 3 and 4 suggested a lower selectivity/affinity. The overall change in fluorescence intensity was not as high as in the solution-based experiments (Figure 3), which can be attributed to a different level of background and an impact of the surface on sensor responses. These NIR fluorescence microscopy experiments provide a spatial resolution and are closer to applications of these sensors for imaging of neurotransmitters in cell networks.

To further evaluate the detection of dopamine with a 50 nM background of norepinephrine, another experiment similar to Figure 5 was carried out. However, in this case we gradually increased the dopamine concentration from 1 nM to 10 μM while maintaining a constant 50 nM norepinephrine background. Figure 6 shows the increasing fluorescence for single SWCNT-$(GT)_{10}$ sensors, as well as the calibration curve generated from n = 11 sensors. The arrows denote the addition of dopamine (a = 1 nM, b = 10 nM, c = 100 nM, d = 1 μM, e = 10 μM).

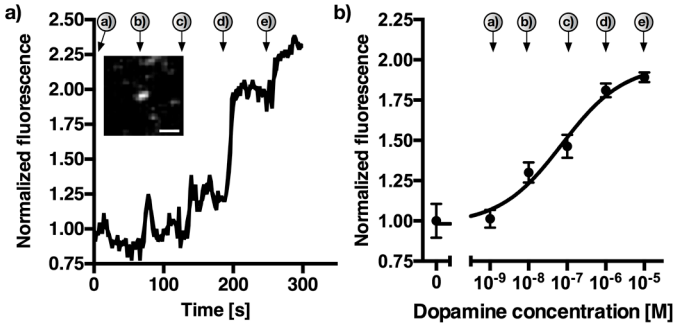

Figure 6. Dynamic detection of dopamine in the presence of norepinephrine. NIR fluorescence image of a single (SWCNT)-DNA sensor. Here, 1 nM to 10 μM dopamine was added approx. each 60 s (a = 1 nM, b = 10 nM, c = 100 nM, d = 1 μM, e = 10 μM) in the presence of 50 nM norepinephrine in phosphate-buffered saline. (**a**) Example SWCNT-$(GT)_{10}$-trace showing a change in fluorescence intensity upon dopamine addition. Inset shows the NIR-fluorescence image of the single sensor at t = 300 s. Fluorescence counts were normalized. Scale bar = 1 μm. (**b**) Dose-response curve generated from the mean fluorescence changes of eleven different SWCNT-$(GT)_{10}$ sensors between each addition-point of dopamine. Errors are standard deviations (n = 11).

The effective K_d increased to 72.9 nM compared to the solution-based value of 9.2 nM without the presence of 50 nM norepinephrine, while the limit of detection under these conditions changed from 0.1 nM to 4.9 nM. These results are very promising as they indicate that dopamine can be detected in the presence of realistic concentrations of the homologous neurotransmitter norepinephrine.

4. Discussion

The properties of nanomaterials depend strongly on their immediate chemical environment. In many cases this is an organic phase (corona), such as the DNA-oligonucleotides used in this work. This organic phase is not only important for dispersion of the hydrophobic SWCNTs, but also for interactions and recognition of other molecules. For sensors this is obviously clear and it is of general relevance when nanoparticles interact with their environment for example during nanoparticle growth or when studying or tailoring cell-nanoparticle interactions [37–41].

In this study we used ten different DNA-oligonucleotides to non-covalently modify (6,5)-enriched SWCNTs. These SWCNT-DNA conjugates were evaluated in terms of recognition ability of the three catecholamine neurotransmitters dopamine, epinephrine, and norepinephrine. They are important neurotransmitters, but so far it is extremely difficult to distinguish them when they are released by cells. As shown in Figure 3, almost all of the generated SWCNT-DNA conjugates showed increasing NIR fluorescence with increasing catecholamine concentration (range between 100 pM and 100 μM). One exception at this point is SWCNT-$(AT)_{15}$, which did not show any response to dopamine or norepinephrine, and only a small increase to epinephrine. This behavior could possibly arise due to the self-complementarity, which leads to DNA-duplex formation in aqueous solution and on the SWCNT surface lowering its flexibility and thus hindering analyte-recognition. Another result are the special sensing capabilities of A_{30}- and $(GT)_{10}$-SWCNTs. Both of them exhibited a large relative fluorescence intensity change upon exposure to dopamine in comparison to both epinephrine and norepinephrine. In addition, as shown in Figure 4, they responded at much lower concentrations of dopamine than that of (nor)epinephrine, which can also be deduced from the measured K_d values summarized in Table 1. These two sequences might be very useful to discriminate between these chemically very similar analytes. The NIR fluorescence microscopy experiments of the $(GT)_{10}$-SWCNT sensor showed, for single immobilized sensors, that low nM concentrations of dopamine are detected in the presence of equimolar amounts of norepinephrine. This result shows how the evaluation of dose-response curves (K_d and LOD values) helps to identify selective sensors and tune them for a

specific application. In the future these insights may also be used in ratiometric sensing approaches with single-chirality SWCNT samples that emit light at different wavelengths.

The 'library' of ten DNA sequences led to sensors with K_d differences of up to six orders of magnitude. This is surprising because there was no rationale behind choosing those ten specific sequences. It is very likely that larger libraries and a screening or high-throughput approach could identify even more selective and sensitive sensors.

5. Conclusions

This study reveals the dose-response curves of several SWCNT/DNA sensors for the neurotransmitters dopamine, epinephrine, and norepinephrine. We find large differences in terms of dissociation constants and limits of detection for different DNA sequences and identify a sensor that can discriminate between the structural homologues dopamine and norepinephrine. These sensors can be used for biological studies that aim to distinguish these chemically very similar neurotransmitters. Our results also show that varying the organic phase around carbon nanotubes is a versatile approach to identify new sensors and to select the most selective and sensitive ones for specific analytical applications.

Acknowledgments: We thank the Fonds der Chemischen Industrie (FCI) for financial support (Liebig fellowship to S.K.). This project was supported by the state of Lower Saxony (life@nano) and the Cluster of Excellence and DFG Research Center Nanoscale Microscopy and Molecular Physiology of the Brain. We acknowledge support by the German Research Foundation and the Open Access Publication Funds of Göttingen University.

Author Contributions: F.A.M. and S.K. conceived and designed the experiments; F.A.M., N.H., and D.M. performed the experiments; F.A.M., N.H., and S.K. analyzed the data. F.A.M and S.K. wrote the paper.

Conflicts of Interest: The authors declare no conflict of interest.

Appendix

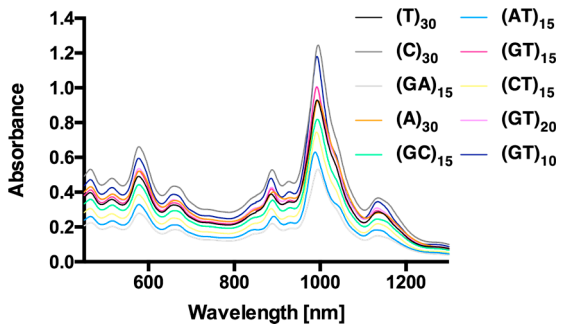

Figure A1. VIS-NIR absorbance spectra of different DNA-dispersed SWCNT samples. VIS-NIR absorbance spectra of DNA-oligonucleotide-dispersed single-walled carbon nanotubes (SWCNT) after centrifugation (see the Materials section) and before concentration adjustment. The (6,5)-peak at around 991 nm was used for concentration estimation and adjustment.

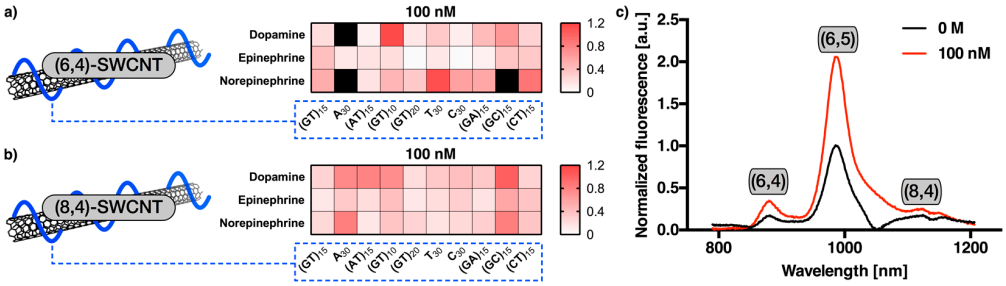

Figure A2. Chirality-dependence of the relative fluorescence change upon exposure to neurotransmitters. Relative fluorescence change of the sensors upon addition of 100 nM of dopamine, epinephrine and norepinephrine in the range from 0, i.e., no change in fluorescence intensity, to 1.2 equaling 120% fluorescence increase. Here, (6,4)-SWCNTs responses at 885 nm (**a**) and (8,4)-SWCNTs responses at 1122 nm (**b**) were evaluated. Black color indicates off-scale fluorescence changes presumably due to the small signal to noise ratios for the (6,4)-SWCNTs. (**c**) Representative fluorescence spectrum (SWCNT-$(GT)_{10}$ and dopamine) and assignment of the nanotube chiralities.

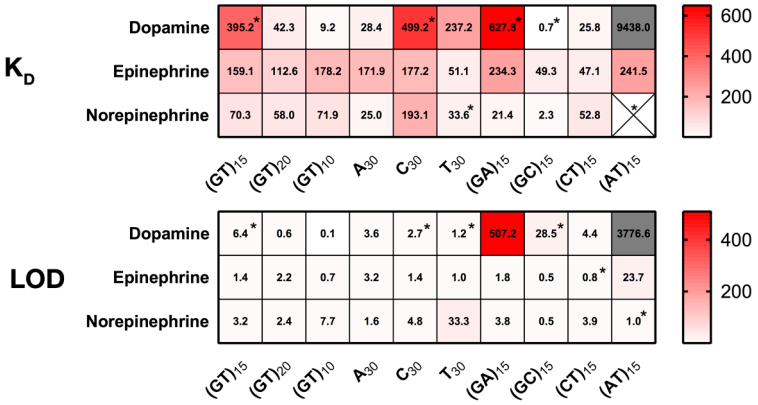

Figure A3. Overview of K_d and LOD values obtained from the dose-response curves for dopamine, epinephrine, and norepinephrine. * No clear (sigmoidal) fit possible.

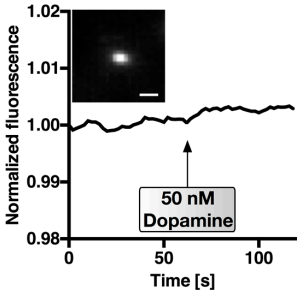

Figure A4. Control experiment for the detection of dopamine in the presence of norepinephrine. NIR fluorescence images of single (SWCNT)-DNA sensors. Here, 50 nM dopamine was added (t = 60 s) in the presence of 50 nM norepinephrine in phosphate-buffered saline. Control experiment using SWCNT-$(AT)_{15}$, which showed a lower affinity/selectivity for dopamine (see Figures 3 and 4). Insets show the fluorescence image of the single sensor at t = 0. Fluorescence counts were normalized. Scale bar = 1 µm.

References

1. Polo, E.; Kruss, S. Nanosensors for neurotransmitters. *Anal. Bioanal. Chem.* **2016**, *408*, 2727–2741. [CrossRef] [PubMed]

2. Adams, K.L.; Puchades, M.; Ewing, A.G. In vitro electrochemistry of biological systems. *Annu. Rev. Anal. Chem.* **2008**, *1*, 329. [CrossRef] [PubMed]
3. Alivisatos, A.P.; Andrews, A.M.; Boyden, E.S.; Chun, M.; Church, G.M.; Deisseroth, K.; Donoghue, J.P.; Fraser, S.E.; Lippincott-Schwartz, J.; Looger, L.L.; et al. Nanotools for neuroscience and brain activity mapping. *ACS Nano* **2013**, *7*, 1850–1866. [CrossRef] [PubMed]
4. Sames, D.; Dunn, M.; Karpowicz, R.J.; Sulzer, D. Visualizing neurotransmitter secretion at individual synapses. *ACS Chem. Neurosci.* **2013**, *4*, 648–651. [CrossRef] [PubMed]
5. Kruss, S.; Salem, D.P.; Vukovic, L.; Lima, B.; Vander Ende, E.; Boyden, E.S.; Strano, M.S. High-resolution imaging of cellular dopamine efflux using a fluorescent nanosensor array. *Proc. Natl. Acad. Sci. USA* **2017**, *114*, 1789–1794. [CrossRef] [PubMed]
6. Shapiro, M.G.; Westmeyer, G.G.; Romero, P.A.; Szablowski, J.O.; Kuster, B.; Shah, A.; Otey, C.R.; Langer, R.; Arnold, F.H.; Jasanoff, A. Directed evolution of a magnetic resonance imaging contrast agent for noninvasive imaging of dopamine. *Nat. Biotechnol.* **2010**, *28*, 264–270. [CrossRef] [PubMed]
7. Kim, D.; Koseoglu, S.; Manning, B.M.; Meyer, A.F.; Haynes, C.L. Electroanalytical eavesdropping on single cell communication. *Anal. Chem.* **2011**, *83*, 7242–7249. [CrossRef] [PubMed]
8. Savtchenko, L.P.; Rusakov, D.A. The optimal height of the synaptic cleft. *Proc. Natl. Acad. Sci. USA* **2007**, *104*, 1823–1828. [CrossRef] [PubMed]
9. Trouillon, R.; Passarelli, M.K.; Wang, J.; Kurczy, M.E.; Ewing, A.G. Chemical analysis of single cells. *Anal. Chem.* **2013**, *85*, 522–542. [CrossRef] [PubMed]
10. Bucher, E.S.; Wightman, R.M. Electrochemical analysis of neurotransmitters. *Annu. Rev. Anal. Chem.* **2015**, *8*, 239–261. [CrossRef] [PubMed]
11. Wightman, R.M.; Jankowski, J.A.; Kennedy, R.T.; Kawagoe, K.T.; Schroeder, T.J.; Leszczyszyn, D.J.; Near, J.A.; Diliberto, E.J., Jr.; Viveros, O.H. Temporally resolved catecholamine spikes correspond to single vesicle release from individual chromaffin cells. *Proc. Natl. Acad. Sci. USA* **1991**, *88*, 10754–10758. [CrossRef] [PubMed]
12. Shen, M.; Colombo, M.L. Electrochemical nanoprobes for the chemical detection of neurotransmitters. *Anal. Methods* **2015**, *7*, 7095–7105. [CrossRef] [PubMed]
13. Masharina, A.; Reymond, L.; Maurel, D.; Umezawa, K.; Johnsson, K. A fluorescent sensor for GABA and synthetic $GABA_B$ receptor ligands. *J. Am. Chem. Soc.* **2012**, *134*, 19026–19034. [CrossRef] [PubMed]
14. Okubo, Y.; Sekiya, H.; Namiki, S.; Sakamoto, H.; Iinuma, S.; Yamasaki, M.; Watanabe, M.; Hirose, K.; Iino, M. Imaging extrasynaptic glutamate dynamics in the brain. *Proc. Natl. Acad. Sci. USA* **2010**, *107*, 6526–6531. [CrossRef] [PubMed]
15. Marvin, J.S.; Borghuis, B.G.; Tian, L.; Cichon, J.; Harnett, M.T.; Akerboom, J.; Gordus, A.; Renninger, S.L.; Chen, T.W.; Bargmann, C.I.; et al. An optimized fluorescent probe for visualizing glutamate neurotransmission. *Nat. Methods* **2013**, *10*, 162–170. [CrossRef] [PubMed]
16. Kruss, S.; Hilmer, A.J.; Zhang, J.; Reuel, N.F.; Mu, B.; Strano, M.S. Carbon nanotubes as optical biomedical sensors. *Adv. Drug Deliv. Rev.* **2013**, *65*, 1933–1950. [CrossRef] [PubMed]
17. Kruss, S.; Landry, M.P.; Vander Ende, E.; Lima, B.M.; Reuel, N.F.; Zhang, J.; Nelson, J.; Mu, B.; Hilmer, A.; Strano, M. Neurotransmitter detection using corona phase molecular recognition on fluorescent single-walled carbon nanotube sensors. *J. Am. Chem. Soc.* **2014**, *136*, 713–724. [CrossRef] [PubMed]
18. Reuel, N.F.; Grassbaugh, B.; Kruss, S.; Mundy, J.Z.; Opel, C.; Ogunniyi, A.O.; Egodage, K.; Wahl, R.; Helk, B.; Zhang, J.; et al. Emergent properties of nanosensor arrays: Applications for monitoring IgG affinity distributions, weakly affined hypermannosylation, and colony selection for biomanufacturing. *ACS Nano* **2013**, *7*, 7472–7482. [CrossRef] [PubMed]
19. Zhang, J.; Kruss, S.; Hilmer, A.J.; Shimizu, S.; Schmois, Z.; De La Cruz, F.; Barone, P.W.; Reuel, N.F.; Heller, D.A.; Strano, M.S. A rapid, direct, quantitative, and label-free detector of cardiac biomarker troponin T using near-infrared fluorescent single-walled carbon nanotube sensors. *Adv. Healthc. Mater.* **2014**, *3*, 412–423. [CrossRef] [PubMed]
20. Bisker, G.; Dong, J.; Park, H.D.; Iverson, N.M.; Ahn, J.; Nelson, J.T.; Landry, M.P.; Kruss, S.; Strano, M.S. Protein-targeted corona phase molecular recognition. *Nat. Commun.* **2016**, *7*, 10241. [CrossRef] [PubMed]
21. Wong, M.H.; Giraldo, J.P.; Kwak, S.Y.; Koman, V.B.; Sinclair, R.; Lew, T.T.; Bisker, G.; Liu, P.; Strano, M.S. Nitroaromatic detection and infrared communication from wild-type plants using plant nanobionics. *Nat. Mater.* **2017**, *16*, 264–272. [CrossRef] [PubMed]

22. Harvey, J.D.; Jena, P.V.; Baker, H.A.; Zerze, G.H.; Williams, R.M.; Galassi, T.V.; Roxbury, D.; Mittal, J.; Heller, D.A. A carbon nanotube reporter of microrna hybridization events in vivo. *Nat. Biomed. Eng* **2017**, *1*. [CrossRef]
23. Zhang, J.; Landry, M.P.; Barone, P.W.; Kim, J.-H.; Lin, S.; Ulissi, Z.W.; Lin, D.; Mu, B.; Boghossian, A.A.; Hilmer, A.J.; et al. Molecular recognition using corona phase complexes made of synthetic polymers adsorbed on carbon nanotubes. *Nat. Nanotechnol.* **2013**, *8*, 959–968. [CrossRef] [PubMed]
24. Antonucci, A.; Kupis-Rozmyslowicz, J.; Boghossian, A.A. Noncovalent protein and peptide functionalization of single-walled carbon nanotubes for biodelivery and optical sensing applications. *ACS Appl. Mater. Interfaces* **2017**, *9*, 11321–11331. [CrossRef] [PubMed]
25. Chio, L.; Yang, D.; Landry, M. Surface engineering of nanoparticles to create synthetic antibodies. *Methods Mol. Biol.* **2017**, *1575*, 363–380. [PubMed]
26. Mu, B.; Zhang, J.; McNicholas, T.P.; Reuel, N.F.; Kruss, S.; Strano, M.S. Recent advances in molecular recognition based on nanoengineered platforms. *Acc. Chem. Res.* **2014**, *47*, 979–988. [CrossRef] [PubMed]
27. Polo, E.; Kruss, S. Impact of redox-active molecules on the fluorescence of polymer-wrapped carbon nanotubes. *J. Phys. Chem. C* **2016**, *120*, 3061–3070. [CrossRef]
28. Bisker, G.; Ahn, J.; Kruss, S.; Ulissi, Z.W.; Salem, D.P.; Strano, M.S. A mathematical formulation and solution of the cophmore inverse problem for helically wrapping polymer corona phases on cylindrical substrates. *J. Phys. Chem. C* **2015**, *119*, 13876–13886. [CrossRef]
29. Hertel, T.; Himmelein, S.; Ackermann, T.; Stich, D.; Crochet, J. Diffusion limited photoluminescence quantum yields in 1-d semiconductors: Single-wall carbon nanotubes. *ACS Nano* **2010**, *4*, 7161–7168. [CrossRef] [PubMed]
30. Meyer, D.; Hagemann, A.; Kruss, S. Kinetic requirements for spatiotemporal chemical imaging with fluorescent nanosensors. *ACS Nano* **2017**, *11*, 4017–4027. [CrossRef] [PubMed]
31. Schöppler, F.; Mann, C.; Hain, T.C.; Neubauer, F.M.; Privitera, G.; Bonaccorso, F.; Chu, D.; Ferrari, A.C.; Hertel, T. Molar extinction coefficient of single-wall carbon nanotubes. *J. Phys. Chem. C* **2011**, *115*, 14682–14686. [CrossRef]
32. Liebscher, J.; Mrowczynski, R.; Scheidt, H.A.; Filip, C.; Hadade, N.D.; Turcu, R.; Bende, A.; Beck, S. Structure of polydopamine: A never-ending story? *Langmuir* **2013**, *29*, 10539–10548. [CrossRef] [PubMed]
33. Lee, H.; Dellatore, S.M.; Miller, W.M.; Messersmith, P.B. Mussel-inspired surface chemistry for multifunctional coatings. *Science* **2007**, *318*, 426–430. [CrossRef] [PubMed]
34. Saavedra, J.M.; Kvetnansky, R.; Kopin, I.J. Adrenaline, noradrenaline and dopamine levels in specific brain stem areas of acutely immobilized rats. *Brain Res.* **1979**, *160*, 271–280. [CrossRef]
35. O'Neill, R.D. Microvoltammetric techniques and sensors for monitoring neurochemical dynamics in vivo. A review. *Analyst* **1994**, *119*, 767–779. [CrossRef] [PubMed]
36. Salem, D.P.; Landry, M.P.; Bisker, G.; Ahn, J.; Kruss, S.; Strano, M.S. Chirality dependent corona phase molecular recognition of DNA-wrapped carbon nanotubes. *Carbon* **2016**, *97*, 147–153. [CrossRef]
37. Kruss, S.; Erpenbeck, L.; Amschler, K.; Mundinger, T.A.; Boehm, H.; Helms, H.J.; Friede, T.; Andrews, R.K.; Schon, M.P.; Spatz, J.P. Adhesion maturation of neutrophils on nanoscopically presented platelet glycoprotein ibalpha. *ACS Nano* **2013**, *7*, 9984–9996. [CrossRef] [PubMed]
38. Kruss, S.; Erpenbeck, L.; Schon, M.P.; Spatz, J.P. Circular, nanostructured and biofunctionalized hydrogel microchannels for dynamic cell adhesion studies. *Lab Chip* **2012**, *12*, 3285–3289. [CrossRef] [PubMed]
39. Kruss, S.; Srot, V.; van Aken, P.A.; Spatz, J.P. Au-Ag hybrid nanoparticle patterns of tunable size and density on glass and polymeric supports. *Langmuir* **2012**, *28*, 1562–1568. [CrossRef] [PubMed]
40. Kruss, S.; Wolfram, T.; Martin, R.; Neubauer, S.; Kessler, H.; Spatz, J.P. Stimulation of cell adhesion at nanostructured teflon interfaces. *Adv. Mater.* **2010**, *22*, 5499–5506. [CrossRef] [PubMed]
41. Amschler, K.; Erpenbeck, L.; Kruss, S.; Schon, M.P. Nanoscale integrin ligand patterns determine melanoma cell behavior. *ACS Nano* **2014**, *8*, 9113–9125. [CrossRef] [PubMed]

4.1.2. Discussion

The detection of neurotransmitters such as dopamine is an important task to understand our brain's function also in the context of related diseases such as Parkinson's or Huntington's. In these diseases, malfunctions of dopamine signaling play a crucial role and it is thus of high importance to develop new tools allowing for better scientific understanding. FSCV is an electrochemical detection technique with low detection limit (up to 1 nM under optimized conditions but decreased temporal resolution[167]) and can operate with a temporal resolution of up to 10 ms.[168] However, due to the size of the electrodes necessary for the measurements, the spatial resolution that can be obtained is not sufficient to evaluate e.g. patterns of release events as the maximum density of electrodes achieved until now was 4-6 on the area of one chromaffin cell.[169,170] Another technique offering a drastically increased spatial resolution are genetically modified variants of receptors which usually take up or transport the respective neurotransmitter. After being previously established for the sensing of GABA and glutamate, Patriarchi et al. published another variant for the *in vivo* sensing of dopamine in 2018.[171] Here, the authors made use of the conformational change the human dopamine receptor undergoes upon binding of dopamine. Through genetic insertion of a GFP-variant into its intracellular loop (and screening of different variants) they were able to couple this conformational change to changes in the GFP fluorescence intensity. The two most promising variants showed a high affinity for dopamine (K_d = 330-770 nM) with significantly higher values for epinephrine and norepinephrine (12.7 μM and 19.9 μM , respectively). Following characterization, the authors applied these variants not only *in cellulo*, but also *in vivo* for dopamine monitoring in behaving mice. Only two weeks later, Sun et al.[172] published a similar concept comprising also a conformationally sensitive GFP variant cloned into a G protein-coupled receptor (GPCR) yielding even more affine dopamine sensors (K_d = 10 nM), yet with smaller fluorescence increase compared to the approach from Patriarchi et al. (90% vs. 230% $\Delta F/F_0$). Here, the genetically encoded sensor was applied for dopamine imaging in mice, flies and zebrafish. While these two examples represent impressive examples of what fluorescent fusion protein-based sensors are capable of, they also have certain shortcomings. These include e.g. the fast bleaching of fluorescent proteins and the (compared to the NIR) low tissue-penetration. In addition, they also require extensive genetic engineering before they can be applied in the system of choice. It is exactly these points, which SWCNT-based optical sensors aim to overcome. In contrast to the traditionally employed systems such as FSCV or microdialysis, they offer the

clear advantage of drastically enhanced spatiotemporal resolution. And in comparison to the GFP-based systems published after this study (see chapter 4.1.2), SWCNT-based dopamine sensors offer a similar or higher affinity (K_d = 9.2 nM) and an even lower limit of detection (LOD, 0.1 nM). As shown in Fig. 3 of the manuscript (see 4.1.2, p. 51), the SWCNT-DNA based sensors respond to all three structurally similar neurotransmitters with a fluorescence increase, yet with different affinities and magnitudes of fluorescence change (highest for dopamine). This effect can also be observed for both genetically encoded sensors with a similar difference in K_d values for dopamine, epinephrine and norepinephrine.[171,172] In their cases the sensitivity and selectivity can be tuned *via* genetic alteration of the GFP insertion site and the linker sequences, whereas SWCNT-DNA based sensors can be easily modified using different DNA sequences, which proved to yield different K_d and LOD values (see 4.1.2, p. 53, Tab. 1). Thus, one can conclude that discrimination between these structurally very similar neurotransmitters is a challenge for all the different techniques, but in each case higher affinities for dopamine were reported allowing its detection also with a (nor)epinephrine background.
One clear advantage of SWCNT-based dopamine sensors is the non-bleaching nature of their NIR-fluorescence allowing for larger tissue-penetration depths. In addition, the synthetic nature of these sensors enables application in diverse systems without prior genetic engineering. In contrast to the approaches by Patriarchi et al. and Sun et al., SWCNT-based dopamine sensors were up to now only applied *in vitro* and *in cellulo*, yet in the latest study by Kruss et al.[97] they also enabled sensing not only at the cell surface, but also between cells. Thus, this feature also allows for studying e.g. volume transmission, which genetically encoded sensors based on membrane proteins can not accomplish. However, genetically engineered systems offer the advantage of easier application in *in vivo* settings as the genetic material can be delivered e.g. by viral delivery vectors. For SWCNT-based sensors, it would either be necessary to implant them e.g. in a hydrogel-sensor-patch or to inject them, which would in turn require a targeting mechanism to bring them to the desired site of action. It is especially this last point, which will be further evaluated in the following chapter.

4.2 Targeted delivery of nanosensors

After the previous chapter elucidated the sensitivity and selectivity of SWCNT-based sensors for neurotransmitters, this chapter/project aims at the decoration of these nanosensors with recognition units enabling targeting or even new sensing concepts. To this end, antibody fragments termed nanobodies are attached to a DNA-oligonucleotide wrapping a SWCNT. The nature of this oligonucleotide was chosen based on the study in chapter 4.1.2. While there are a few examples of antibody immobilization on SWCNTs, both covalently[173] and non-covalently[159,163], the only study reporting SWCNT-nanobody conjugation was published in 2018 by Filipiak et al., who used a anti-GFP nanobody as a recognition unit on a FET for the label-free, electrical detection of GFP.[174] Here, the authors used carboxylic acid-bearing pyrenes to coat the SWCNT surface and serve as an attachment site for the nanobody's lysine residues after EDC/NHS activation. This process, however, leads to a large variety of mixed configurations. Thus, in this study, a GFP-targeting nanobody comprising a single ectopic cysteine (at the C-terminus) is used for attachment to maleimide-modified DNA-oligonucleotides. The aims of this combination of biomolecular units for this project are:

(a) The generation of colloidally stable SWCNT-DNA-Nanobody conjugates, which are still showing NIR fluorescence and can thus be used for NIR microscopy.

(b) Controlling retained function of the nanobody after conjugation to the SWCNT-DNA hybrid.

(c) The use of the SWCNT-DNA-Nanobody conjugate as a NIR labelling agent for *in vivo* NIR fluorescence microscopy.

(d) To show that SWCNT-DNA hybrids are able to respond to the neurotransmitter dopamine even after conjugation of the nanobody. Together with the targeting capabilities of the nanobody, this would enable targeted delivery of dopamine sensors.

4.2.1. Nanobody Conjugated Nanotubes for Targeted Near-Infrared in vivo Imaging and Sensing (Manuscript 2)

This chapter was published in the following journal:

Florian A. Mann, Zhiyi Lv, Jörg Großhans, Felipe Opazo and Sebastian Kruss

"Nanobody-Conjugated Nanotubes for Targeted Near-Infrared In Vivo Imaging and Sensing"

Angew. Chem. Int. Ed. **2019**, 58, 11469 - 11473

This article is available using at: DOI:10.1002/anie.201904167

Responsibility assignment: S.K. and F.A.M designed and conceived the project with inputs from F.O., Z.L. and J.G.. F.A.M. performed all experiments except for *Drosophila* embryo preparation and injection, which was performed by Z.L.. F.A.M. performed the data analysis. F.A.M. and S.K wrote the manuscript with input from Z.L., F.O. and J.G..

In Vivo Imaging

International Edition: DOI: 10.1002/anie.201904167
German Edition: DOI: 10.1002/ange.201904167

Nanobody-Conjugated Nanotubes for Targeted Near-Infrared In Vivo Imaging and Sensing

*Florian A. Mann, Zhiyi Lv, Jörg Großhans, Felipe Opazo, and Sebastian Kruss**

Abstract: *Fluorescent nanomaterials such as single-walled carbon nanotubes (SWCNTs) have many advantages in terms of their photophysics, but it is difficult to target them to specific locations in living systems. In contrast, the green fluorescent protein (GFP) has been genetically fused to proteins in many cells and organisms. Therefore, GFP can be seen not only as a fluorophore but as a universal target/handle. Here, we report the conjugation of GFP-binding nanobodies to DNA-wrapped SWCNTs. This approach combines the targeting capabilities of GFP-binding nanobodies and the nonbleaching near-infrared fluorescence (850–1700 nm) of SWCNTs. These conjugates allow us to track single Kinesin-5-GFP motor proteins in developing embryos of Drosophila melanogaster. Additionally, they are sensitive to the neurotransmitter dopamine and can be used for targeted sensing of dopamine in the nM regime.*

Single-walled carbon nanotubes (SWCNT) are a 1D material and display unique optoelectronic properties such as near-infrared (nIR) fluorescence (850–1700 nm).[1] This spectral window is highly beneficial for biological and especially deep-tissue imaging due to reduced phototoxicity, background fluorescence, and scattering.[2] In addition, SWCNTs do not bleach or blink such as many organic dyes or quantum dots.[3] As a result, single-walled carbon nanotubes have already found applications in diverse areas ranging from sensors to photodynamic therapy and drug delivery.[4–10] Regardless of their beneficial photophysical properties, biological imaging typically requires targeting of the fluorophore to the desired epitope. This step remains a challenge for all nanomaterial-based approaches.

In this work, we use nanobodies as a recognition element on the surface of SWCNTs. Nanobodies have several advantages over their larger counterparts (antibodies). They possess a comparable specificity for their antigens while being only ≈1/10 in size and molecular weight.[11–13] Since their discovery (derived as the variable domain from naturally evolved heavy-chain antibodies from, for example, camels), nanobodies have been successfully employed both in labeling[14,15] and therapeutic studies making use of their advantageous smaller structure, which allows a different way of antigen binding as well as robust expression in both bacterial and eukaryotic hosts.[16,17] Their small size is utilized frequently in superresolution microscopy as it leads to a drastically decreased linkage error with respect to the bound antigen.[11,12,18] In addition, they were recently modified semisynthetically with cyclic cell-penetrating peptides for live cell immunostaining[19] as well as used for isotopic labeling of biological samples imaged by secondary-ion mass spectrometry (SIMS).[20]

In this study, we aimed to combine the photophysical advantages of SWCNTs with the size and targeting capabilities of nanobodies. To this end, we conjugated a GFP-binding nanobody (GFP-binding protein, GBP, **4**) to a DNA oligonucleotide (**2**) -wrapped SWCNT (see Figure 1 a). GFP is a valuable target because a large number of transgenic organisms and cells are available with GFP-tagged proteins. Noncovalent functionalization is used in order not to alter or destroy the nIR fluorescence of SWCNTs,[21–25] although recently Setaro et al. also reported a covalent modification strategy preserving the nIR fluorescence.[26] While there are many different noncovalent functionalization concepts available,[21,27,28] DNA/SWCNTs have the additional advantage that they can be used for the sensing of small molecules.[29]

Recently, Filipiak et al. used nanobodies to generate SWCNT-based amperometric sensors/transistors for the detection of GFP using EDC/NHS chemistry leading to a mixture of orientations of the nanobody on the SWCNT surface yet still enabling the detection of GFP in the picomolar range.[30] In contrast, we employ a maleimide-based coupling strategy allowing for site-specific and oriented attachment of the GBP through a C-terminally introduced cysteine. In this way, we are able to generate more defined conjugates with the antigen-binding region pointing away from the SWCNT surface. By using a GFP-binding nanobody we generate a highly versatile platform, which can be directly applied in many biological systems containing GFP-modified variants of the protein of interest.

[*] F. A. Mann, Dr. S. Kruss
Institute of Physical Chemistry
Georg-August Universität Göttingen
Tammannstraße 6, 37077 Göttingen (Germany)
E-mail: skruss@uni-goettingen.de
Dr. Z. Lv, Prof. Dr. J. Großhans
Institut Für Entwicklungsbiochemie
UMG/Georg-August Universität Göttingen
Justus-von-Liebig Weg 11, 37077 Göttingen (Germany)
Dr. F. Opazo
Center for Biostructural Imaging of Neurodegeneration
Von-Siebold-Strasse 3a, 37075 Göttingen (Germany)
Dr. F. Opazo, Dr. S. Kruss
Center for Nanoscale Microscopy and Molecular Physiology of the Brain (CNMPB)
Humboldtallee 23, 37073 Göttingen (Germany)
Dr. F. Opazo
NanoTag Biotechnologies GmbH
Rudolf-Wissell-Straße 28a, 37079 Göttingen (Germany)
Supporting information and the ORCID identification number(s) for the author(s) of this article can be found under: https://doi.org/10.1002/anie.201904167.

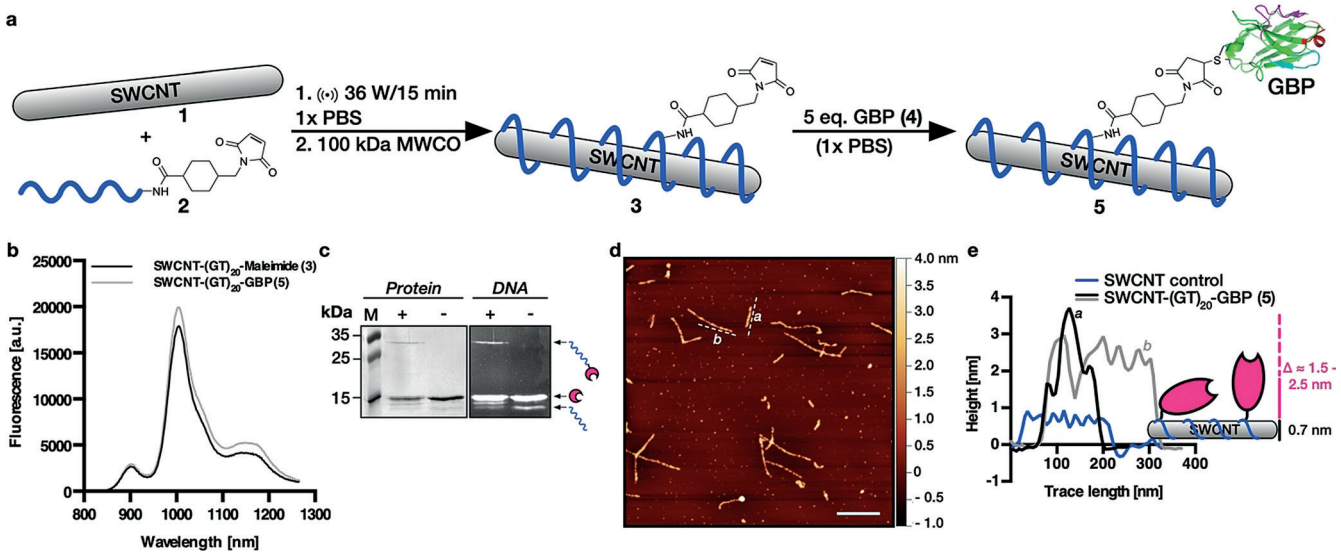

Figure 1. Site-specific and oriented conjugation of a GFP-binding nanobody (GBP, **4**) to DNA-oligonucleotide-wrapped single-walled carbon nanotubes (SWCNT, **1**). a) General conjugation scheme for linking a GFP-binding nanobody to DNA-wrapped SWCNTs via maleimide chemistry. b) Near-infrared fluorescence spectra before and after conjugation show retained fluorescence features ($c_{SWCNT} = 35$ nM, $t_{exp} = 1$ s). c) SDS-PAGE analysis proves DNA–GBP conjugation. +: reaction mixture, −: reaction mixture without SMCC, M: marker. d) Atomic force microscopy images of GBP-conjugated SWCNTs. Scale bar = 500 nm. e) The height traces (black and gray) of two exemplary SWCNT-$(GT)_{20}$-GBP conjugates (depicted in (d) as slightly offset dashed lines labeled a and b) show an increase in comparison to the unmodified SWCNT-$(GT)_{20}$ control.

To conjugate the GBP to the SWCNT, first the 3′-amine-modified $d(GT)_{20}$ oligonucleotides are reacted with the bifunctional crosslinker sulfosuccinimidyl 4-(*N*-maleimidomethyl)cyclohexane-1-carboxylate (Sulfo-SMCC) to generate thiol/cysteine-reactive DNA oligonucleotides (**2**). Next, these modified DNA sequences are used to noncovalently wrap the hydrophobic SWCNT surface via ultrasonication, resulting in a colloidally stable aqueous solution of SWCNT-DNA-Maleimide (**3**). After removal of excess DNA-Maleimide (**2**), ≈5 equivalents (with respect to the number of DNA oligonucleotides present on the SWCNT surface[31–33]) of the reduced GFP-binding nanobody are added to the solution of **3**. The excess of GBP (**4**) was adjusted based on previous optimization experiments (see Figures S1 and S2). Here, fine-tuning of the experimental parameters is crucial to prevent colloidal instability resulting from the conjugation of too many nanobodies to the SWCNT surface. This colloidal stability is a known and important, but still often neglected factor in research on peptide- or protein-modified SWCNTs.[24] Using the optimized GBP/SWCNT-$(GT)_{20}$ ratio, the conjugates were still stable even after more than six weeks of storage at 4 °C (see Figure S3). Figure 1b shows the retained nIR fluorescence properties after conjugation of the GFP-binding nanobody upon excitation at 561 nm compared to the unconjugated sample. To prove the successful conjugation of GBP (**4**) to the SWCNT, we employed DNA- and protein-stained sodium dodecylsulfate polyacrylamide gel electrophoresis (SDS-PAGE) (Figure 1c). Both Coomassie Brilliant Blue (protein) and GelRed (nucleic acid) staining showed a band at ≈28 kDa corresponding to the formed $d(GT)_{20}$-GBP conjugate eluted/detached from the SWCNT during SDS-PAGE sample preparation (boiling at 95 °C in 1× Laemmli sample buffer, see the Supporting Information, SI).

To further confirm the conjugation directly on the SWCNT, we used atomic force microscopy (AFM, Figure 1d). Heights increased by values fitting almost exactly the additional height introduced by the conjugated GBP, whereas SWCNTs not activated by SMCC showed heights matching the diameter of (almost) naked SWCNTs (≈0.7 nm, see Figure 1e (blue) and Figure S4). Together with an observed change in ζ-potential upon conjugation to more negative values (see Figure S5, $pI_{GBP} = 5.45$), these results show that the conjugation worked successfully and the nIR fluorescence is retained, making these conjugates suitable for imaging applications.

Next, we wanted to test whether the nanobody is still functional when conjugated to the hydrophobic SWCNT wrapped by a negatively charged oligonucleotide. For this purpose, we developed an in vitro assay with conjugate **5** micropatterned on a glass surface by polydimethylsiloxane (PDMS)-based microcontact printing (Figure 2a). After the surface was blocked using bovine serum albumin (BSA), a 1 μM eGFP solution was added and incubated on the surface for one hour. Fluorescence images show colocalization of GFP and SWCNT fluorescence as opposed to the control SWCNT-DNA without GBP (Figure 2b, further controls in Figure S6), indicating the preserved nanobody function and the targeting capabilities of the conjugate.

SWCNTs are not only static fluorophores but they have also been successfully used as building blocks in sensors to detect small molecules, mRNA, sugars, and proteins.[2,34–40] DNA/SWCNT conjugates in particular have previously served as optical sensors for the spatiotemporal detection of the neurotransmitter dopamine.[29,41,42] Depending on the sequence of the wrapping oligonucleotide, the nIR fluorescence increases between 50–400 % upon dopamine binding with K_d values between 1 nM and 1 μM.[7,29] The $(GT)_{20}$

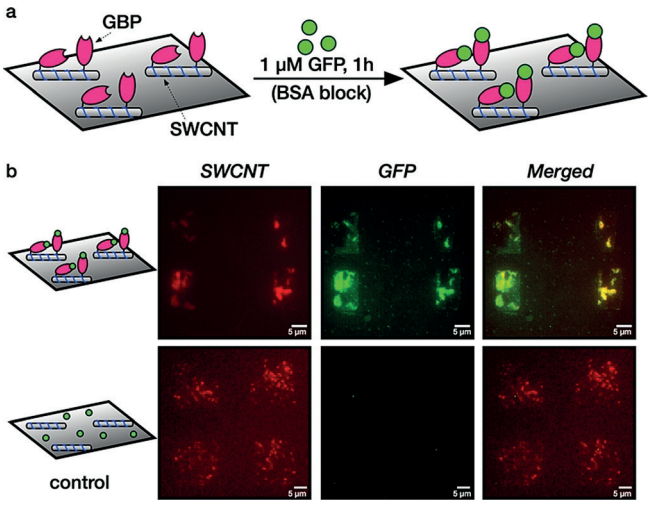

Figure 2. Functionality of nanobody–SWCNT conjugates. a) Schematic of the assay that uses microcontact printing of SWCNT-GBP conjugates **5**, BSA blocking, and GFP addition. b) nIR and GFP fluorescence images show colocalization SWCNT-GBP and GFP. In contrast, the SWCNT-DNA control shows no colocalization. Scale bars = 5 μm.

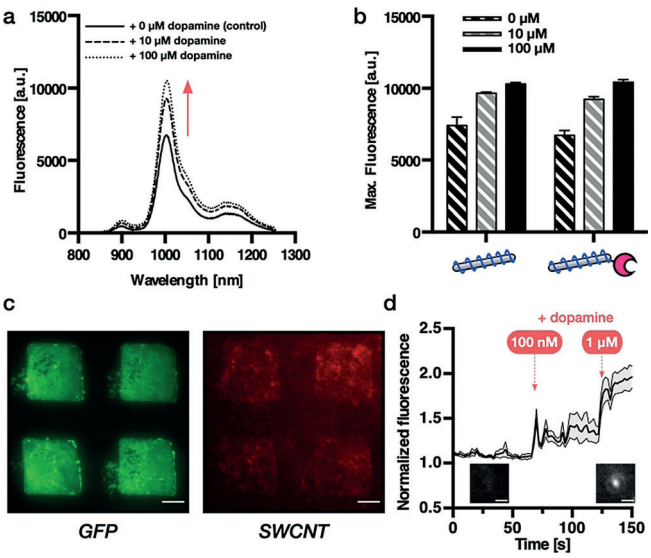

Figure 3. Targeted near-infrared fluorescent dopamine sensors. a) nIR fluorescence response of GBP-modified SWCNT increases upon dopamine addition. b) Fluorescence changes after addition of the neurotransmitter dopamine show that the dopamine-sensing capability of DNA-functionalized SWCNTs is retained in nanobody-conjugated SWCNTs (c_{SWCNT} = 10 nM, t_{exp} = 2 s, mean and s.d., n = 3). c) SWCNT-GBP conjugate **5** bound to surface-immobilized GFP. d) Fluorescence response of immobilized single SWCNT-GBP sensors (mean and s.e., n = 5) upon addition of the neurotransmitter dopamine at concentrations of 100 nM and 1 μM. Scale bars = 10 μm (c), = 1 μm (d).

sequence used in this study for the conjugation of the GBP previously showed fluorescence increases of up to 70% with a $K_{d,dopamine}$ of 42 nM.[7] Thus, we investigated next whether the SWCNT-GBP conjugate (**5**) still responds to dopamine. The fluorescence response remained unchanged (Figure 3a,b) compared to SWCNT-$(GT)_{20}$, showing an increase of ≈61% upon addition of dopamine (100 μM). Encouraged by this result, we tested whether it is also possible to target **5** to immobilized GFP and detect dopamine. Figure 3c shows the SWCNT-GBP conjugate bound to micropatterned GFP structures and the average of five fluorescence traces of single nanotubes (Figure 3d). We observed a fluorescence increase of GFP-bound SWCNTs both for 100 nM and 1 μM concentrations of dopamine. The increase was greater than in solution (Figure 3a,b) because in this case single sensors were analyzed as opposed to an ensemble, which decreases background and prevents scattering, quenching, and reabsorption. Therefore, it is possible to detect dopamine with carbon nanotubes bound to GFP, which opens up great possibilities for targeting GFP-fusion proteins of, for example, dopamine transporters on neurons and with the ability to sense single-neurotransmitter release events locally.

To further demonstrate the versatility of the SWCNT-GBP platform and make use of the unique properties of SWCNTs for deep-tissue imaging, we injected the nanotube–nanobody conjugate (1 nM) into live *Drosophila* embryos expressing the motor protein Kinesin-5 (Kin-5) as a GFP-fusion protein (Figure 4a,b). These syncytial embryos have not yet formed cell membranes between the nuclei, are approximately 150 μm in height, and thus provide an ideal scenario for high-contrast imaging at greater light penetration depths than in classic cell culture. Kin-5 is an indispensable motor protein for spindle formation and separation of the chromosomes. It binds to antiparallel microtubule arrays and exerts repulsive forces due to its (+)-end directed motor activity. In addition, Kin-5 is also involved in microtubule

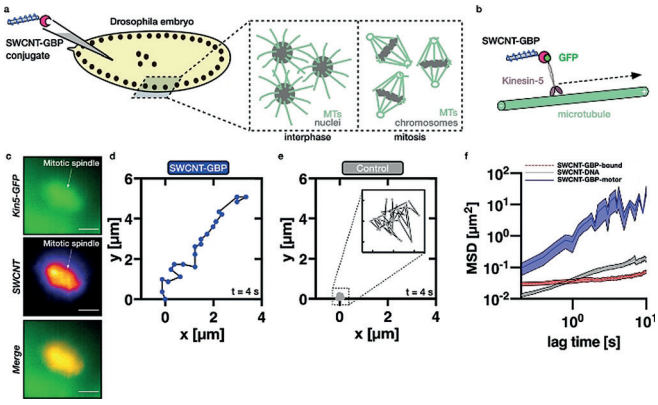

Figure 4. Injection of SWCNT-DNA-GBP conjugate **5** in *Drosophila* embryos, near-infrared labeling, and in vivo tracking of the motor protein Kinesin-5 (Kin-5). a) General scheme showing the injection of conjugate **5** into live *Drosophila* embryos expressing GFP fusion proteins of Kin-5 motors, which show a different morphology depending on the developmental stage (interphase/mitosis). b) Schematic of a SWCNT-tagged Kin-5-GFP moving along a microtubule. c) GFP and SWCNT channel images showing colocalization of Kin-5 and conjugate **5** at a mitotic spindle (scale bars = 10 μm). d) Real-time tracking of the directional movement of a single Kin-5 motor in the *Drosophila* embryo compared to random movement of the SWCNT-$(GT)_{20}$ control (e, t = 4 s, 5 frames per second). f) Mean-square displacement (MSD) plots of several SWCNT-GBP conjugates show directed movement in comparison to the control (SWCNT-DNA) and SWCNT-GBP conjugates bound to inactive (static) Kin-5-GFP (mean and s.e., n = 1–13 [SWCNT-GBP], n = 9 [SWCNT-GBP-bound], n = 28 [SWCNT-DNA]).

network dynamics in the interphase.[43] Therefore, Kin-5 is present in the whole organism but enriched in spindles during mitosis. Figure 4c shows colocalization of the (low signal/noise) GFP signal and the SWCNT's nIR fluorescence in a mitotic spindle, emphasizing their use as high-contrast immunolabeling agents. The conjugate **5** is thus a highly versatile tool for near-infrared experiments in *Drosophila*, as there are numerous variants containing different GFP-fusion proteins. In addition, the SWCNT fluorescence does not bleach as for example GFP, which (see Figure S7) renders them highly suitable candidates for long-term observation and fast fluorescent tracking of almost any molecule of interest.

In this study, we used our SWCNT-GBP platform to acquire real-time tracks of Kin-5 motors in vivo. Earlier studies already used SWCNT-Halo-tag variants or quantum dot/nanobody conjugates for Kinesin tracking in COS7 cells and were able to resolve tracks over several micrometers.[44,45] Tracking of single motor proteins in vivo, however, is more challenging due to active movement or diffusion/movement in the z-direction. In addition, Kin-5 exists in multiple states inside this living organism. First, Kin-5 molecules are diffusing around in the whole organism. Second, another fraction of Kin-5 is bound to microtubules in mitotic spindles but does not move (inactive). And lastly, a third fraction is bound to microtubules and active, which means they move along microtubules carrying cargo. Figure 4d shows the trajectory of a single SWCNT-GBP conjugate bound to a moving Kin-5 protein over four seconds, while Figure 4e depicts a representative trace of a SWCNT-$(GT)_{20}$ control in the same time frame (see also movie M1, SI). Whereas only random movement can be observed for the control, the SWCNT-GBP conjugate's trace shows directional movement over several micrometers with a mean velocity of $\approx 1340\,nm\,s^{-1}$. The directionality of this movement represents a direct proof for the successful binding of the SWCNT-GBP to Kin-5-GFP. To our knowledge, this represents the first real-time tracking of Kin-5 in *Drosophila*. Such directional tracks were analyzed and yield a motor velocity of $613 \pm 328\,nm\,s^{-1}$ (mean $\pm$ SD, $n = 14$). This value is in the same order of magnitude as values previously described for other members of the Kinesin family in vitro ($780 \pm 110\,nm\,s^{-1}$ [Kin1 in COS7 cells],[46] $570 \pm 20\,nm\,s^{-1}$ [Kin in HeLa cells],[47] $300 \pm 210\,nm\,s^{-1}$ [Kin1 in COS7 cells][44]). The SWCNT-GBP conjugate does most likely not affect the movement of Kin-5 because the additional friction is small compared to the energy of ATP hydrolysis. To further analyze the different types of movement observable in the nIR SWCNT tracks, we calculated the mean-squared displacement (MSD) for both conjugate **5** and the control (Figure 4f). These averaged MSDs show the different behavior of the SWCNT probes depending on their binding status. While DNA/SWCNTs were found to freely diffuse through the syncytial organism, SWCNT-GBP conjugates were found to be either bound to static Kin-5-GFP (red dashed line, as, for example, in the spindle in Figure 4c) or active Kin-5-GFP motors carrying out active movement and thus showing superdiffusive behavior (blue line). Analysis of the diffusive motion of SWCNTs has already been used to probe the extracellular space in brain slices and our novel nanobody-based targeting could add a new level of spatial control to such approaches.[48]

In summary, we conjugated GFP-targeting nanobodies to the surface of DNA-wrapped SWCNTs and showed that the SWCNT's nIR fluorescence is preserved after protein conjugation. We also proved that the nanobody is still functional after SWCNT conjugation and that these GBP-conjugated SWCNT are able to detect the important neurotransmitter dopamine, as previously observed with unconjugated SWCNTs. Furthermore, we injected the SWCNT-GBP conjugate into living embryos of *Drosophila melanogaster* for deep-tissue nIR labeling of the spindle apparatus as well as single-molecule tracking of the motor protein Kinesin-5. Taken together, these results demonstrate the robustness and the broad applicability of these novel nanotube–nanobody conjugates for in vitro and in vivo applications as well as targeted sensing.

Acknowledgements

We thank the FCI (Fonds der Chemischen Industrie), the VW foundation, and the DFG (SFB 937) for funding. S.K. acknowledges funding by the State of Lower Saxony (life@-nano). We thank Andreas Janshoff and Claudia Steinem for their support as well as Wentao Peng for help with ζ-potential measurements.

Conflict of interest

F. Opazo is shareholder of NanoTag Biotechnologies GmbH; all other authors declare no conflict of interest.

Keywords: fluorescent probes · kinesin · nanobodies · nanotubes · near-infrared fluorescence

How to cite: *Angew. Chem. Int. Ed.* **2019**, *58*, 11469–11473
Angew. Chem. **2019**, *131*, 11591–11596

[1] M. J. O'Connell, S. M. Bachilo, C. B. Huffman, V. C. Moore, M. S. Strano, E. H. Haroz, K. L. Rialon, P. J. Boul, W. H. Noon, C. Kittrell, et al., *Science* **2002**, *297*, 593–596.
[2] S. Kruss, A. J. Hilmer, J. Zhang, N. F. Reuel, B. Mu, M. S. Strano, *Adv. Drug Delivery Rev.* **2013**, *65*, 1933–1950.
[3] S. M. Bachilo, M. S. Strano, C. Kittrell, R. H. Hauge, R. E. Smalley, R. B. Weisman, *Science* **2002**, *298*, 2361–2366.
[4] J. Li, N. Wu, *Electroanalysis* **2005**, *17*, 7–14.
[5] T. Murakami, H. Nakatsuji, M. Inada, Y. Matoba, T. Umeyama, M. Tsujimoto, S. Isoda, M. Hashida, H. Imahori, *J. Am. Chem. Soc.* **2012**, *134*, 17862–17865.
[6] G. Hong, S. Diao, A. L. Antaris, H. Dai, *Chem. Rev.* **2015**, *115*, 10816–10906.
[7] F. A. Mann, N. Herrmann, D. Meyer, S. Kruss, *Sensors* **2017**, *17*, 1521.
[8] J. Zhang, M. P. Landry, P. W. Barone, J.-H. H. Kim, S. Lin, Z. W. Ulissi, D. Lin, B. Mu, A. A. Boghossian, A. J. Hilmer, et al., *Nat. Nanotechnol.* **2013**, *8*, 959–968.
[9] E. Polo, S. Kruss, *J. Phys. Chem. C* **2016**, *120*, 3061–3070.
[10] G. Hong, S. Diao, J. Chang, A. L. Antaris, C. Chen, B. Zhang, S. Zhao, D. N. Atochin, P. L. Huang, K. I. Andreasson, et al., *Nat. Photonics* **2014**, *8*, 723–730.

[11] J. Helma, M. C. Cardoso, S. Muyldermans, H. Leonhardt, *J. Cell Biol.* **2015**, *209*, 633 – 644.
[12] J. Ries, C. Kaplan, E. Platonova, H. Eghlidi, H. Ewers, *Nat. Methods* **2012**, *9*, 582 – 584.
[13] M. Reth, *Nat. Immunol.* **2013**, *14*, 765 – 767.
[14] M. Maidorn, A. Olichon, S. O. Rizzoli, F. Opazo, *MAbs* **2019**, *11*, 305 – 321.
[15] A. Kirchhofer, J. Helma, K. Schmidthals, C. Frauer, S. Cui, A. Karcher, M. Pellis, S. Muyldermans, C. S. Casas-Delucchi, M. C. Cardoso, et al., *Nat. Struct. Mol. Biol.* **2010**, *17*, 133 – 139.
[16] U. Rothbauer, K. Zolghadr, S. Tillib, D. Nowak, L. Schermelleh, A. Gahl, N. Backmann, K. Conrath, S. Muyldermans, M. C. Cardoso, et al., *Nat. Methods* **2006**, *3*, 887 – 889.
[17] D. Schumacher, J. Helma, A. F. L. Schneider, H. Leonhardt, C. P. R. Hackenberger, *Angew. Chem. Int. Ed.* **2018**, *57*, 2314 – 2333; *Angew. Chem.* **2018**, *130*, 2336 – 2357.
[18] M. Mikhaylova, B. M. C. Cloin, K. Finan, R. Van Den Berg, J. Teeuw, M. M. Kijanka, M. Sokolowski, E. A. Katrukha, M. Maidorn, F. Opazo, et al., *Nat. Commun.* **2015**, *6*, 1 – 7.
[19] H. D. Herce, D. Schumacher, A. F. L. L. Schneider, A. K. Ludwig, F. A. Mann, M. Fillies, M.-A. A. Kasper, S. Reinke, E. Krause, H. Leonhardt, et al., *Nat. Chem.* **2017**, *9*, 762 – 771.
[20] S. Kabatas, P. Agüi-Gonzalez, K. A. Saal, S. Jähne, F. Opazo, S. O. Rizzoli, N. T. N. Phan, *Angew. Chem. Int. Ed.* **2019**, *58*, 3438 – 3443; *Angew. Chem.* **2019**, *131*, 3476 – 3481.
[21] A. Hirsch, *Angew. Chem. Int. Ed.* **2002**, *41*, 1853 – 1859; *Angew. Chem.* **2002**, *114*, 1933 – 1939.
[22] M. Prato, K. Kostarelos, A. Bianco, *Acc. Chem. Res.* **2008**, *41*, 60 – 68.
[23] G. Clavé, S. Campidelli, *Chem. Sci.* **2011**, *2*, 1887 – 1896.
[24] A. Antonucci, J. Kupis-Rozmysłowicz, A. A. Boghossian, *ACS Appl. Mater. Interfaces* **2017**, *9*, 11321 – 11331.
[25] E. Polo, T. T. Nitka, E. Neubert, L. Erpenbeck, L. Vuković, S. Kruss, *ACS Appl. Mater. Interfaces* **2018**, *10*, 17693 – 17703.
[26] A. Setaro, M. Adeli, M. Glaeske, D. Przyrembel, T. Bisswanger, G. Gordeev, F. Maschietto, A. Faghani, B. Paulus, M. Weinelt, et al., *Nat. Commun.* **2017**, *8*, 1 – 7.
[27] F. A. Mann, J. Horlebein, N. F. Meyer, D. Meyer, F. Thomas, S. Kruss, *Chem. Eur. J.* **2018**, *24*, 12241 – 12245.
[28] F. Ernst, T. Heek, A. Setaro, R. Haag, S. Reich, *J. Phys. Chem. C* **2013**, *117*, 1157 – 1162.
[29] S. Kruss, M. P. Landry, E. Vander Ende, B. M. A. Lima, N. F. Reuel, J. Zhang, J. Nelson, B. Mu, A. Hilmer, M. Strano, *J. Am. Chem. Soc.* **2014**, *136*, 713 – 724.
[30] M. S. Filipiak, M. Rother, N. M. Andoy, A. C. Knudsen, S. Grimm, C. Bachran, L. K. Swee, J. Zaumseil, A. Tarasov, *Sens. Actuators B* **2018**, *255*, 1507 – 1516.
[31] R. Nißler, F. A. Mann, P. Chaturvedi, J. Horlebein, D. Meyer, L. Vuković, S. Kruss, *J. Phys. Chem. C* **2019**, *123*, 4837 – 4847.
[32] F. K. Brunecker, F. Schöppler, T. Hertel, *J. Phys. Chem. C* **2016**, *120*, 10094 – 10103.
[33] F. Schöppler, C. Mann, T. C. Hain, F. M. Neubauer, G. Privitera, F. Bonaccorso, D. Chu, A. C. Ferrari, T. Hertel, *J. Phys. Chem. C* **2011**, *115*, 14682 – 14686.
[34] E. Polo, S. Kruss, *Anal. Bioanal. Chem.* **2016**, *408*, 2727 – 2741.
[35] N. F. Reuel, B. Grassbaugh, S. Kruss, J. Z. Mundy, C. Opel, A. O. Ogunniyi, K. Egodage, R. Wahl, B. Helk, J. Zhang, et al., *ACS Nano* **2013**, *7*, 7472 – 7482.
[36] T. V. Galassi, P. V. Jena, J. Shah, G. Ao, E. Molitor, Y. Bram, A. Frankel, J. Park, J. Jessurun, D. S. Ory, et al., *Sci. Transl. Med.* **2018**, *10*, eaar2680.
[37] J. D. Harvey, P. V. Jena, H. A. Baker, G. H. Zerze, R. M. Williams, T. V. Galassi, D. Roxbury, J. Mittal, D. A. Heller, *Nat. Biomed. Eng.* **2017**, *1*, 1 – 43.
[38] G. Bisker, J. Dong, H. D. Park, N. M. Iverson, J. Ahn, J. T. Nelson, M. P. Landry, S. Kruss, M. S. Strano, *Nat. Commun.* **2016**, *7*, 1 – 14.
[39] V. Zubkovs, N. Schuergers, B. Lambert, E. Ahunbay, A. A. Boghossian, *Small* **2017**, *13*, 1701654.
[40] M. H. Wong, J. P. Giraldo, S. Y. Kwak, V. B. Koman, R. Sinclair, T. T. S. Lew, G. Bisker, P. Liu, M. S. Strano, *Nat. Mater.* **2017**, *16*, 264 – 272.
[41] S. Kruss, D. P. Salem, L. Vuković, B. Lima, E. Vander Ende, E. S. Boyden, M. S. Strano, L. Vukovic, B. Lima, E. Vander Ende, et al., *Proc. Natl. Acad. Sci. USA* **2017**, *114*, 1789 – 1794.
[42] D. Meyer, A. Hagemann, S. Kruss, *ACS Nano* **2017**, *11*, 4017 – 4027.
[43] Z. Lv, J. Rosenbaum, T. Aspelmeier, J. Großhans, *J. Cell Sci.* **2018**, *131*, jcs210583.
[44] N. Fakhri, A. D. Wessel, C. Willms, M. Pasquali, D. R. Klopfenstein, F. C. MacKintosh, C. F. Schmidt, *Science* **2014**, *344*, 1031 – 1035.
[45] E. A. Katrukha, M. Mikhaylova, H. X. Van Brakel, P. M. Van Bergen En Henegouwen, A. Akhmanova, C. C. Hoogenraad, L. C. Kapitein, *Nat. Commun.* **2017**, *8*, 1 – 8.
[46] D. Cai, K. J. Verhey, E. Meyhöfer, *Biophys. J.* **2007**, *92*, 4137 – 4144.
[47] S. Courty, C. Luccardini, Y. Bellaiche, G. Cappello, M. Dahan, *Nano Lett.* **2006**, *6*, 1491 – 1495.
[48] A. G. Godin, J. A. Varela, Z. Gao, N. Danné, J. P. Dupuis, B. Lounis, L. Groc, L. Cognet, *Nat. Nanotechnol.* **2017**, *12*, 238 – 243.

Manuscript received: April 4, 2019
Revised manuscript received: May 3, 2019
Accepted manuscript online: May 21, 2019
Version of record online: July 8, 2019

Angewandte Chemie
Eine Zeitschrift der Gesellschaft Deutscher Chemiker

Supporting Information

Nanobody-Conjugated Nanotubes for Targeted Near-Infrared In Vivo Imaging and Sensing

*Florian A. Mann, Zhiyi Lv, Jörg Großhans, Felipe Opazo, and Sebastian Kruss**

anie_201904167_sm_miscellaneous_information.pdf
anie_201904167_sm_movie_m1.avi

SUPPORTING INFORMATION

Table of contents

70

1. Supplementary figures

1.1. Figure S1

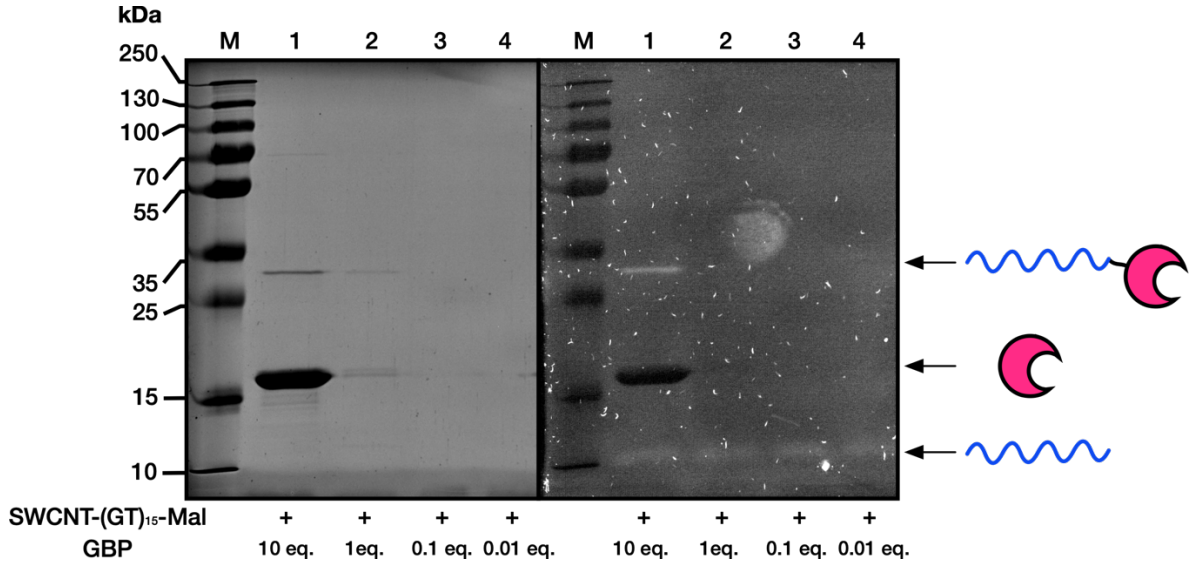

Figure S1. DNA- and protein stained SDS-PAGE analysis of the conjugation of the GFP-binding nanobody (GBP, equivalents with respect to the number of DNA oligos on the SWCNT surface) to a $(GT)_{15}$ wrapped single-walled carbon nanotube.

1.2. Figure S2

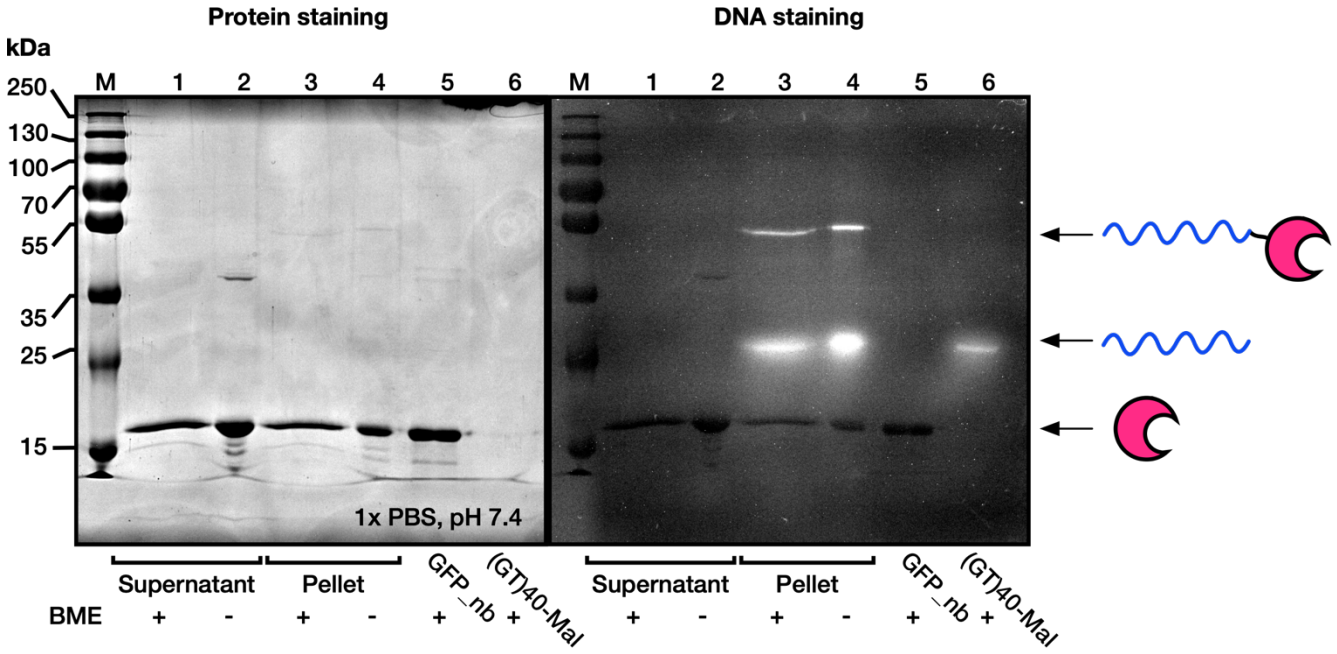

Figure S2. DNA- and protein stained SDS-PAGE showing precipitation at high equivalents of GBP (~50 eq. with respect to the number of DNA oligos on the SWCNT surface) during the conjugation. This emphasizes the importance of choosing the right ratio of GBP/SWCNT.

1.3. Figure S3

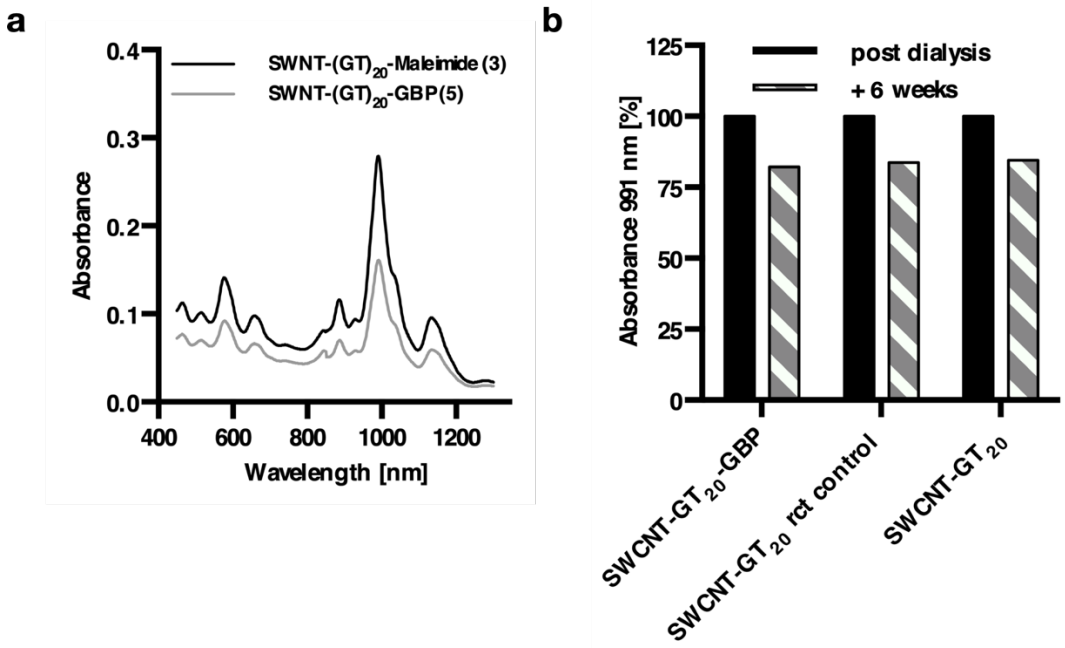

Figure S3. (a) UV/vis/nIR absorbance spectra before and after the conjugation of the GFP-binding nanobody (GBP). (b) Comparison of maximal absorbance of the conjugate **5**, the SWCNT-$(GT)_{20}$ reaction control (no SMCC activation) and SWCNT-$(GT)_{20}$ directly after the reaction/dialysis and after 6 weeks at 4 °C. For absorbance measurements, the top 75% of the solution after centrifugation were taken. This comparison shows, that all SWCNT variants display comparable colloidal stability.

1.4. Figure S4

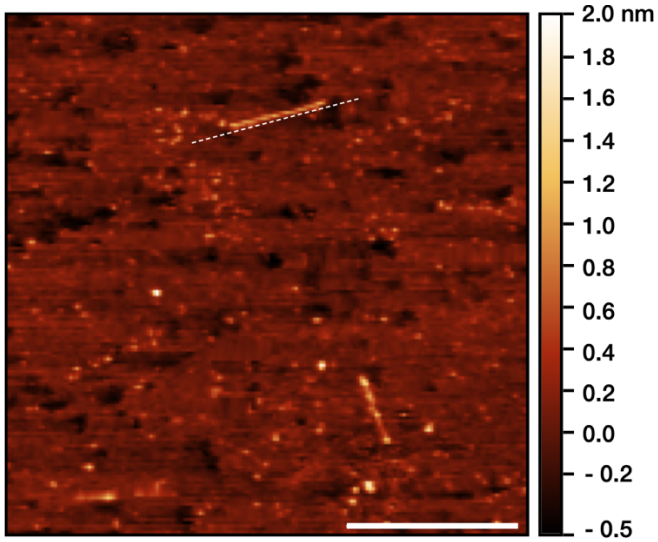

Figure S4. Atomic Force Microscopy image showing the non-SMCC activated SWCNT-DNA control. The white dashed line indicates the height-trace taken for the comparison in Fig. 1e (slightly offset for better visibility of the SWCNT). Scale bar = 500 nm.

1.5. Figure S5

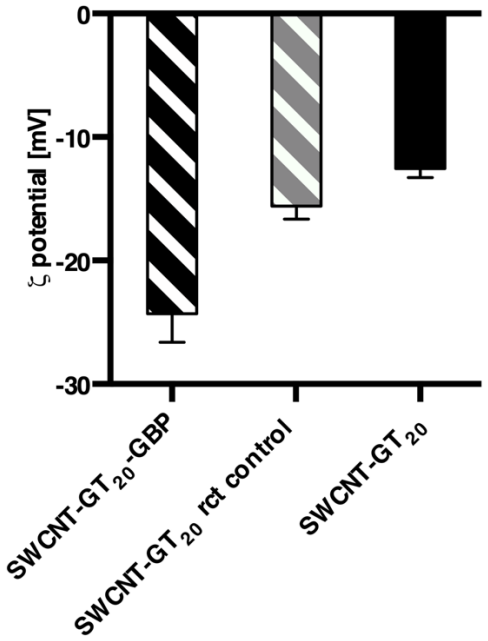

Figure S5. ζ-potential measurement showing the difference between the conjugate **5** (left), the reaction control (without SMCC activation of the GT_{20}-NH_2, middle) and SWCNT-GT_{20} (mean and s.e., n = 6). The shift to more negative values can be explained by the additional charges introduced by the negatively charged anti-GFP nanobody (pI = 5.45).

1.6. Figure S6

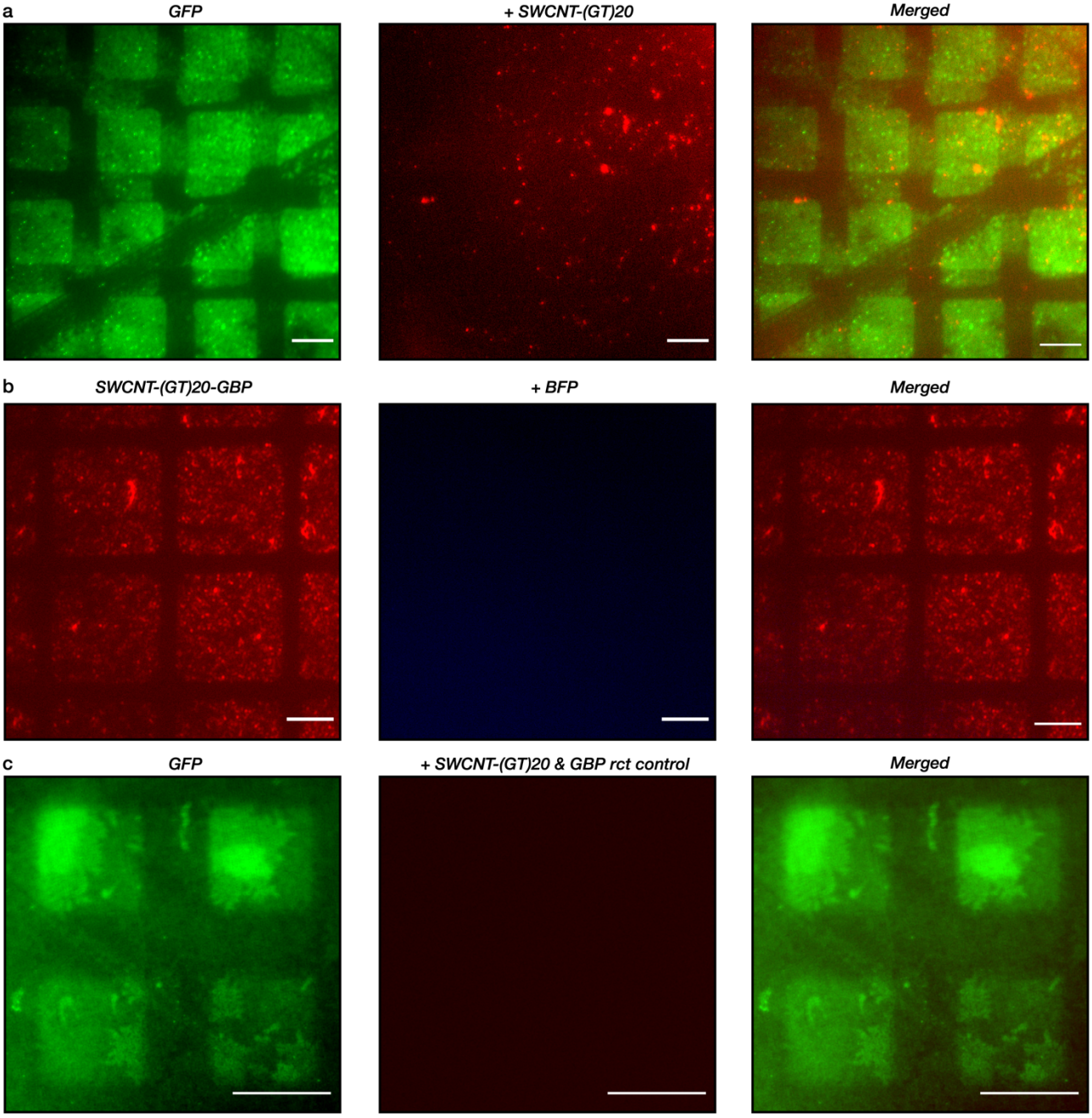

Figure S6. Different *in vitro* assay controls. (a) Control assay with immobilized GFP and addition of the $(GT)_{20}$-SWCNT control. Despite a certain degree of unspecific binding, no colocalization of GFP and nIR signal could be observed. (b) Control assay with immobilized SWCNT-GBP conjugate **5** and addition of the blue fluorescent protein Tag-BFP. This clearly shows, when compared to Fig. 2b, that the binding of SWCNT-GBP is specific to GFP. (c) Control assay with immobilized GFP and incubation with the control **6** (conjugation reaction without SMCC activation) showing no binding of SWCNTs to GFP. Scale bars = 10 µm.

1.7. Figure S7

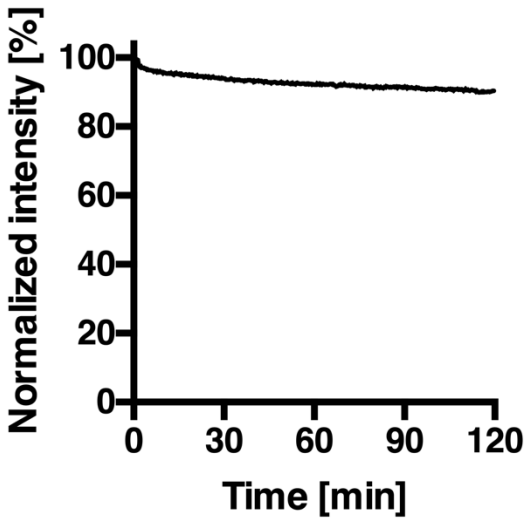

Figure S7. Intensity vs. time analysis of single-walled carbon nanotubes under continuous excitation using a 561 nm laser (Cobolt) at 500 mW.

1.8. Supplementary movie M1

Supplementary movie M1 showing a SWCNT-$(GT)_{20}$-GBP conjugate bound to Kin5-GFP moving inside a *drosophila* embryo. Movie was acquired at 5 fps (exposure time = 200 ms). Start (green) and end (red) of the track are indicated by arrows.

2. General Information

(6,5)-chirality enriched single-walled carbon nanotubes (SWCNT, Product No.: 773735), Sulfo-SMCC crosslinker and 3'-amino functionalized DNA oligonucleotides were acquired from *Sigma Aldrich* (Darmstadt, Germany). All reagents were of synthesis grade quality and were used as supplied. Unless otherwise stated, experiments and measurements were performed in phosphate buffered saline (PBS, 8.2 mM Na_2HPO_4, 1.8 mM K_2HPO_4, 137 mM NaCl, 2.7 mM KCl, pH 7.4). Protein concentrations were determined by UV-absorbance at 280 nm using a *NanoDrop 2000* Spectrophotometer from *Thermo Scientific*.

2.1. UV/vis/nIR absorbance spectroscopy and SWCNT concentration estimation

200 µL of a solution containing individualized SWCNTs were submitted to UV/vis/nIR absorbance spectroscopy on a JASCO V-670 (Spectra Manager Software) using a 10 mm-path cuvette. Spectra were acquired using a scan speed of 1000 nm/min, a data interval of 0.5 nm and a UV/vis and nIR bandwidth of 2 nm and 4 nm, respectively.
SWCNT concentration was estimated using the maximal absorbance at approx. 991 nm using the molar extinction coefficient determined by Schöppler *et al*.[1]

2.2. nIR fluorescence spectroscopy

In a 96-well plate, 100 µL of the SWCNT-DNA-(GBP)-solutions were excited at 561 nm using a 300 W Xe-lamp guided through a monochromator (LOT, Germany) and their fluorescence spectra recorded in the range between 850 and 1250 nm using a Shamrock 193i spectrograph (Andor Technology Ltd., Belfast, Northern Ireland) coupled to an Olympus IX73 microscope and an exposure time of 1 s, a slit width of 500 µm and an Andor iDus InGaAs 491 array NIR detector.

2.3. SDS-PAGE with Coomassie-/GelRed-Stain

The samples subjected to sodiumdodecylsulfate-polyacrylamide gel electrophoresis (SDS-PAGE) were mixed with the corresponding amount of 4x reducing Laemmli sample buffer to reach a final 1x concentration. SDS-PAGE was performed at 220 V/400 mA for 45 min in 1x Tris/Glycine/SDS-running buffer with 12% acrylamide gels using PageRuler Plus Prestained (life technologies) as a size marker. Staining of nucleic acids was carried out with the dye GelRed (Biotium Inc., USA, 3x solution in 30 % (*v/v*) ethanol, 10% (v*/v*) acetic acid) for 60 minutes after heating in the microwave and five subsequent washing steps using ddH_2O.
Staining of proteins was performed with a solution of Coomassie Brilliant Blue R-250 (0,25% (*w/v*) Coomassie Brilliant Blue R-250, 30 % (*v/v*) ethanol, 10% (*v/v*) acetic acid) for 15 minutes after heating in the microwave. Subsequent incubation with destaining solution (50% (*v/v*) ethanol, 10% (*v/v*) acetic acid, 40% (*v/v*) Millipore H_2O) for 10 minutes after microwave-heating was repeated three times. The destained gel was captured using a c300 imaging system (Cambridge Bioscience) both for protein (vis) and nucleic acid detection (UV).

2.4. Atomic Force Microscopy (AFM)

20 µL of each of the SWCNT-DNA-(GBP) solutions were immobilized on freshly cleaved muscovite mica by spin-coating, ten minutes incubation, subsequent washing of the surface with MilliQ water and drying using a N_2-stream. AFM images were acquired in tapping mode (scan rate = 0.5 Hz, 512 lines) using an Asylum Research MFP-3D Infinity® instrument equipped with rectangular cantilevers (Opus, MikroMasch Europe, Al-coating, tetrahedral tip, ν_{res} = 300 kHz, k = 26 $N \cdot m^{-1}$).
Analysis of the acquired images was performed via the open-source software Gwyddion. For all

images, the background/tilt was removed via a 2nd order polynomial fit. The surface plane was set to zero using three-point levelling.

2.5. nIR fluorescence microscopy

nIR imaging was carried out under 561 nm-laser excitation (Cobolt Jive™ laser (Cobolt AB, Solna, Sweden, 500 mW) on an Olympus IX53 microscope equipped with a 100x oil-immersion objective (Olympus 100x UPLSAPO 100XS, NA=1.35). Detection of the near-infrared photoluminescence was carried using either a Xenics® Xeva-1.7-320 NIR camera (Xenics, Heverlee, Belgium) or an Andor Zyla 5.5 sCMOS camera (Andor Technology Ltd., Belfast, Northern Ireland).

2.6. ζ-potential measurement

ζ-potential measurements were carried out using a Zetasizer Nano S (Malvern Instruments, UK) in 1x PBS at a SWCNT concentration of ~0.5 nM (pH 7.4). Analysis was performed using the corresponding Zetasizer software.

3. Experimental Procedures

3.1. Single-walled carbon nanotube dispersion, conjugation to GBP and characterization

3.1.1. SWCNT-GT_{20}-GBP conjugation

3.1.1.1 $(GT)_{20}$-SMCC-Maleimide (2)

3 mg Sulfo-SMCC (in 15 µL DMSO) and 28 µL 10x PBS buffer were added to 250 µL of a 2 mg/mL DNA-oligonucleotide solution in ddH_2O. The pH was adjusted to pH 7.4 via addition of 1 µL 1M NaOH and the solution agitated at 400 rpm/RT for 60 minutes.

3.1.1.2 Dispersion of (6,5) enriched carbon nanotubes using DNA-maleimide (3)

Based on a 2 mg/mL (6,5)-chirality-enriched SWCNT stock suspension in MilliQ™-grade H_2O, ~ 250 µg SWCNTs were added to a 1.5 mL centrifuge tube, spun down at 16,100 g for 15 minutes and the supernatant discarded.
In the next step, 290 µL of DNA-oligo-Maleimide solution **2** were added to the raw SWCNT material. The solution was tip sonicated for 15 minutes (Fisher Scientific™ Model 120 Sonic Dismembrator, 30% amplitude, 36 W, 4 °C) and subsequently centrifuged at 16100 g (30 min) to remove large bundles, aggregates or metal catalyst remaining from SWCNT synthesis. The supernatant was transferred to 100 kDa-MWCO centrifugal filters and washed 5x with 1xPBS. The remaining solution was resuspended in 500 µL 1xPBS using tip-sonication (36 W, 2 min, 4 °C) and again centrifuged (30 min, 16100 g). The SWCNT concentration in the supernatant was determined as described in 2.1.

3.1.1.3 Conjugation of an anti-GFP nanobody to SWCNT-DNA-Maleimide (5)

The SWCNT-DNA-Maleimide solutions **3** were diluted to a concentration of 10 nM using 1xPBS and transferred to two different microcentrifuge tubes each (v = 250 µL).
The anti-GFP nanobody bearing a single ectopic cysteine at the C-terminus (NanoTag Biotechnologies GmbH, Cat# N0301) was reduced on ice for 30 minutes using 5 mM TCEP and 5 mM EDTA and rebuffered subsequently to 1xPBS (5 mM EDTA, pH 7.4) using ZebaSpin Desalting columns (7 kDa MWCO). The protein concentration was estimated using A(280 nm) using the NanoDrop 2000.
After addition of the reagents the pH was checked, and the reaction solution agitated at 250 rpm for five minutes at RT and then incubated without shaking for 14 hours.

The solution was transferred to 300.000 MWCO dialysis tubings and dialyzed against 1xPBS (4x change of PBS) to remove unconjugated nanobody.

3.2. *In vitro* binding assay

Based on a previously created silicon master, patterned PDMS stamps were created. Next, a 1 nM SWCNT solution (either SWCNT-GBP conjugate **5** or the $(GT)_{20}$/SWCNT control) was added to the stamp and incubated for 30 min at room temperature. After washing (1xPBS, 0.3% TritonX100, 3x) stamping was carried out via 30 min of incubation on a glass bottom petri dish. Excess SWCNT-material on the surface was again removed via washing (1xPBS, 0.3% TritonX100, 3x). In the next step, the surface was passivated using a 5% *w/v* BSA solution and subsequently washed again with

washing buffer (3x). Either purified green fluorescent protein (GFP form *Aequorea Victoria*) or Blue fluorescent protein (tagBFP from *Entacmaea quadricolor*) were then incubated on the surface at a concentration of 2 µM for one hour at ambient temperature in a buffer containing 1% *w/v* BSA. After washing (see above), imaging was carried out using a 100x objective on an Olympus IX53 microscope.

3.3. *Drosophila* embryo preparation and injection

Drosophila embryos (0-30 min old) expressing Kinesin-5-GFP[2] were dechorionated with commercial klorix solution (hypochlorite) for 90 to 120 s, rinsed with water thoroughly, aligned on a piece of agar, transferred to a cover slip coated with glue, desiccated in open air for 15 min and covered with halocarbon oil (Voltalef 10S, Lehmann & Voss). SWCNT-GBP conjugate **5** was injected using a Microinjector FemtoJet® (Eppendorf) on an inverted microscope. After 30-120 min incubation, the image of nIR and GFP channels were acquired. Nanotube without conjugated GBP was used as a negative control.

3.4. Dopamine sensing

In order to detect the fluorescence increase upon addition of the neurotransmitter dopamine, 5 µL of the corresponding and freshly prepared dopamine•HCl solution (0, 100 µM, 1 mM) in 1xPBS were added to 50 µL of **5** and the corresponding control (both 10 nM, in 1xPBS) in a 96-well plate format and the fluorescence spectra were recorded before and after addition (exposure time 2 sec, n = 3).

3.5. Targeted dopamine sensing

Based on a previously created silicon master, patterned PDMS stamps were created. Next, a 2 µM GFP solution was added to the stamp, incubated for 10 minutes and the stamp subsequently rinsed with 1x PBS. In the next step, the PDMS stamp was transferred to a glass bottom petri dish and incubated for 30 minutes. Excess GFP was removed by washing (1xPBS, 0.3% TritonX100, 3x). The GFP-patterned surface was passivated using a 5% w/v BSA solution and subsequently washed again with washing buffer (3x). To immobilize the SWCNT-GBP conjugate **5** on GFP, the surface was then incubated with a 1 nM solution of 5 for 1 h and subsequently washed again three times (washing buffer). Imaging was carried out using a 100x objective and dopamine•HCl was added after 30 frames (c_{final} = 100 nM) and 60 frames (c_{final} = 1 µM) at a frame rate of 0.5 fps (2 s exposure time).

4. References

[1] F. Schöppler, C. Mann, T. C. Hain, F. M. Neubauer, G. Privitera, F. Bonaccorso, D. Chu, A. C. Ferrari, T. Hertel, *J. Phys. Chem. C* **2011**, *115*, 14682–14686.

[2] Z. Lv, J. Rosenbaum, T. Aspelmeier, J. Großhans, *J. Cell Sci.* **2018**, *131*, jcs210583.

4.2.2. Discussion

The manuscript in chapter 4.2.1 describes the conjugation of a GFP-binding nanobody to a DNA-wrapped carbon nanotube and the subsequent characterization, use for a proof-of-concept targeted dopamine sensing experiment and utilization for the first tracking of a motor protein inside a living organism. But how does this study compare to previous or later studies? The first report on a combination of antibodies and SWCNTs was published in 2001 by Erlanger et al., who showed, that a previously raised anti-C_{60} antibody can also bind SWCNTs *via* a binding cavity rich in hydrophobic amino acids.[159] The authors verified successful antibody binding using AFM *versus* a control with another IgG specific for the aldosterone receptor, that did not show binding to the nanotube. Further examples include the non-covalent immobilization of a prostate-specific antigen (PSA) binding antibody using 1-pyrenebutanoic acid succinimidyl ester (and the antibody's lysine residues) by Li et al. in 2005[175] and several studies by the group of Hongjie Dai in 2008/2009, where they immobilized the therapeutic antibody Herceptin on SWCNTs wrapped by phospholipid-PEG using amine- or thiol-chemistries.[163,176–178] In the last examples, the studies aimed mostly at using SWCNTs as targeted Raman- or NIR-labels for Her2 positive beast cancer cells. However, besides functional studies these early examples of bioconjugation to SWCNTs did not include any characterization or control of successful bioconjugation. At best, the authors performed AFM/SEM imaging of the final conjugate, but without including any negative controls. In 2011, Venturelli et al. reported the covalent immobilization of an anti-MUC1 antibody on MWCNTs and DWCNTs using both carboxylated tubes and the 1,3-dipolar cycloaddition of azomethine ylides (see chapter 2.2.3.2) for the attachment of NHS- or maleimide-anchors, which could subsequently be linked to the antibody.[173] Here and in two follow-up studies by the same laboratories[179,180], the authors also made use of many different characterization techniques such as thermogravimetric analysis (TGA), sodium dodecyl sulfate-polyacrylamide gel electrophoresis (SDS-PAGE), transmission electron microscopy (TEM) and UV-absorbance spectroscopy. In addition, they confirmed retained function of the antibody after conjugation using surface plasmon resonance (SPR). However, if carried out for SWCNTs, the use of these types of covalent functionalization would destroy their NIR fluorescence and thus prevent their use in e.g. microscopy applications. In contrast, Williams et al. reported in two separate studies the conjugation of an anti-HE4 antibody and an anti-uPA antibody to $(TAT)_6$-DNA wrapped SWCNTs to create sensors for the ovarian cancer biomarker HE4 (human epididymis protein 4)[96]

and the metastatic prostate cancer biomarker uPA[181], respectively. Here, however, the authors only carried out ζ-potential measurements to assess the bioconjugation success. In contrast to the studies described above, this work (see section 4.2.1) does not rely on full-length antibodies, but makes use of the retained specificity and the decreased size of nanobodies (see section 2.3.3).[125] Consequently, they offer the advantage of a reduced distance between the antigen binding event and e.g. the signal generation in SWCNT-based optical sensors. Furthermore, they were shown to be more stable e.g. in the reducing intracellular environment opening up possibilities also for intracellular sensing or targeted drug delivery. In this study at hand, a GFP-binding nanobody (GBP) with a C-terminal ectopic cysteine was attached to a 3'-amine modified $d(GT)_{20}$ oligonucleotide, which was previously shown to cause a fluorescence increase in response to the neurotransmitter dopamine, when wrapping a SWCNT. The conjugation of the GBP was also carried out with the $d(GT)_{10}$ oligonucleotide, which was shown to yield the most selective and sensitive sensors for dopamine, however, its decreased length led to reduced colloidal stability of the SWCNT-DNA after GBP conjugation. Also, it is important to note, that the excess of GBP in the reaction mixture is crucial to prevent SWCNT aggregation, which likely results from too many GBPs per nanotube. To control the success of the conjugation reaction, a combination of different methods was carried out including AFM, ζ-potential measurements and SDS-PAGE. In addition, the retained functionality after the conjugation was tested using an *in vitro* fluorescence colocalization assay. Taken together, these methods of analysis and characterization clearly show successful conjugation and desired function of the SWCNT-$d(GT)_{20}$-GBP conjugate.

Fig. 3 (p. 66) shows that the SWCNT-$d(GT)_{20}$-GBP conjugate still responds to the neurotransmitter dopamine in solution, but also when bound to its surface-immobilized antigen GFP. This proof-of-concept experiment exemplifies that targeting of SWCNT-based optical sensors is possible and that they still show a sensor response even on the single-nanotube level. This in turn opens up a lot of possibilities for using this technique to target SWCNT-based dopamine sensors to e.g. dopaminergic neurons after injection in an *in vivo* setting, so that they can act only at the desired sites.

In addition to targeted sensing, the conjugate was also used as an *in vivo* NIR-tag. After injection into *drosophila* embryos, the SWCNT-$d(GT)_{20}$-GBP conjugate did not only enable high-contrast deep-tissue imaging of the spindle-apparatus in the NIR, but also tracking of a Kinesin-5 motor protein inside this living organism. The proteins of the kinesin family are, together with dynein and myosin, essential for transport of e.g. cargo

and organelles inside our cells. Under consumption of ATP, they are able to move (with their cargo) along microtubules (from - to +-end). SWCNTs were already used in an earlier study by Fakhri et al. for the tracking of Kinesin motor proteins *in cellulo*.[182] Here, the authors used the Halo-Tag platform (see section 2.4.1, Fig. 2.14) to attach DNA-wrapped SWCNTs to Kinesin-1 in cultured COS-7 cells. By this means, they were able to track single SWCNTs bound to a molecular motor over several seconds and retrieve biophysical parameters such as velocity or mean-square-displacement (MSD). Specifically for their system, they reported a mean velocity of 300 $\pm$ 210 nm/s (mean $\pm$ SD), whereas Courty et al. determined a mean velocity of 600 $\pm$ 10 nm/s *in vitro* and 570 $\pm$ 20 nm/s in HeLa cells using quantum dot-streptavidin conjugates and biotin-labelled kinesin.[183] These values are in the same range as other values previously determined for other *in vitro* or *in cellulo* systems.[184–187] In contrast, this study comprises the injection of the SWCNT-d$(GT)_{20}$-GBP conjugate into living *drosophila* embryos and their use for tracking of single kinesin-5 motor proteins inside this living organism. The determined mean velocity of 610 $\pm$ 330 nm/s (mean $\pm$ SD) represents, to the best of the author's knowledge, the first value for kinesin movement speed in an *in vivo* setting and is in the same order of magnitude as those values determined *in vitro* or *in cellulo*. This measurement represents an important step in understanding molecular motors not only *in vitro*, but in their real, native environment. Furthermore, it emphasizes the strengths of SWCNTs for bioimaging, where the extremely low background (autofluorescence) and the non-bleaching (see Fig. S7, p. 75) nature of the NIR-fluorescence enables deep-tissue tracking of single nanotubes for several seconds or minutes.

In summary, this study showed that it is possible to install small targeting units on SWCNTs with preserved sensing capabilities. This allows not only targeted sensing of e.g. dopamine, but also NIR-immunofluorescence microscopy and tracking of molecular motors in live animals. The next step is now, to modify these conjugates further to tailor their cell-penetration properties according to the specific needs of the application. If for instance sensing outside the cell is desired, the SWCNT-conjugate should not be taken up into the cell, whereas for intracellular drug delivery or sensing, derivatives are required, that are able to cross cellular membranes. This fine-tuning of cellular localization properties will be studied and addressed in the following chapter.

4.3 Peptide barrels as a novel functionalization platform for SWCNTs

The biopolymer wrapping of SWCNTs can be used to tailor their properties generating e.g. optical sensors. It can also carry an additional functional group (anchor group) allowing attachment of further units such as fluorophores, drugs or recognition units (see chapter 4.2.1). In the preceding chapters of this thesis, DNA oligonucleotides were used to mask the hydrophobic carbon nanotube surface imparting aqueous solubility and sensing capabilities through conformational changes upon analyte exposure. While the DNA's nucleobases bind and stack to the SWCNT's surface, the phosphate backbone interacts with the solvent leading to stable colloidal dispersion and preventing the SWCNTs from reaggregation. The space of nucleobases is very limited consisting of adenine (A), guanine (G), cytosine (C), thymine (T) and a few unnatural derivatives. These unnatural derivatives can also be synthesized in a way enabling e.g. click chemistry to generate site-specific DNA-protein hybrids.[188] With respect to SWCNT-based optical sensors, however, it is especially the sequential arrangement of nucleobases determining the sensitivity and selectivity of the respective sensor (see chapter 4.1). Here, it is of high desire to increase the sequence space in order to be able to fine-tune the SWCNTs characteristics to the application's specific needs. Peptides and proteins offer a drastically increased degree of flexibility consisting of 20 proteinogenic amino acids as building blocks with a vast variety of also commercially available unnatural amino acids. Translated to a sequence space this would mean e.g. for a pentamer 1024 (DNA) compared to 3.200.000 different possibilities (peptide). However, compared to oligonucleotides, peptides and proteins were only scarcely used for SWCNT dispersion, which is mainly due to the fact, that in many cases they did not yield colloidally stable systems.[189]

In this chapter, α-helical coiled-coil peptide barrels (αHBs, see section 2.3.2) will be evaluated for the ability to encapsulate and thus debundle/disperse SWCNTs depending e.g. on their pore size. If successful, this non-covalent wrapping could serve as a functionalization platform, where outer residues of the barrel can be modified before or after SWCNT-wrapping with functional units. As outlined in section 2.3.2, they can be *de novo* designed to contain an inner pore of varying size depending on their amino acid sequence. To study the effect of the peptide's tertiary/quaternary structure on SWCNT encapsulation, two different barrels will be compared containing on the one hand a 7.6 Å pore (coiled-coil heptamer, CC-Hept) and on the other hand a control peptide forming

an inner cavity of just 3.9 Å (see Fig. 1, p. 87). The resulting SWCNT@Barrel hybrids should then be evaluated regarding their:

(a) SWCNT dispersion yield using NIR absorbance spectroscopy

(b) Structural and spatial arrangement of the barrels on a nanotube (using AFM)

(c) Their retained NIR fluorescence properties.

4.3.1. Carbon Nanotubes Encapsulated in Coiled-coil Peptide Barrels (Manuscript 3)

This chapter was published in the following journal:

Florian A. Mann, Jan Horlebein, Nils Frederik Meyer, Daniel Meyer, Franziska Thomas* and Sebastian Kruss*

"Carbon Nanotubes Encapsulated in Coiled-Coil Peptide Barrels"

Chem. Eur. J. **2018**, 24, 12241 - 12245

This article is available using at: DOI:10.1002/chem.201800993 * Corresponding authors

Responsibility assignment: S.K., F.T. and F.A.M designed and conceived the project. F.A.M. and J.H. performed SWCNT dispersion, absorbance/fluorescence spectroscopy/microscopy and AFM. N.F.M., J.H. and F.A.M. carried out peptide synthesis and purification. J.H., F.T. and F.A.M. carried out CD measurements. F.A.M. and J.H. did data analysis and D.M. built the NIR microscopy setup. F.A.M., F.T. and S.K wrote the manuscript with input from J.H..

ChemPubSoc Europe

DOI: 10.1002/chem.201800993

CHEMISTRY A European Journal Communication

Biosensors

Carbon Nanotubes Encapsulated in Coiled-Coil Peptide Barrels

Florian A. Mann,[a] Jan Horlebein,[a] Nils Frederik Meyer,[b] Daniel Meyer,[a] Franziska Thomas,*[b, d] and Sebastian Kruss*[a, c]

Abstract: Specific functionalization of 1D nanomaterials such as near infrared (nIR) fluorescent single-walled carbon nanotubes (SWCNTs) is essential for colloidal stability and tailoring of their interactions with the environment. Here, we show that de novo designed alpha-helical coiled-coil peptide barrels (αHBs) with appropriate pores encapsulate and solubilize SWCNTs. In contrast, barrels without or with narrow pores showed a much smaller efficiency. Absorption/fluorescence spectroscopy and atomic force microscopy indicate that the SWCNTs are incorporated into the αHB's pore. The resulting hybrid **SWCNT@αHBs** display periodic surface coverage with a 40 nm pitch and remain fluorescent in the nIR. This approach presents a novel concept to encapsulate, discriminate and functionalize SWCNTs non-covalently with peptides and holds great promise for future applications in bioimaging or drug delivery.

1D Materials such as single-walled carbon nanotubes (SWCNT) and their properties are of high fundamental interest and potential building blocks for optoelectronic devices. Semiconducting SWCNTs are fluorescent in the near-infrared (nIR) region and show ultra-low photobleaching and blinking.[1–2] These properties make them promising candidates for applications in biosensing, drug delivery and imaging.[3–7] The key challenge is to tailor their surface and thus render them stable in aqueous solution but also to control interactions with their environment.[8] To preserve their nIR fluorescence, mainly non-covalent functionalization schemes including amphiphilic (bio)-polymers, modified polyethyleneglycols, proteins and especially single-stranded DNA (ssDNA) have been used.[9–16] Covalent conjugation strategies of SWCNTs are highly promising but they alter the nanotube's conjugated sp^2 system and thus their excitonic fluorescence.[17–19] Therefore, these approaches are less used if unchanged optoelectronic properties such as the nIR fluorescence are important.

Peptides would be ideal to tailor the surface of SWCNTs due to their chemical diversity. However, peptides have so far been used much less than DNA for non-covalent functionalization.[20–22] The major reason is that successful solubilization/dispersion/functionalization requires a fine balance between adsorption to the SWCNT surface, aggregation and colloidal stability of SWCNT/peptide complexes. Therefore, not every peptide sequence leads to colloidally stable SWCNTs. In contrast, most ssDNA sequences lead to stable suspensions of DNA/SWCNT complexes. As a consequence, the high potential of peptide functionalization is not yet fully explored with only a few exceptions.[23–27] In one example Dieckmann et al. used an amphiphilic peptide (nano-1) to disperse SWCNTs.[23] Grigoryan et al. used a different approach and computationally designed peptides. They could preferentially bind to for example, SWCNTs of (3,8) chirality and self-assembled into antiparallel hexameric helical bundles upon adhesion. Interestingly, peptide assembly and geometry of the SWCNTs were matched and used as parameter to predict and achieve discrimination in binding.[24]

In this work, we explore the potential of coiled-coil peptide barrels to solubilize and functionalize SWCNTs (Figure 1). Coiled coils are highly abundant amphiphilic helical peptides and form very defined assemblies ranging from coiled-coil dimers to heptamers or even dodecamers.[28,29] The rules of folding are largely uncovered, hence coiled-coil assemblies are available by de novo design.[29] These insights render them highly promising tools for functionalization of SWCNTs as one could make use of a pool of well-studied and pre-assembled peptidic barrels circumventing the need for optimization. Recently, a computational approach towards the design of coiled-coil pentamers to heptamers has been reported.[30] These peptide assemblies are highly stable and mutable and have successfully been applied in synthetic-biology applications or as building blocks in the synthesis of peptide nanotubes.[31–34] Furthermore, it was shown that the pore is accessible to hydrophobic molecules.[32,35]

[a] F. A. Mann, J. Horlebein, D. Meyer, Dr. S. Kruss
Institute of Physical Chemistry
Georg-August Universität Göttingen
Tammannstraße 6, 37077 Göttingen (Germany)
E-mail: skruss@uni-goettingen.de

[b] N. F. Meyer, Dr. F. Thomas
Institute of Organic and Biomolecular Chemistry
Georg-August Universität Göttingen
Tammannstraße 2, 37077 Göttingen (Germany)
E-mail: fthomas@gwdg.de

[c] Dr. S. Kruss
Center for Nanoscale Microscopy and Molecular Physiology of the Brain (CNMPB)
Humboldtallee 23, 37073 Göttingen (Germany)

[d] Dr. F. Thomas
Center for Biostructural Imaging of Neurodegeneration
Von-Siebold-Strasse 3a, 37075 Göttingen (Germany)

Supporting information and the ORCID number(s) for the author(s) of this article can be found under https://doi.org/10.1002/chem.201800993.

Part of a Special Issue to commemorate young and emerging scientists. To view the complete issue, visit Issue 47.

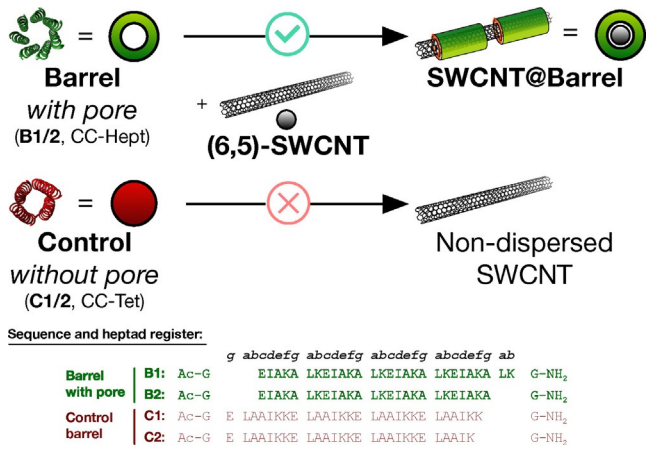

Figure 1. α-Helical coiled-coil peptide barrels (αHBs) encapsulate single-walled carbon nanotubes (SWCNTs) and form stable SWCNT@αHBs hybrids. Coiled-coil peptides (CC-Hept-K) that form heptameric barrels with pores (B1 and B2) encapsulate SWCNTs. In contrast, control peptides (CC-Tet-K) that form tetrameric barrels with no (too small) pore (C1 and C2) do not solubilize SWCNTs. Therefore, encapsulation is most efficient if barrel pore size and SWCNT diameter match.

We were especially interested in the coiled-coil heptamer (CC-Hept), which forms a channel/pore of 0.76 nm in diameter.[30] The size of this pore is in a similar range as diameters of typical SWCNT species such as SWCNTs of (6,5)-chirality. Therefore, we hypothesized that CC-Hept could efficiently encapsulate and solubilize SWCNTs. For this purpose, we chose a variant of CC-Hept containing lysine residues at all *f* positions of the coiled-coil register (CC-Hept-K = Barrel 1 = **B1**, Figure 1). This modification should increase solubility and diminish peptide-induced aggregation due to charge repulsion.[31] To distinguish if SWCNTs incorporate into the pore of CC-Hept-K or physisorb, we selected the tetrameric CC-Tet-K peptide, a lysine variant of de novo designed CC-Tet, as a control (Control 1 = **C1**, Figure 1[36]) This peptide has the same amino acid composition as CC-Hept-K, but should not be able to encapsulate SWCNTs due to its much smaller inner cavity (≈0.39 nm, derived from crystallographic data[37]).

First, we quantified how efficient the peptides **B1** and **C1** (see S3 and S4 for characterization and circular dichroism spectroscopy) disperse SWCNTs. The S_{11} transitions of (6,5)-SWCNT species at around 991 nm (Figure 2a) show that **B1** solubilized (6,5)-SWCNT 4.5× better than the control. The S_{11} transition of (6,5)- **SWCNT@B1** (994.0 ± 1.1 nm) versus **SWCNT@C1** (989.8 ± 1.3 nm) are redshifted. This shift might be associated with a higher surface coverage of the **C1** wrapping peptide and less exposure to water.[38,39]

As proven by CD-thermal denaturation experiments (Figure S4D and S4H) both peptides form very stable assemblies in aqueous solution. We reasoned that this type of self-assembly might reduce efficient solubilization of SWCNTs. Hence, we synthesized C-terminally truncated versions of CC-Hept-K (CC-Hept-K-LK, **B2**, see Figure 1) and CC-Tet-K (CC-Tet-K-K, **C2**) to slightly destabilize the coiled coils in solution,[40,41] which could in turn improve their dispersion capabilities for diameter-matching SWCNTs. This approach should improve SWCNT dispersion yield. As shown in Figure 2b, truncation led to a dramatic increase in SWCNT dispersion. **B2** was about 15 times more efficient to disperse (6,5)-SWCNT compared to control peptide **C2**. This increase in SWCNT concentration is also reflected in the corresponding nIR fluorescence spectra (excited at 561 nm) in Figure 2c.

Commonly used surfactants such as sodium cholate (SC) solubilize all SWCNT chiralities including the major (6,5)-species used in the samples shown in Figure 2. SC dispersed also samples with larger diameter SWCNTs (Figure S1a). In contrast, **B2** could not efficiently solubilize larger diameter SWCNTs, indicating that the yield depends on SWNCT diameter. The large difference in dispersion yield between **B1/C1** or **B2/C2** is a first indication that αHBs encapsulate SWCNTs if αHB pore diameter and SWCNT diameter match.

To further support the hypothesis of barrel formation on the SWCNT surface, we analyzed the samples via intermittent contact mode atomic force microscopy (AFM). In the case of peptide-barrel formation around the SWCNT, we would expect an increase in height from ≈0.7 nm ((6,5)-SWCNT diameter) to ≈1.9 nm due to the size of the heptameric αHB (Scheme Figure 3, based on peptide structural data obtained by X-ray crystallography and analytical ultracentrifugation[30]). Figure 3a shows **SWCNT@B2** and **SWCNT@C2** physisorbed on freshly cleaved muscovite mica. The comparison of the height topography images in Figure 3a and the two histograms (mean height along SWCNT-axis) in Figure 3b show a clear difference in height. The measured mean heights for the nanotubes dis-

Franziska Thomas (neé Mende) studied chemistry at Humboldt University, where she obtained her Ph.D. in 2010, working under the supervision of Prof. Oliver Seitz. Afterwards, she joined the group of Prof. Derek Woolfson for a postdoctoral stay, where she worked on the de novo design of coiled-coil peptides and coiled-coil-based materials. Since 2015, she has been an independent research group leader at the University of Göttingen. Her research interests include protein design, de novo design of functional peptide entities und mini enzymes as well as the identification of small molecules and peptides as drug candidates for the treatment of amytrophic lateral sclerosis.

Sebastian Kruss, born 1982, studied chemistry at Heidelberg University. In 2011, he received his Ph.D. in physical chemistry at the Max Planck Institute for Intelligent Systems (Prof. Joachim Spatz). He then moved to the group of Prof. Michael Strano at the Massachusetts Institute of Technology, where he worked on carbon nanomaterials. At the end of 2014, he started his independent research at Göttingen University with a Liebig fellowship. Currently, he is a principal investigator in the life@nano initiative and the Cluster of Excellence concerning nanoscale microscopy of the brain (CNMPB). His research focuses on novel materials, spectroscopy and microscopy, biosensors and biophysics.

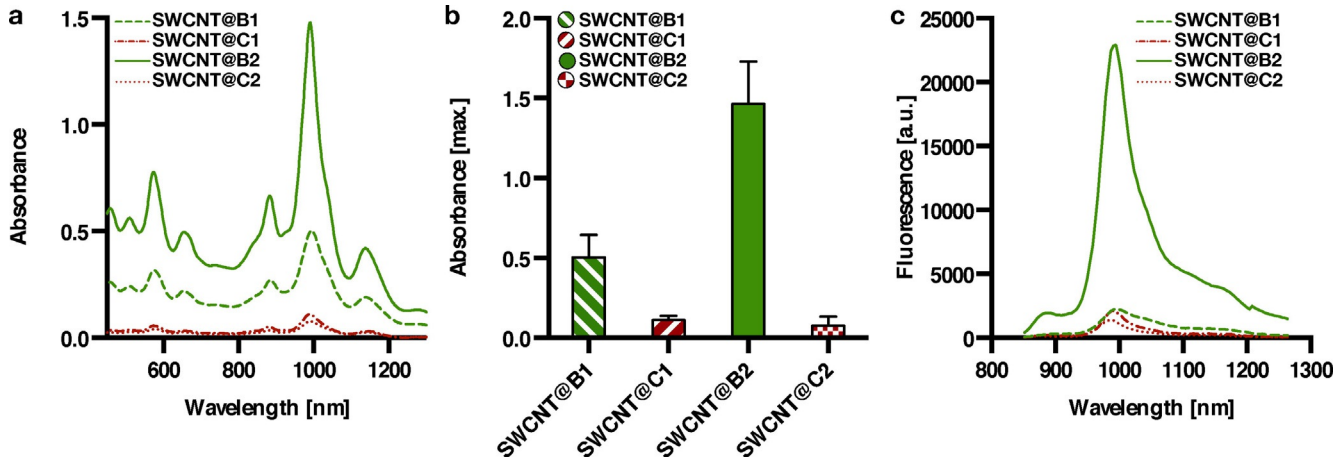

Figure 2. Dispersion efficiency depends on peptide barrel type. a) Absorbance spectra of the peptide-dispersed single-walled carbon nanotubes (SWCNTs) show a clear tendency in dispersion yield (CC-Hept-K-LK(B2) > CC-Hept-K(B1) ≫ CC-Tet-K(C1) = CC-Tet-K-K(C2)). b) Dispersion yield as quantified by the absorbance of the (6,5) S_{11} peak. Error bars are standard errors of the mean (SEM). $n = 3$. c) Fluorescence spectra of CC-Tet-K- and CC-Hept-K-dispersed SWCNTs.

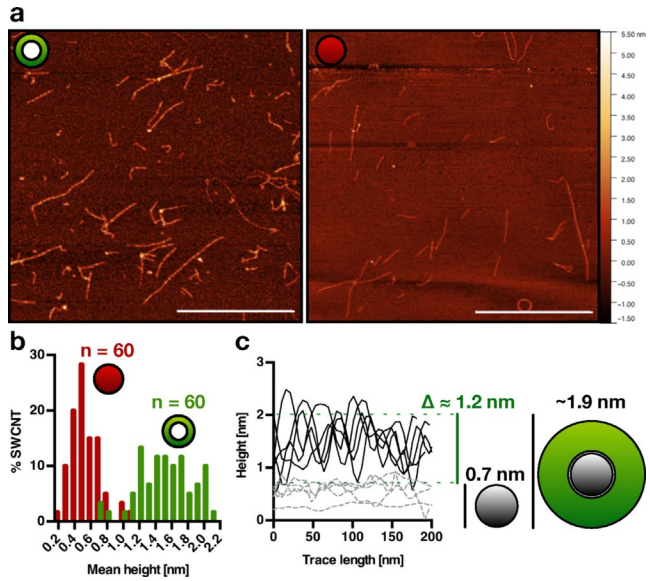

Figure 3. Height profiles of peptide-barrel encapsulated single-walled carbon nanotubes (SWCNT). a) Atomic force microscopy images of B2- and C2-dispersed (6,5)-chirality enriched SWCNTs. The two samples show a clear difference in height. b) Histogram of mean SWCNT heights for the B2- (green) and C2-dispersed (red) SWCNTs. The mean height of SWCNT@B2 origins from a repeating height pattern of free and encapsulated SWCNTs surface. c) Height traces ($n = 5$ each) along the axis of single SWCNT@B2 or C2-dispersed SWCNT. The height of SWCNT@B2 (≈1.9 nm) fits well to the value of free (6,5)-SWCNT (≈0.7 nm) and the height additionally introduced by the heptameric α-helical barrel (≈1.2 nm). Scale bars = 1 μm.

persed by the peptide **C2** peak at ≈0.5 nm, whereas **SWCNT@B2** shows a broader height distribution ranging from 0.7 to 2.2 nm. We attribute the rather low measured height (around 0.5 nm) for **SWCNT@C2** to adsorption of peptide onto the mica reducing the effective height difference. The large differences in height between **SWCNT@B2** and **SWCNT@C2** imply that **B2** self-assembles around the SWCNT and C2 adsorbs randomly with much lower efficiency and overall affinity. These results are in best agreement with a SWCNT incorporated into the pores of **B2** barrels.

To further investigate the reason for the broad height distribution, representative height profiles for **SWCNT@B2** and **SWCNT@C2** were collected (Figure 3c). Line-scans for **SWCNT@B2** show a repetitive pattern and height variations between ≈0.7 and 1.9 nm. This difference fits exceptionally well to the additional height introduced by the heptameric peptide **B2** as previously estimated (see above). This result together with the drastic differences in SWCNT dispersion yield compared to the control peptides **C1** and **C2** is a strong indication that diameter-matching SWCNTs are encapsulated by α-helical coiled-coil peptide barrels.

We further investigated the repetitive pattern on **SWCNT@B2**, which was not found for **SWCNT@C2**. Figure 4a,b show a height-trace along the axis of a single SWCNT. While free CC-Hept-based αHB's should have a length of ≈4 nm in aqueous solution, we found repeating peak–peak-distances of 43.6 ± 6.7 nm via autocorrelation analysis (example in Figure 4c, more autocorrelation plots [$n = 8$] in Figure S5).

There are two possible explanations for this periodicity. First, the repeating height pattern could be due to supramolecular assembly of the barrels along the SWCNT axis driven by the helical read through (pitch length 28–48 nm[30]) or the instability of barrel-stacking over long length scales. Second, processes during drying of the sample could lead to the formation of regions without peptide (dewetting). Even though the lateral resolution of the AFM could influence the measured pattern, it is not likely that the periodicity is an artefact. Similar patterns have been described for DNA functionalized SWCNTs with pitch lengths of for example, 14 ± 5 nm.[42,43]

In summary, we introduced de novo designed αHBs as a new functionalization and encapsulation platform for single-walled carbon nanotubes. Spectroscopy and microscopy data indicate that barrels are formed around the single-walled carbon nanotubes. Importantly, the optical properties are retained in **SWCNTs@αHBs** as demonstrated by nIR spectroscopy (Figure 2c) and microscopy (Figure 4d). Coiled coils can be functionalized via their *f* positions and their termini, which leaves the overall coiled-coil assembly unaffected.[44,45] The

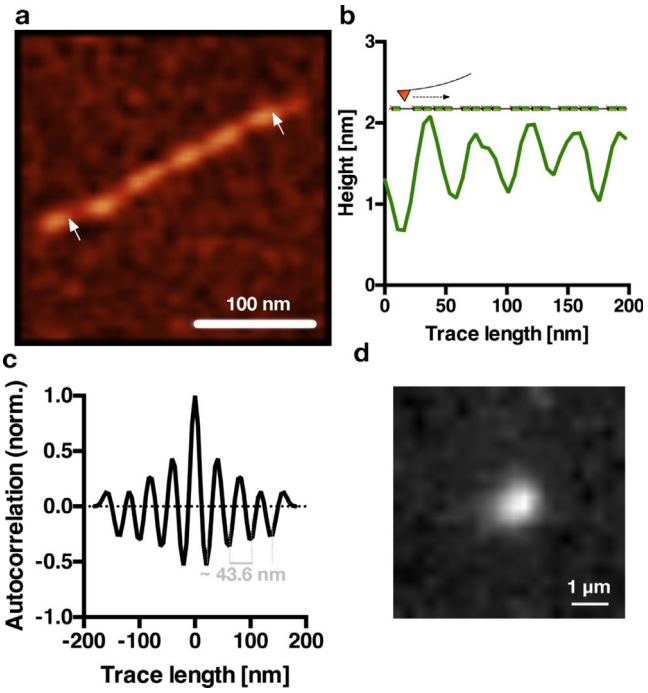

Figure 4. Periodicity of peptide-barrel functionalization on single-walled carbon nanotubes. a) Magnification of a single SWCNT encapsulated by peptide B2 showing repeating changes in height. b) Height trace along the SWCNT@B2 axis. Arrows in a) show the start and end point. Note that the schematic including the number of barrels/peak is not to scale. c) Autocorrelation function of the height trace from b) of a SWCNT@B2 demonstrates height periodicity. d) nIR fluorescent image of a single SWCNT@B2 reveals that the fluorescent properties are maintained by barrel functionalization.

outer surface of αHBs is therefore promising as functionalization platform while the SWCNTs are colloidally stabilized. This approach could be used to tailor the organic phase around SWCNTs to for example, control molecular interactions, conformational kinetics and photophysical processes.[39,46–49] In contrast to other functionalization approaches for SWCNTs, de novo designed αHBs could be easily tailored for certain carbon nanotube diameters.[30] This approach opens up a plethora of possibilities to attach additional entities, such as fluorophores and pharmacophores, or recognition units for example, antibodies or nanobodies to the outer surface of the functionalized SWCNT.

Acknowledgements

The authors thank the FCI (Fonds der chemischen Industrie), the DFG (Deutsche Forschungsgemeinschaft) and the VW foundation for funding. This project was supported by the state of Lower Saxony (life@nano) and the Cluster of Excellence and DFG Research Center Nanoscale Microscopy and Molecular Physiology of the Brain. We thank Andreas Janshoff, Ulf Diederichsen and Claudia Steinem for their support.

Conflict of interest

The authors declare no conflict of interest.

Keywords: biosensors · carbon · coiled coil · nanotubes · peptides

[1] S. Kruss, A. J. Hilmer, J. Zhang, N. F. Reuel, B. Mu, M. S. Strano, *Adv. Drug Delivery Rev.* **2013**, *65*, 1933 – 1950.
[2] M. J. O'Connell, S. M. Bachilo, C. B. Huffman, V. C. Moore, M. S. Strano, E. H. Haroz, K. L. Rialon, P. J. Boul, W. H. Noon, C. Kittrell, J. Ma, R. H. Hauge, R. B. Weisman, R. E. Smalley, *Science* **2002**, *297*, 593 – 596.
[3] G. Hong, S. Diao, A. L. Antaris, H. Dai, *Chem. Rev.* **2015**, *115*, 10816 – 10906.
[4] S. Kruss, D. P. Salem, L. Vukovic, B. Lima, E. Vander Ende, E. S. Boyden, M. S. Strano, *Proc. Natl. Acad. Sci. USA* **2017**, *114*, 1789 – 1794.
[5] S. Kruss, M. P. Landry, E. Vander Ende, B. M. Lima, N. F. Reuel, J. Zhang, J. Nelson, B. Mu, A. Hilmer, M. Strano, *J. Am. Chem. Soc.* **2014**, *136*, 713 – 724.
[6] C. Cha, S. R. Shin, N. Annabi, M. R. Dokmeci, A. Khademhosseini, *ACS Nano* **2013**, *7*, 2891 – 2897.
[7] E. Polo, S. Kruss, *Anal. Bioanal. Chem.* **2016**, *408*, 2727 – 2741.
[8] Z. Liu, S. M. Tabakman, Z. Chen, H. Dai, *Nat. Protoc.* **2009**, *4*, 1372 – 1381.
[9] L. Liang, W. Xie, S. Fang, F. He, B. Yin, C. Tlili, D. Wang, S. Qiu, Q. Li, *J. Mater. Chem. C* **2017**, *5*, 11339 – 11368.
[10] P. Bilalis, D. Katsigiannopoulos, A. Avgeropoulos, G. Sakellariou, *RSC Adv.* **2014**, *4*, 2911 – 2934.
[11] A. Di Crescenzo, V. Ettorre, A. Fontana, *Beilstein J. Nanotechnol.* **2014**, *5*, 1675 – 1690.
[12] V. Zubkovs, N. Schuergers, B. Lambert, E. Ahunbay, A. A. Boghossian, *Small* **2017**, *13*, 1701654.
[13] J. Budhathoki-Uprety, P. V. Jena, D. Roxbury, D. A. Heller, *J. Am. Chem. Soc.* **2014**, *136*, 15545 – 15550.
[14] M. Zheng, A. Jagota, E. D. Semke, B. A. Diner, R. S. Mclean, S. R. Lustig, R. E. Richardson, N. G. Tassi, *Nat. Mater.* **2003**, *2*, 338 – 342.
[15] J. Zhang, S. Kruss, A. J. Hilmer, S. Shimizu, Z. Schmois, F. De La Cruz, P. W. Barone, N. F. Reuel, D. A. Heller, M. S. Strano, *Adv. Healthcare Mater.* **2014**, *3*, 412 – 423.
[16] N. F. Reuel, B. Grassbaugh, S. Kruss, J. Z. Mundy, C. Opel, A. O. Ogunniyi, K. Egodage, R. Wahl, B. Helk, J. Zhang, Z. I. Kalcioglu, K. Tvrdy, D. O. Bellisario, B. Mu, S. S. Blake, K. J. Van Vliet, J. C. Love, K. D. Wittrup, M. S. Strano, *ACS Nano* **2013**, *7*, 7472 – 7482.
[17] A. Hirsch, *Angew. Chem. Int. Ed.* **2002**, *41*, 1853 – 1859; *Angew. Chem.* **2002**, *114*, 1933 – 1939.
[18] M. Prato, K. Kostarelos, A. Bianco, *Acc. Chem. Res.* **2008**, *41*, 60 – 68.
[19] G. Clavé, S. Campidelli, *Chem. Sci.* **2011**, *2*, 1887 – 1896.
[20] S. Wang, E. S. Humphreys, S. Y. Chung, D. F. Delduco, S. R. Lustig, H. Wang, K. N. Parker, N. W. Rizzo, S. Subramoney, Y. M. Chiang, A. Jagota, *Nat. Mater.* **2003**, *2*, 196 – 200.
[21] V. Zorbas, A. Ortiz-Acevedo, A. B. Dalton, M. M. Yoshida, G. R. Dieckmann, R. K. Draper, R. H. Baughman, M. Jose-Yacaman, I. H. Musselman, *J. Am. Chem. Soc.* **2004**, *126*, 7222 – 7227.
[22] M. S. Arnold, M. O. Guler, M. C. Hersam, S. I. Stupp, *Langmuir* **2005**, *21*, 4705 – 4709.
[23] G. R. Dieckmann, A. B. Dalton, P. A. Johnson, J. Razal, J. Chen, G. M. Giordano, E. Muñoz, I. H. Musselman, R. H. Baughman, R. K. Draper, *J. Am. Chem. Soc.* **2003**, *125*, 1770 – 1777.
[24] G. Grigoryan, Y. H. Kim, R. Acharya, K. Axelrod, R. M. Jain, L. Willis, M. Drndic, J. M. Kikkawa, W. F. DeGrado, *Science* **2011**, *332*, 1071 – 1076.
[25] J. Montenegro, C. Vazquez-Vazquez, A. Kalinin, K. E. Geckeler, J. R. Granja, *J. Am. Chem. Soc.* **2014**, *136*, 2484 – 2491.
[26] Y. Hashida, T. Umeyama, J. Mihara, H. Imahori, M. Tsujimoto, S. Isoda, M. Takano, M. Hashida, *J. Pharm. Sci.* **2012**, *101*, 3398 – 3412.
[27] A. Ortiz-Acevedo, H. Xie, V. Zorbas, W. M. Sampson, A. B. Dalton, R. H. Baughman, R. K. Draper, I. H. Musselman, G. R. Dieckmann, *J. Am. Chem. Soc.* **2005**, *127*, 9512 – 9517.
[28] A. N. Lupas, J. Bassler, *Trends Biochem. Sci.* **2017**, *42*, 130 – 140.
[29] D. N. Woolfson, *Subcell. Biochem.* **2017**, *82*, 35 – 61.
[30] A. R. Thomson, C. W. Wood, A. J. Burton, G. J. Bartlett, R. B. Sessions, R. L. Brady, D. N. Woolfson, *Science* **2014**, *346*, 485 – 488.
[31] F. Thomas, N. C. Burgess, A. R. Thomson, D. N. Woolfson, *Angew. Chem. Int. Ed.* **2016**, *55*, 987 – 991; *Angew. Chem.* **2016**, *128*, 999 – 1003.

[32] N. C. Burgess, T. H. Sharp, F. Thomas, C. W. Wood, A. R. Thomson, N. R. Zaccai, R. L. Brady, L. C. Serpell, D. N. Woolfson, *J. Am. Chem. Soc.* **2015**, *137*, 10554 – 10562.
[33] C. Xu, R. Liu, A. K. Mehta, R. C. Guerrero-Ferreira, E. R. Wright, S. Dunin-Horkawicz, K. Morris, L. C. Serpell, X. Zuo, J. S. Wall, V. P. Conticello, *J. Am. Chem. Soc.* **2013**, *135*, 15565 – 15578.
[34] A. J. Burton, A. R. Thomson, W. M. Dawson, R. L. Brady, D. N. Woolfson, *Nat. Chem.* **2016**, *8*, 837 – 844.
[35] A. J. Burton, F. Thomas, C. Agnew, K. L. Hudson, S. E. Halford, R. L. Brady, D. N. Woolfson, *J. Am. Chem. Soc.* **2013**, *135*, 12524 – 12527.
[36] J. M. Fletcher, A. L. Boyle, M. Bruning, G. J. Bartlett, T. L. Vincent, N. R. Zaccai, C. T. Armstrong, E. H. Bromley, P. J. Booth, R. L. Brady, A. R. Thomson, D. N. Woolfson, *ACS Synth. Biol.* **2012**, *1*, 240 – 250.
[37] N. R. Zaccai, B. Chi, A. R. Thomson, A. L. Boyle, G. J. Bartlett, M. Bruning, N. Linden, R. B. Sessions, P. J. Boot, R L. Brady, D. N. Woolfson, *Nat. Chem. Biol.* **2011**, *7*, 935 – 941.
[38] J. H. Choi, M. S. Strano, *Appl. Phys. Lett.* **2007**, *90*, 223114.
[39] E. Polo, S. Kruss, *J. Phys. Chem. C* **2016**, *120*, 3061 – 3070.
[40] J. Y. Su, R. S. Hodges, C. M. Kay, *Biochemistry* **1994**, *33*, 15501 – 15510.
[41] F. Thomas, A. L. Boyle, A. J. Burton, D. N. Woolfson, *J. Am. Chem. Soc.* **2013**, *135*, 5161 – 5166.
[42] J. F. Campbell, I. Tessmer, H. H. Thorp, D. A. Erie, *J. Am. Chem. Soc.* **2008**, *130*, 10648 – 10655.
[43] F. Schöppler, C. Mann, T. C. Hain, F. M. Neubauer, G. Privitera, F. Bonaccorso, D. Chu, A. C. Ferrari, T. Hertel, *J. Phys. Chem. C* **2011**, *115*, 14682 – 14686.
[44] J. M. Fletcher, R. L. Harniman, F. R. Barnes, A. L. Boyle, A. Collins, J. Mantell, T. H. Sharp, M. Antognozzi, P. J. Booth, N. Linden, M. J. Miles, R. B. Sessions, P. Verkade, D. N. Woolfson, *Science* **2013**, *340*, 595 – 599.
[45] E. K. O'Shea, K. J. Lumb, P. S. Kim, *Curr. Biol.* **1993**, *3*, 658 – 667.
[46] D. Meyer, A. Hagemann, S. Kruss, *ACS Nano* **2017**, *11*, 4017 – 4027.
[47] F. A. Mann, N. Herrmann, D. Meyer, S. Kruss, *Sensors* **2017**, *17*, 1521.
[48] G. Bisker, J. Ahn, S. Kruss, Z. W. Ulissi, D. P. Salem, M. S. Strano, *J. Phys. Chem. C* **2015**, *119*, 13876 – 13886.
[49] J. J. Crochet, J. G. Duque, J. H. Werner, S. K. Doorn, *Nat. Nanotechnol.* **2012**, *7*, 126 – 132.

Manuscript received: February 26, 2018
Accepted manuscript online: February 28, 2018
Version of record online: March 23, 2018

CHEMISTRY
A European Journal

Supporting Information

Carbon Nanotubes Encapsulated in Coiled-Coil Peptide Barrels

Florian A. Mann,[a] Jan Horlebein,[a] Nils Frederik Meyer,[b] Daniel Meyer,[a] Franziska Thomas,*[b, d] and Sebastian Kruss*[a, c]

chem_201800993_sm_miscellaneous_information.pdf

Supporting Information

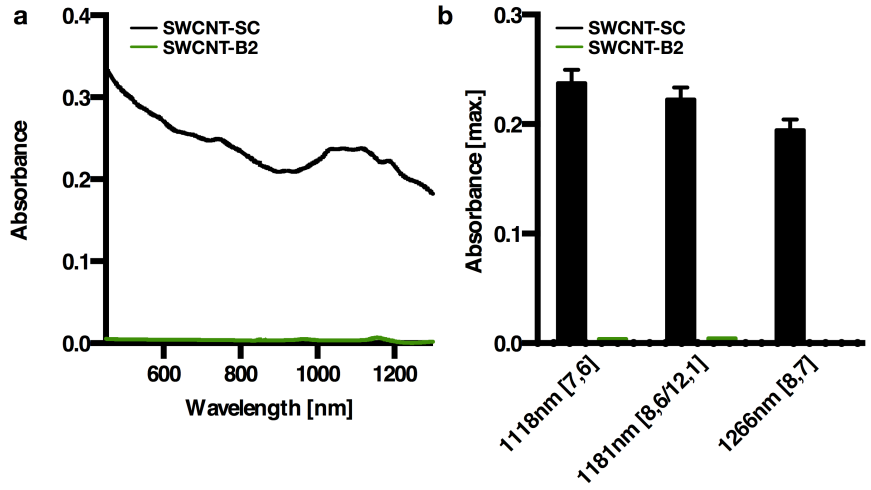

Figure S1, Comparison of dispersion ability of larger diameter single-walled carbon nanotube (SWCNT) samples by sodium cholate (SC) and the helical peptide CC-Hept-K-LK (B2). (a) Absorbance spectra of SC- and **B2-**dispersed SWCNTs. (b) Comparison of the absorbance maxima of different larger diameter carbon nanotube species dispersed by SC and **B2**. n=2.

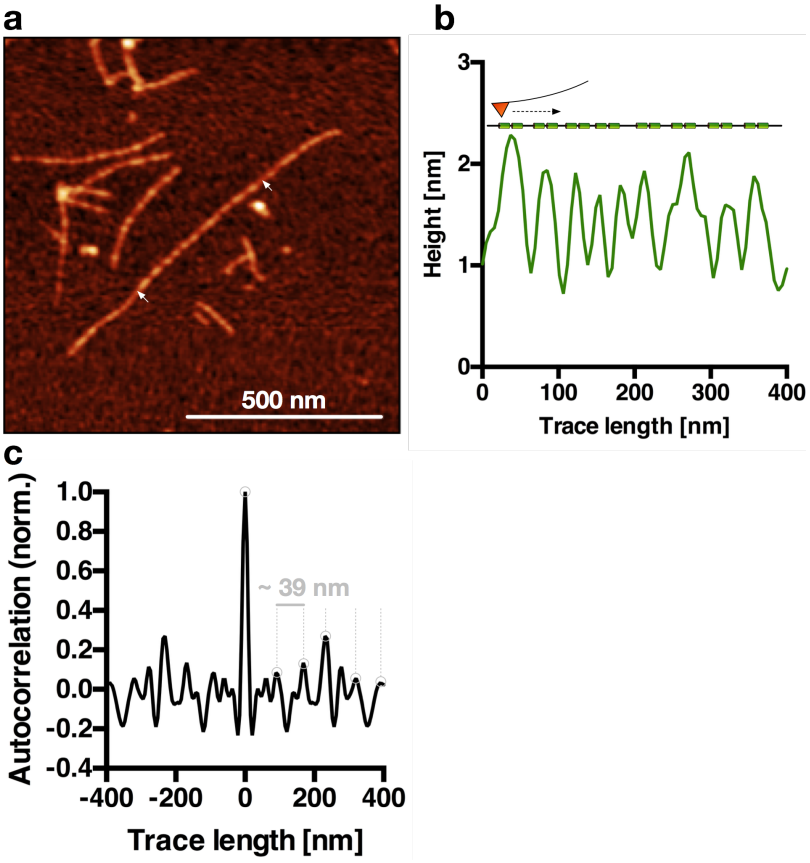

Figure S2, Line profile of a long SWCNT@B2 adsorbed to mica surface. (a) SWCNT@B2 adsorbed to muscovite mica. Arrows indicate start and end of height profile acquired along the axis of the nanotube (b) Height profile

along the SWCNT@B2 axis shown in a). Start and end points are indicated in a) by the white arrows. Note that the schematic is not to scale and the number of barrels corresponding to one peak are not to scale. (c) Autocorrelation of the trace shown in b).

Characterization of coiled-coil peptides

Sequences of the coiled-coil peptides applied in this work

Table S1. Sequences of the coiled-coil peptides applied in this project.

		Sequence and heptad register[a]
		g abcdefg abcdefg abcdefg abcdefg ab
B2	CC-Hept-K (L28_K29del)	G EIAKA LKEIAKA LKEIAKA LKEIAKA G
B1	CC-Hept-K	G EIAKA LKEIAKA LKEIAKA LKEIAKA LK G
C2	CC-Tet-K (K29del)	G E LAAIKKE LAAIKKE LAAIKKE LAAIK G
C1	CC-Tet-K	G E LAAIKKE LAAIKKE LAAIKKE LAAIKK G

[a)] Peptides were synthesized as C-terminal amides and N-terminally acetylated.

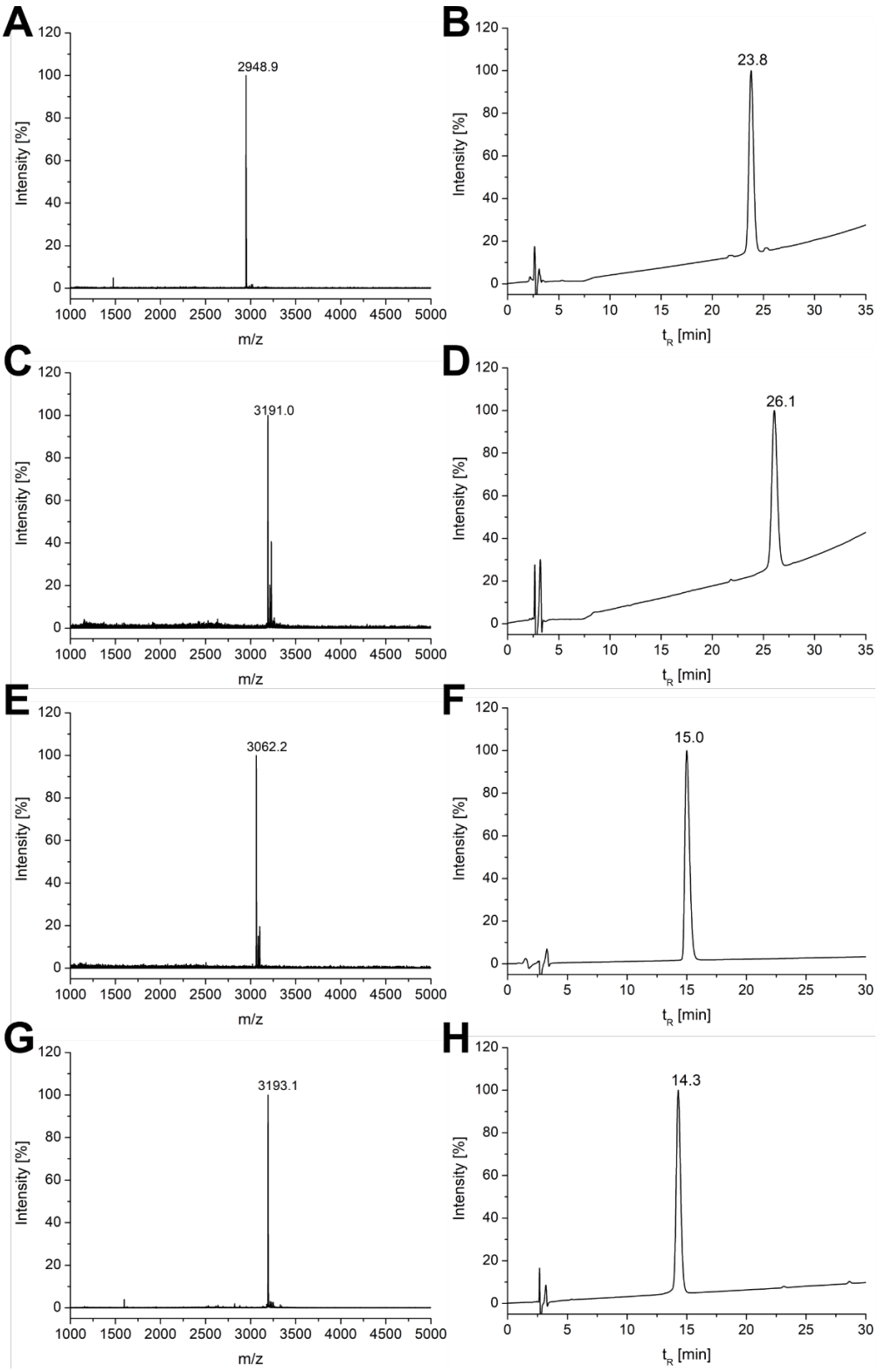

Figure S3, MALDI/TOF mass spectra and HPLC traces of coiled-coil peptides. (A-B: CC-Hept-K (L28_K29del) calc. [M+H$^+$]: 2948.6, C-D: CC-Hept-K calc. [M+H$^+$]: 3190.0, E-F: CC-Tet-K (K29del) calc. [M+H$^+$]: 3061.7, G-H: CC-Tet-K calc. [M+H$^+$]: 3190.0,).

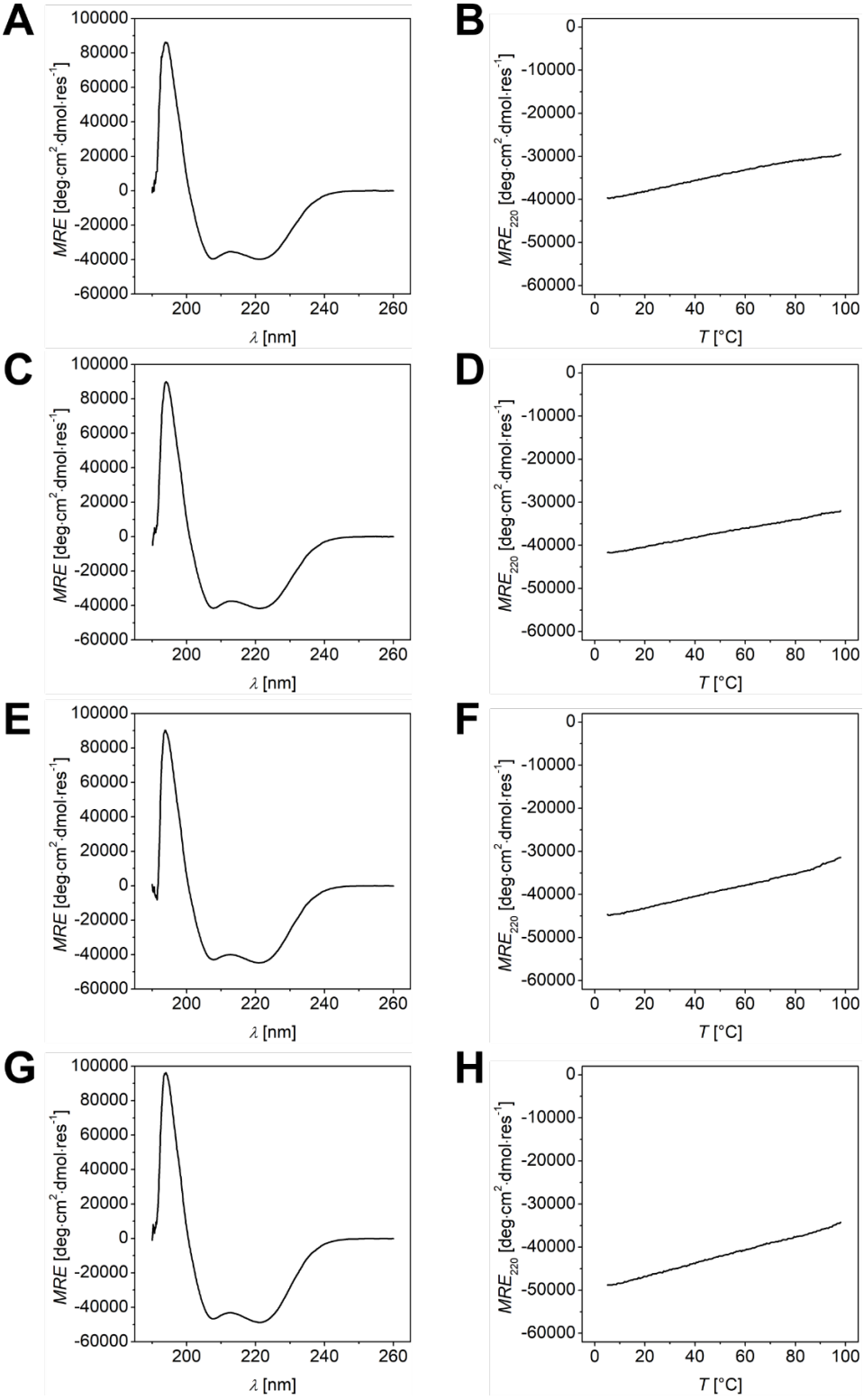

Figure S4, CD spectra and CD thermal denaturation profiles of A-B) CC-Hept-K (L28_K29del), C-D) CC-Hept-K, E-F) CC-Tet-K (K29del), G-H) CC-Tet-K. Data are presented as an average over three independent measurements, respectively.

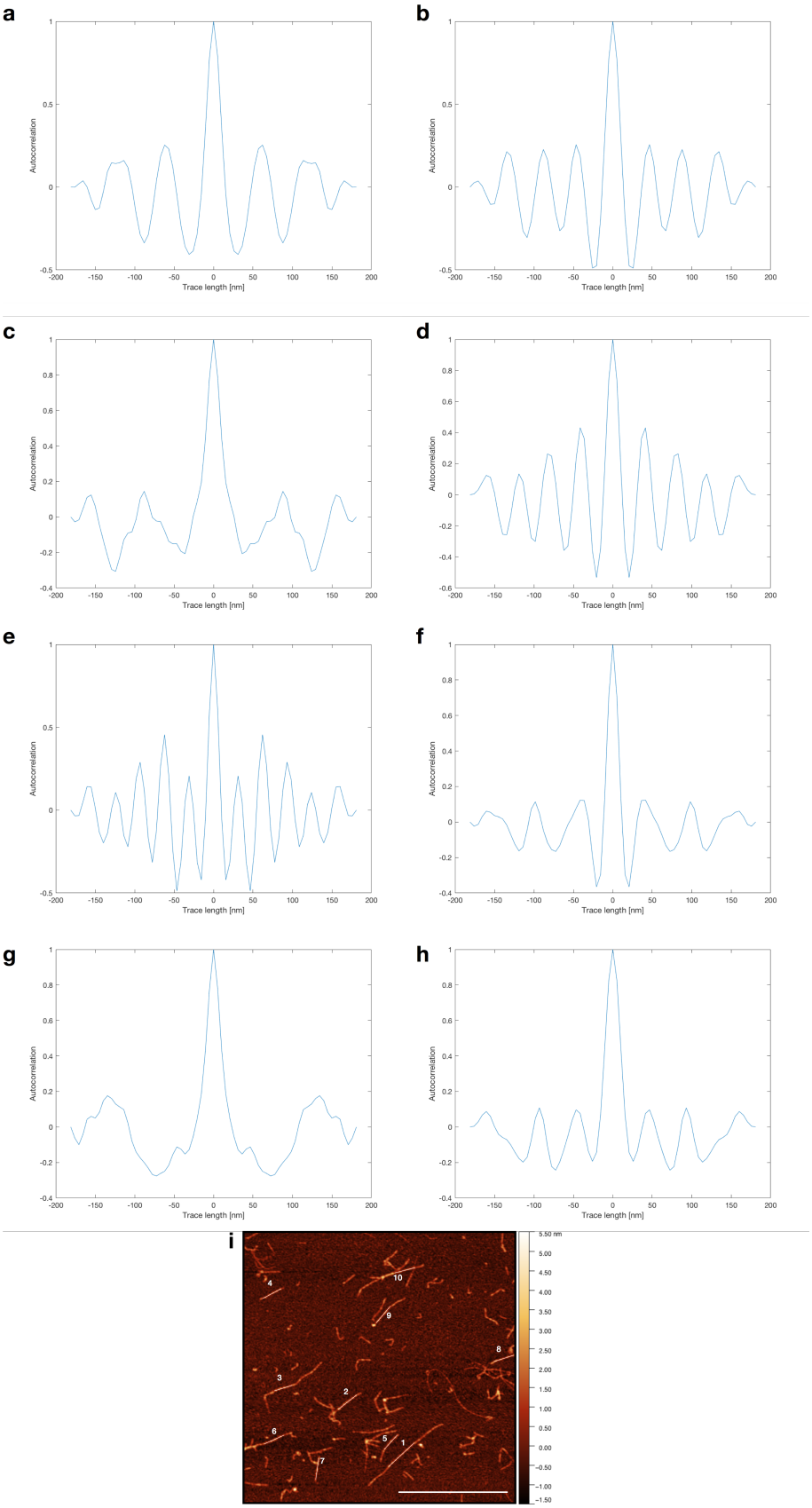

Figure S5, Autocorrelation plots of ten independent SWCNT@*α*HB height traces.

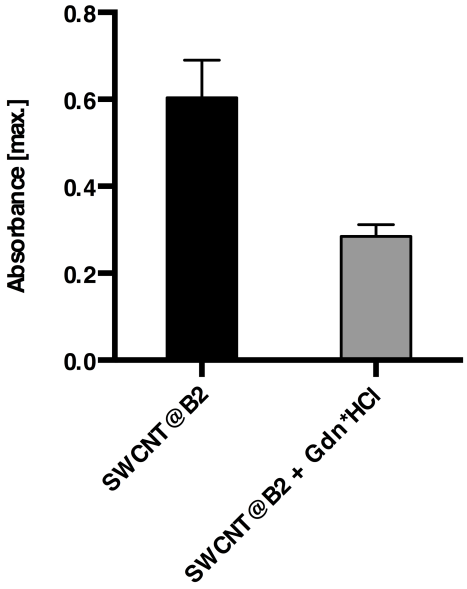

Figure S6, Comparison of the S11 absorbance maxima of (6,5)-SWCNT@B2 before and after the addition of 6 M guanidine hydrochloride. When peptide is removed from the SWCNT surface the SWCNT are not water-soluble anymore and tend to aggregate. After a centrifugation step the absorption spectra were taken to compare the SWCNT concentration. The decrease indicates (partial) reversible defunctionalisation of the SWCNTs (n=3).

2. Supplementary Methods

2.1 General Information

Fmoc-protected amino acids were purchased from *GL Biochem LTD* (Shanghai, China). DIC and OxymaPure were purchased from *Iris Biotech GmbH* (Marktredwitz, Germany). (6,5)-chirality enriched single-walled carbon nanotubes (SWCNT, Sigma Aldrich, Product No.: 773735) and H-Rink Amide-Chemmatrix® resin were acquired from *Sigma Aldrich* (Darmstadt, Germany). Larger diameter SWCNTs were purchased from PlasmaChem GmbH (LOT: SCNP-M135). DMF used for peptide synthesis was supplied by *Fisher Scientific* (Schwerte, Germany) and was of peptide grade quality. Acetonitrile used for HPLC was supplied by *Fisher Scientific* (Schwerte, Germany) with HPLC grade quality. Water used for HPLC and reactions was obtained by purifying distilled water with the purification device SIMPLICITY from MILLIPORE. All other reagents were supplied by *Sigma Aldrich* (Taufkirchen, Germany), *Thermo Fisher Scientific* (Langenselbold, Germany), *VWR International* (Darmstadt, Germany) and *Carl Roth* (Karlsruhe, Germany). All reagents were of synthesis grade quality and were used as supplied. Unless otherwise stated, biophysical measurements were performed in phosphate buffered saline (PBS, 8.2 mM Na_2HPO_4, 1.8 mM K_2HPO_4, 137 mM NaCl, 2.7 mM KCl, pH 7.4). Peptide concentrations were determined by UV-absorbance at 214 nm using a *NanoDrop 2000* Spectrophotometer from *Thermo Scientific*. Extinction coefficients at 214 nm were calculated according to Kuipers et al.[1]

2.2 Solid-phase peptide synthesis

De novo designed peptide amides were synthesized on a H-Rink Amide-Chemmatrix® resin on a 0.1 mmol scale on a Liberty Blue *CEM* microwave-assisted peptide synthesizer. The synthesis was conducted *via* a standard Fmoc/tBu-protocol using DIC and OxymaPure as coupling reagents and a solution of piperidine in DMF (1:4) for Fmoc-removal. *N*-Acetylation of the peptides was carried out by equilibrating the peptide resin with 5 mL of acetic acid anhydride / pyridine (1:9) for 5 min at room temperature. Acidic cleavage from the resin was achieved by a treatment with a mixture of trifluoroacetic acid (TFA) / triisopropylsilane / water (90:5:5, 3 h). The resin was extracted with additional TFA (5 mL), and the combined extracts were concentrated to a third of the initial volume under a flow of nitrogen. The crude peptide was then precipitated in cold diethylether (40 mL) and isolated by centrifugation and decantation of the supernatant. The precipitate was washed twice with ice-cold diethylether and subsequently dissolved in 5 mL of a 1:1 mixture of acetonitrile and water and then freeze-dried to give a fine white solid.

2.3 Peptide purification

Peptides were purified by semi-preparative reversed-phase HPLC using a *JASCO* chromatography system (pumps PU-2080 Plus, degasser DG-2080-53, detector MD-2010 Plus) at flow rates of 3 ml/min, and a *Nucleodur* 100-5-C18 ec, (250 mm by 10 mm, 5 µm) reversed-phase column. Linear gradients of water and acetonitrile (buffer A: water, 0.1 % TFA, buffer B: acetonitrile, 0.1 % TFA) of 30-80 % buffer B over 30 min for coiled-coil heptamers and 30-60 % buffer B over 30 min for coiled-coil tetramers were used for purification. During purification the column was run at a controlled temperature of 60 °C. Chromatograms were recorded at 220 nm.

2.4 Peptide characterization

Peptides were characterized by mass spectrometry on a *Bruker Autoflex Speed* MALDI-TOF mass spectrometer operating in positive-ion reflector mode. (matrix: α-cyano-4-hydroxycinnamic acid (CHCA), external calibration). Analytical HPLC measurements were performed using a *JASCO* chromatography system (pumps PU-2085 Plus, detector MD-2010 Plus, autosampler AS-2055 Plus) and a *Nucleodur* 100-5-C18 (5 µm, 4.6 x 250 mm) reversed-phase column at a flow rate of 1 ml/min. For peptide characterization a linear gradient of water and acetonitrile (buffer A: water, 0.1 % TFA, buffer B: acetonitrile, 0.1 % TFA) run from 30-80 % buffer B over 20 min for coiled-coil heptamers and 30-60 % buffer B over 20 min for coiled-coil tetramers was used.

Chromatograms were monitored at 220 nm wavelengths. The column was run at a controlled temperature of 60 °C.

2.5 Circular dichroism (CD) spectroscopy

CD spectra and CD thermal-denaturation curves were recorded using a *JASCO J-1500* which was equipped with a *JASCO PTC510* temperature measuring unit. CD spectra were measured at 50 µM peptide concentration in PBS at 20 °C in 1 mm quartz cuvettes from *Starna* at 50 nm / min scanning speed. CD thermal-denaturation experiments were performed by heating from 2 to 98 °C at a heat rate of 60 °C / h. The CD signal at 222 nm was recorded at 0.1 °C intervals (1 nm interval, 1 nm bandwidth, 16 s response time). The midpoints of the thermal denaturation curves (T_m) were determined from the second derivative of the variable temperature slope.

2.6 Dispersion of carbon nanotubes using alpha-helical peptides

Based on a 2 mg/mL (6,5)-chirality-enriched SWCNT stock suspension in MilliQ™-grade H_2O, ~ 62.5 µg SWCNTs were added to a 1.5 mL centrifuge tube, spun down at 16,100 g for 30 minutes and the supernatant discarded.

In the next step, 250 µL of a 2 mg/mL α-helical peptide solution (**B1**, **B2**, **C1** or **C2** in 1x PBS) were added to the raw SWCNT material. The solution was vortexed, tip sonicated for 5 minutes (Fisher Scientific™ Model 120 Sonic Dismembrator, 20% amplitude) and subsequently centrifuged at 16,100 g (2 x 30 min) to remove large bundles, aggregates or metal catalyst remaining from SWCNT synthesis. The supernatant was used for further experiments.

2.7 UV/vis/nIR absorbance spectroscopy and SWCNT concentration estimation

200 µL of the supernatant containing individualized SWCNTs was submitted to UV/vis/nIR absorbance spectroscopy on a JASCO V-670 (Spectra Manager Software) using a 10 mm-path cuvette. Spectra were acquired using a scan speed of 1000 nm/min, a data interval of 0.5 nm and a UV/vis and nIR bandwidth of 2 nm and 4 nm, respectively.

SWCNT concentration was estimated using the maximal absorbance at approx. 991 nm using the molar extinction coefficient.[2]

2.8 nIR fluorescence spectroscopy

In a 96-well plate, 100 µL of the SWCNT-αHB solutions were excited at 561 nm using a Cobolt Jive™ laser (Cobolt AB, Solna, Sweden, 100 mW) and their fluorescence spectra in the range between 850 and 1300 nm recorded using a Shamrock 193i spectrograph (Andor Technology Ltd., Belfast, Northern Ireland) coupled to an Olympus BX53 microscope and an exposure time of 1 s, a slit width of 500 µm and an Andor iDus InGaAs 491 array NIR detector.

2.9 nIR fluorescence microscopy of immobilized SWCNT@barrels

20 µL of a 6.6 nM SWCNT@B2 solution were incubated on a glass-bottom petri dish for one hour at 4 °C. After a 1x PBS wash, nIR imaging was carried out on an Olympus BX53 microscope equipped with a laser (see above) using a 60× oil-immersion objective and a Xenics® Xeva-1.7-320 NIR camera (Xenics, Heverlee, Belgium).

2.10 Atomic Force Microscopy (AFM) of immobilized SWCNT-αHB

20 µL of each of the SWCNT-αHB solutions were immobilized on freshly cleaved muscovite mica via ten minutes incubation and subsequent washing of the surface with MilliQ water. AFM images were acquired in tapping mode using an Asylum Research MFP-3D Infinity® instrument equipped with Olympus AC-160-TS cantilevers.

Analysis of the acquired images was performed via the open-source software Gwyddion. For all images, the background/tilt was removed via a 2nd polynomial fit. The surface plane was set to zero using three-point levelling.

References

1. Kuipers, B. J.; Gruppen, H., Prediction of molar extinction coefficients of proteins and peptides using UV absorption of the constituent amino acids at 214 nm to enable quantitative reverse phase high-performance liquid chromatography-mass spectrometry analysis. *J. Agric. Food. Chem.* **2007,** *55* (14), 5445-51.
2. Schöppler, F.; Mann, C.; Hain, T. C.; Neubauer, F. M.; Privitera, G.; Bonaccorso, F.; Chu, D.; Ferrari, A. C.; Hertel, T., Molar Extinction Coefficient of Single-Wall Carbon Nanotubes. *J. Phys. Chem. C* **2011,** *115* (30), 14682-14686.

4.3.2. Do peptide barrels allow SWCNT chirality enrichment?

The manuscript in section 4.3.1 shows, that it is possible to use αHBs for the dispersion of SWCNTs. Their predefined pore diameter should - in principle - also allow for enrichment of certain SWCNT chiralities/diameters. The AFM experiment shown in Fig. 3 (p. 88) also suggests, that there is a difference even when comparing the two αHBs with their different pore diameters. Whereas the B2-barrel (d = 7.6 Å) shows alternating heights corresponding to peptide barrels wrapping (6,5)-SWCNTs (d = 7.6 Å), the control sample with the barrel C2 shows 'naked' tubes with a mean diameter of 5 Å. These could, amongst others, correspond e.g. to the smaller metallic (5,2)-SWCNTs with a diameter of 5 Å, which would not be detectable in the absorbance spectra due to their metallic nature. In this case, however, the C2 peptide would have been desorbed under the

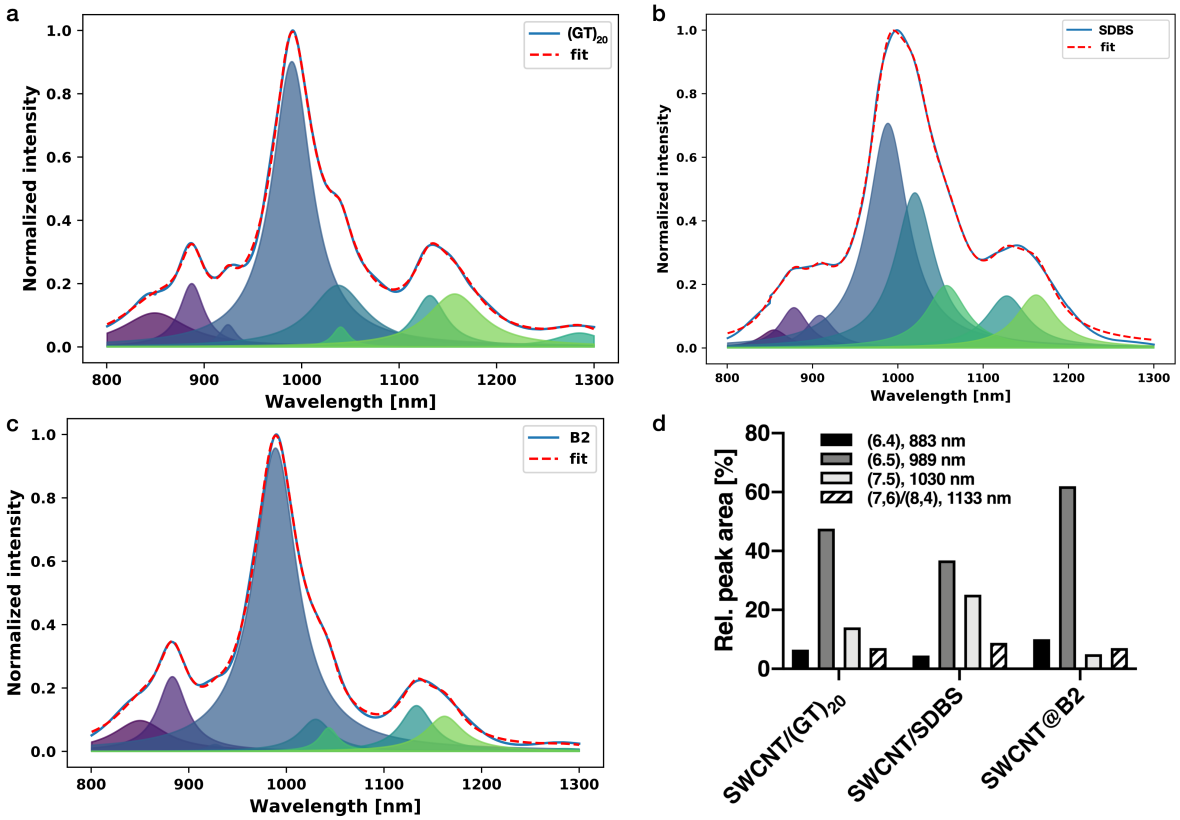

Figure 4.1.: **Fitted NIR absorbance spectra of different SWCNT samples.** a) NIR-absorbance spectrum of $(GT)_{20}$-DNA dispersed SWCNTs and the corresponding fit. b) NIR-absorbance spectrum of a SWCNT/SDBS sample and the corresponding fit. c) NIR-absorbance spectrum of SWCNT@B2 and the corresponding fit. d) Comparison of the relative peak areas of the three different samples for four SWCNT-chiralities.

same washing procedure applied also to the SWCNT@B2 sample indicating a weaker C2-SWCNT-binding. Fig. 4.1 shows the background subtracted ($e^{-b\lambda}$) NIR absorbance spectra of carbon nanotubes dispersed using $(GT)_{20}$-DNA, the B2 αHB and the surfactant SDBS fitted with nine Lorentzians corresponding to different SWCNT-chiralities. The barrel B2 does not exclusively disperse a single SWCNT-chirality, but does show a trend towards encapsulating smaller SWCNT diameters compared to the SWCNT/$(GT)_{20}$ and SWCNT/SDBS sample (e.g. for (6,5)-SWCNTs: 48% ($(GT)_{20}$), 62% (B2), 37% (SDBS)). From the combination of AFM and NIR absorbance spectroscopy one can conclude, that the peptide barrels can 'breathe' and adjust to encapsulate different chiralities, yet still preferentially binds those with exactly fitting diameters.
While these AFM studies are not representative for the whole sample and NIR absorbance spectroscopy does only show the semiconducting SWCNTs, as a next step also Raman-spectroscopy should be employed to get a better understanding of all involved chiralities characterized by their radial breathing modes (RBM). In future studies, one could also combine the preferential binding with enrichment techniques such as aqueous-two-phase (ATP) separation[190] to use αHBs for single-chirality isolation.

4.3.3. Discussion

Up to now, peptides were - despite their great versatility - only rarely utilized for the modification of carbon nanotubes. For comparison, a PubMed search with the terms "carbon nanotube AND peptide" in the title/abstract yielded 121 results compared to 492 results for "carbon nanotube AND DNA". In general, the reported studies can be categorized into three distinct approaches.
First, the use of phage-displayed peptide libraries to find peptide sequences with a high affinity for carbon nanotubes, which led to the peptides containing conserved hydrophobic/aromatic residues found by Wang et al.[191] and Su et al.[192]. In a follow-up study, Su et al. found especially the amino acid tryptophan crucial for effective nanotube binding.[193] Second, peptides were also conjugated covalently to SWCNTs leading to destroyed NIR fluorescence. This approach includes mainly examples, where the SWCNTs were used e.g. as delivery vehicles for bioactive peptides to cross cellular membranes[80] or as shielding agents preventing the generation of immune responses against the conjugated peptide.[194] Third, researchers made use of special peptide characteristics such as amphiphilicity, reversible cyclization or the formation of α-helices on SWCNTs for the dispersion of carbon nanotubes. The first study using peptides to coat SWCNTs was carried

out by Dieckmann et al. in 2003, who used a peptide sequence they termed nano-1. This peptide was then shown to ab able to fold into an α-helix in the presence of SWCNTs leading to their dispersion.[120,195] In 2005, Arnold et al. used an anionic peptide amphiphile (containing an alkyl-tail for SWCNT-binding) termed PA3 for SWCNT dispersion[196], while Ortiz-Acevedo et al. showed the possibility of using reversible cyclic peptides for reversible SWCNT dispersion (upon disulfide formation/cleavage).[121] In 2011, Grygorian et al. further expanded on the idea of Dieckmann et al. with a computational design approach addressing a variety of different parameters such as residues interacting with the SWCNT, the pitch angles of different SWCNT chiralities and the feasibility of peptide design and stability. Using these parameters, they found two sequences, which form α-helical coiled-coil hexamers with parameters matching the geometry of (3,8)-SWCNTs and were also able to show that they can enrich, yet not exclusively bind this chirality. Furthermore, they also used cysteine-residues introduced close to the N-terminus for the templated attachment of gold nanoparticles.[122]

In contrast to these examples of peptides encapsulating carbon nanotubes, this work makes use of previously characterized, *de novo* designed α-helical coiled-coil barrels. While the work of Grygorian et al. is a truly impressive example of what computational peptide design can yield, it is a clear advantage to be able to rationally 'choose from a catalogue' of αHBs with different diameters[114] rendering the whole procedure a very straightforward process. The fact, that αHBs self-assemble in aqueous solution and are very well characterized themselves in terms of sequence-structure relationships is crucial for this attempt to gain also further use in other applications. Figure 2 (p. 88) shows the difference in dispersion yield for the four peptides chosen - two with a larger (B1/B2, $d = 7.6$ Å) and two control peptides with a very narrow pore (C1/C2, $d = 3.9$ Å). While the two peptides containing the larger pore were able to disperse SWCNTs, the C1/C2 peptide were not successful. But also the C-terminal truncation of B1 leading to B2 led to a significant increase in dispersion yield, which could be attributed to a reduced stability of the αHBs on their own leading to increased assembly on the nanotube and thus enhanced dispersion. While it is important to note that the pore diameters estimated from the X-Ray structures of the barrels themselves are not fixed values, but can rather 'breathe', Fig. 3 (p. 88) as well as section 4.3.2 show a trend towards smaller SWCNTs being enriched with the smaller pore peptides (C1/C2) compared to B1/B2. This is especially apparent in the AFM images shown in Fig. 3. Whereas this could also be attributed to larger adsorptive forces of the C2-peptide on mica, it is more likely that

the smaller measured heights (approx. 0.5 nm) are due to a more stable dispersion of smaller SWCNT species. The smallest free-standing SWCNT reported to date has a diameter of 0.43 nm.[7] However, in the absorbance as well as fluorescence spectra with excess peptide present in the solution, this difference is not as apparent as in the AFM images. This could also be due to the tubes in the AFM image being mainly smaller diameter, metallic tubes which are not visible in the optical signature of the sample. These assumptions will be subject of further study including techniques such as Raman spectroscopy.

The next important step is now to further increase the colloidal stability of the SWCNT@Barrel hybrids to the point, where no excess peptide in solution is necessary anymore. This in turn would enable functionalization of outwards-facing residues (e.g. f-positions, compare Fig. 2.12) with fluorophores or targeting-units. It is, however, important to note, that this was also not accomplished in all other approaches mentioned above emphasizing the need for novel techniques for stabilization. In preliminary experiments Jan Horlebein (in his B.Sc. thesis) achieved together with the author of this thesis a slight stabilization of the hybrid structures towards removal of excess peptide by utilizing so-called peptide nanotubes (PNTs) instead of single αHBs. These structures based on αHBs with 'sticky ends' were recently described by the Woolfson lab[118,119] to form tubular structures of several micrometers in length and could thus also possibly lead to a more densely covered SWCNT surface and thus increased colloidal stability. In addition, also carbodiimide-initiated cross-linking or native chemical ligation could be used to covalently link adjacent barrels to one another fixing the structures and preventing disassembly upon removal of excess peptide. While these approaches will be subject of further study to generate a stable peptidic platform for carbon nanotube functionalization, the work described in the following section will employ sp^3 defects for the covalent attachment of peptides and proteins with retained optoelectronic properties.

4.4 sp^3-defects as versatile anchors for the generation of covalent SWCNT-bioconjugates

Carbon nanotubes possess a large variety of unique properties that make them interesting for diverse applications ranging from chip production and quantum computers over biosensing to drug delivery. In order to carry out their desired function especially in the latter two areas, they have to be chemically modified to create e.g. specificity. Next to non-covalent wrapping, which was addressed in the preceding chapters, covalent modifications offer increased stability, which can be crucial in demanding applications such as drug delivery. If the attached drug is e.g. replaced by a protein before it can reach the desired target site, this would lead to more off-site effects and consequently a worse therapeutic outcome. Thus, the generation of stably linked conjugates is of high desire. With respect to covalent SWCNT-peptide or SWCNT-protein conjugates, there were already a few different strategies reported. The laboratories of Prato, Bianco and Kostarelos utilized the 1,3-dipolar cycloaddition of azomethine ylides for the attachment of previously synthesized and purified peptides to guide the peptides into cells or shield them from eliciting an immune response.[79,194,197] The same reaction was also made use of by Spinato et al. for the attachment of the Cetuximab antibody for targeting of epidermal growth factor receptor (EGFR) expressing cells.[180] Another type of chemistry for covalent SWCNT modification is the carbodiimide-activation of -COOH groups formed *via* oxidative treatment followed by a nucleophilic attack of a protein's or peptide's amine. This approach was first used by Huang et al. for the covalent attachment of bovine serum albumine (BSA) in 2002[56] and followed Jiang et al. with MWCNT-BSA and MWCNT-ferritin conjugates[198] and Yu et al., who created covalently linked SWCNT-anti-HSA antibody conjugates.[199] However, all approaches mentioned have a destroyed NIR fluorescence in common and could thus not be used for optical sensing, photodynamic therapy or theranostics. Recently, Setaro et al. reported the covalent derivatization of SWCNTs with preserved NIR emission features, which they used to create photo-switchable and AuNP-functionalized SWCNTs.[53] In 2020, Chio et al. used the same [2+1]-cycloaddition for the attachment of small molecules such as biotin or glycine.[200] These two studies show, that it is indeed possible to create covalently functionalized, yet still NIR-fluorescent carbon nanotubes. The authors of these two studies did, however, not achieve functionalization with larger biomolecules.
Another type of covalent SWCNT modification is the radical arylation using aryl diazo-

nium salts[14,40], which was recently shown to induce a brightening of prior dark excitonic states leading to further red-shifted emission.[39] At this point it is crucial to achieve the right defect density as too high defect densities would again lead to diminished NIR fluorescence (see section 2.2.2.3). It is now the aim of this work to introduce two novel aryldiazonium salts containing anchor groups allowing for subsequent attachment of fluorophores, peptides and even whole proteins, while preserving the NIR fluorescence. In order to achieve this goal, the following points are addressed:

(a) Synthesis of a maleimide-containing diazonium salt as well as a phenylalanine diazonium salt

(b) Optimize and prove successful defect introduction using the new diazonium salts

(c) Use the maleimide-defects for protein attachment and show retained protein function

(d) Use the phenylalanine defects for fluorophore attachment and peptide growth

4.4.1. Quantum defects as a toolbox for covalent carbon nanotube functionalization with peptides and proteins (Manuscript 4)

This chapter is in revision at Angewandte Chemie International Edition (April 2020).

Florian A. Mann, Niklas Herrmann, Felipe Opazo and Sebastian Kruss*

"Quantum defects as a toolbox for covalent carbon nanotube functionalization with peptides and proteins"

* Corresponding author

Responsibility assignment: S.K. and F.A.M. designed and conceived the project. N.H. performed synthesis of the MalPh diazonium salt, NMR/MS analysis, initial experiments and optimized the conditions for MalPh-defect incorporation. F.A.M. performed AFM experiments, synthesized the Fmoc-Phe diazonium salt with N.H., optimized the conditions for Fmoc-Phe defect incorporation, performed the nanobody conjugation and validation experiments, synthesized multi-color SWCNTs, SWCNT-R6 and performed the 96-well SWCNT-Peptide synthesis as well as the subsequent characterization. F.O. provided the GFP-binding nanobody. F.A.M., N.H. and S.K wrote the manuscript with input from F.O..

COMMUNICATION

Quantum defects as a toolbox for covalent carbon nanotube functionalization with peptides and proteins

Florian A. Mann[a], Niklas Herrmann[a], Felipe Opazo[b] and Sebastian Kruss*[a]

[a] F. A. Mann, N. Herrmann, Dr. S. Kruss
Institute of Physical Chemistry
Georg-August Universität
Tammannstraße 6, 37077 Göttingen, Germany
E-mail: skruss@uni-goettingen.de
[b] Dr. F. Opazo
Center for Biostructural Imaging of Neurodegeneration
Von-Siebold-Straße 3a, 37075 Göttingen (Germany)

Supporting information for this article is given via a link at the end of the document.

Abstract: Single-walled carbon nanotubes (SWCNT) are a 1D nanomaterial that shows fluorescence in the near-infrared (NIR, > 800 nm). In the past, covalent chemistry was less explored to functionalize SWCNTs as it impairs NIR emission. However, certain sp^3 defects (quantum defects) in the carbon lattice have emerged that preserve NIR fluorescence and even introduce a new, red-shifted emission peak. Here, we report on quantum defects, introduced using light-driven diazonium chemistry, that serve as anchor points for peptides and proteins. We show that maleimide anchors allow conjugation of cysteine-containing proteins such as a GFP-binding nanobody. In addition, a Fmoc protected phenylalanine defect serves as a starting point for conjugation of visible fluorophores to create multicolor SWCNTs and in situ peptide synthesis directly on the nanotube. Therefore, these quantum defects are a versatile platform to tailor both the nanotube's photophysical properties as well as their surface chemistry.

Since their discovery[1] single-walled carbon nanotubes (SWCNT) attracted a lot of attention not only because of their unique chemical structure, but also because of their outstanding photophysical properties such as non-bleaching/blinking near-infrared (NIR) fluorescence.[2-4] This NIR-fluorescence is beneficial especially for bioimaging as the emission wavelength of SWCNTs falls into the so-called tissue-transparency window where the absorption of water, hemoglobin and lipids reaches a combined minimum and scattering is reduced compared to visible light.[5] Consequently, SWCNTs already found application in diverse settings ranging from *in vivo* NIR imaging[6-8] over drug delivery vehicles[9,10] to NIR optical sensors.[11-20] In order to carry out their desired function in these important applications, the pure carbon tube has to be modified with e.g. the cargo to be carried or a recognition unit imparting specificity for the analyte to be detected. Furthermore, carbon nanotubes are not water-soluble preventing applications in aqueous systems unless the hydrophobic surface is coated with an amphiphilic surfactant.[12] In the last 20 years, both covalent and non-covalent functionalization were employed for the decoration of SWCNTs with functional units. Non-covalent functionalization as for example adsorption of DNA is by far the most frequently applied approach owing to its ease-of-use and mild conditions.[21-23] Furthermore, conformational changes of the coating molecule can directly translate into changes of the NIR fluorescence, which is interesting for sensing.[16,24] On the other hand, covalent functionalization leads to more stable conjugates, but destroys the SWCNT's extended π-network and thus also the NIR-fluorescence.[2,25] In 2017, Setaro et al. reported preserved fluorescence by using a [2+1]-cycloaddition with electron-poor aromatic nitrenes, which they also used for the attachment of gold nanoparticles and spiropyranes.[26] Very recently, Godin et al. used spyropyran-switchable SWCNTs for NIR super-resolution microscopy[27] while Chio et al. used the same nitrene [2+1]-cycloaddition for the attachment of small molecules such as biotin.[28]

However, sp^3 defects can not only diminish the NIR-fluorescence, but were also found to modulate it depending on the nature and density of the defects. In 2010, Ghosh et al. reported on a NIR emission peak red-shifted by approx. 130 nm (termed E_{11}^*) upon introduction of oxygen defects.[29] Later, Piao et al. observed a similar peak shift and enhanced fluorescence quantum yield upon introduction of aryl defects using diazonium salts (quantum defects).[30] This technique also enabled tuning of the defect-fluorescence both in terms of intensity and emission wavelength via different substituents on the aryl/alkyl-defect.[31-34]

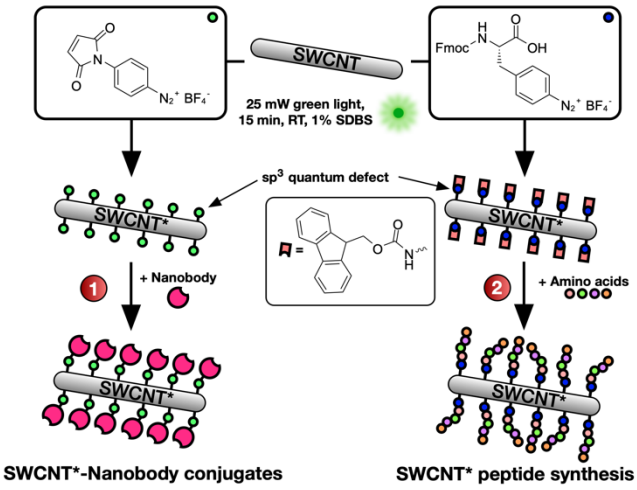

Figure 1. Defects as a generic handle to functionalize single-walled carbon nanotubes (SWCNT*). Differently substituted aryl-defects are introduced into the nanotube's sidewall and used to conjugate biomolecules such as nanobodies (1) or for the direct growth of peptide chains on the SWCNT* (2).

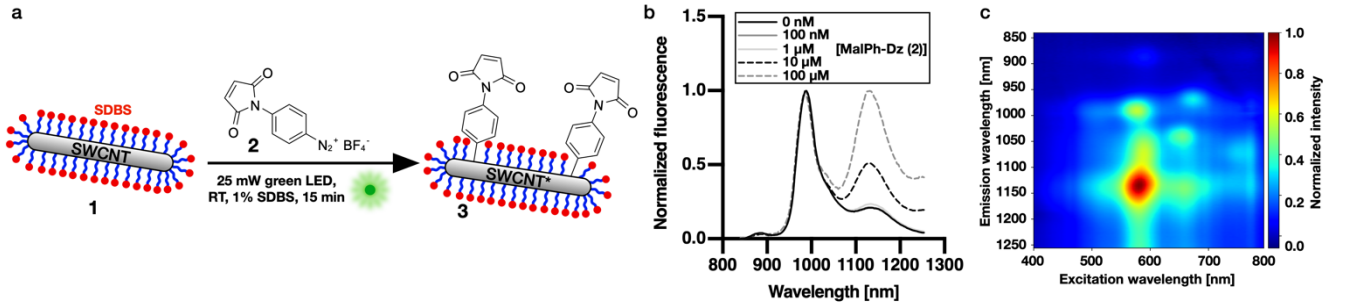

Figure 2. Light-driven introduction of maleimide-carrying quantum defects into SWCNTs. a) Schematic of the photo-induced defect introduction based on aqueous diazonium chemistry. Size of the structures is not to scale. b) NIR-fluorescence spectra of SWCNT*/SDBS samples after the photoinduced defect reaction (15 min illumination) with different concentrations of MalPh-Dz. c) NIR fluorescence excitation-emission map after introduction of the covalent MalPh defects, removal of excess **2** and resuspension in 1% SDBS (a control 2D-spectrum can be found in Fig. S3).

In the last years, a number of different oxygen and aryl-defects were reported, that are now very promising tools for the generation of brighter/modified SWCNTs[31,35,36], pH-[37] or saccharide[38] sensors, short fluorescent SWCNTs for super-resolution microscopy[39] or single-photon sources for quantum computing.[40,41] Furthermore, this new defect-induced fluorescence feature moves the emission even further into the bio-transparency window leading to even better tissue penetration properties.[42,43]

In this work, we expand the use of quantum defects from modulation of the SWCNT's photophysical properties towards using them as modular anchors for the attachment of peptides and proteins (Fig. 1). To this end, we employed a (*N*-maleimido)phenyl diazonium salt (MalPh-Dz, **2**), which – after defect introduction – can be targeted by thiol-containing molecules such as proteins, while at the same time generating a further red-shifted E_{11}^* emission feature (defect-carrying SWCNTs are thus referred to as SWCNT* from now on).

We started our investigations by optimizing the narrow window of reaction conditions[44] between sodium dodecylbenzenesulfonate (SDBS) dispersed SWCNTs **1** and 4-(*N*-maleimido)phenyl-diazonium tetrafluoroborate (MalPh-Dz, **2**) allowing for the NIR-fluorescence to be altered, yet not diminished (Fig. 2a). For a fast and efficient screening of conditions (reaction time and reactant concentration, see Fig. S1), we made use of a 96-well green LED array for SWCNT excitation driving the radical arylation reaction. The best results were achieved when a 10 nM SWCNT ($c_{carbon} \approx 530$ µM) solution (dispersed in 1% SDBS/H_2O) was mixed with **2** (100 µM) and irradiated for 15 minutes. Higher MalPh-Dz concentrations would lead to too many defects and diminish NIR fluorescence.[30]

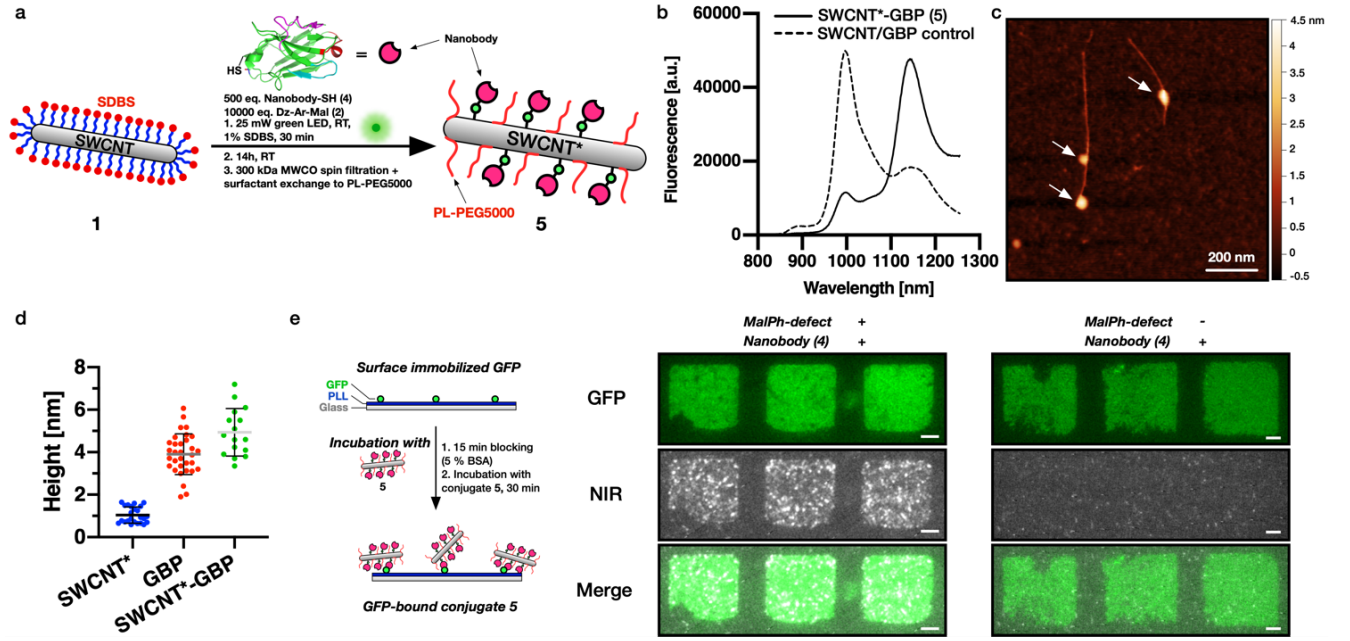

Figure 3. One-pot introduction of quantum defects and nanobody conjugation to SWCNT*. a) Schematic of the one-pot defect reaction and bioconjugation to GFP-binding nanobodies (GBP). b) NIR-fluorescence spectra comparing the SWCNT*-GBP conjugate **5** and its negative control where no MalPh-Dz was added showing the successful introduction of quantum defects despite the simultaneous addition of the anti-GFP nanobody. c) Atomic Force microscopy (AFM) image of a SWCNT after defect/conjugation reaction to GBP. Scale bar = 200 nm. The arrows point at locations of increased height indicating the conjugation of the nanobody. The reaction conditions (low defect density, reactant concentration) were chosen to immobilize only a few GBPs per tube. d) Measured heights of SWCNT*s only non-covalently wrapped by phospholipid-polyethyleneglycol-5000 (PL-PEG5000), isolated GBP nanobodies and SWCNT*-GBP showing the increased height after nanobody-conjugation (mean ± SD, n ≥ 16). e) Pattern of green-fluorescent protein (GFP) on a glass surface incubated with SWCNT*-GBP. The colocalization shows retained functionality of the nanobody even after covalent conjugation to the SWCNT. Scale bars = 5 µm.

The success of the defect reaction was monitored by NIR-fluorescence spectroscopy (Fig. 2b) and the SWCNT's structural integrity and colloidal stability was controlled using VIS-NIR absorbance spectroscopy (Fig. S2). The fluorescence spectra and the excitation/emission map (see Fig. 2c) clearly show a growing E_{11}^* peak at approx. 1135 nm with increasing concentration of **2** (control 2D-spectrum with a non-modified SWCNT/SDBS sample can be found in Fig. S3). The increased E_{11}^*/E_{11} ratio of the 2D versus the 1D NIR-fluorescence spectrum could be attributed to prolonged exposure to MalPh-Dz **2** before spin filtration and measurement of the 2D-spectrum or due to preferential redispersion of MalPh-SWCNT*.

After successful introduction of (*N*-Maleimido)phenyl quantum defects (MalPh defects), we tested whether biomolecules can be conjugated to this anchor. As a first example, we chose a nanobody against green-fluorescent protein (GFP). Nanobodies are the isolated antigen-binding region of heavy-chain antibodies found e.g. in *Camelidae* and are only 10% of the size of conventional antibodies.[45,46] This renders them very useful as binders for diverse applications such as super-resolution microscopy[47-49], live-cell immunostaining after modification with cell-penetrating peptides[50] or isotopic labeling of biological samples for secondary-ion mass spectrometry (SIMS) imaging.[51] Nanobodies binding GFP (GFP-binding protein, GBP) in particular can be used as a platform technology due to the widespread availability of GFP-fusion proteins or even whole genetically modified organisms expressing GFP-fusion proteins giving the possibility to target a whole variety of proteins with just one single conjugate. Similar to our previous (non-covalent) work[13], we used a GBP with a single ectopic C-terminal cysteine for oriented conjugation to the MalPh-SWCNT* **3** leaving the antigen-binding region pointing away from the SWCNT*'s surface. With the fast hydrolysis kinetics of *N*-aryl maleimides[52] in mind, we evaluated both the sequential defect introduction followed by nanobody conjugation as well as a one-step approach combining all three reaction partners at once (Fig. 3a). For the sequential reaction, the excess diazonium salt **2** was removed using 300 kDa molecular weight cut-off (MWCO) spin filters followed by resuspension of the now naked MalPh-SWCNT* **3** in 1x phosphate-buffered saline (PBS, pH 7.4) and reaction with 500 eq. (~25 eq. with respect to introduced maleimides) of the nanobody **4** (16 h at room temperature). In the one-step approach, the same excess of GBP was added directly during the defect-introduction (30 minutes instead of 15 minutes for the sequential reaction) and left reacting for 16 h at room temperature as well. After defect-introduction/bioconjugation, the excess nanobody was removed using 300kDa-MWCO-spin-filtration and the SWCNT*-GBP conjugate **5** resuspended in 1xPBS using 1,2-distearoyl-*sn*-glycero-3-phosphoethanolamine-N-[methoxy(polyethylene glycol)-5000] (ammonium salt, PL-PEG5000). As shown in Fig. S4, the redispersion step was efficient only for the conjugate **5** synthesized *via* the one-step approach yielding a highly concentrated solution (OD = 1.8). Consequently, we proceeded with the resuspended conjugate **5** resulting from the one-step procedure in the following.

Fig. 3b shows the NIR-fluorescence spectra of the conjugate **5** as well as the negative control, where no diazonium salt **2** was added, both resuspended using PL-PEG5000. A comparison of both spectra shows successful introduction of sp^3 quantum defects and E_{11}^* emission. To further evaluate, whether these defects also contain the covalently attached nanobody, we employed atomic force microscopy (AFM). Here, the one-step-synthesized sample clearly shows nanobodies attached to the SWCNT* (see Fig. 3c, control without **2** in Fig. S5) with the additional height introduced by the GBP fitting both the value measured by AFM (d = 4.3±0.9 nm) as well as the diameter obtained from the crystal structure (PDB: 3G9A, d = 3.4-4.3 nm, see Fig. S6). In a few cases, also larger heights of SWCNT*-GBP conjugates (approx. 7 nm) were measured, which could be explained by the possible side reaction of the diazonium salt **2** with the GBP's aromatic residues leading to dimer formation. Taken together, these results indicate successful conjugation of the nanobody to maleimide-bearing quantum defects, which in turn are still able to modulate the SWCNT*'s NIR-fluorescence yielding emission at 1143 nm.

As a next step, we verified that the nanobody is still able to bind GFP even after covalent conjugation to the SWCNT. Therefore, we immobilized GFP (patterned using polydimethylsiloxane (PDMS)-based micro-contact printing) on a poly-L-lysine (PLL) coated glass surface followed by blocking (with bovine serum albumin [BSA])/washing steps and incubation with the conjugate **5**.

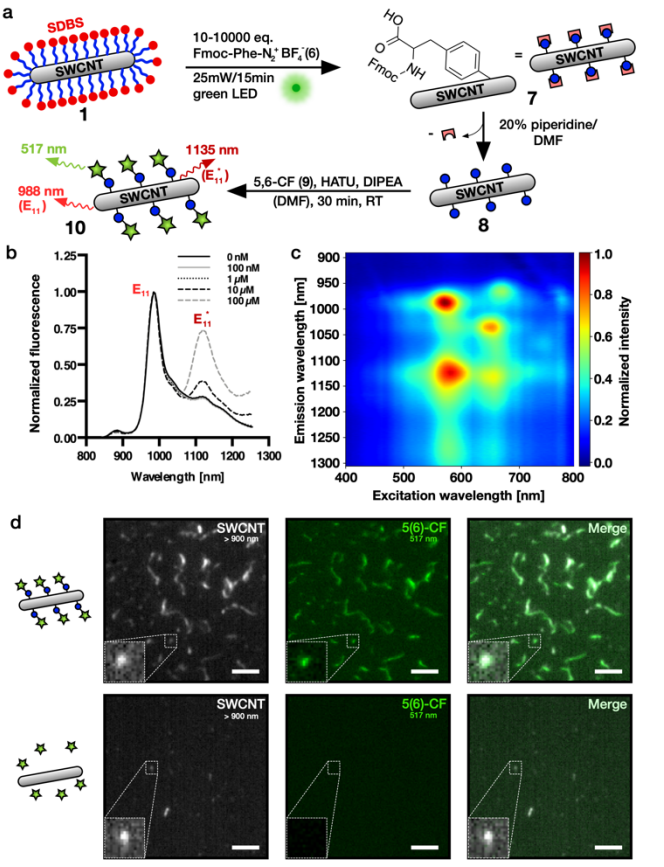

Figure 4. Fmoc-Phenylalanine quantum defects and multi-color single-walled carbon nanotubes (SWCNTs). A) Strategy for defect introduction and subsequent Fmoc-deprotection followed by 5(6)-carboxyfluorescein (CF)-conjugation. B) NIR-fluorescence spectra of SWCNTs treated with different concentrations of Fmoc-Phe-Dz showing increased E_{11}^*/E_{11} ratios at higher diazonium salt concentrations. C) Excitation-emission map of Fmoc-Phe-SWCNT* showing the E_{11}^*-fluorescence amongst other minor SWCNT species and E_{11}-fluorescence. d) SWCNT*-Phe-CF immobilized on a glass slide showing colocalization of the NIR (>900 nm) and the CF-channel (500-550 nm), whereas the control without sp^3-defects does not show a CF-signal, indicating successful conjugation. Scale bars = 5 µm.

The observed colocalization of the GFP- and the NIR-channel indicates retained function of the GBP even after covalent conjugation to the SWCNT* (Fig. 3e, control without the MalPh defect on the right and without GBP in Fig. S7). This is, to the best of our knowledge, the first covalent conjugation of a functional (immuno)protein to a SWCNT under preserved/enhanced NIR-fluorescence.

After having successfully established MalPh quantum defects as an anchor for the attachment of (immuno)proteins, we wanted to challenge this defect-based approach even further with the aim of synthesizing peptide chains directly on the SWCNT's sidewall. While there are a few reports on the use of coiled-coil or cyclic peptides for SWCNT dispersion[53-55] or the non-covalent immobilization of RGD-motifs[56], covalent immobilization of peptides is less explored. Pantarotto et al. and Bianco et al. utilized the 1,3-dipolar cycloaddition of azomethine ylides for the covalent modification of SWCNTs and for subsequent attachment of previously synthesized, short peptides.[57,58] However, this approach destroys the SWCNT's optical properties and rules out NIR fluorescence imaging applications.

To use quantum defects as a starting point for peptide growth, we synthesized a diazonium salt containing a fluorenylmethoxycarbonyl (Fmoc)-protected L-Phenylalanine (Fmoc-Phe-Dz, **6**) in a one-step procedure. Next, we again optimized the conditions for defect introduction (Fmoc-Phe defects) and evaluated the success using 1D/2D-NIR-fluorescence spectroscopy (Fig. 4b/c, control 2D-spectrum in Fig. S8). We carried out the Fmoc-deprotection using 20% piperidine/DMF in a 1 mL syringe reactor equipped with a standard 20 µm pore-size frit. After washing, we coupled the fluorophore 5(6)-carboxyfluorescein (CF) to assess addressability of the unprotected amine. Fig. 4d shows colocalization of the NIR- and the CF-channel after immobilization on glass and washing steps using 1xPBS with 0.1% Triton-X-100 as opposed to the negative controls (without **6** [Fig. 4d] or without Fmoc-deprotection [Fig. S9]). This result shows that the unprotected amine is still addressable and the conjugation of carboxyfluorescein led to the generation of covalently linked multi-color SWCNT*.

Encouraged by these promising results, we wanted to test next, whether it is also possible to synthesize a whole peptide sequence on the Fmoc-Phe-SWCNT* **7**. Here, we decided for a positively charged hexaarginine peptide to also evaluate its impact on the SWCNT*'s solubility in aqueous environments (Fig. 5a). To evaluate the success of the SWCNT*-Peptide synthesis, neither the Kaiser test for free amines nor UV-measurements after Fmoc cleavage could be used due to their insufficient sensitivities on the small scale of these experiments (n_{SWCNT} = 100 pmol in 1 mL solution). Thus, we decided to couple 5(6)-CF to the N-terminus before global deprotection of the arginine's side chains using a deprotection cocktail (75% trifluoroacetic acid [TFA], 15% dichloromethane [DCM], 5% ddH_2O, 5% tri*iso*propylsilane [TIS]). This was followed by tip-sonication in 1xPBS (3 min, 30% amp, 4°C) and centrifugation (16100g, 30min) to remove insoluble SWCNTs. Fig. 5b shows colocalization of the NIR- and the CF-channel on the single-nanotube level indicating successful synthesis of SWCNT*-F-R_6-CF in contrast to the control (without **6**, see Fig. S10) and retained optoelectronic properties after TFA deprotection. In fact, the negative control did not contain any SWCNTs indicating increased solubility in aqueous environments by covalent peptide functionalization. However, due to the small number of defects (approx. 1 defect per 20 nm tube[30]) the SWCNT*-F-R_6-CF (**8**) did not display high solubility in water and therefore additional wrapping was used to increase the concentration and colloidal stability. In future studies, this aspect could be further evaluated with higher defect densities and/or longer peptide sequences.

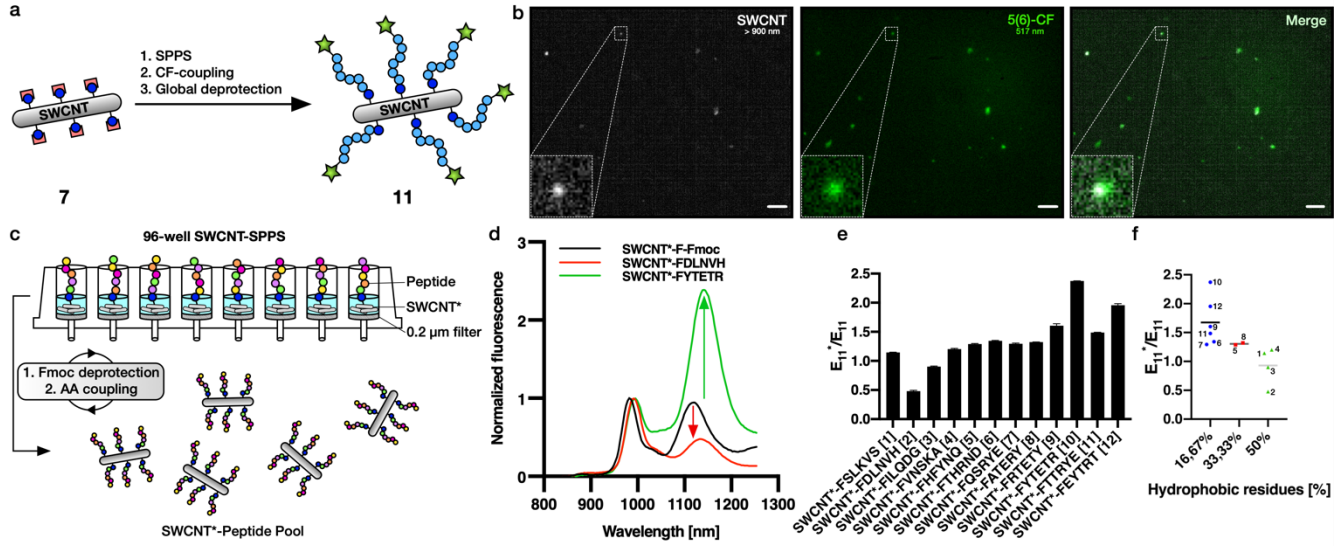

Figure 5. In situ peptide synthesis and modulation of E_{11}*-peak intensities. A) Strategy for the generation of covalent and fluorescent SWCNT-F-R_6-CF conjugates based on Fmoc/O^{t}Bu-solid phase peptide synthesis (SPPS) followed by N-terminal 5(6)-carboxyfluorescein (CF) coupling and Pbf-deprotection of the arginine's side chains. B) SWCNT-R_6-CF spin-coated on a glass coverslip showing colocalization of the near-infrared (NIR) and the CF-channel indicating successful peptide-synthesis and N-terminal CF-coupling directly on the SWCNT's sidewall (scale bars = 10 µm). c) 96-well peptide synthesis for the generation of a SWCNT-peptide pool following the same Fmoc/O^{t}Bu-SPPS protocol as shown in a), yet here in a 96 well-plate with filters (0.2 µm pore size). d) Normalized NIR-PL spectra before and after synthesis of two selected peptide sequences showing the modulation of the defect-induced fluorescence. The red-shift from the protected to the unprotected sample could be attributed to the different surfactant (SWCNT*-F-Fmoc: SDBS, SWCNT*-Peptide: DOC). e) The SWCNT's fluorescence properties (in particular the E_{11}*/E_{11} ratio) depends on peptide sequence on the sidewall (mean ± SD, n=3). f) E_{11}*/E_{11} ratio increases with the number of hydrophobic residues (mean and individual values, n=6,2,4).

As a next step we upscaled SWCNT*-based peptide synthesis and synthesized multiple SWCNT-peptide conjugates at the same time in a 96-well format (equipped with 0.2 µm pore size filters, Fig. 5c). Again, the synthesis followed the same protocol as above, yet with smaller reaction volumes. Using this technique, we synthesized twelve different peptide sequences directly on NIR-fluorescent carbon nanotubes. After side-chain deprotection using the same deprotection cocktail as for SWCNT*-F-R_6-CF, the carbon nanotubes were redispersed in an aqueous 1% DOC solution *via* tip-sonication. While DOC leads to slightly red-shifted emission compared to SDBS-dispersed SWCNT*-F-Fmoc/SDBS (**7**)[59,60], both Fig. 5d and e show the impact of peptide sequence on the NIR-fluorescence. For some sequences the original E_{11} peak was almost twice as intense as the E_{11}^* peak - other sequences showed exactly the opposite behavior with the E_{11}^* signal being 2.5-fold stronger than the signal arising from the E_{11} transition (VIS/NIR absorbance and NIR fluorescence spectra in Fig. S11). A closer evaluation of the sequence-dependence of this fluorescence modulation shows that the E_{11}^*/E_{11} ratio decreases with an increasing number of hydrophobic residues in the peptide sequence attached to the defect responsible for exciton trapping (Fig. 5f). A similar effect was already observed by Kwon et al., who found changing E_{11}^* emission wavelengths and E_{11}^*/E_{11} ratios for differently substituted (fluoro)alkyl/aryl sp^3-defects.[32] This interesting impact on the SWCNT's photophysics could be attributed to the peptides folding differently on the SWCNT and changing the charge landscape through which the exciton diffuses or where it gets trapped, thus leading to enhanced E_{11}^*-fluorescence for less hydrophobic sequences. Different folding of peptides is known from non-covalent SWCNT/Peptide hybrids.[61] Furthermore, a comparison of the sequences 9-12 consisting of identical amino acids shows that not only the nature of the attached amino acids, but also their sequential arrangement is of high importance for the SWCNT*'s NIR-fluorescence properties. These results demonstrate the possibilities of employing Fmoc-protected phenylalanine defects for the growth of peptidic chains directly on the nanotube's sidewall and indicate, that this method can not only be used for modulation of the SWCNT's fluorescence, but also to tailor their surface properties. This in turn could enable SWCNTs with enhanced cellular uptake/retention[62,63], tailored molecular recognition motifs or novel and more stable optical sensors operating in the NIR. Furthermore, the coupling of a second optically active molecule (fluorophore) *via* a peptide sequence to a SWCNT could serve as general design principle for molecular recognition and signal transduction. Similar to Förster resonance energy transfer (FRET), conformational changes upon binding to a target structure could affect the SWCNT's NIR fluorescence and enable novel fluorescent probes and labels.

In summary, we introduced two new sp^3 quantum defects in SWCNTs, which serve as anchors for the attachment of biomolecules. The versatility of this new functionalization platform was demonstrated by conjugation of a GFP-binding nanobody as an example for a protein and the synthesis of peptides directly on the carbon nanotube surface. This new technique for covalent decoration of SWCNTs with biomolecules opens up great possibilities for applications in (bio)photonics, biosensing or biomedicine.

Acknowledgements

We thank the VW foundation and the State of Lower Saxony (life@nano) for funding. We thank Andreas Janshoff and Claudia Steinem for their support.

Keywords: nanotube • quantum defect • bioconjugation • nanobody • peptide

[1] S. Iijima, *Nature* **1991**, *354*, 56–58.
[2] S. Kruss, A. J. Hilmer, J. Zhang, N. F. Reuel, Bin Mu, M. S. Strano, *Adv. Drug Deliv. Rev.* **2013**, *65*, 1933–1950.
[3] M. J. O'Connell, S. M. Bachilo, C. B. Huffman, V. C. Moore, M. S. Strano, E. H. Haroz, K. L. Rialon, P. J. Boul, W. H. Noon, C. Kittrell, et al., *Science* **2002**, *297*, 593–596.
[4] S. M. Bachilo, M. S. Strano, C. Kittrell, R. H. Hauge, R. E. Smalley, R. B. Weisman, *Science* **2002**, *298*, 2361–2366.
[5] C. Farrera, F. Torres Andón, N. Feliu, *ACS Nano* **2017**, *11*, 10637–10643.
[6] K. Welsher, Z. Liu, S. P. Sherlock, J. T. Robinson, Z. Chen, D. Daranciang, H. Dai, *Nat. Nanotechnol.* **2009**, *4*, 773–780.
[7] Z. Liu, S. M. Tabakman, Z. Chen, H. Dai, *Nat. Protoc.* **2009**, *4*, 1372–1381.
[8] T. V. Galassi, P. V. Jena, J. Shah, G. Ao, E. Molitor, Y. Bram, A. Frankel, J. Park, J. Jessurun, D. S. Ory, et al., *Sci. Transl. Med.* **2018**, *10*, eaar2680.
[9] G. Pastorin, *Pharm. Res.* **2009**, *26*, 746–769.
[10] H. Huang, Q. Yuan, J. S. Shah, R. D. K. Misra, *Adv. Drug Deliv. Rev.* **2011**, *63*, 1332–1339.
[11] P. W. Barone, R. S. Parker, M. S. Strano, *Anal. Chem.* **2005**, *77*, 7556–7562.
[12] A. J. Gillen, A. A. Boghossian, *Front. Chem.* **2019**, *7*, 13793–13.
[13] F. A. Mann, Z. Lv, J. Grosshans, F. Opazo, S. Kruss, *Angew. Chem. Int. Ed.* **2019**, *58*, 11469–11473.
[14] F. A. Mann, N. Herrmann, D. Meyer, S. Kruss, *Sensors (Basel)* **2017**, *17*, 1521.
[15] M. Dinarvand, E. Neubert, D. Meyer, G. Selvaggio, F. A. Mann, L. Erpenbeck, S. Kruss, *Nano Lett.* **2019**, *19*, 6604–6611.
[16] S. Kruss, D. P. Salem, L. Vuković, B. Lima, E. Vander Ende, E. S. Boyden, M. S. Strano, *Proc. Natl. Acad. Sci.* **2017**, *114*, 1789–1794.
[17] S. Kruss, M. P. Landry, E. Vander Ende, B. M. A. Lima, N. F. Reuel, J. Zhang, J. Nelson, B. Mu, A. Hilmer, M. Strano, *J. Am. Chem. Soc.* **2014**, *136*, 713–724.
[18] H. Wu, R. Nißler, V. Morris, N. Herrmann, P. Hu, S.-J. Jeon, S. Kruss, J. P. Giraldo, *Nano Lett.* **2020**, acs.nanolett.9b05159–28.
[19] G. Bisker, J. Dong, H. D. Park, N. M. Iverson, J. Ahn, J. T. Nelson, M. P. Landry, S. Kruss, M. S. Strano, *Nat. Commun.* **2016**, *7*, 10241.
[20] R. M. Williams, C. Lee, T. V. Galassi, J. D. Harvey, R. Leicher, M. Sirenko, M. A. Dorso, J. Shah, N. Olvera, F. Dao, et al., *Sci. Adv.* **2018**, *4*.
[21] M. Zheng, A. Jagota, M. S. Strano, A. P. Santos, P. Barone, S. G. Chou, B. A. Diner, M. S. Dresselhaus, R. S. Mclean, G. B. Onoa, et al., *Science* **2003**, *302*, 1545–1548.
[22] R. Nißler, F. A. Mann, P. Chaturvedi, J. Horlebein, D. Meyer, L. Vuković, S. Kruss, *J. Phys. Chem. C* **2019**, *123*, 4837–4847.
[23] A. J. Gillen, J. Kupis-Rozmysłowicz, C. Gigli, N. Schuergers, A. A. Boghossian, *J. Phys. Chem. Lett.* **2018**, *9*, 4336–4343.
[24] E. Polo, S. Kruss, *J. Phys. Chem. C* **2016**, *120*, 3061–3070.
[25] A. Hirsch, *Angew. Chem. Int. Ed. Engl.* **2002**, *41*, 1853–9.
[26] A. Setaro, M. Adeli, M. Glaeske, D. Przyrembel, T. Bisswanger, G. Gordeev, F. Maschietto, A. Faghani, B. Paulus, M. Weinelt, et al., *Nat. Commun.* **2017**, *8*, 838–7.
[27] A. G. Godin, A. Setaro, M. Gandil, R. Haag, M. Adeli, S. Reich, L. Cognet, *Sci. Adv.* **2019**, *5*, eaax1166.
[28] L. Chio, R. L. Pinals, A. Murali, N. S. Goh, M. P. Landry, *Adv. Funct. Mater.* **2020**, 1910556–8.
[29] S. Ghosh, S. M. Bachilo, R. A. Simonette, K. M. Beckingham, R. B. Weisman, *Science* **2010**, *330*, 1656–1659.
[30] Y. M. Piao, B. Meany, L. R. Powell, N. Valley, H. Kwon, G. C. Schatz, Y. H. Wang, *Nat. Chem.* **2013**, *5*, 840–845.
[31] F. J. Berger, J. Lüttgens, T. Nowack, T. Kutsch, S. Lindenthal, L. Kistner, C. C. Müller, L. M. Bongartz, V. A. Lumsargis, Y. Zakharko, et al., *ACS Nano* **2019**, *13*, 9259–9269.
[32] H. Kwon, M. Furmanchuk, M. Kim, B. Meany, Y. Guo, G. C. Schatz, Y. Wang, *J. Am. Chem. Soc.* **2016**, *138*, 6878–6885.
[33] Y. Miyauchi, M. Iwamura, S. Mouri, T. Kawazoe, M. Ohtsu, K. Matsuda, *Nat. Photonics* **2013**, *7*, 715–719.
[34] M. Kim, X. Wu, G. Ao, X. He, H. Kwon, N. F. Hartmann, M. Zheng, S. K. Doom, Y. Wang, *Chem* **2018**, *4*, 2180–2191.

[35] C. F. Chiu, W. A. Saidi, V. E. Kagan, A. Star, *J. Am. Chem. Soc.* **2017**, *139*, 4859–4865.
[36] P. Clement, P. Trinchera, K. Cervantes Salguero, Q. Ye, C. R. Jones, M. Palma, *ChemPlusChem* **2019**, *84*, 1235–1238.
[37] H. Kwon, M. Kim, B. Meany, Y. Piao, L. R. Powell, Y. Wang, *J. Phys. Chem. C* **2015**, *119*, 3733–3739.
[38] T. Shiraki, H. Onitsuka, T. Shiraishi, N. Nakashima, *Chem. Commun.* **2016**, *52*, 12972–12975.
[39] N. Danné, M. Kim, A. G. Godin, H. Kwon, Z. Gao, X. Wu, N. F. Hartmann, S. K. Doorn, B. Lounis, Y. Wang, et al., *ACS Nano* **2018**, *12*, 6059–6065.
[40] X. He, H. Htoon, S. K. Doorn, W. H. P. Pernice, F. Pyatkov, R. Krupke, A. Jeantet, Y. Chassagneux, C. Voisin, *Nat. Mater.* **2018**, *17*, 663–670.
[41] X. He, N. F. Hartmann, X. Ma, Y. Kim, R. Ihly, J. L. Blackburn, W. Gao, J. Kono, Y. Yomogida, A. Hirano, et al., *Nat. Photonics* **2017**, *11*, 577–.
[42] A. K. Mandal, X. Wu, J. S. Ferreira, M. Kim, L. R. Powell, H. Kwon, L. Groc, Y. Wang, L. Cognet, *bioRxiv* **2019**, 636860.
[43] C.-W. Lin, S. M. Bachilo, Y. Zheng, U. Tsedev, S. Huang, R. B. Weisman, A. M. Belcher, *Nat. Commun.* **2019**, 1–9.
[44] A. H. Brozena, M. Kim, L. R. Powell, Y. Wang, *Nat. Rev. Chem.* **2019**, *3*, 375–392.
[45] J. Helma, M. C. Cardoso, S. Muyldermans, H. Leonhardt, *J. Cell Biol.* **2015**, *209*, 633–644.
[46] C. Hamers-Casterman, T. Atarhouch, S. Muyldermans, G. Robinson, C. Hammers, E. B. Songa, N. Bendahman, R. Hammers, *Nature* **1993**, *363*, 446–448.
[47] J. Ries, C. Kaplan, E. Platonova, H. Eghlidi, H. Ewers, *Nat. Methods* **2012**, *9*, 582–584.
[48] M. Mikhaylova, B. M. C. Cloin, K. Finan, R. Van Den Berg, J. Teeuw, M. M. Kijanka, M. Sokolowski, E. A. Katrukha, M. Maidorn, F. Opazo, et al., *Nat. Commun.* **2015**, *6*, 1–7.
[49] S. Sograte-Idrissi, N. Oleksiievets, S. Isbaner, M. Eggert-Martinez, J. Enderlein, R. Tsukanov, F. Opazo, *Cells* **2019**, *8*, 48–13.
[50] H. D. Herce, D. Schumacher, A. F. L. Schneider, A. K. Ludwig, F. A. Mann, M. Fillies, M.-A. Kasper, S. Reinke, E. Krause, H. Leonhardt, et al., *Nat. Chem.* **2017**, *9*, 762–771.
[51] S. Kabatas, P. Agüi-Gonzalez, K. A. Saal, S. Jähne, F. Opazo, S. O. Rizzoli, N. T. N. Phan, *Angew. Chem. Int. Ed.* **2019**, *58*, 3438–3443.
[52] J. M. J. M. Ravasco, H. Faustino, A. Trindade, P. M. P. Gois, *Chem. Eur. J.* **2018**, *25*, 43–59.
[53] G. Grigoryan, Y. H. Kim, R. Acharya, K. Axelrod, R. M. Jain, L. Willis, M. Drndic, J. M. Kikkawa, W. F. DeGrado, *Science* **2011**, *332*, 1071–1076.
[54] F. A. Mann, J. Horlebein, N. F. Meyer, D. Meyer, F. Thomas, S. Kruss, *Chem. Eur. J.* **2018**, *24*, 12241–12245.
[55] G. R. Dieckmann, A. B. Dalton, P. A. Johnson, J. Razal, J. Chen, G. M. Giordano, E. Muñoz, I. H. Musselman, R. H. Baughman, R. K. Draper, *J. Am. Chem. Soc.* **2003**, *125*, 1770–1777.
[56] E. Polo, T. T. Nitka, E. Neubert, L. Erpenbeck, L. Vuković, S. Kruss, *ACS Appl. Mater. Interfaces* **2018**, *10*, 17693–17703.
[57] A. Bianco, K. Kostarelos, C. D. Partidos, M. Prato, *Chem. Commun.* **2005**, *14*, 571–7.
[58] D. Pantarotto, C. D. Partidos, R. Graff, J. Hoebeke, J.-P. Briand, M. Prato, A. Bianco, *J. Am. Chem. Soc.* **2003**, *125*, 6160–6164.
[59] R. Haggenmueller, S. S. Rahatekar, J. A. Fagan, J. Chun, M. L. Becker, R. R. Naik, T. Krauss, L. Carlson, J. F. Kadla, P. C. Trulove, et al., *Langmuir* **2008**, *24*, 5070–5078.
[60] T. Shiraki, Y. Niidome, F. Toshimitsu, T. Shiraishi, T. Shiga, B. Yu, T. Fujigaya, *Chem. Commun.* **2019**, *55*, 3662–3665.
[61] D. A. Heller, G. W. Pratt, J. Zhang, N. Nair, A. J. Hansborough, A. A. Boghossian, N. F. Reuel, P. W. Barone, M. S. Strano, *Proc. Natl. Acad. Sci.* **2011**, *108*, 8544–8549.
[62] M. Gravely, M. M. Safaee, D. Roxbury, *Nano Lett.* **2019**, DOI 10.1021/acs.nanolett.9b02267.
[63] D. Meyer, S. Telele, A. Zelená, A. J. Gillen, A. Antonucci, E. Neubert, R. Nißler, F. A. Mann, L. Erpenbeck, A. A. Boghossian, et al., *Nanoscale* **2020**, *2*, 751.

Entry for the Table of Contents

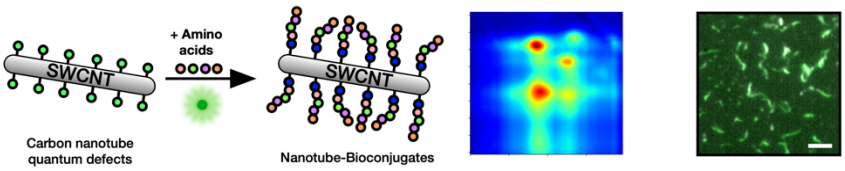

Quantum defects as multifunctional handles for the covalent decoration of carbon nanotubes. Here, we incorporate two new quantum defects into single-walled carbon nanotubes (SWCNT) carrying anchor groups for functionalization with biomolecules. We demonstrate the potential and versatility of this approach by the conjugation of a GFP-binding nanobody as well as the growth of (fluorescent) peptide chains directly on the nanotube's carbon lattice.

Institute and/or researcher Twitter usernames: @florian_a_mann, @KrussLab, @uniGoettingen, @niklas_herr

Supporting Information

69451 Weinheim, Germany

Quantum defects as a toolbox for covalent carbon nanotube functionalization with peptides and proteins

Florian A. Mann, Niklas Herrmann, Felipe Opazo and Sebastian Kruss*

Abstract: Single-walled carbon nanotubes (SWCNT) are a 1D nanomaterial that shows fluorescence in the near-infrared (NIR, > 800 nm). In the past, covalent chemistry was less explored to functionalize SWCNTs as it impairs NIR emission. However, certain sp^3 defects (quantum defects) in the carbon lattice have emerged that preserve NIR fluorescence and even introduce a new, red-shifted emission peak. Here, we report on quantum defects, introduced using light-driven diazonium chemistry, that serve as anchor points for peptides and proteins. We show that maleimide anchors allow conjugation of cysteine-containing proteins such as a GFP-binding nanobody. In addition, a Fmoc protected phenylalanine defect serves as a starting point for conjugation of visible fluorophores to create multicolor SWCNTs and in situ peptide synthesis directly on the nanotube. Therefore, these quantum defects are a versatile platform to tailor both the nanotube's photophysical properties as well as their surface chemistry.

DOI: 10.1002/anie.2016XXXXX

Table of contents

1. Experimental Procedures

1.1. General Information

NMR spectra were recorded with a Bruker™ Avance III HD 300 device (Bruker Corp., USA), equipped with a 5 mm probe. For a measurement, approx. 15 mg of substance were dissolved in approx. 600 µL of the deuterated solvent stated and transferred to a standard glass NMR tube (d = 5 mm). The chemical shifts are reported in ppm relative to the residual solvent peak(s). Analysis was performed within MestReNova™ 10.

ESI-TOF-MS measurements of diazonium salts were performed on a Bruker™ micrOTOF ESI-TOF-MS using the non-deuterated form of the solvent also used for NMR measurements.

VIS-fluorescence spectra were acquired between 500 and 600 nm using an excitation wavelength of 490 nm on a FluoroMax-4 spectrofluorometer (Horiba Scientific, Japan).

Reagents and solvents were, unless stated otherwise, of synthesis grade quality and used without further purification. Fmoc-protected amino acids were purchased either from IRIS Biotech (Germany) or Novabiochem (Germany).

(6,5)-chirality enriched single-walled carbon nanotubes (SWCNTs, Product No.: 773735) were acquired from Sigma Aldrich (Darmstadt, Germany).

SWCNT/SDBS stock solutions were generated by tip sonication of a SWCNT/SDBS (1%) suspension for 15 minutes (Fisher Scientific™ Model 120 Sonic Dismembrator, 30% amplitude, 36 W) followed by centrifugation (2x, 16100g). Only the supernatant (top 80%) was used for further studies.

Experiments and measurements were, unless otherwise stated, performed in phosphate buffered saline (PBS, 8.2 mM Na2HPO4, 1.8 mM K2HPO4, 137 mM NaCl, 2.7 mM KCl, pH 7.4).

Protein concentrations were determined *via* absorbance measurements at 280 nm with a NanoDrop 2000™ spectrophotometer (ThermoFisher Scientific Inc., USA) using the extinction coefficient of the respective protein at 280 nm. The mean value of at least three independent measurements was taken for concentration calculation.

VIS/NIR absorbance spectroscopy was conducted on a JASCO V-670 (Spectra Manager Software) using a 10 mm-path cuvette. Spectra were acquired using a scan speed of 1000 nm·min^{-1}, a data interval of 0.5 nm and a UV/vis and nIR bandwidth of 2 nm and 4 nm, respectively.
SWCNT concentration was estimated using the maximal absorbance at approx. 990 nm using the molar extinction coefficient determined by Schöppler *et al*.[1]

NIR fluorescence spectroscopy was conducted in glass-bottom 96-well plates *via* excitation at 561 nm using a gem-561 laser (LaserQuantum™, Germany) at 100 mW excitation power and fluorescence spectra were recorded in the range between 850 and 1250 nm using a Shamrock 193i spectrograph (Andor Technology Ltd., Belfast, Northern Ireland) coupled to an Olympus IX73 microscope and an exposure time of 1 s, a slit width of 500 µm and an Andor iDus InGaAs 491 array NIR detector

2D-excitation-emission maps were recorded in glass-bottom 96-well plates *via* excitation between 400 and 800 nm using a 300 W Xe-lamp guided through a monochromator (LOT, Germany) and detection between 850 and 1250 nm using a Shamrock 193i spectrograph (Andor Technology Ltd., Belfast, Northern Ireland) coupled to an Olympus IX73 microscope and an exposure time of 5 s, a slit width of 500 µm and an Andor iDus InGaAs 491 array NIR detector.

Atomic Force Microscopy (AFM) was conducted in intermittent-contact mode (scan rate = 0.5 Hz, 512 lines) using an Asylum Research MFP-3D Infinity® instrument equipped with rectangular cantilevers (Opus, MikroMasch Europe, Al-coating, tetrahedral tip, ν_{res} = 300 kHz, k = 26 N·m^{-1}). Freshly cleaved muscovite mica was incubated with a poly-L-lysine (PLL, 0.1 mg·mL^{-1}, 10 min) solution. After washing with MilliQ water, the coated mica was incubated with 10 µL of the sample solution for another 10 minutes followed by repeated washing of the surface with MilliQ water and drying using a N_2-stream before sample measurement.
Analysis of the acquired images was performed via the open-source software Gwyddion.

VIS-NIR-fluorescence microscopy was carried out under 561 nm-laser excitation (Cobolt Jive laser, Cobolt AB, Solna, Sweden, $P_{max.}$ = 500 mW) on an Olympus IX53 microscope equipped with a 100x oil-immersion objective (Olympus 100x UPLSAPO 100XS, NA = 1.35). Detection of the near-infrared photoluminescence was carried using a Xenics Cheetah-640-TE3 NIR camera (Xenics,

Heverlee, Belgium), while the VIS-fluorescence was detected with an Andor Zyla 5.5 sCMOS camera (Andor Technology Ltd., Belfast, Northern Ireland).

1.2. Chemical synthesis

1.2.1. 4-(*N*-maleimido)phenyldiazonium tetrafluoroborate (2)

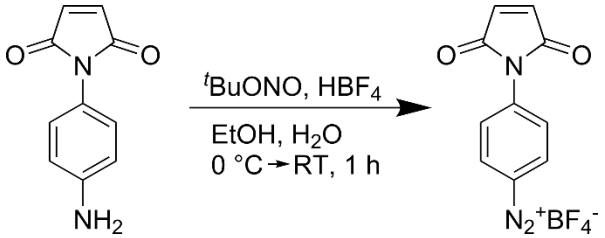

4-(*N*-Maleimido)phenyldiazonium tetrafluoroborate was synthesized using an optimized procedure based on the general procedure given in [2]. In a glass snap-cap vial, 4-(*N*-aminophenyl)maleimide (95.1 mg, 505 µmol, 1.0 eq.) was dissolved in ethanol (500 µL). Tetrafluoroboronic acid (50% aqueous solution, 125 µL, 175 mg, 996 µmol, 2.0 eq.) was added and the resulting red suspension was cooled to 0 °C in an ice/water bath. Under magnetic stirring, *tert*-butyl nitrite (135 µL, 117 mg, 1.13 mmol, 2.2 eq.) was added dropwise *via* syringe. The resulting greyish suspension was stirred for 1 h at room temperature. Diethyl ether (1 mL) was added and the resulting grey suspension was transferred to a polypropylene vial and centrifuged (2 min at 16100 g). The yellow supernatant was decanted off and the remaining solid was suspended in diethyl ether (1 mL). The centrifugation-decantation-suspension washing cycle was repeated three times before the resulting solid was dried under reduced pressure at room temperature to yield a slightly yellow solid.
While standard precautions were taken during synthesis and handling of the herein presented diazonium salts, no decomposition was observed even over several weeks.

^{1}H-NMR (300 MHz**, CD_3CN):** δ (ppm) = 8.54-8.60 (m, 2*H*, $H_{2,6}$), 8.09-8.15 (m, 2*H*, $H_{3,5}$), 7.08 (s, 2*H*, $H_{maleimide}$).

^{11}B-NMR (96 MHz**, CD_3CN):** δ (ppm) = −1.16 (s).

^{19}F-NMR (282 MHz**, CD_3CN):** δ (ppm) = −151.48 (s), −151.54 (s) (two signals due to the two NMR-active boron isotopomers).

^{13}C-NMR (75 MHz**, CD_3CN):** δ (ppm) = 169.4, 144.8, 136.5, 134.7, 127.4, 111.2.

The NMR data is in good agreement with literature data. [3]

HRMS (ESI (pos.) [*m/z*]**):** calculated ($C_{10}H_6N_3O_2$ [M^+]): 200.0455, found: 200.0448; calculated ($C_{10}H_6NO_2$ [$M-N_2$]$^+$): 172.0393, found: 172.0389; ($C_{11}H_{10}NO_3$ [$M-N_2$+MeOH]$^+$): 204.0645, found: 204.0655.

Fmoc-L-4-diazonium-phenylalanine tetrafluoroborate (6)

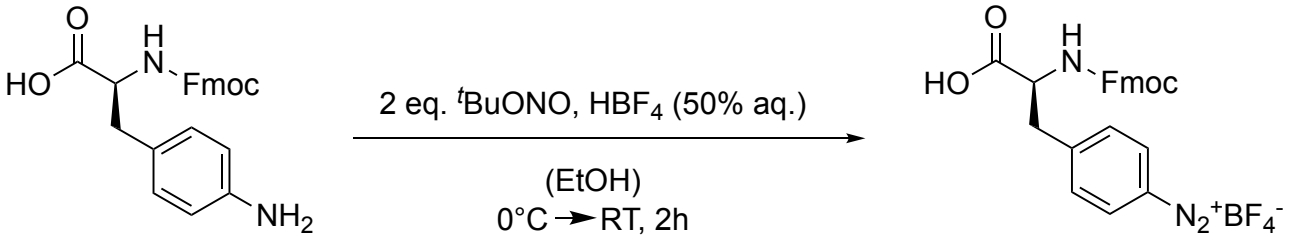

Fmoc-L-4-diazonium-phenylalanine tetrafluoroborate was synthesized using an optimized procedure based on the general procedure given in [2]. Fmoc-L-4-aminophenylalanine (0.2 g, 0.497 mmol) was dissolved in 500 µL ethanol in a 5 mL glass scintillation vial. Next, approx. 125 µL HBF_4 (50% aqueous,) were added dropwise. The solution was placed in an ice bath and stirred constantly while 135 µL ^{t}Bu-ONO (2 eq., 1.1 mmol, 117 mg) were added dropwise over the course of 30 min. Next, the solution was stirred for two hours at rt. After the reaction was completed, a white/slightly yellow precipitate was observed and transferred to a 2 mL Eppendorf tube using 1 mL diethyl ether. The precipitate was centrifuged at 16100g for five minutes and the supernatant discarded. This process was repeated five times and the crude product was dried under reduced pressure at room temperature.

While standard precautions were taken during synthesis and handling of the herein presented diazonium salts, no decomposition was observed even over several weeks.

^{1}H-NMR (300 MHz**, CD_3CN):** δ (ppm) = 8.35 (d, *J* = 8.5 Hz, 2H), 7.84 (d, *J* = 7.5 Hz, 2H), 7.76 (d, *J* = 8.4 Hz, 2H), 7.61 (dd, *J* = 7.5, 4.6 Hz, 2H), 7.43 (t, *J* = 7.5 Hz, 2H), 7.35 (t, *J* = 7.5 Hz, 2H), 6.13 (d, *J* = 8.7 Hz, 1H), 4.53 (s, 1H), 4.30 (d, *J* = 6.2 Hz, 2H), 4.18 (t, *J* = 6.8 Hz, 1H), 3.50 – 3.41 (m, 1H), 3.27 – 3.16 (m, 1H).

^{11}B-NMR (96 MHz**, CD_3CN):** δ (ppm) = −1.15 (s).

^{19}F-NMR (282 MHz**, CD_3CN):** δ (ppm) = −151.47 (s), −151.53 (s) (two signals due to the two NMR-active boron isotopomers).

HRMS (ESI (pos.) [*m/z*]**):** calculated ($C_{24}H_{21}NO_4$ $[M\text{-}N_2]^+$): 386.1392, found: 386.1387.

1.3. Carbon nanotube reactions

1.3.1.Synthesis of SWCNT*-Ph-Mal (3)

A (6,5)-chirality enriched SWCNT solution (**1,** 180 µL of a 10 nmol L^{-1} solution in 1% SDBS) was mixed with an aqueous solution of 4-(*N*-maleimido)phenyldiazonium tetrafluoroborate (**2,** 20 µL, 1 mmol L^{-1}) and irradiated in a 96-well plate using a Lumidox™ (Analytical Sales & Services, Inc., Flanders, NJ, USA) 96 green LED array with an LED current of 25 mA. After reaction control using nIR fluorescence spectroscopy, the reaction mixtures were transferred to spin filters (Vivaspin™ 500, MWCO = 100 kDa, *v* = 500 µL, Sartorius, Göttingen, Germany) and centrifuged (12000 g, RT, final volume = approx. 50 µL). The SWCNT* precipitated on the filter's membrane were washed with water (5× 450 µL), each time followed by a centrifugation step, and finally resuspended in a solution of the chosen surfactant (either 1% SDBS or 2 mg/mL 1,2-distearoyl-*sn*-glycero-3-phosphoethanolamine-N-[methoxy(polyethylene glycol)-5000] (ammonium salt) [PL-PEG5000]) by scraping off the filter and repeated pipetting. For redispersion, those suspensions were tip-sonicated (30% amplitude, 36 W, 5 min, 0 °C), centrifuged (16100g, 30 min) and the supernatant used for further studies.

1.3.2.Synthesis of SWCNT*-Ph-GBP (5)

1.3.2.1. Sequential reaction

A (6,5)-chirality enriched SWCNT solution (**1,** 180 µL of a 10 nmol L^{-1} solution in 1% SDBS) was mixed with an aqueous solution of 4-(*N*-maleimido)phenyldiazonium tetrafluoroborate (**2,** 20 µL, 1 mmol L^{-1}) and 6.4 µL of a 156 µM GBP-Nanobody (**4**, previously reduced on ice using TCEP [5 mM] for 30 minutes) solution in a 96-well plate. The mixed solution was irradiated using a Lumidox™ (Analytical Sales & Services, Inc., Flanders, NJ, USA) 96 green LED array with an LED current of 25 mA for 15 minutes followed by removal of the excess MalPh-Dz **2** using spin-filtration (300 kDa MWCO) and subsequent resuspension of the MalPh-SWCNT* **3** in 1x phosphate-buffered saline (PBS, pH 7.4). 500 eq. (~25 eq. with respect to introduced maleimides) of the nanobody **4** were added and the solution left shaking gently for 16 hours at room temperature. To remove excess unreacted nanobody, 300 kDa-MWCO spin filtration was carried out (5x washing with 1x PBS) followed by redispersion using PL-PEG5000 (2 mg·mL^{-1}).

1.3.2.2. One-step reaction

A (6,5)-chirality enriched SWCNT solution (**1,** 180 µL of a 10 nmol L^{-1} solution in 1% SDBS) was mixed with an aqueous solution of 4-(*N*-maleimido)phenyldiazonium tetrafluoroborate (**2,** 20 µL, 1 mmol L^{-1}) and 6.4 µL of a 156 µM GBP-Nanobody (**4**, previously reduced on ice using TCEP [5 mM] for 30 minutes) solution in a 96-well plate. The mixed solution was irradiated using a Lumidox™ (Analytical Sales & Services, Inc., Flanders, NJ, USA) 96 green LED array with an LED current of 25 mA for 30 minutes and subsequently transferred to a microcentrifuge tube and left shaking gently for 15 hours at room temperature. To remove excess unreacted nanobody, 300 kDa-MWCO spin filtration was carried out (5x washing with 1x PBS) followed by redispersion using PL-PEG5000 (2 mg·mL^{-1}).

1.3.3.Synthesis of SWCNT*-Phe-Fmoc (7)

To generate a SWCNT-SDBS dispersion (1% SDBS), 500 µL of an aqueous 2% SDBS solution were added to 500 µL of a 2 mg/mL SWCNT/water suspension. This solution was tip-sonicated for 15 minutes (Fisher Scientific™ Model 120 Sonic Dismembrator, 30% amplitude, 36 W) followed by centrifugation (2x, 16100g) and only the supernatant (top 80%) used for

further studies. In the next step, the supernatant was diluted using 1%SDBS to yield a 10 nM solution (**1,** see SWCNT concentration determination, section 1.1). In a 96well-plate, 180 µL of this solution were added to 15 wells followed by the addition of different concentrations of Fmoc-Phe-$N_2^+BF_4^-$ (**6**, 0 nM-100 µM). After careful mixing via repeating pipetting, the solutions were irradiated using a green 96-LED-array irradiator (Lumidox™, Analytical Sales & Services, Inc., Flanders, NJ, USA) at 25 mA for 15 minutes to yield solutions of **7**. The solutions were analyzed by nIR fluorescence spectroscopy for the degree of defect-introduction. The excess diazonium salt **6** was removed via repeated 300kDa-cut-off spin filtration (5x 600 µL ddH_2O washing) and the remaining SWCNT* were resuspended in 500 µL ddH_2O. In the last step, supernatant and pellet were then separated by centrifugation (16100g, 15 minutes) and the pellet containing SWCNT*-Phe-Fmoc **7** was used for downstream experiments.

1.3.4. Synthesis of SWCNT*-Phe-5(6)-CF (10)

The solutions of three wells from the Fmoc-Phe defect introduction process (v = 600 µL, approx. 5.4 pmol SWCNT*-Phe-Fmoc **7**) were added to a frit (20 µm pore size)-equipped syringe reactor (v = 2 mL), mixed with 1 mL EtOH for SWCNT precipitation and subsequent washing and removal of residual SDBS surfactant and excess Fmoc-Phe-Dz (5x 1 mL dH_2O, 3x DMF, 3x DCM, 3x DMF). Deprotection of the Fmoc-group was achieved via incubation with 200 µL of 20% piperidine/dimethylformamide (DMF, 2x 15 min). Excess reagents were removed by repeated washing with DMF/dichloromethane (DCM)/DMF (3x 1 mL). Subsequent amide coupling to 5(6)-carboxyfluorescein (CF) was carried out in the dark for 30 minutes at room temperature after the addition of 1.88 mg 5(6)-CF (5 µmol), 1.9 mg HATU (5 µmol) and 1.74 µL N,N-Diisopropylethylamine (DIPEA, 10 µmol) in 50 µL DMF. Excess reagents were removed by repeated washing with DMF/DCM/DMF (3x 1 mL). The crude product **10** was scraped off the frit using 50 µL DMF, transferred to a 1.5 mL microcentrifuge tube and centrifuged at 16100 g (15 min). The pellet was resuspended in 100 µL of a 1% SDBS solution and ultrasonicated (3 min, RT, 30% amplitude) followed by centrifugation (15 min, 16100g) and separation of pellet and supernatant. The latter was used for fluorescence microscopy and spectroscopy applications.

1.3.3 Synthesis of SWCNT*-Phe-R_6-CF (11)

The solutions of 20 wells from the Fmoc-Phe defect introduction process (v = 4 mL, approx. 36 pmol SWCNT*-Phe-Fmoc **7**) were pooled, mixed with 6 mL EtOH for SWCNT precipitation in a glass vial and the suspension subsequently transferred to a frit (20 µm pore size)-equipped syringe reactor (v = 2 mL). Residual SDBS surfactant and excess Fmoc-Phe-Dz were removed *via* washing (5x 1 mL dH_2O, 3x DMF, 3x DCM, 3x DMF). Deprotection of the Fmoc-group was achieved via incubation with 200 µL of 20% piperidine/DMF (2x 15 min). Fmoc-based solid-phase peptide synthesis (SPPS) couplings to Fmoc-Arg(Pbf)-OH (11.7 mg, 18 µmol) and 5(6)-CF (6.8 mg, 18 µmol) were carried out for 30 minutes at room temperature with 6.8 mg 1-[Bis(dimethylamino)methylene]-1*H*-1,2,3-triazolo[4,5-b]pyridinium 3-oxide hexafluorophosphate (HATU, 18 µmol) and 6.3 µL DIPEA (36 µmol) in 100 µL DMF. Excess reagents were removed by repeated washing with DMF/DCM/DMF (3x 1 mL). After 5(6)-CF coupling and washing, the side-chain protecting groups ((2,2,4,6,7-pentamethyldihydrobenzofuran-5-sulfonyl), Pbf) were cleaved upon gentle shaking with the cleavage cocktail (75% TFA/20% DCM/2.5% H_2O/2.5% TIS, v_{total} = 500 µL) for one hour. Subsequently, the crude product **5** was washed again with DMF and 10x DCM and then scraped off the frit using 100 µL H_2O, transferred to a 1.5 mL microcentrifuge tube and stored in the dark at 4°C. For fluorescence microscopy and spectroscopy applications, the product **11** in 100 µL H_2O was submitted to ultrasonication (5 min, 30% amp, 4°C) followed by separation of supernatant and pellet by centrifugation (16100g, 30 min). The supernatant was used for fluorescence microscopy and spectroscopy applications.

1.3.4 96-well synthesis of SWCNT*-Peptides

Approx. 30 pmol SWCNT*-Phe-Fmoc (c = 10 nM, V = 3 mL) were added to and filtered through individual wells of a 96-well plate equipped with 0.2 µm pore size filters (Chromafil Multi 96 plate with PTFE filters, Macherey-Nagel, Germany). The samples were washed (with 5x H_2O, 3x DMF, 3x DCM, 3x DMF)) followed by standard Fmoc/OtBu SPPS (2x15min Fmoc deprotection [20% Piperidine/DMF], 30min amino acid coupling [13.5 µmol amino acid/HATU, 27 µmol DIPEA]) and final deprotection of side-chain protecting groups using the deprotection cocktail (375 µL TFA, 100 µL DCM, 12.5 µL TIS, 12.5 µL H_2O, 60 min). All steps were carried out under mild agitation of the 96-well plate on a shaker (150 rpm). After final deprotection, the SWCNT samples were again washed (using 3xDCM, 3xDMF, 10xDCM) and then resuspended using 600 µL H_2O and transferred to 1.5 mL centrifuge tubes. Next, the samples were spun down (16100g, 30 min), resuspended in 200 µL 1% sodium deoxycholate (DOC) solution and submitted to tip-sonication (5 min, 4°C, 30% amplitude). After centrifugation, the top 80% of the supernatant were again transferred to fresh microcentrifuge tubes and used for absorbance/fluorescence spectroscopy applications.

The following Fmoc-protected amino acids were used:

Fmoc-Asn(Trt)-OH	Fmoc-Gly-OH	Fmoc-Tyr(tBu)-OH	Fmoc-Asp(OtBu)-OH
Fmoc-His(Trt)-OH	Fmoc-Gln(Trt)-OH	Fmoc-Ser(tBu)-OH	Fmoc-Glu(OtBu)-OH
Fmoc-Leu-OH	Fmoc-Lys(Boc)-OH	Fmoc-Val-OH	Fmoc-Phe-OH
Fmoc-Ile-OH	Fmoc-Ala-OH	Fmoc-Thr(tBu)-OH	

1.4 In vitro GFP-binding assay

Based on a previously created silicon master, patterned PDMS stamps were created. Next, a 2 µM GFP solution was added to the stamp, incubated for 10 minutes and the stamp subsequently rinsed with 1x PBS. In the next step, the PDMS stamp was transferred to a glass-bottom 96well-plate (previously coated with poly-L-lysine [0.1 mg mL^{-1}, 10 min] and incubated for 30 minutes followed by washing (1xPBS, 0.3% TritonX100, 3x). In the next step, the GFP-modified surface was passivated using a 5% w/v BSA solution (15 min) and subsequently washed again (1xPBS, 0.3% TritonX100, 3x). Finally, the conjugate **5** and its corresponding controls were added to the wells and incubated for 30 minutes, followed again by washing (1xPBS, 0.3% TritonX100, 3x) and addition of 200 µL of 1x PBS before imaging.

1.5 VIS/NIR fluorescence microscopy of SWCNT*-F-CF, SWCNT*-F-R_6-CF and the corresponding controls

Each 5 µL of the respective solutions were immobilized on a glass-coverslip *via* spin-coating (RT, 1000 rpm). Mounted on a glass-cover-slide, CF/nIR imaging was carried out on an Olympus IX53 microscope with a 100x oil-immersion objective (Olympus 100x UPLSAPO 100XS, NA=1.35) using 561 nm excitation by a Cobolt Jive™ laser (Cobolt AB, Solna, Sweden, 200 mW). CF fluorophores were excited by a xCite 120Q lamp (Excelitas Technologies, USA) using the lowest intensity/iris step. Detection of the near-infrared photoluminescence was carried using a Xenics® Cheetah SWIR camera (Xenics, Heverlee, Belgium, t_{int} = 1 s), whereas CF fluorescence was observed by an Andor Zyla 5.5 sCMOS camera (Andor Technology Ltd., Belfast, Northern Ireland, t_{int} = 0.1 s). Image overlay was conducted using a custom Python script.

1.6 VIS-fluorescence spectroscopy of SWCNT*-F-CF

The samples were diluted 200-fold to a final volume of 1000 µL and the fluorescence spectra recorded as described in section 1.1.

2. Results and Discussion

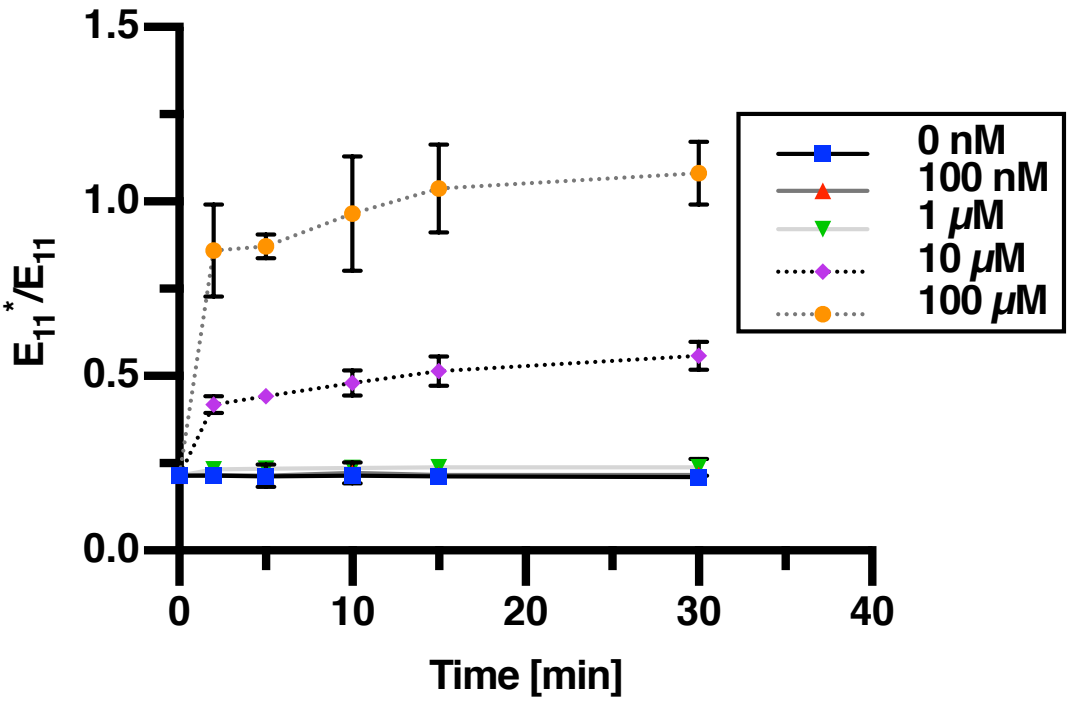

Figure S1. Evolution of the E_{11}^* emission peak over time when irradiated with a green 96-LED-array and different concentrations of MalPh diazonium salt **2** (*n* = 3, mean ± SD). The defect introduction was carried out in triplicates for each MalPh-Dz concentration in a 96-well plate following the procedure described in section 1.3.1. At the indicated time points (2, 5, 10, 15, 30 minutes) 30 µL aliquots were taken for NIR fluorescence measurement (see section 1.1).

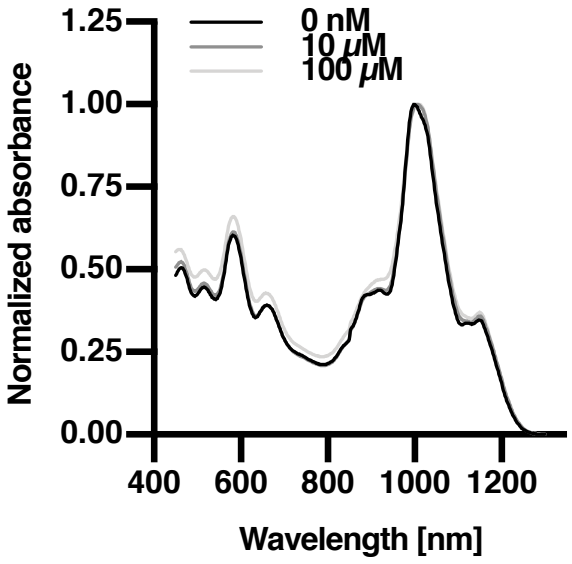

Figure S2. VIS/NIR absorbance spectroscopy of SDBS-dispersed SWCNTs before and after introduction of MalPh quantum defects [0, 10 and 100 µM MalPh-Dz **2** concentration].

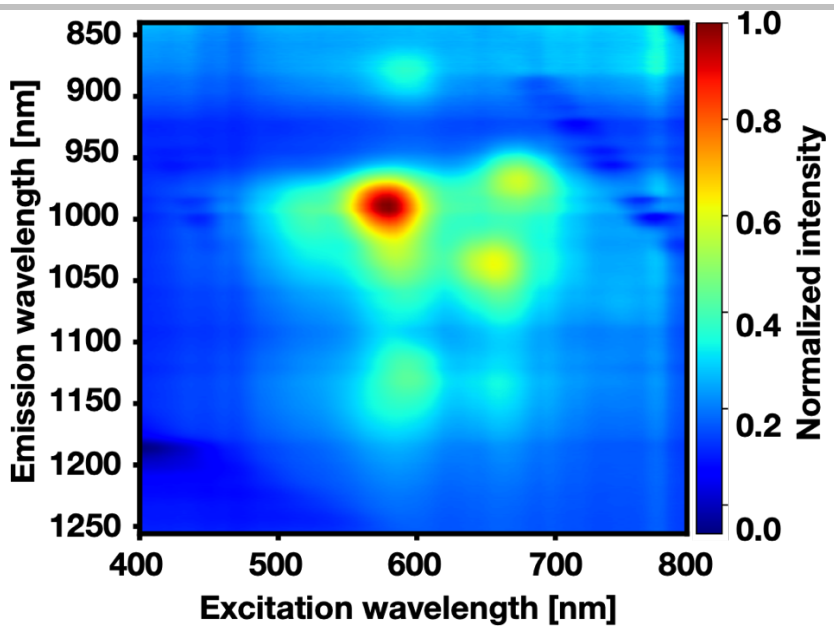

Figure S3. Excitation-emission map (2D spectrum) of SDBS-dispersed SWCNTs before introduction of MalPh quantum defects showing a major emission peak at approx. 1000 nm.

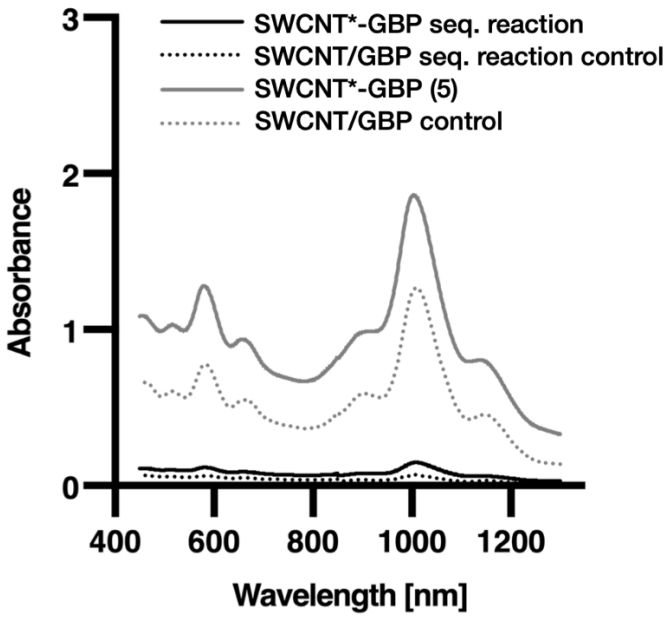

Figure S4. VIS/NIR absorbance spectroscopy of SWCNT*-GBP and the SWCNT/GBP control (comparing the sequential and the one-pot reaction) after removal of excess GBP using spin-filtration and redispersion in PL-PEG5000 of both positive and negative control of the GBP conjugation to SWCNTs. In contrast to the one-pot reaction (grey lines), redispersion of the samples originating from the sequential reactions did not lead to well-dispersed samples. The samples were prepared according to the procedures described in section 1.3.2 (for both controls without the addition of the MalPh diazonium salt and consequently without sp^3 defects).

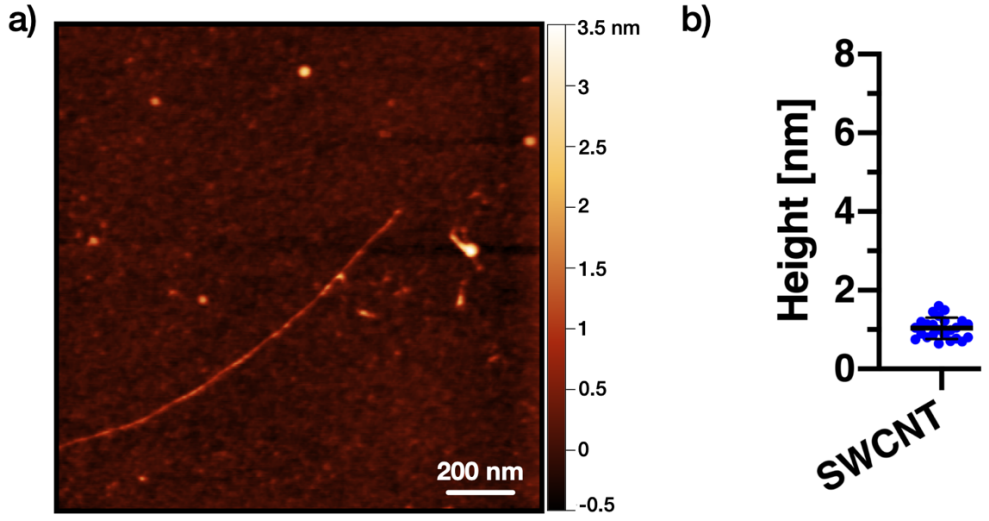

Figure S5. A) Representative atomic force microscopy image of a control SWCNT after following the same reaction steps as for conjugate **5** (one-step reaction, details see section 1.3.2.2) yet without the addition of MalPh-Dz **2** showing no conjugation of the nanobody. B) Measured heights of SWCNTs from the same control sample (mean ± SD, n = 24).

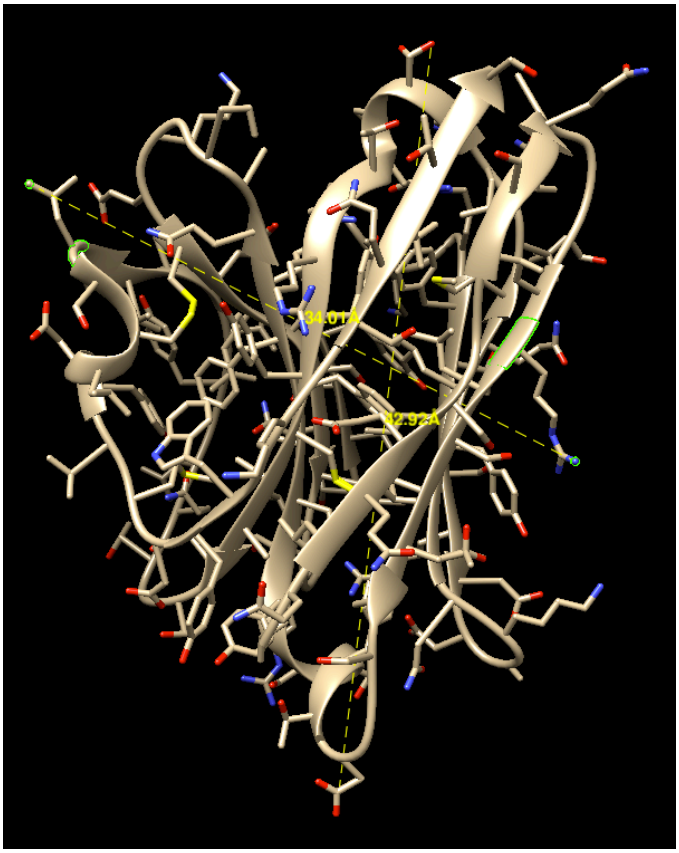

Figure S6. X-ray structure of a GFP-Minimizer nanobody (PDB: 3G9A) and distance measurements.

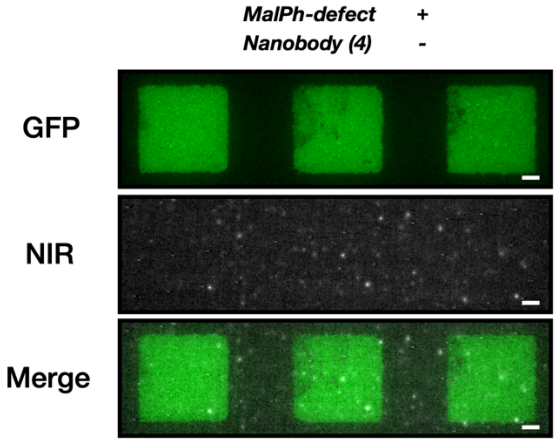

Figure S7. Control VIS/NIR fluorescence experiment with a microcontact-printed GFP-pattern incubated with MalPh-SWCNT* following the same procedure as described in section 1.4. The absence of colocalization in this experiment shows the importance of the nanobody for GFP-binding and rules out binding as a result from possibly unoccupied und unhydrolyzed MalPh groups on the SWCNT surface, that could be captured by GFP's thiols. Scale bars = 5 µm. The three columns are technical replicates.

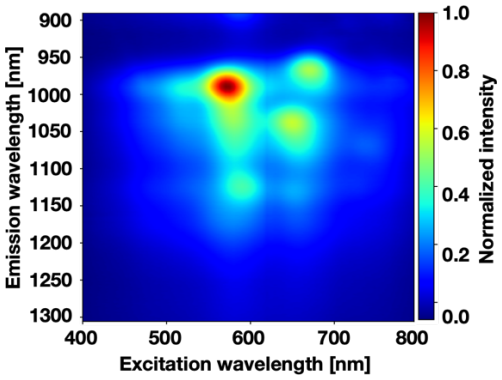

Figure S8. Excitation-emission map (2D spectrum) of a SWCNT/SDBS sample illuminated with green light for 15 minutes following the same procedure as for the synthesis of **7** (see section 1.3.3), but without the addition of Fmoc-Phe diazonium salt **6**.

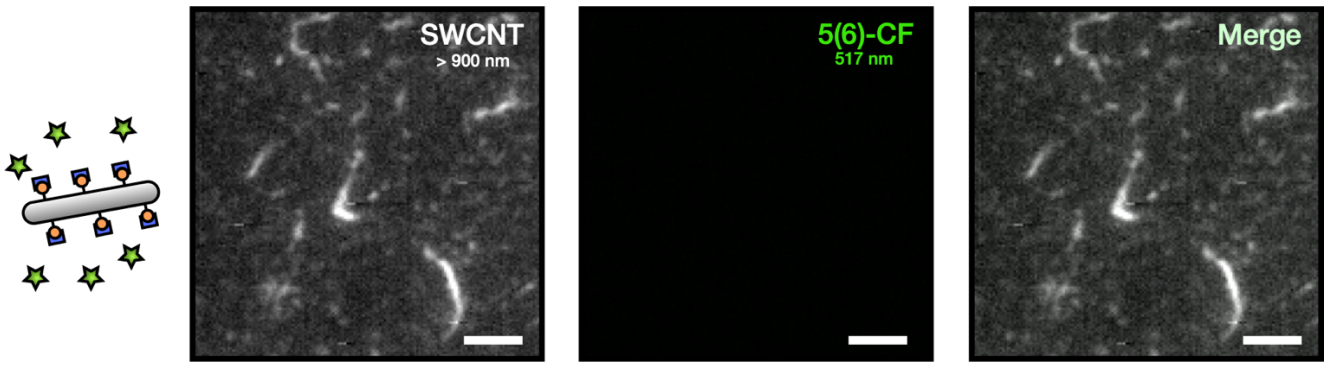

Figure S9. VIS/NIR fluorescence microscopy control experiment showing SWCNT*-F-Fmoc, that were treated using the same procedure as for the synthesis of **10** (see section 1.3.4) including the 5(6)-carboxyfluorescein coupling reaction, but without the Fmoc deprotection using 20% piperidine/DMF. After washing (see 1.3.4), they were immobilized on a glass surface and imaged. While they still show NIR fluorescence, no 5(6)-CF fluorescence can be observed and consequently no colocalization. Scale bars = 5 µm.

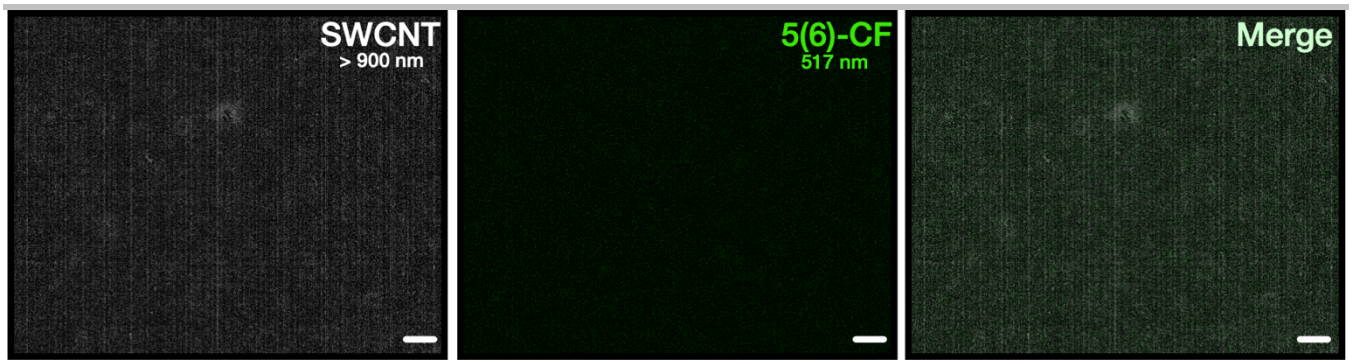

Figure S10. VIS/NIR fluorescence microscopy control experiment showing the SWCNT-R_6-CF control (without the addition of diazonium salt **6** and thus without F-Fmoc defects) after centrifugation and spin-coating on a glass coverslip showing neither carbon nanotube NIR-fluorescence nor CF fluorescence (scale bars = 10 µm).

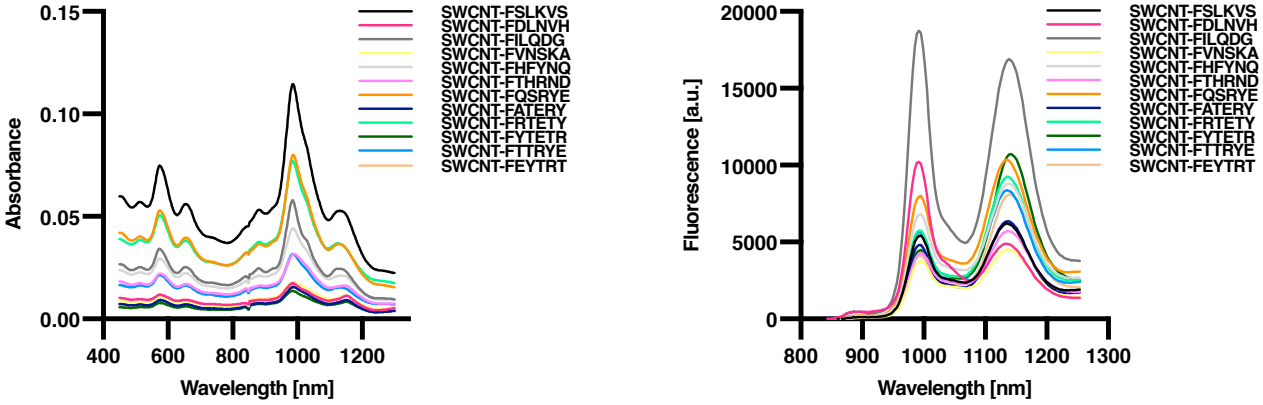

Figure S11. VIS/NIR absorbance and NIR fluorescence spectra of the SWCNT*-Peptides after redispersion using sodium deoxycholate (DOC). The absorbance intensity and thus also the absolute SWCNT concentrations are subject to variation due to small deviations in the tip-sonication process required for redispersion. For fluorescence measurements, the solutions were brought to the same SWCNT concentrations based on their absorbance at approx. 1000 nm (see section 1.1 for concentration determination).

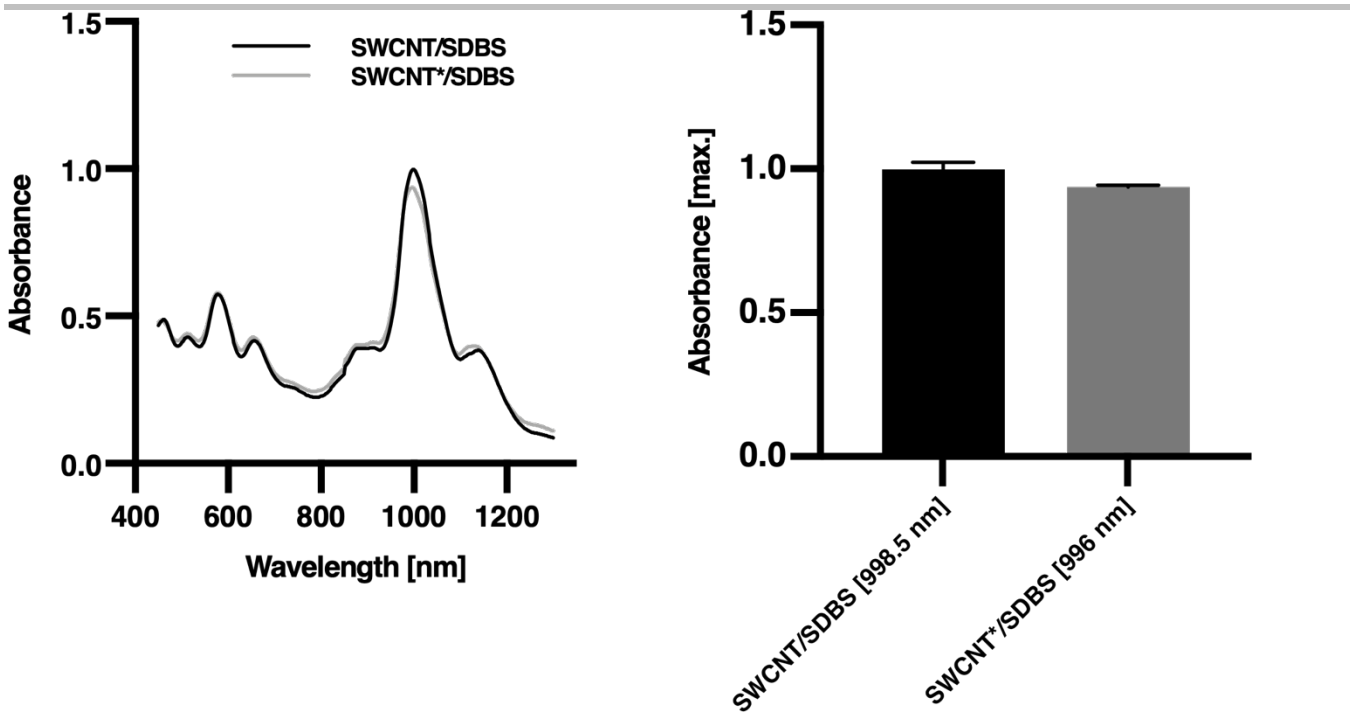

Figure S11. Absorbance spectra of a SWCNT/SDBS sample treated using green light for 15 minutes with (grey) and without the addition of diazonium salt **6** (black) measured in the supernatant after centrifugation (30 min, 16100g). Mean ± SD (*N* = 3).

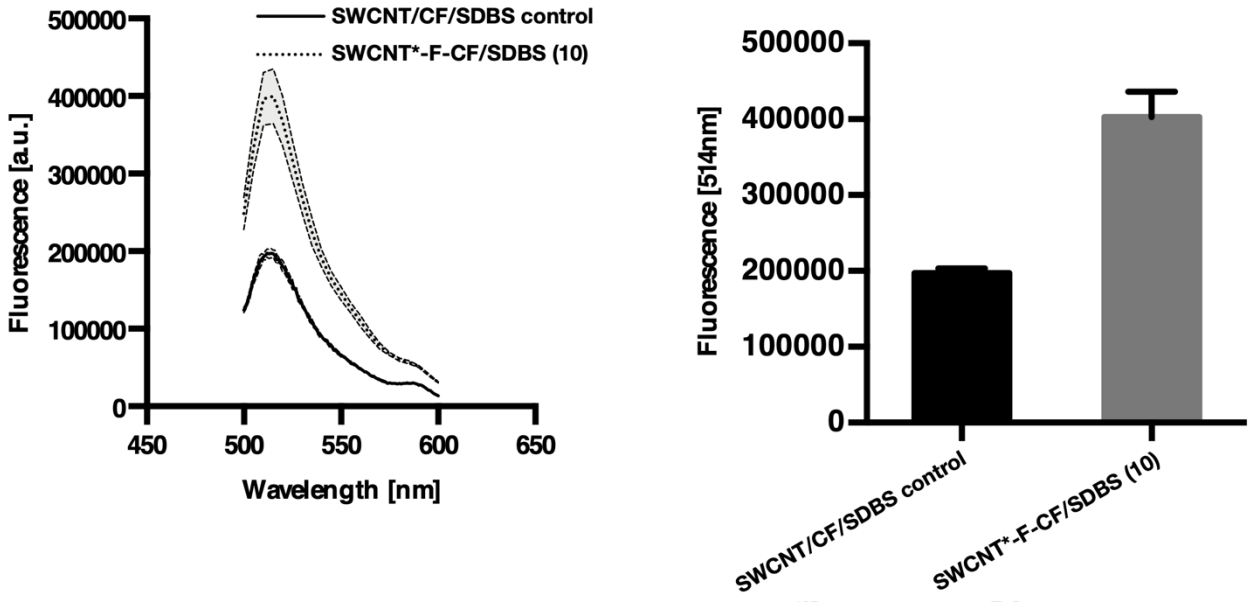

Figure S12. Fluorescence spectroscopy of positive and negative control samples for the conjugation of 5(6)-CF to SWCNT*-F-NH_2. The control was generated following the same procedure as for the synthesis of **10** (see section 1.3.4), yet without prior F-Fmoc defect introduction. Despite some degree of background fluorescence also in the control sample, which might arise from non-covalent adsorption to the hydrophobic SWCNT surface, the positive sample having the F-defect shows a significantly higher CF-fluorescence. Mean ± SD (*N* = 3).

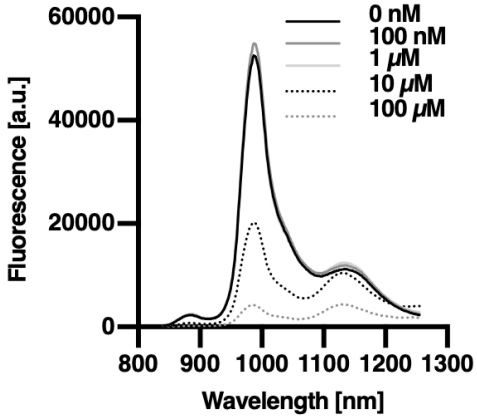

Figure S13. Absolute NIR fluorescence spectra of SWCNTs before and after introduction of MalPh defects with different concentrations of MalPh-Dz (15 minutes illumination time) showing the decrease of the E_{11} with increasing MalPh-Dz concentration.

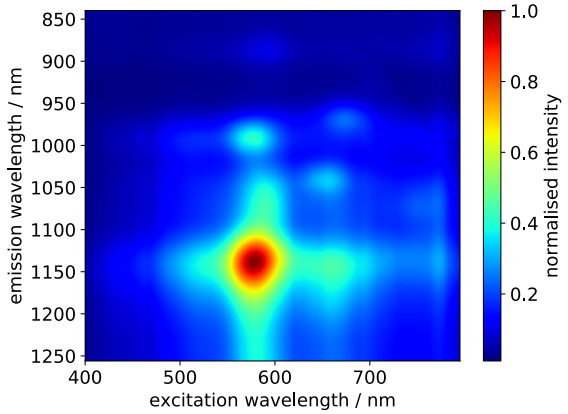

Figure S14. Excitation-emission map (2D spectrum) of a MalPh-SWCNT* sample after spin-filtration and redispersion using PL-PEG5000 following the process described in section 1.3.1.

3. References

[1] F. Schöppler, C. Mann, T.-C. Hain, F.-M. Neubauer, G. Privitera, F. Bonaccorso, D. Chu, A.-C. Ferrari, T. Hertel, *J. Phys. Chem. C* **2011**, 115, 14682-14686.

[2] K. Zhang, X.-H. Xu, F.L. Qing, *Eur. J. Org. Chem.* **2016**, *30*, 5088–5090.

[3] J.-C. Harper, R. Polsky, D.-R. Wheeler, S.-M. Brozik, *Langmuir* **2008**, *24*, 2206-2211.

4. Author Contributions

S.K. and F.A.M. designed and conceived the project. N.H. performed synthesis of the MalPh diazonium salt, NMR/MS analysis, initial experiments and optimized the conditions for MalPh-defect incorporation. F.A.M. performed AFM experiments, synthesized the Fmoc-Phe diazonium salt with N.H., optimized the conditions for Fmoc-Phe defect incorporation, performed the nanobody conjugation and validation experiments, synthesized multi-color SWCNTs, SWCNT-R_6 and performed the 96-well SWCNT-Peptide synthesis as well as the subsequent characterization. F.O. provided the GFP-binding nanobody. F.A.M., N.H. and S.K wrote the manuscript with input from F.O.

5. NMR spectra of diazonium salts 2 and 6

5.1. 4-(*N*-maleimido)phenyldiazonium tetrafluoroborate (2)

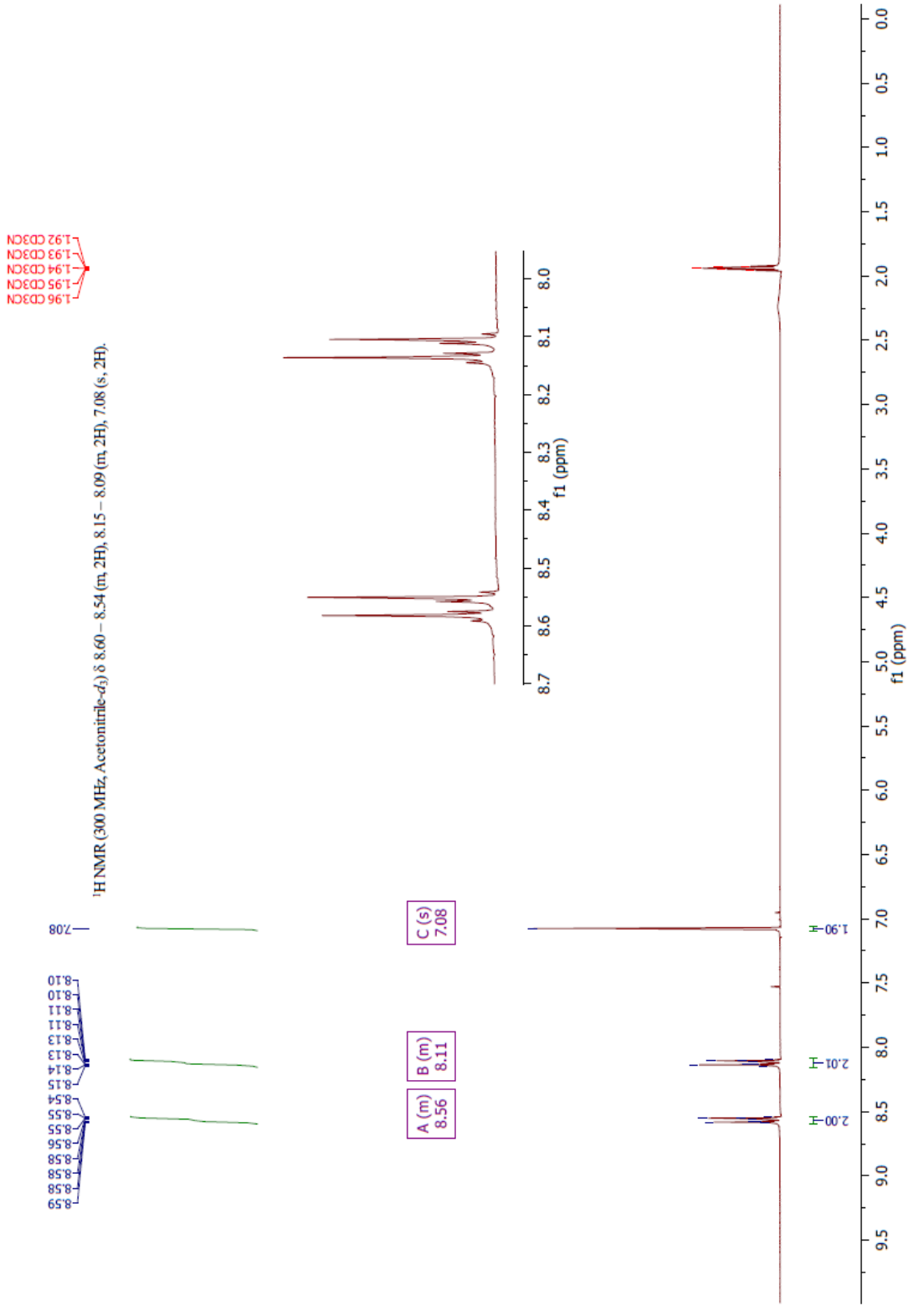

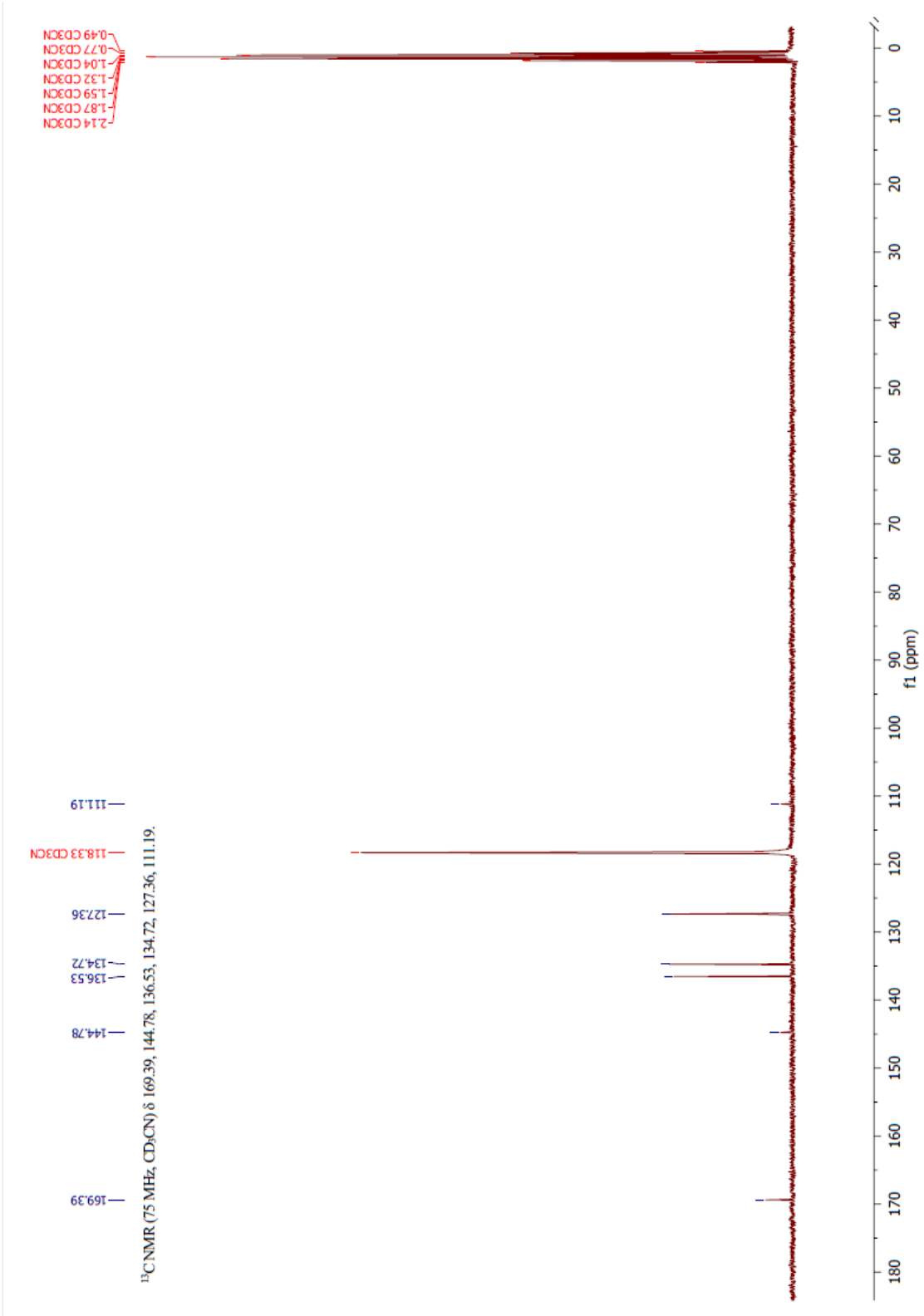
0.49 CD3CN
0.77 CD3CN
1.04 CD3CN
1.32 CD3CN
1.59 CD3CN
1.87 CD3CN
2.14 CD3CN
111.19
118.33 CD3CN
127.36
134.72
136.53
144.78
169.39
f1 (ppm)
^{13}C NMR (75 MHz, CD$_3$CN) δ 169.39, 144.78, 136.53, 134.72, 127.36, 111.19.

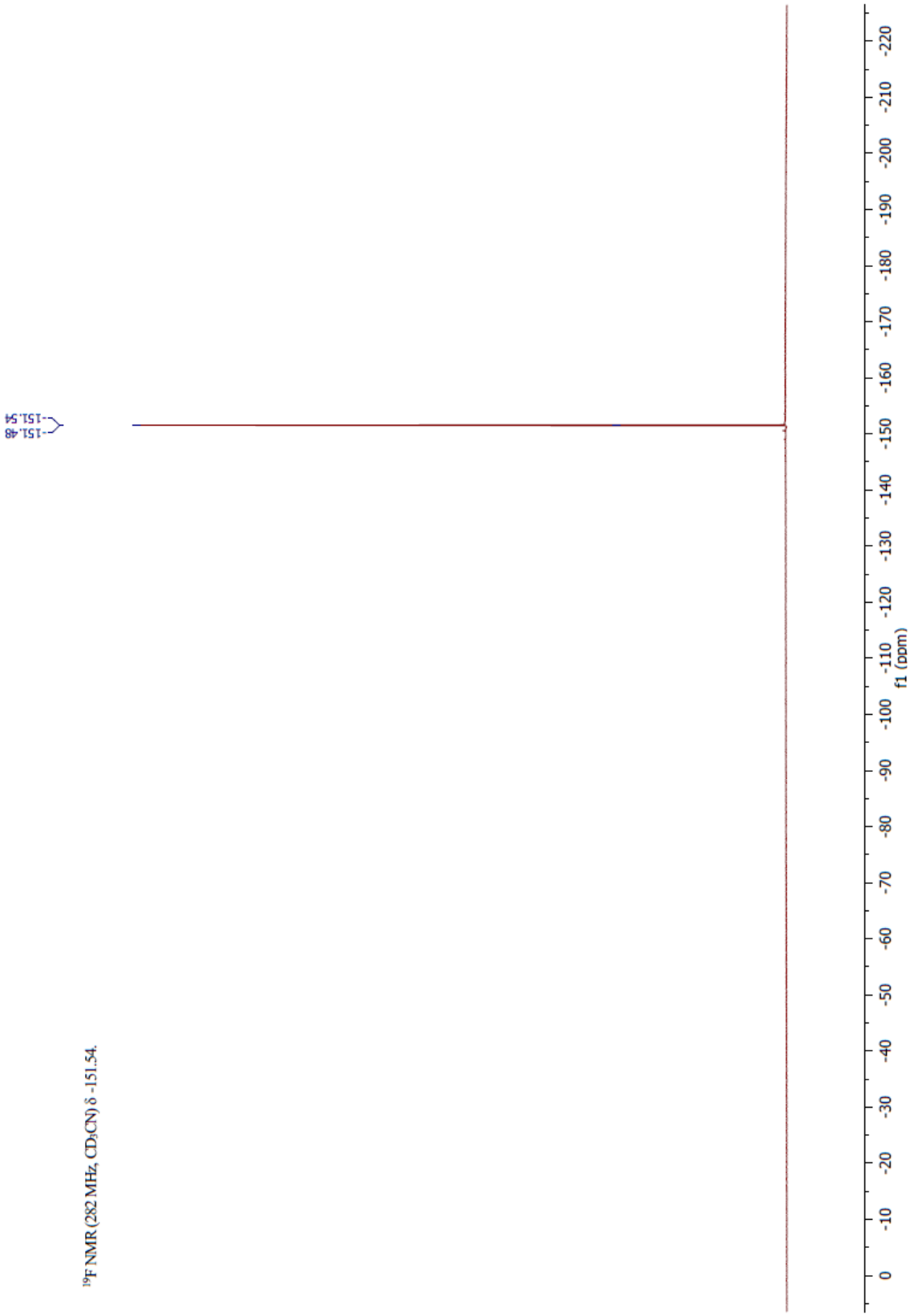

^{19}F NMR (282 MHz, CD_3CN) δ -151.54.

132

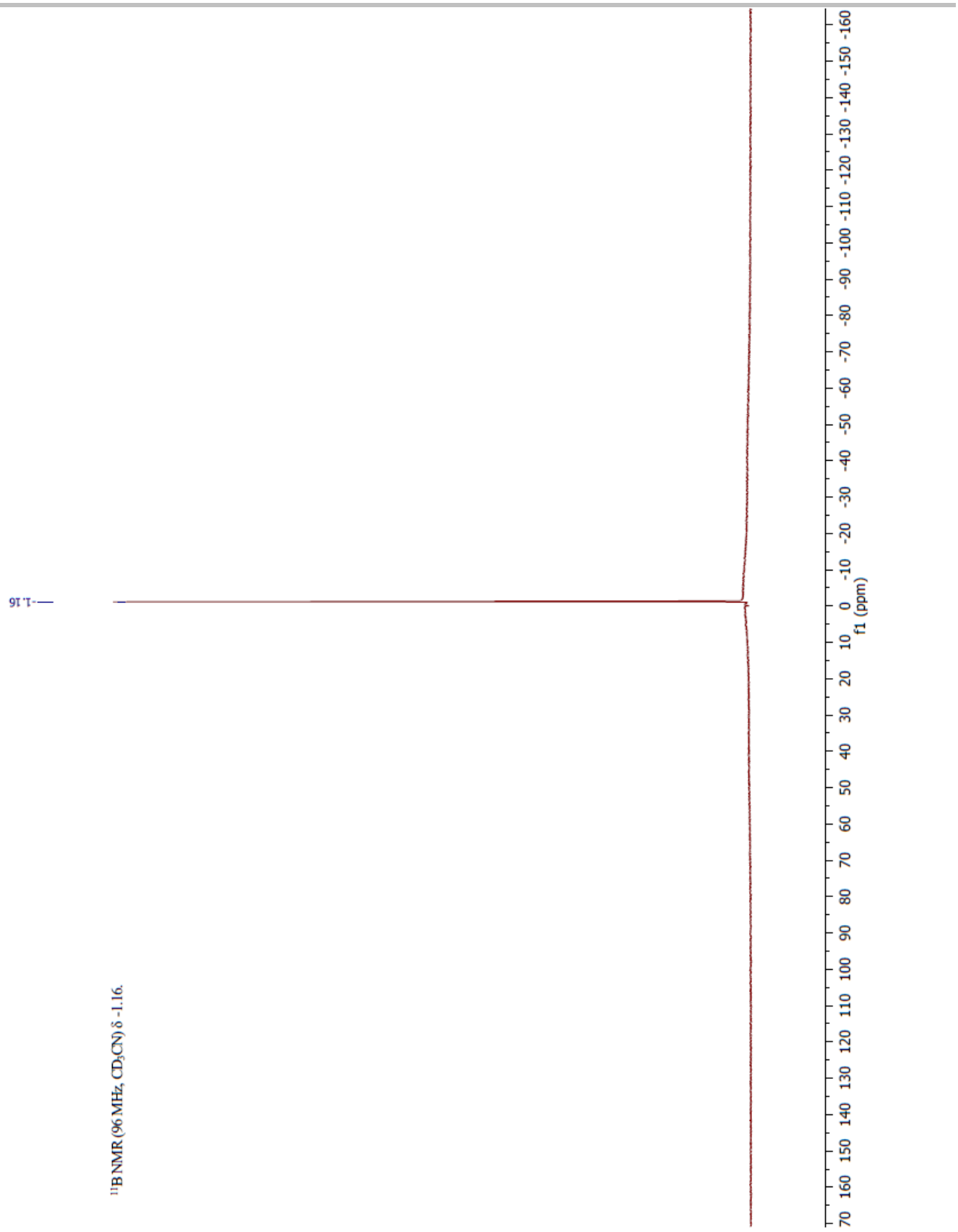
-1.16
f1 (ppm)
70 60 50 40 30 20 10 0 -10 -20 -30 -40 -50 -60 -70 -80 -90 -100 -110 -120 -130 -140 -150 -160
^{11}B NMR (96 MHz, CD_3CN) δ -1.16.

5.2. Fmoc-L-4-diazonium-phenylalanine tetrafluoroborate (6)

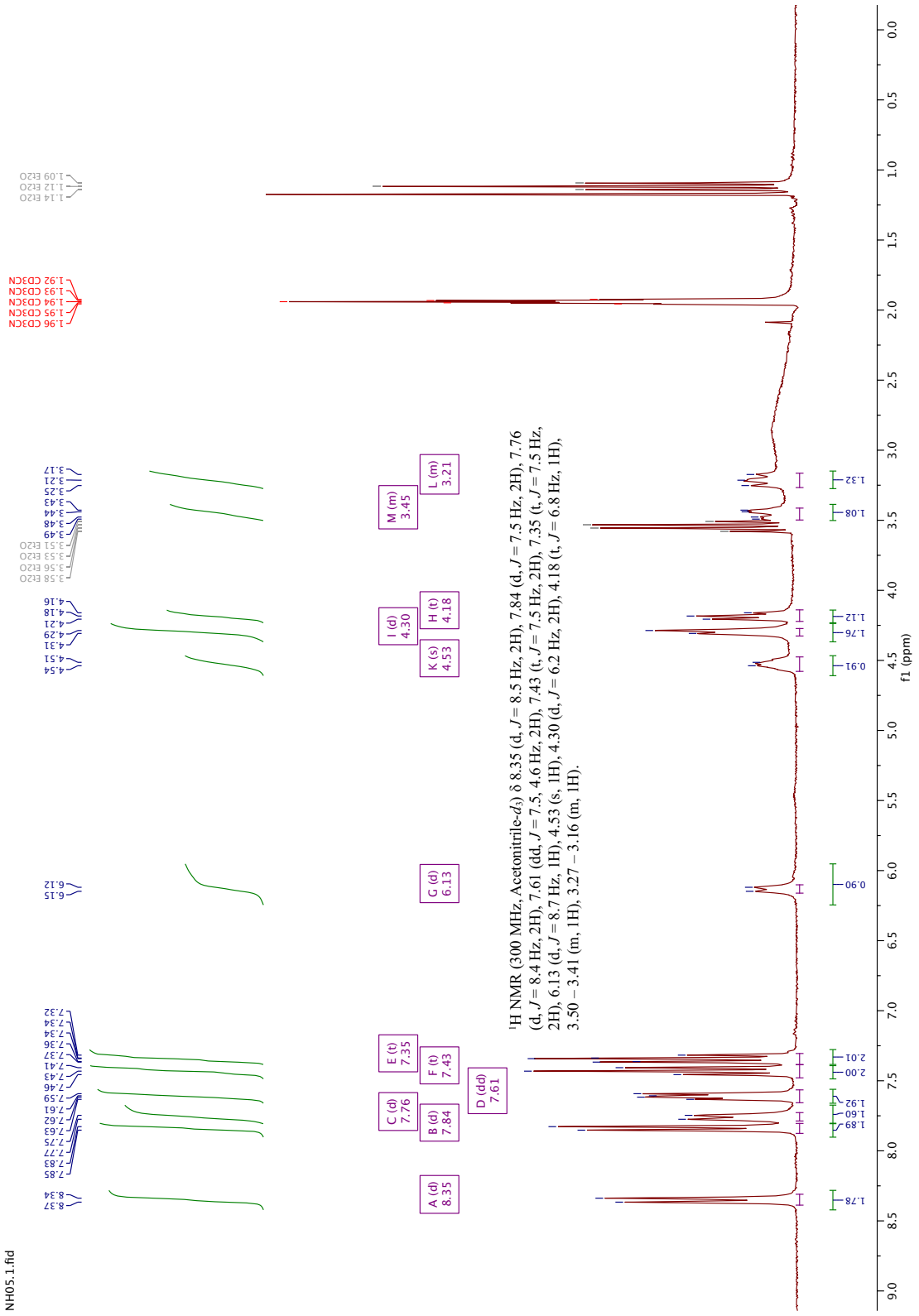

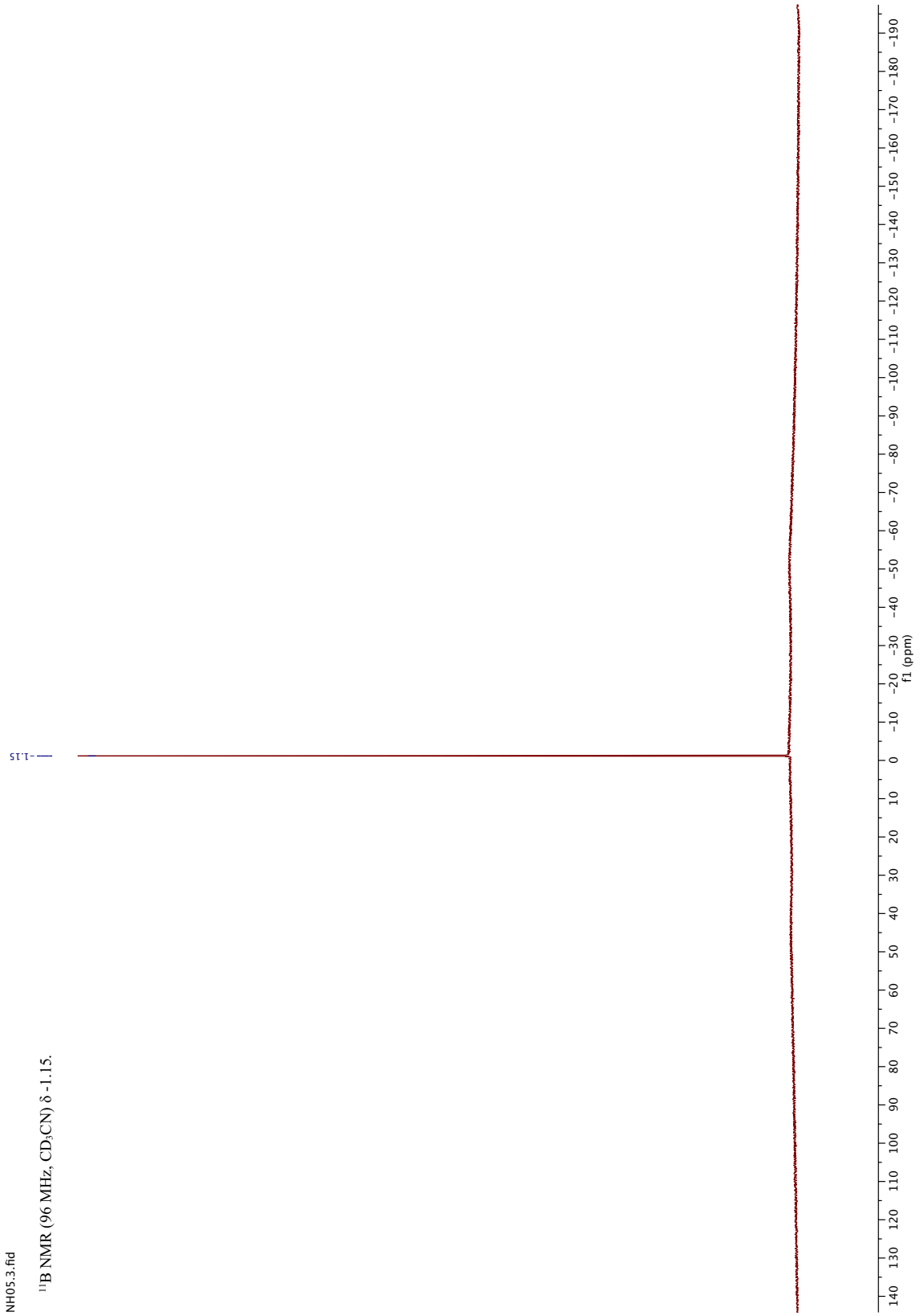

135

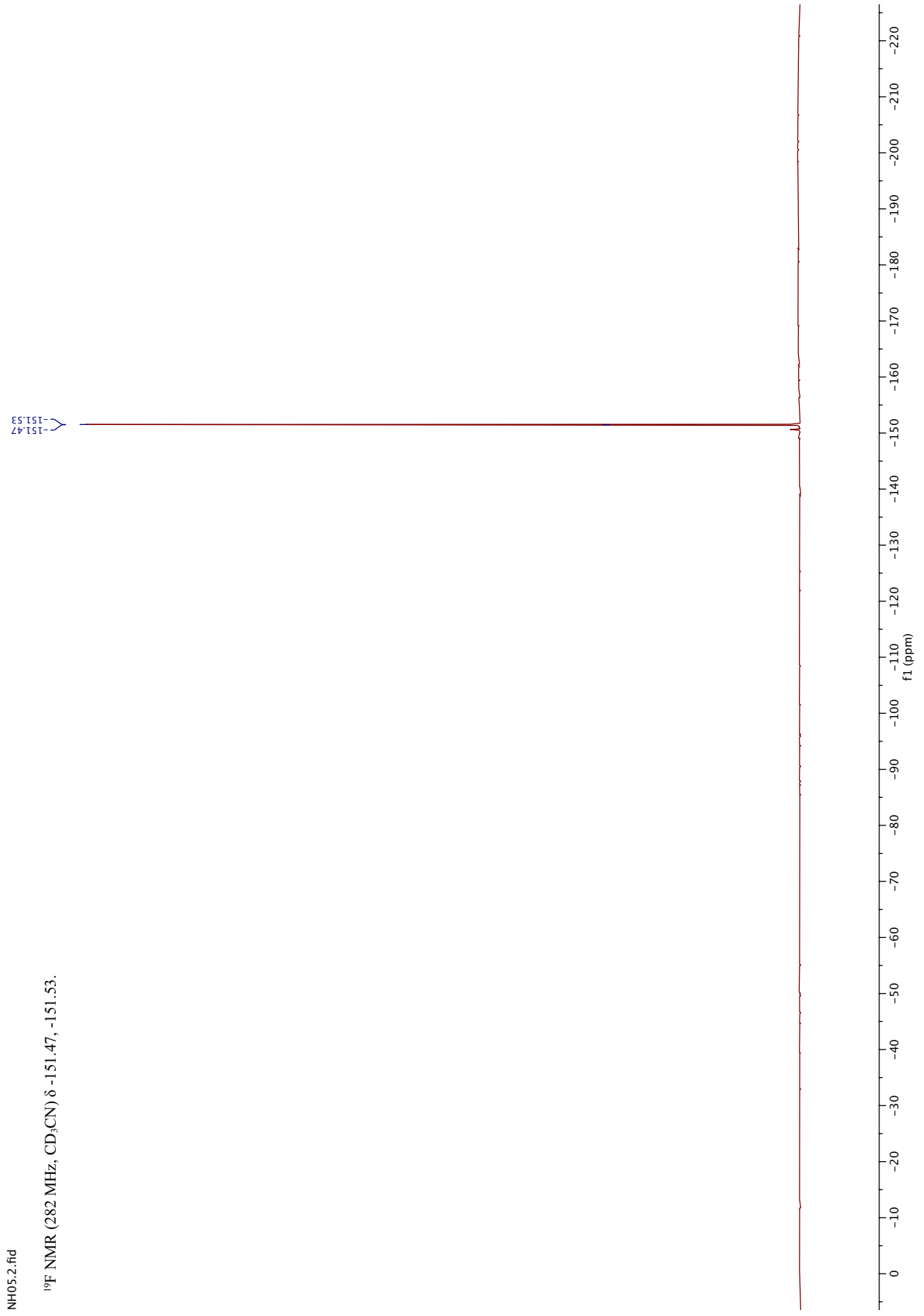

NH05.2.fid

^{19}F NMR (282 MHz, CD_3CN) δ -151.47, -151.53.

136

4.4.2. Discussion

The covalent decoration of carbon nanotubes with preserved NIR fluorescence is a goal that was thought to be impossible to reach for a long time since the discovery of carbon nanotubes in 1991.[9] In 2017, however, Setaro et al. made use of a [2+1] cycloaddition of electron-poor aromatic nitrenes to the π-conjugated carbon network.[53] After a rehybridization step, the SWCNT's π-conjugation is thought to be reestablished preserving the optoelectronic properties. Setaro et al. used this technique to create AuNP-functionalized and spiropyran-switchable SWCNTs. The latter were also applied later by Godin et al. as photoswitchable nanotubes in NIR super-resolution microscopy.[201] In 2020, Chio et al. used the same [2+1] cycloaddition for the attachment of a -$(PEG)_2$-biotin as well as an amine, a thiol and the amino acids glycine.[200] They then wrapped these modified SWCNTs with different surfactants corresponding to previously created SWCNT-based optical sensors such as $(GT)_{15}$/$(GT)_6$ DNA oligos (for dopamine[5,202]), DPPE-PEG5000 (for fibrinogen[50]) and a C_{16}-PEG2000-ceramide phospholipid (for insulin[203]) and evaluated changes in the sensor response induced by the covalent modifications. The authors observed a decrease in sensor performance for the dopamine sensors after covalent modification and retained performance in case of the phospholipid-based fibrinogen and insulin sensors. Furthermore, they also used the attached biotin for neutravidin-binding, which they verified by retention on neutravidin-modified beads as well as using AFM.
These examples are a large step forward in the field of SWCNT functionalization, however, they did not accomplish covalent attachment of fluorophores or biomolecules yet. In this work, two novel quantum defects are used for the covalent attachment of 5(6)-carboxyfluorescein (5(6)-CF), peptides and a protein. This technique has a few important advantages:

1. The modularity of the approach allows installation of anchors and their subsequent modification with any molecule of choice.

2. The red-shifted emission allows for deeper tissue penetration using 990 nm instead of 560 nm excitation.

3. The 96-well setup for both defect introduction as well as peptide synthesis makes large-scale parallel processing possible

Building on top of these points, this work utilizes the strengths of this modular technique for the attachment of GFP-binding nanobodies. Fig. 3 (p. 109) shows the nanobod-

ies covalently attached to SWCNTs in AFM and their retained GFP-binding ability in a fluorescence colocalization assay. This represents the first covalent conjugation of a nanobody to SWCNTs and the first covalent conjugation of a protein in general to SWCNTs with preserved optoelectronic properties. The Fmoc-protected phenylalanine defect was used for the attachment of 5(6)-CF generating multi-color SWCNTs showing fluorescence not only at 990 nm, but also at 517 nm and at 1135 nm. Combining three emission wavelengths in just one molecule/material can open up many possibilities in e.g. microscopy or multiplexed sensing. Furthermore, this defect can also serve as a starting point for peptide growth directly on the nanotube's sidewall. In this case, the nanotube can be compared to the resin used commonly in SPPS, yet with a drastically reduced size and thus increased accessible surface area. This feature was used not only for the attachment of a positively charged R_6 peptide, but also for the growth 0.2 μm filters (see Fig. 5c, p. 111). This, again also represent the first time, where carbon nanotubes were used as a template for peptide synthesis and also the first NIR fluorescent SWCNT-Peptide conjugates. In addition, the modification with these peptides composed of different amino acids also modulates the SWCNT's NIR fluorescence and here especially the E_{11}^*/E_{11} ratio. A comparison of the different peptides and their amino acid building blocks indicates, that more hydrophobic residues yield a decreased E_{11}^*/E_{11} ratio, which could be due to different folding of the peptides on the nanotube's surface and consequently an altered electronic landscape surrounding the trapped exciton. Effects of differently substituted diazonium salts or differently folded peptides on the SWCNT's fluorescence were also observed before by other authors.[41,204]

The two new functional quantum defects could in the future be used e.g. to create targeted NIR fluorophores for *in vivo* applications, which could be especially interesting when combined with the approach reported lately by Danné et al., who used C_6F_{13}-defects to brighten ultrashort SWCNTs below 100 nm in length.[43] If these ultrashort tubes could now be covalently functionalized in a way enabling targeting e.g. using antibodies, their decreased size would allow labelling of sites, that would not be accessible to longer SWCNTs (e.g. intracellular compartments). Furthermore, the covalent attachment of recognition units could also lead to new, more stable optical sensors, that can be developed using the parallel processing showed in Fig. 5c (p. 111). Taken together, these results show, that it is not only possible to use these two novel quantum defects for the modification of the SWCNT's chemical and surface properties, but also to tailor their NIR emission.

5 | Conclusion and Outlook

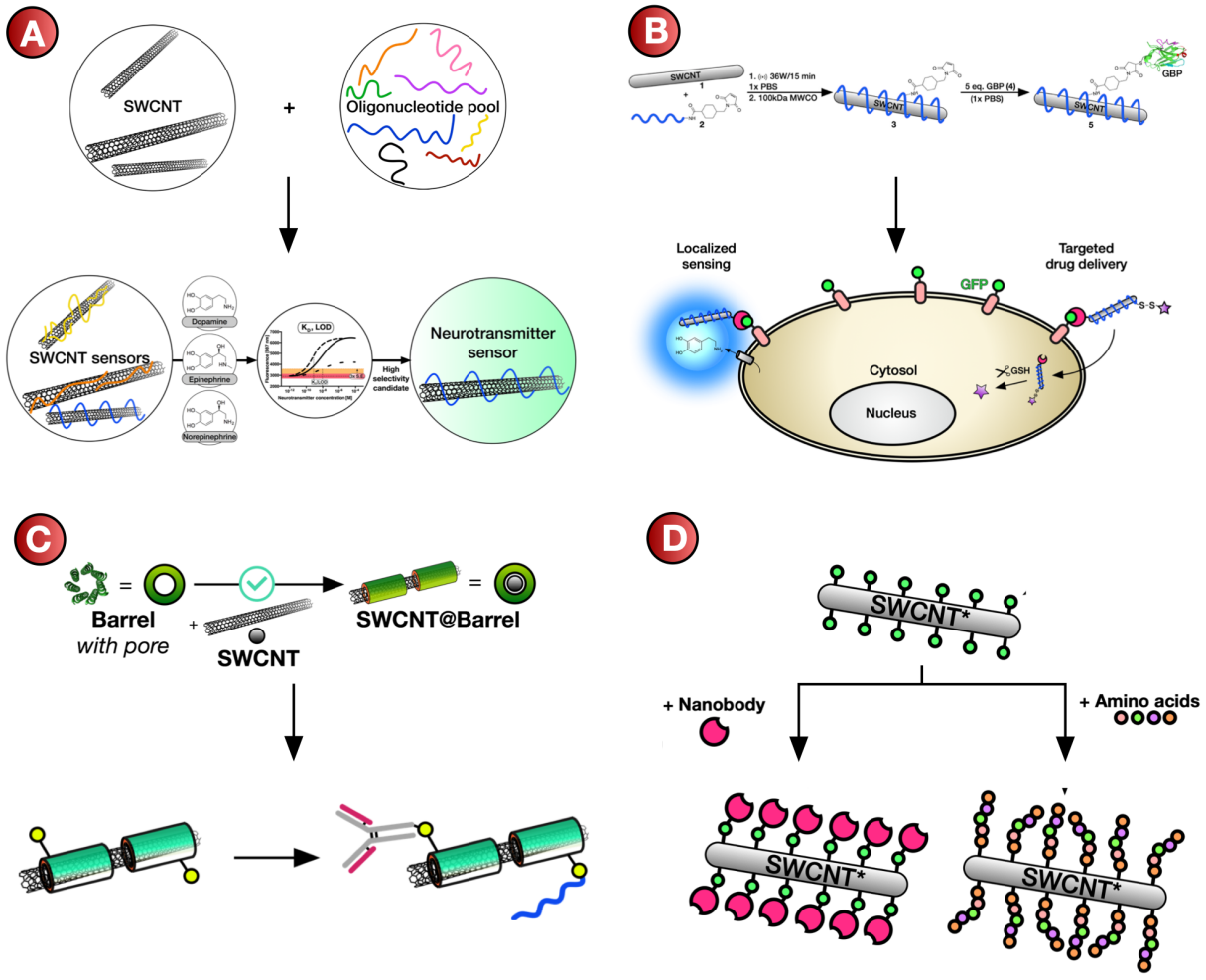

Figure 5.1.: **Overview on different parts of the thesis.** A) Competitive detection of the neurotransmitter dopamine after screening of a nanosensor pool. B) Generation of nanotube-nanobody conjugates for targeted delivery of dopamine sensors and NIR-immunolabeling. C) Encapsulation of SWCNT using α-helical peptide barrels to generate a functionalization platform. D) Use of quantum defects for covalent SWCNT-Nanobioconjugates.

Aging societies lead to an increased need for improved diagnosis and therapy options for more and more diseases. Nanoparticle-based systems have been proven to be effective in both diagnosis and therapy settings, but still face several problems regarding especially sensitivity, selectivity, stability or spatiotemporal resolution. Especially these characteristics of nanoparticle-based systems should be tackled within this thesis to find solutions with the focus on NIR-fluorescent SWCNTs.
In order to improve SWCNT-based systems, this thesis spans over different areas from generation and tuning of biosensors (Fig. 5.1 A) over targeting using small antibodies (Fig. 5.1 B) to different novel methodologies, that can now be applied as platform technologies for the fast and straightforward development of new nanosized devices (Fig. 5.1 C/D). This chapter provides an overview over the achievements of this thesis and an outlook on the next steps of research for more advanced SWCNT-based diagnosis and therapy systems.

5.1 Competitive detection of the neurotransmitter dopamine

In this work, ten different short, single-stranded DNA sequences were screened for their ability to wrap SWCNTs in a way allowing the detection of the neurotransmitter dopamine. As a first step, the ten different SWCNT/DNA hybrids generated *via* tip-sonication were characterized using NIR absorbance showing the same features, but different dispersion capabilities of the different oligonucleotides leading to different SWCNT concentrations. After concentration adjustment, the NIR fluorescence of the different samples was measured before and after addition of different concentrations of the neurotransmitter dopamine and its structural analogues epinephrine and norepinephrine. Already in this limited set of different SWCNT/DNA hybrids differences were observed in the response towards these structurally similar molecules, which only differ in one additional hydroxy or methyl group and are also not resolvable by other established techniques (see section 4.1.2). These differences also manifested in the dissociation constants determined from calibration curves as well as in the limits of detection. While e.g. $(GT)_{10}$ showed a large fluorescence increase upon dopamine addition (100 nM), $(GA)_{15}$ did not respond at this concentration. This was also observed in NIR fluorescence microscopy and the SWCNT/$(GT)_{10}$ hybrid even allowed detection of dopamine in the presence of equimolar amounts of norepinephrine. Taken together,

these results show, that it is possible to achieve discrimination between structurally similar neurotransmitters already using a small set of different oligonucleotides. This can be and is already very useful for (ongoing) studies in the Kruss lab with cultured mouse neurons, that can be stimulated for dopamine release. To achieve even better discrimination, a next step would be to increase the size of the oligonucleotide pool incorporating different nucleotide compositions and oligonucleotide lengths. By this, it should be possible to further enhance sensitivity and selectivity. Combined with the ease of use, especially when compared with genetically encoded sensors, this SWCNT/DNA based technique can find widespread use also in *in vivo* settings.

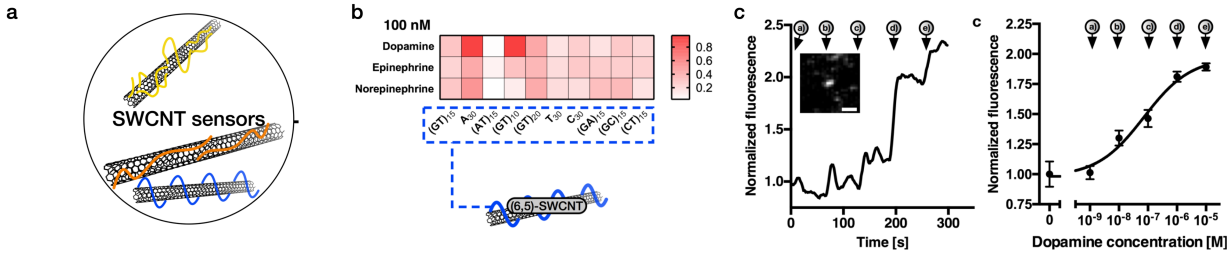

Figure 5.2.: **Competitive detection of dopamine.** a) SWCNT/DNA nanosensor pool. b) Difference between the different SWCNT/DNA hybrids with respect to their fluorescence change upon addition of the neurotransmitters dopamine, epinephrine and norepinephrine (100 nM). c) NIR microscopy of a single SWCNT/$(GT)_{10}$ sensor and its response towards different concentrations of dopamine [for details see section 4.1.1]

5.2 Targeting of nanosensors using nanobodies

In this part, GFP-binding nanobodies were attached to a $(GT)_{20}$ DNA-oligonucleotide wrapping a SWCNT in order to impart selective binding of its antigen. GFP is a proof-of-concept, but very versatile antigen as it widely used as a fusion protein in transgenic organisms for fluorescence detection. The decoration of SWCNTs with the GBP now allows targeting of these fusion proteins and co-staining in the NIR with enhanced signal-noise-ratio.

In order to achieve conjugation, a 3'-amine modified $(GT)_{20}$ oligonucleotide was used for SWCNT dispersion, which was modified in the next step using the heterobifunctional linker Sulfo-SMCC allowing for oriented attachment of the ectopic cysteine's thiol of the nanobody. After characterization and reaction control using UV/vis/NIR absorbance spectroscopy, NIR fluorescence spectroscopy, SDS-PAGE, AFM and ζ-potential measure-

ments, the SWCNT/$(GT)_{20}$-GBP conjugate was tested for retained function in a vis/NIR microscopy colocalization assay. Next, the conjugate was evaluated regarding its capability to detect dopamine even in this GFP-bound state. The observed retained fluorescence increase upon addition of 100 nM or 1 µM dopamine paves the way for the use of these targeted sensors also for the targeting of other locations e.g. in *in vivo* applications using GFP-fusion proteins or nanobodies directed against other functional targets such as dopamine transporters. With these promising *in vitro* results in hand, the Nanotube-Nanobody conjugate was applied next to *drosophila* embryos expressing Kinesin-5 as a GFP-fusion protein *via* microinjection. Here, the protein was bound by the SWCNT/$(GT)_{20}$-GBP conjugate enabling NIR-immunostaining for imaging of the spindle apparatus as well as tracking of single molecular motors inside this living organism. The latter also allowed estimation of Kinesin-5's velocity and its MSD for the first time *in vivo*.

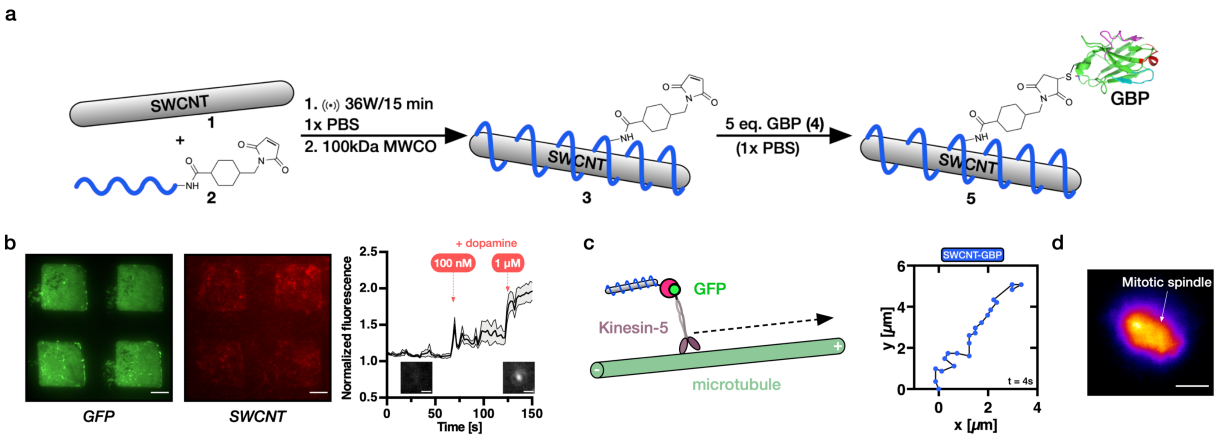

Figure 5.3.: **Targeted dopamine sensors.** a) Conjugation of a GFP-binding nanobody to a DNA-wrapped SWCNT. b) Targeting of micro-printed GFP structures by the SWCNT/DNA-Nanobody and subsequent detection of dopamine. c) Tracking of a Kinesin motor protein *in vivo*. d) *In vivo* NIR immunostaining of the spindle apparatus.

Both the *in vitro* and *in vivo* applications show the potential of this approach. However, in order to carry out e.g. intracellular NIR immunofluorescence microscopy, the SWCNTs have to be shortened to approx. 50 nm in length. First studies on short SWCNTs conjugated to GBP have already been carried out, but have to be deepened in the future. Here, combination with quantum defects to create localized defect emission could be helpful to achieve PLQY suitable for microscopy applications. Furthermore, also other nanobodies against different, more relevant targets such as IgG will be conjugated in the future and evaluated regarding their capability to optically detect this antigen binding event.

First studies interrogating the vis/NIR fluorescence upon GFP-binding were inconclusive, however, they could be repeated using different nanobody/antigen pairs. A combination of short SWCNTs and nanobodies targeting e.g. cell surface receptors or intracellular targets could also pave the way for drug delivery applications. Lastly, for challenging applications it might be necessary to switch from this hybrid non-covalent/covalent conjugation approach to a solely covalent one in order to achieve an increased stability (see quantum defect conjugation).

5.3 Peptide barrels encapsulate SWCNTs

Next to DNA-oligonucleotides, which are widely used for SWCNT dispersion, peptides are an interesting class of biomolecules largely unexplored for this purpose in the past, although it theoretically offers a higher structural flexibility. In this work, α-helical coiled-coil peptide barrels (αHBs) were tested for their capability to encapsulate SWCNTs. For comparison, two peptide sequences with the same amino acid composition, but different quaternary structures (i.e. pore size) were evaluated for their SWCNT dispersion yield. NIR absorbance spectroscopy showed, that the peptide containing a 0.76 nm pore was able to bring substantially more SWCNTs into aqueous solution than the control tetrameric barrel with a smaller pore underlining the importance of the preformed 3D-structure. Additional experiments also showed a slight enrichment of diameter-matching chiralities. The fact, that no exclusive encapsulation of e.g. (6,5)-SWCNTs was observed, can be attributed to 'breathing' of the peptide barrels, which are able to adjust to larger or smaller SWCNT diameters to a certain extent. In future experiments, this chirality enrichment could be further advanced by carrying out repetitive cycles or combination with the aqueous two-phase extraction (ATPE).[205] Further structural analysis was carried out using intermittent-contact mode AFM indicating a mode of SWCNT/Peptide binding, where the SWCNT is 'inserted' into the heptameric αHB's pore. Additionally, heights regularly alternating between 'naked' (6,5)-SWCNTs and peptide-encapsulated (6,5)-SWCNTs were measured. This assembly could be attributed to either be driven by the helical pitch of the coiled-coil barrel or to be a result of the drying process during sample preparation ('dewetting'). These results show that it is possible to use αHBs with defined and known pore sizes for the straightforward encapsulation of SWCNTs and their dispersion in aqueous environments. Furthermore, the outwards-facing residues of these barrels (f-position, see section 2.3.2) can be used for the attachment of further

functional units and thus serve as a two-step functionalization platform consisting of first, SWCNT encapsulation and second, covalent attachment of e.g. a fluorophore to a f-position residue.

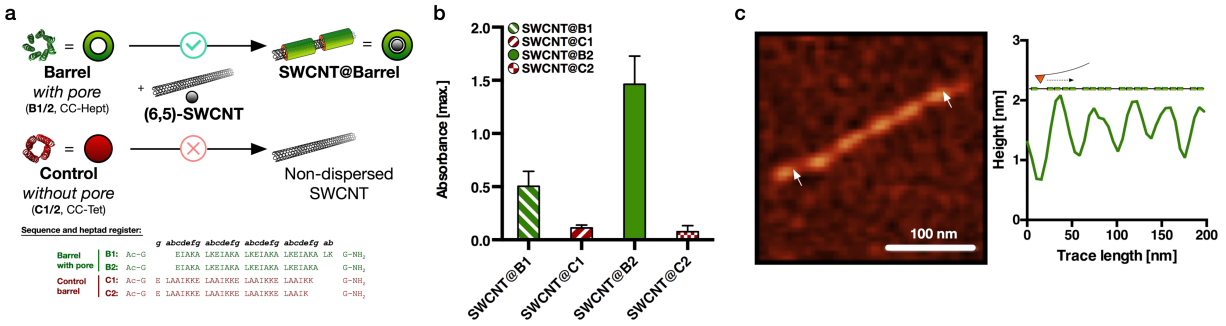

Figure 5.4.: **Peptide barrel encapsulated SWCNTs.** a) Barrels with a pore encapsulate matching SWCNTs whereas barrels without the pore do not disperse the same SWCNTs. b) Dispersion efficiency of different peptide barrels evaluated using UV/vis/NIR absorbance spectroscopy. c) AFM imaging of a barrel-encapsulated SWCNT showing periodic height differences.

However, for efficient conjugation reactions it is crucial to achieve colloidal stability high enough to render excess peptide in solution unnecessary. In order to achieve this goal, different strategies could be employed. First, the αHBs can be chemically altered generating e.g. oppositely charged ends leading to peptide nanotube (PNT) formation. This in turn could yield an increased SWCNT surface coverage and thus higher colloidal stability. While this attempt was already tested in first experiments, that also pointed towards increased, yet not sufficiently high colloidal stability, another strategy could be the synthesis of the coiled-coil monomers as C-terminal thioesters with N-terminal cysteines allowing for native-chemical ligation (NCL) to assemble PNTs selectively on the SWCNTs.

Furthermore, the alternating height pattern created by αHB encapsulation could be an interesting subject of further study. Here, it should be evaluated next, whether these structures can also be observed, when the AFM experiments are not carried out in air, but in a buffered solution. In addition, the structures generated with the repetitive height patterns could serve as an interesting tool for basic SWCNT photoluminescence investigations using tip-enhanced near-field optical microscopy.[206] Studies like these could reveal differences in photoluminescence arising from different SWCNT-regions covered or not covered by the αHB.

5.4 Quantum defects as anchors for covalent SWCNT-bioconjugates

Since their discovery in 1991, carbon nanotubes have been subject to a large variety of attempts to alter their chemical nature and tailor them for specific applications. While the majority of studies employed non-covalent functionalization, also different approaches for covalent functionalization were reported, however, almost all of them resulted in diminished NIR fluorescence. In order to make use of the superior stability of covalent conjugation yet still profit from the beneficial NIR emission, this project aimed at the use of previously reported aryl defects as anchors for covalent decoration of SWCNTs while maintaining their optoelectronic properties.
In a first step, two different diazonium salts containing on the one hand a phenylmaleimide and on the other hand a Fmoc-protected phenylalanine were synthesized in a one-step procedure. These phenyl diazonium salts were then used to incorporate sp^3-defects into the SWCNT's sidewall, that were previously described to create luminescent exciton traps (so-called quantum defects). After confirming successful defect introduction by NIR fluorescence spectroscopy, the maleimide defects were used for the attachment of a GFP-binding nanobody. Similar to the work described in section 4.2.1 the success of conjugation was tested using AFM and an *in vitro* binding assay relying on colocalization of GFP and NIR fluorescence. The protected phenylalanine defect on the other hand was used for the attachment of 5(6)-carboxyfluorescein yielding covalently linked three-color SWCNTs emitting light at 517 nm, 991 nm and 1135 nm. Furthermore, the Fmoc-protected phenylalanine residue can also serve as a starting point for peptide synthesis directly on the SWCNT's sidewall. This was tested and shown with a hydrophilic and fluorescently modified R_6 peptide as well as with twelve other peptide sequences, that were synthesized in parallel in a 96-well format. These different peptide sequences also showed the importance of the amino acid's hydrophobicity and their sequential arrangement for the modulation of the SWCNT's fluorescence. All in all, the results of this study show, that it is possible to use quantum defects for the covalent functionalization of SWCNTs while maintaining their optoelectronic properties. In addition to showing the feasibility of this approach, this also led to the first covalent and still NIR fluorescent SWCNT-fluorophore, SWCNT-peptide and SWCNT-protein conjugate described in the literature. With these tools in hand, demanding applications in biosensing or *in vivo* fluorescent tracing can become reality. If this technique is combined

e.g. with shorter SWCNTs, which were recently brightened up again through quantum defect incorporation, small yet powerful molecular devices are generated with possible applications in diagnostics or guided therapy. Furthermore, the high-throughput nature of this approach makes screening of e.g. different linker lengths or different peptides a very straightforward process leading to the fast generation of new biosensors, selective NIR imaging agents or fluorescent drug delivery vehicles.

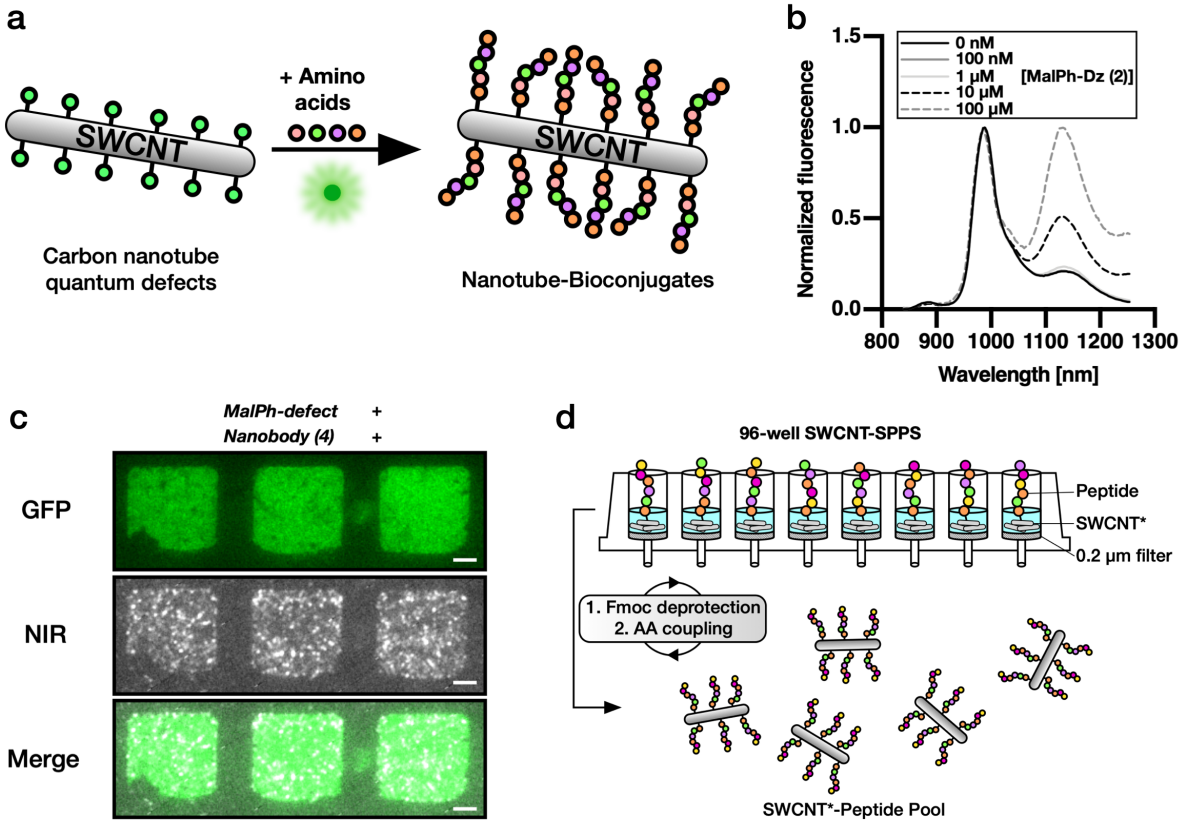

Figure 5.5.: **Quantum defects for covalent SWCNT functionalization.** a) Quantum defects can serve as anchors for the attachment of peptides or proteins to NIR-fluorescent SWCNTs. b) Red-shift of the SWCNT's fluorescence after defect introduction. c) Covalent SWCNT-Nanobody conjugates binding GFP as analyzed with Vis/NIR fluorescence microscopy. d) SWCNT-Phe-Fmoc defects allow SWCNT-based peptide synthesis in a 96-well format.

5.5 General overview

In summary, this work has not only contributed to the improved characterization of optical sensors for neurotransmitters, but also introduced new concepts for their functionalization.
Initially, SWCNT-DNA based sensors were characterized in detail regarding the DNA sequence-sensor relationship, thus enabling the competitive detection of the neurotransmitter dopamine in the presence of structurally similar analytes. Furthermore, these sensors were linked to nanobodies, which give the sensors targeting capabilities. As a consequence, it is now possible to place SWCNT-based optical sensors in the location where they should carry out their task. In the future, this may be used in *in vivo* analysis, for example, when the communication of neuronal cells by means of neurotransmitters is to be investigated in more detail.
In addition to these further developments on advanced NIR optical sensors, new basic concepts for the general functionalization of carbon nanotubes were developed. It was shown that pore-containing αHBs can encapsulate carbon nanotubes and thus stabilize them in aqueous solution. Due to the high variability of peptide structures, this could in the future not only represent another method for the purification of different nanotube chiralities, but also enable the versatile attachment of functional units to the outer surface of the peptide shell. Last but not least, so-called quantum defects have been chemically modified so that they can serve as anchor groups for the covalent attachment of functional biomolecules. Through this stable and modular combination, it is now possible to tune carbon nanotubes simultaneously with respect to their photophysics and functionality. In the future this could be used, for example, to generate stable NIR fluorescent probes that combine both diagnosis and therapy in one molecular device allowing operation in challenging environments such as e.g. the cytoplasm.
To sum up, the approaches for covalent and non-covalent functionalization of carbon nanotubes presented in this work not only provide new possibilities for tailoring their photophysics and surface chemistry, but also enable the production of targeted sensors and new tools for NIR fluorescence microscopy.

6 | Materials and Methods

6.1 General Information

6.1.1. Reagents and solvents

(6,5)-chirality enriched single-walled carbon nanotubes (SWCNT, Sigma Aldrich, Product No.: 773735) and H-Rink Amide-Chemmatrix® resin were acquired from Sigma Aldrich (Darmstadt, Germany). Larger diameter SWCNTs were purchased from PlasmaChem GmbH (LOT: SCNP-M135). Fmoc-protected amino acids were purchased from GL Biochem LTD (Shanghai, China). DIC and OxymaPure were purchased from Iris Biotech GmbH (Marktredwitz, Germany). DMF used for peptide synthesis was supplied by Fisher Scientific (Schwerte, Germany) and was of peptide grade quality. Acetonitrile used for HPLC was supplied by Fisher Scientific (Schwerte, Germany) with HPLC grade quality. All other reagents were supplied by Sigma Aldrich (Taufkirchen, Germany), Thermo Fisher Scientific (Langenselbold, Germany), VWR International (Darmstadt, Germany) and Carl Roth (Karlsruhe, Germany). All reagents were of synthesis grade quality and were used as supplied.

6.1.2. UV/vis/nIR absorbance spectroscopy

SWCNT-containing solutions were submitted to UV/vis/nIR absorbance spectroscopy on a JASCO V-670 (Spectra Manager Software) using a 10 mm-path cuvette. Spectra were acquired using a scan speed of 1000 nm/min, a data interval of 0.5 nm and a UV/vis and nIR bandwidth of 2 nm and 4 nm, respectively.
The SWCNT concentration was determined using the maximal absorbance at approx. 990 nm using the molar extinction coefficient determined by Schöppler et al.[207]

6.1.3. nIR fluorescence spectroscopy

In a 96-well plate, 50-100 μL of the SWCNT-containing solution were excited at 561 nm using a 300 W Xe-lamp guided through a monochromator (LOT, Germany) and their

fluorescence spectra recorded in the range between 850 and 1250 nm using a Shamrock 193i spectrograph (Andor Technology Ltd., Belfast, Northern Ireland) coupled to an Olympus IX73 microscope and an exposure time of 1 s, a slit width of 500 μm and an Andor iDus InGaAs 491 array NIR detector.

6.1.4. Atomic Force Microscopy (AFM)

20 μL of the SWCNT-containing dispersions were immobilized on freshly cleaved muscovite mica *via* ten minutes incubation and subsequent washing of the surface with MilliQ water. AFM images were acquired in intermittent contact mode using an Asylum Research MFP-3D Infinity® instrument equipped with Olympus AC-160-TS cantilevers. Analysis of the acquired images was performed via the open-source software Gwyddion. For all images, the background/tilt was removed via a 2nd order polynomial fit. The surface plane was set to zero using three-point leveling.

6.1.5. nIR fluorescence microscopy

nIR imaging was carried out under 561 nm-laser excitation (Cobolt Jive® laser, Cobolt AB, Solna, Sweden, $P_{max.}$ = 500 mW) on an Olympus IX53 microscope equipped with a 100x oil-immersion objective (Olympus 100x UPLSAPO 100XS, NA = 1.35). Detection of the near-infrared photoluminescence was carried using either a Xenics Xeva®-1.7-320 or a Xenics Cheetah®-640-TE3 NIR camera (Xenics, Heverlee, Belgium) or an Andor Zyla 5.5 sCMOS camera (Andor Technology Ltd., Belfast, Northern Ireland).

The optical setup for simultaneous vis/nIR imaging was planned and built together with Dr. Sebastian Kruss and Dr. Claudia Geisler as part of this thesis enabling simultaneous vis/NIR fluorescence imaging.

VIS/NIR-Setup
Version 2019-Sept-17
C. Geisler/F. A. Mann

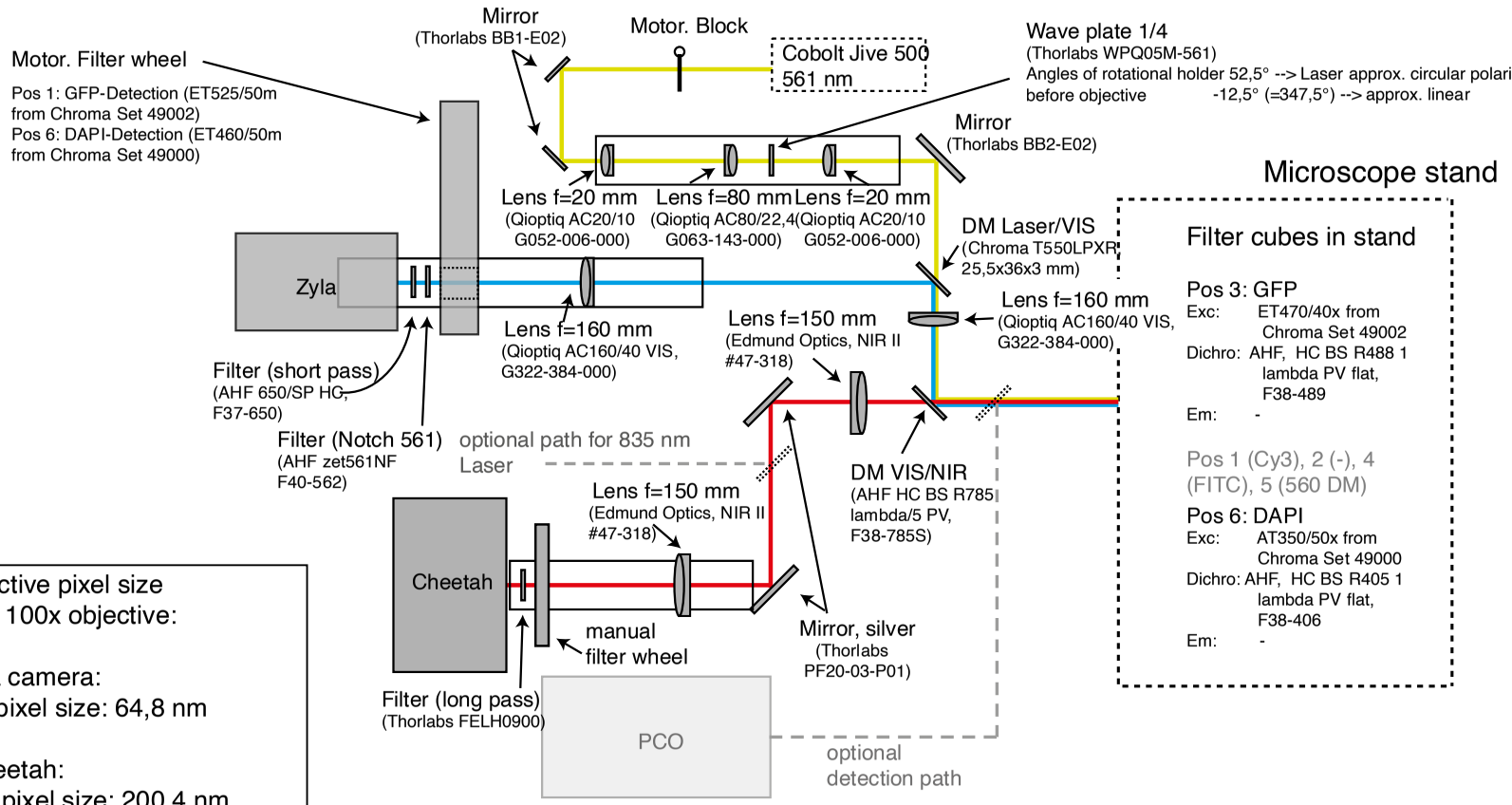

Effective pixel size
with 100x objective:

Zyla camera:
eff. pixel size: 64,8 nm

Cheetah:
eff. pixel size: 200,4 nm

(calibrated with BF illumination
and Thorlabs grid R1L3S3P
(10 μm line distance))

6.1.6. SDS-PAGE with Coomassie-/GelRed-Stain

The samples subjected to sodiumdodecylsulfate-polyacrylamide gel electrophoresis (SDS-PAGE) were mixed with the corresponding amount of 4x reducing Laemmli sample buffer to reach a final 1x concentration. SDS-PAGE was performed at 220 V/400 mA for 45 minutes in running buffer with 12% acrylamide gels using PageRuler Plus Prestained (life technologies) as a size marker. Staining of nucleic acids was carried out with the dye GelRed (Biotium Inc., USA) for 60 minutes after heating in the microwave and five subsequent washing steps using dH_2O. Staining of proteins was performed with a solution of Coomassie Brilliant Blue R-250 (Staining solution) for 15 minutes after heating in the microwave. Subsequent incubation with destaining solution for 10 minutes after microwave-heating was repeated three times. The destained gel was captured using a c300 imaging system (Cambridge Bioscience) both for protein (vis) and nucleic acid detection (UV).

Table 6.1.: Staining solution

EtOH	300 mL
MeCOOH	100 mL
Coomassie Brilliant Blue R-250	2.5 g
dH_2O	*ad* 1000 mL

Table 6.2.: Destaining solution

EtOH	500 mL
MeCOOH	100 mL
dH_2O	*ad* 1000 mL

Table 6.3.: Stacking buffer

Tris-base	4.84 g
dH_2O	*ad* 80 mL (pH 6.8 with HCl)

Table 6.4.: Resolving buffer

Tris-base	14.53 g
dH_2O	*ad* 80 mL (pH 8.8 with HCl)

Table 6.5.: 4x SDS sample buffer

0.5 M Tris-HCl, pH 6.8	5 mL
SDS	800 mg
Glycerol	4 mL
Bromophenol blue	2 mg
dH_2O	*ad* 10 mL

Table 6.6.: 4x red. SDS sample buffer

4x SDS sample buffer	5 mL
2-Mercaptoethanol	500 µL

Table 6.7.: Running buffer

Tris-base	- mL
Glycine	- mg
SDS	- mL
dH_2O	*ad* 2500 mL

Table 6.8.: 3x GelRed staining solution

EtOH	15 mL
MeCOOH	5 mL
GelRed (10000x)	12 µL
dH_2O	*ad* 50 mL

Table 6.9.: Gel composition

	Stacking gel	**Resolving gel**		
	4%	7.5%	12%	15%
dH_2O	2993 µL	4845 µL	3345 µL	2345 µL
30% Acrylamide/Bisacrylamide	667 µL	2500 µL	4000 µL	5000 µL
Stacking buffer	1260 µL	-	-	-
Resolving buffer	-	2500 µL	2500 µL	2500 µL
10% SDS	50 µL	100 µL	100 µL	100 µL
10% APS	25 µL	50 µL	50 µL	50 µL
TEMED	5 µL	5 µL	5 µL	5 µL
Total volume	5000 µL	10000 µL	10000 µL	10000 µL

6.1.7. ζ-potential measurement

ζ-potential measurements were carried out using a Zetasizer Nano S (Malvern Instruments, UK) in 1x PBS at a SWCNT concentration of 0.5 nM (pH 7.4). Analysis was performed using the corresponding Zetasizer software.

6.1.8. Circular dichroism (CD) spectroscopy

CD spectra and CD thermal-denaturation curves were recorded using a JASCO J-1500 which was equipped with a JASCO PTC510 temperature measuring unit. CD spectra were measured at 50 μM peptide concentration in PBS at 20 °C in 1 mm quartz cuvettes (Starna Scientific Ltd., UK) at 50 nm/min scanning speed. CD thermal-denaturation experiments were performed by heating from 2 to 98 °C at a heat rate of 60 °C/h. The CD signal at 222 nm was recorded at 0.1 °C intervals (1 nm interval, 1 nm bandwidth, 16 s response time). The midpoints of the thermal denaturation curves (Tm) were determined from the second derivative of the variable temperature slope.

6.1.9. Solid-phase peptide synthesis

Peptide amides were synthesized on a H-Rink Amide-Chemmatrix® resin on a 0.1 mmol scale on a Liberty Blue® CEM microwave-assisted peptide synthesizer. The synthesis was conducted via a standard Fmoc/^{t}Bu-protocol using DIC and OxymaPure as coupling reagents and a solution of piperidine in DMF (1:4) for Fmoc-removal. N-Acetylation of the peptides was carried out by equilibrating the peptide resin with 5 mL of acetic acid anhydride/pyridine (1:9) for 5 min at room temperature. Acidic cleavage from the resin was achieved by a treatment with a mixture of trifluoroacetic acid (TFA)/triisopropylsilane (TIS)/water (90:5:5, 3 h). The resin was extracted with additional TFA (5 mL), and the combined extracts were concentrated to a third of the initial volume under nitrogen flow. The crude peptide was then precipitated in cold diethylether (40 mL) and isolated by centrifugation and decantation of the supernatant. The precipitate was washed twice with ice-cold diethylether and subsequently dissolved in 5 mL of a 1:1 mixture of acetonitrile and water and then freeze-dried to give a fine white solid.

6.1.10. Semi-preparative high-performance liquid chromatography (HPLC)

Peptides were purified by semi-preparative reversed-phase HPLC using a JASCO chromatography system (pumps PU-2080 Plus, degasser DG-2080-53, detector MD-2010 Plus) at flow rates of 3 mL/min, and a Nucleodur 100-5-C18 ec (250 mm by 10 mm, 5 μm) reversed-phase column. Linear gradients of water and acetonitrile (buffer A: water, 0.1% TFA, buffer B: acetonitrile, 0.1% TFA) of 30-80% buffer B over 30 min for coiled-coil heptamers and 30-60% buffer B over 30 min for coiled-coil tetramers were used for purification. During purification the column was run at a controlled temperature of 60 °C. Chromatograms were recorded at 220 nm.

6.1.11. Analytical HPLC

Analytical HPLC measurements were performed using a JASCO chromatography system (pumps PU-2085 Plus, detector MD-2010 Plus, autosampler AS-2055 Plus) and a Nucleodur 100-5-C18 (5 μm, 4.6 x 250 mm) reversed-phase column at a flow rate of 1 ml/min. For peptide characterization a linear gradient of water and acetonitrile (buffer A: water, 0.1% TFA, buffer B: acetonitrile, 0.1% TFA) run from 30-80% buffer B over 20 min for coiled-coil heptamers and 30-60% buffer B over 20 min for coiled-coil tetramers was

used. Chromatograms were monitored at 220 nm wavelengths. The column was run at a controlled temperature of 60 °C.

6.1.12. Matrix-assisted laser desorption/ionization - time of flight mass spectrometry (MALDI-TOF-MS)

Peptides were characterized by mass spectrometry on a Bruker Autoflex Speed® MALDI-TOF mass spectrometer operating in positive-ion reflector mode. (matrix: α-cyano-4-hydroxycinnamic acid (CHCA), external calibration).

6.1.13. Nuclear magnetic resonance (NMR)

NMR spectroscopy was performed on a Bruker Avance™III HD 300 device (Bruker Corp., USA), equipped with a 5 mm probe. For a measurement, approx. 15 mg of substance were dissolved in approx. 600 μL of the deuterated solvent stated and transferred to a standard glass NMR tube (d = 5 mm). The chemical shifts are reported in ppm relative to the residual solvent peak(s). Analysis was performed within the MestReNova® 10 program.

6.1.14. Electrospray ionization time of flight mass spectrometry (ESI-TOF-MS)

Mass spectrometry measurements of diazonium salts were performed on a Bruker™micrOTOF ESI-TOF-MS using the non-deuterated form of the solvent also used for NMR measurements.

6.1.15. Protein concentration determination

Protein concentration was determined *via* absorbance measurements at 280 nm with a NanoDrop 2000™spectrophotometer (ThermoFisher Scientific Inc., USA) using the extinction coefficient of the respective protein at 280 nm. The mean value of at least three independent measurements was taken for concentration calculation.

6.2 Introduction of Fmoc-Phe-quantum defects

6.2.1. Synthesis of Fmoc-L-4-diazonium-phenylalanine tetrafluoroborate

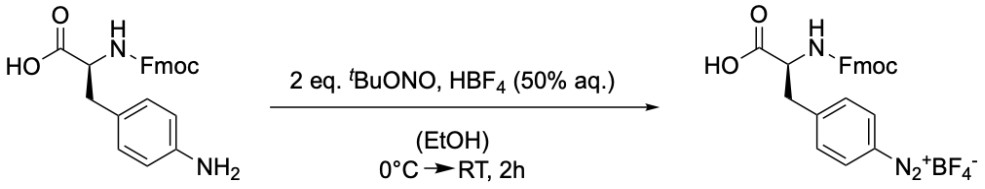

Fmoc-L-4-diazonium-phenylalanine tetrafluoroborate was synthesized using an optimized procedure based on the previously published general procedure.[208] Fmoc-L-4-aminophenylalanine (0.2 g, 0.497 mmol) was dissolved in 500 µL ethanol in a 5 mL glass scintillation vial. Next, approx. 125 µL HBF_4 (50% aqueous) were added dropwise. The solution was placed in an ice bath and stirred constantly while 135 µL ^{t}Bu-ONO (2 eq., 1.1 mmol, 117 mg) were added drop-wise over the course of 30 min. Next, the solution was stirred for two hours at room temperature. After the reaction was completed, a white/slightly yellow precipitate was observed and transferred to a 2 mL Eppendorf tube using 1 mL diethyl ether. The precipitate was centrifuged at 16100g for five minutes and the supernatant discarded. This process was repeated five times and the crude product was dried under reduced pressure at room temperature.

6.2.2. Defect introduction

In this thesis a defect introduction protocol based on a 96-LED array for SWCNT illumination was used. The steps for generation of a defect-carrying SWCNT-dispersion consisted of:

1. Dispersion of (6,5)-enriched SWCNTs in an aqueous 1% SDBS solution
2. Addition of 180 µL of a 10 nM SWCNT/SDBS dispersion and 20 µL of a Fmoc-Phe-Dz solution (10x the final concentration) to one well of a 96-well plate
3. 15 minutes of illumination using the 96-LED array (placed on top of the 96-well plate)

4. Control of the degree of defect introduction using NIR-fluorescence spectroscopy (either directly in the 96-well plate or a glass-bottom 96-well plate suitable for fluorescence spectroscopy)

5. Removal of excess Fmoc-Phe-Dz using spin-filtration (optional)

6. Redispersion using a surfactant of choice (e.g. 1% SDBS or PL-PEG5000)

To generate a SWCNT-SDBS dispersion (1% SDBS), 500 µL of an aqueous 2% SDBS solution were added to 500 µL of a 2 mg mL^{-1} SWCNT/water suspension. This solution was tip-sonicated for 15 minutes (Fisher Scientific™ Model 120 Sonic Dismembrator, 30% amplitude, 36 W) followed by centrifugation (2x, 16100g) and only the supernatant (top 80%) used for further studies. In the next step, the supernatant was diluted using 1% SDBS to yield a 10 nM solution. In a 96well-plate, 180 µL of this solution were added to 15 wells followed by the addition of different concentrations of Fmoc-Phe-$N_2^+BF_4^-$ (0 nM-100 µM). After careful mixing via repeating pipetting, the solutions were irradiated using a green 96-LED-array irradiator (Lumidox™, Analytical Sales & Services, Inc., Flanders, NJ, USA) at 25 mA for 15 minutes to yield solutions of SWCNT-Phe-Fmoc. The solutions were analyzed by nIR fluorescence spectroscopy for the degree of defect-introduction. The excess diazonium salt was removed via repeated 300kDa-cut-off spin filtration (5x 600 µL dH_2O washing) and the remaining SWCNT* were re-suspended in 500 µL dH_2O. In the last step, supernatant and pellet were then separated by centrifugation (16100g, 15 minutes) and the pellet containing SWCNT*-Phe-Fmoc was used for downstream experiments.

6.2.3. SWCNT* peptide synthesis

For the synthesis of SWCNT*-Phe-Peptides or the coupling of the fluorophore 5(6)-carboxyfluorescein directly to the unprotected Phe, two different methods were employed in the course of this thesis. First, 2 mL syringes equipped with a 20 µm pore size frit were used resembling the standard procedure in solid-phase peptide synthesis (for SWCNT*-F-CF and SWCNT*-F-R_6-CF). Here it was also tested to place a 0.2 µm filter on top or below the frit, however, this system did not the display the necessary mechanical stability for the following deprotection and coupling reactions as well as the washing steps, which all involve shaking and uptake and release of solvent to and from the syringe reactor. To circumvent this problem and still achieve smaller pore sizes (to

prevent a 'loss' of smaller SWCNTs) and a format compatible with peptide synthesis, it was switched to a higher throughput format consisting of a 96-well plate equipped with 0.2 μm pore size filters (Chromafil Multi 96 plate with PTFE filters, Macherey-Nagel, Germany). In the following, the two methods will be described in more detail for the synthesis of SWCNT*-F-R_6-CF and other SWCNT*-F-Peptides.

6.2.3.1. SWCNT*-F-R_6-CF synthesis

The solutions of 20 wells from the Fmoc-Phe defect introduction process (v = 4 mL, approx. 36 pmol SWCNT*-Phe-Fmoc) were pooled, mixed with 6 mL EtOH for SWCNT precipitation in a glass vial and the suspension subsequently transferred to a frit (20 μm pore size)-equipped syringe reactor (v = 2 mL). Residual SDBS surfactant and excess Fmoc-Phe-Dz were removed via washing (5x 1 mL dH_2O, 3x DMF, 3x DCM, 3x DMF). Deprotection of the Fmoc-group was achieved via incubation with 200 μL of 20% piperidine/DMF (2x 15 min). Fmoc-based solid-phase peptide synthesis (SPPS) couplings to Fmoc-Arg(Pbf)-OH (11.7 mg, 18 μmol) and 5(6)-CF (6.8 mg, 18 μmol) were carried out for 30 minutes at room temperature with 6.8 mg 1-[Bis(dimethylamino)methylene]-1H-1,2,3-triazolo[4,5-b]pyridinium 3-oxide hexafluorophosphate (HATU, 18 μmol) and 6.3 μL DIPEA (36 μmol) in 100 μL DMF. Excess reagents were removed by repeated washing with DMF/DCM/DMF (3x 1 mL). After 5(6)-CF coupling and washing, the side-chain protecting groups ((2,2,4,6,7-pentamethyldihydrobenzofuran-5-sulfonyl), Pbf) were cleaved upon gentle shaking with the cleavage cocktail (75% TFA/20% DCM/2.5% dH_2O/2.5% TIS, v_{total} = 500 μL) for one hour. Subsequently, the crude product was washed again with DMF and 10x DCM and then scraped off the frit using 100 μL dH_2O, transferred to a 1.5 mL microcentrifuge tube and stored in the dark at 4°C. For fluorescence microscopy and spectroscopy applications, the product in 100 μL dH_2O was submitted to ultrasonication (5 min, 30% amp, 4°C) followed by separation of supernatant and pellet by centrifugation (16100g, 30 min). The supernatant was used for fluorescence microscopy and spectroscopy applications.

6.2.3.2. 96-well SWCNT*-F-Peptide synthesis

Approx. 30 pmol SWCNT*-Phe-Fmoc (c = 10 nM, V = 3 mL) were added to and filtered through individual wells of a 96-well plate equipped with 0.2 μm pore size filters (Chromafil Multi 96 plate with PTFE filters, Macherey-Nagel, Germany). The samples were

washed (with 5x dH_2O, 3x DMF, 3x DCM, 3x DMF)) followed by standard Fmoc/OtBu SPPS (2x15 min Fmoc deprotection [20% Piperidine/DMF], 30min amino acid coupling [13.5 μmol amino acid/HATU, 27 μmol DIPEA]) and final deprotection of side-chain protecting groups using the deprotection cocktail (375 μL TFA, 100 μL DCM, 12.5 μL TIS, 12.5 μL dH_2O, 60 min). All steps were carried out under mild agitation of the 96-well plate on a shaker (150 rpm). After final deprotection, the SWCNT samples were again washed (using 3xDCM, 3xDMF, 10xDCM) and then resuspended using 600 μL dH_2O and transferred to 1.5 mL centrifuge tubes. Next, the samples were spun down (16100g, 30 min), resuspended in 200 μL 1% sodium deoxycholate (DOC) solution and submitted to tip-sonication (5 min, 4°C, 30% amplitude). After centrifugation, the top 80% of the supernatant were again transferred to fresh microcentrifuge tubes and used for absorbance/fluorescence spectroscopy applications.
The following Fmoc-protected amino acids were used:

Table 6.10.: Gel composition

Fmoc-Asn(Trt)-OH	Fmoc-Gly-OH	Fmoc-Tyr(tBu)-OH	Fmoc-Asp(OtBu)-OH
Fmoc-His(Trt)-OH	Fmoc-Gln(Trt)-OH	Fmoc-Ser(tBu)-OH	Fmoc-Glu(OtBu)-OH
Fmoc-Leu-OH	Fmoc-Lys(Boc)-OH	Fmoc-Val-OH	Fmoc-Phe-OH
Fmoc-Ile-OH	Fmoc-Ala-OH	Fmoc-Thr(tBu)-OH	

7 References

[1] World Health Organization, Coronavirus disease 2019 (COVID-19), tech. rep., **2020**.

[2] I. Mellman, G. Coukos, G. Dranoff, *Nature* **2011**, *480*, 480–489.

[3] C. H. June, R. S. O'Connor, O. U. Kawalekar, S. Ghassemi, M. C. Milone, *Science* **2018**, *359*, 1361–1365.

[4] H. Kwon, M. Kim, B. Meany, Y. Piao, L. R. Powell, Y. Wang, *J. Phys. Chem. C* **2015**, *119*, 3733–3739.

[5] S. Kruss, M. P. Landry, E. Vander Ende, B. M. A. Lima, N. F. Reuel, J. Zhang, J. Nelson, B. Mu, A. Hilmer, M. Strano, *J. Am. Chem. Soc.* **2014**, *136*, 713–724.

[6] D. R. Boverhof, C. M. Bramante, J. H. Butala, S. F. Clancy, M. Lafranconi, J. West, S. C. Gordon, *Regulatory Toxicology and Pharmacology* **2015**, *73*, 137–150.

[7] T. Hayashi, Y. A. Kim, T. Matoba, M. Esaka, K. Nishimura, T. Tsukada, M. Endo, M. S. Dresselhaus, *Nano Lett.* **2003**, *3*, 887–889.

[8] H. W. Kroto, J. R. Heath, S. C. O'Brien, R. F. Curl, R. E. Smalley, *Nature* **1985**, *318*, 162–163.

[9] S. Iijima, *Nature* **1991**, *354*, 56–58.

[10] K. S. Novoselov, A. K. Geim, S. V. Morozov, D. Jiang, Y. Zhang, S. V. Dubonos, I. V. Grigorieva, A. A. Firsov, *Science* **2004**, *306*, 666–669.

[11] S. Kruss, A. J. Hilmer, J. Zhang, N. F. Reuel, B. Mu, M. S. Strano, *Adv. Drug Deliv. Rev.* **2013**, *65*, 1933–1950.

[12] M. S. Dresselhaus, G. Dresselhaus, P. Avouris, Carbon nanotubes: synthesis, structure, properties, and applications, Springer-Verlag Berlin Heidelberg, **2001**.

[13] A. Jorio, M. S. Dresselhaus, R. Saito, G. Dresselhaus, *Raman spectroscopy in graphene related systems*, **2011**.

[14] N. Karousis, N. Tagmatarchis, D. Tasis, *Chem. Rev.* **2010**, *110*, 5366–5397.

[15] W. Krätschmer, L. D. Lamb, K. Fostiropoulos, D. R. Huffman, *Nature* **1990**, *347*, 354–358.

[16] D. S. Bethune, C. H. Kiang, M. S. De Vries, G. Gorman, R. Savoy, J. Vazquez, R. Beyers, *Nature* **1993**, *363*, 605–607.

[17] S. Iijima, T. Ichihashi, *Nature* **1993**, *363*, 603–605.

[18] T. GUO, P. Nikolaev, A. Thess, D. C. C. physics, *Chemical Physics Letters* **1995**.

[19] A. E. Agboola in *LSU Master's Thesis*, **2005**.

[20] P. Nikolaev, M. J. Bronikowski, R. K. Bradley, F. Rohmund, D. T. Colbert, K. A. Smith, R. E. Smalley, *Chemical Physics Letters* **1999**, *313*, 91–97.

[21] D. E. Resasco, W. E. Alvarez, F. Pompeo, L. Balzano, J. E. Herrera, B. Kitiyanan, A. Borgna, *Journal of Nanoparticle Research* **2002**, *4*, 131–136.

[22] M. He, S. Zhang, Q. Wu, H. Xue, B. Xin, D. Wang, J. Zhang, *Adv. Mater.* **2018**, *31*, 1800805–25.

[23] G. Dresselhaus, S. Riichiro, Physical properties of carbon nanotubes, World Scientific, **1998**.

[24] S. Reich, C. Thomsen, J. Maultzsch, *Carbon nanotubes: basic concepts and physical properties*, Wiley-VCH Verlag GmbH, **2004**.

[25] A. Graf, PhD thesis, Universität Heidelberg, Heidelberg, **2019**.

[26] P. Avouris, M. Freitag, V. Perebeinos, *Nat. Photonics* **2008**, *2*, 341–350.

[27] H. Wong, D. Akinwande, *Carbon nanotube and graphene device physics*, Cambridge University Press, Cambridge University Press, **2011**.

[28] C. Voisin, S. Berger, S. Berciaud, H. Yan, J.-S. Lauret, G. Cassabois, P. Roussignol, J. Hone, T. F. Heinz, *Phys. Status Solidi B* **2012**, *249*, 900–906.

[29] R. Saito, G. Dresselhaus, M. S. Dresselhaus, *Phys. Rev. B* **2000**, *61*, 2981–2990.

[30] J. W. G. Wilder, L. C. Venema, A. G. Rinzler, R. E. Smalley, C. Dekker, *Nature* **1998**, *391*, 59–62.

[31] R. B. Weisman, S. M. Bachilo, *Nano Lett.* **2003**, *3*, 1235–1238.

[32] C. D. Spataru, S. Ismail-Beigi, L. X. Benedict, S. G. Louie, *Phys. Rev. Lett.* **2004**, *92*, 1066–4.

[33] J. Maultzsch, R. Pomraenke, S. Reich, E. Chang, D. Prezzi, A. Ruini, E. Molinari, M. S. Strano, C. Thomsen, C. Lienau, *Phys. Rev. B* **2005**, *72*, 6680–4.

[34] A. R. Amori, Z. Hou, T. D. Krauss, *Annu. Rev. Phys. Chem.* **2018**, *69*, 81–99.

[35] E. B. Barros, A. Jorio, G. G. Samsonidze, R. B. Capaz, A. G. Souza Filho, J. Mendes Filho, G. Dresselhaus, M. S. Dresselhaus, *Physics Reports* **2006**, *431*, 261–302.

[36] X. He, H. Htoon, S. K. Doorn, W. H. P. Pernice, F. Pyatkov, R. Krupke, A. Jeantet, Y. Chassagneux, C. Voisin, *Nat. Mater.* **2018**, *17*, 663–670.

[37] I. B. Mortimer, R. J. Nicholas, *Phys. Rev. Lett.* **2007**, *98*, 027404.

[38] V. Perebeinos, J. Tersoff, P. Avouris, *Nano Lett.* **2005**, *5*, 2495–2499.

[39] Y. M. Piao, B. Meany, L. R. Powell, N. Valley, H. Kwon, G. C. Schatz, Y. H. Wang, *Nat. Chem.* **2013**, *5*, 840–845.

[40] X. Peng, S. S. Wong, *Adv. Mater.* **2009**, *21*, 625–642.

[41] H. Kwon, M. Furmanchuk, M. Kim, B. Meany, Y. Guo, G. C. Schatz, Y. Wang, *J. Am. Chem. Soc.* **2016**, *138*, 6878–6885.

[42] N. F. Hartmann, S. E. Yalcin, L. Adamska, E. H. Hároz, X. Ma, S. Tretiak, H. Htoon, S. K. Doorn, *Nanoscale* **2015**, *7*, 20521–20530.

[43] N. Danné, M. Kim, A. G. Godin, H. Kwon, Z. Gao, X. Wu, N. F. Hartmann, S. K. Doorn, B. Lounis, Y. Wang, L. Cognet, *ACS Nano* **2018**, *12*, 6059–6065.

[44] A. H. Brozena, M. Kim, L. R. Powell, Y. Wang, *Nat. Rev. Chem.* **2019**, *3*, 375–392.

[45] F. J. Berger, J. Lüttgens, T. Nowack, T. Kutsch, S. Lindenthal, L. Kistner, C. C. Müller, L. M. Bongartz, V. A. Lumsargis, Y. Zakharko, J. Zaumseil, *ACS Nano* **2019**, *13*, 9259–9269.

[46] A. K. Mandal, X. Wu, J. S. Ferreira, M. Kim, L. R. Powell, H. Kwon, L. Groc, Y. Wang, L. Cognet, *Scientific Reports* **2020**, 1–9.

[47] J. M. Bonard, T. Stora, J. P. Salvetat, F. Maier, T. Stockli, C. Duschl, L. Forro, W. A. deHeer, A. Chatelain, *Advanced Materials* **1997**, *9*, 827–&.

[48] J. Zhang, M. P. Landry, P. W. Barone, J.-H. Kim, S. Lin, Z. W. Ulissi, D. Lin, B. Mu, A. A. Boghossian, A. J. Hilmer, A. Rwei, A. C. Hinckley, S. Kruss, M. A. Shandell, N. Nair, S. Blake, F. Şen, S. Şen, R. G. Croy, D. Li, K. Yum, J. H. Ahn, H. Jin, D. A. Heller, J. M. Essigmann, D. Blankschtein, M. S. Strano, *Nat. Nanotechnol.* **2013**, *8*, 959–968.

[49] D. P. Salem, M. P. Landry, G. Bisker, J. Ahn, S. Kruss, M. S. Strano, *Carbon* **2016**, *97*, 147–153.

[50] G. Bisker, J. Dong, H. D. Park, N. M. Iverson, J. Ahn, J. T. Nelson, M. P. Landry, S. Kruss, M. S. Strano, *Nat. Commun.* **2016**, *7*, 10241.

[51] A. J. Gillen, A. A. Boghossian, *Front. Chem.* **2019**, *7*, 13793–13.

[52] A. Antonucci, J. Kupis-Rozmysłowicz, A. A. Boghossian, *ACS Appl. Mater. Interfaces* **2017**, *9*, 11321–11331.

[53] A. Setaro, M. Adeli, M. Glaeske, D. Przyrembel, T. Bisswanger, G. Gordeev, F. Maschietto, A. Faghani, B. Paulus, M. Weinelt, R. Arenal, R. Haag, S. Reich, *Nat. Commun.* **2017**, *8*, 838–7.

[54] A. Hirsch, *Angew. Chem. Int. Ed. Engl.* **2002**, *41*, 1853–9.

[55] P. Singh, S. Campidelli, S. Giordani, D. Bonifazi, A. Bianco, M. Prato, *Chem. Soc. Rev.* **2009**, *38*, 2214–17.

[56] W. J. Huang, S. Taylor, K. F. Fu, Y. Lin, D. H. Zhang, T. W. Hanks, A. M. Rao, Y. P. Sun, *Nano Lett.* **2002**, *2*, 311–314.

[57] M. Sano, A. Kamino, J. Okamura, S. Shinkai, *Langmuir* **2001**, *17*, 5125–5128.

[58] F. Pompeo, D. R. N. Letters, *Nano Lett.* **2002**.

[59] S. E. Baker, W. Cai, T. L. Lasseter, K. P. Weidkamp, R. J. Hamers, *Nano Lett.* **2002**, *2*, 1413–1417.

[60] K. A. Williams, P. Veenhuizen, B. G. de la Torre, R. Eritja, C. Dekker, *Nature* **2002**, *420*, 761–761.

[61] E. T. Mickelson, C. B. Huffman, A. G. Rinzler, R. E. Smalley, R. H. Hauge, J. L. Margrave, *Chemical Physics Letters* **1998**, *296*, 188–194.

[62] H. Hu, B. Zhao, M. A. Hamon, K. Kamaras, M. E. Itkis, R. C. Haddon, *J. Am. Chem. Soc.* **2003**, *125*, 14893–14900.

[63] M. Holzinger, O. Vostrowsky, A. Hirsch, F. Hennrich, M. Kappes, R. Weiss, F. Jellen, *Angew. Chem. Int. Ed.* **2001**, *40*, 4002–+.

[64] Z. Yinghuai, A. T. Peng, K. Carpenter, J. A. Maguire, N. S. Hosmane, M. Takagaki, *J. Am. Chem. Soc.* **2005**, *127*, 9875–9880.

[65] J. L. Delgado, P. de la Cruz, F. Langa, A. Urbina, J. Casado, J. T. López Navarrete, *Chem. Commun.* **2004**, 1734–1735.

[66] K. S. Coleman, S. R. Bailey, S. Fogden, M. L. H. Green, *J. Am. Chem. Soc.* **2003**, *125*, 8722–8723.

[67] A. Pénicaud, P. Poulin, A. Derré, E. Anglaret, P. Petit, *J. Am. Chem. Soc.* **2005**, *127*, 8–9.

[68] F. Liang, A. K. Sadana, A. Peera, J. Chattopadhyay, Z. Gu, R. H. Hauge, W. E. Billups, *Nano Lett.* **2004**, *4*, 1257–1260.

[69] T. Nakamura, M. Ishihara, T. Ohana, A. Tanaka, Y. Koga, *Chem. Commun.* **2004**, 1336–2.

[70] H. Peng, L. B. Alemany, J. L. Margrave, V. N. Khabashesku, *J. Am. Chem. Soc.* **2003**, *125*, 15174–15182.

[71] V. Georgakilas, A. Bourlinos, D. Gournis, T. Tsoufis, C. Trapalis, A. Mateo-Alonso, M. Prato, *J. Am. Chem. Soc.* **2008**, *130*, 8733–8740.

[72] F. G. Brunetti, M. A. Herrero, J. d. M. Muñoz, S. Giordani, A. Diaz-Ortiz, S. Filippone, G. Ruaro, M. Meneghetti, M. Prato, E. Vázquez, *J. Am. Chem. Soc.* **2007**, *129*, 14580–14581.

[73] W. Zhang, T. M. Swager, *J. Am. Chem. Soc.* **2007**, *129*, 7714–7715.

[74] J. L. Hudson, H. Jian, A. D. Leonard, J. J. Stephenson, J. M. Tour, *Chem. Mater.* **2006**, *18*, 2766–2770.

[75] Z. Guo, F. Du, D. Ren, Y. Chen, J. Zheng, Z. Liu, J. Tian, *J. Mater. Chem.* **2006**, *16*, 3021–3030.

[76] V. N. Khabashesku, W. E. Billups, J. L. Margrave, *Acc. Chem. Res.* **2002**, *35*, 1087–1095.

[77] M. Maggini, G. Scorrano, M. Prato, *J. Am. Chem. Soc.* **1993**, *115*, 9798–9799.

[78] V. Georgakilas, K. Kordatos, M. Prato, D. M. Guldi, M. Holzinger, A. Hirsch, *Journal of the American Chemical Society* **2002**, *124*, 760–761.

[79] D. Pantarotto, C. D. Partidos, R. Graff, J. Hoebeke, J.-P. Briand, M. Prato, A. Bianco, *J. Am. Chem. Soc.* **2003**, *125*, 6160–6164.

[80] D. Pantarotto, J.-P. Briand, M. Prato, A. Bianco, *Chem. Commun.* **2004**, 16–17.

[81] G. Pastorin, W. Wu, S. Wieckowski, J.-P. Briand, K. Kostarelos, M. Prato, A. Bianco, *Chem. Commun.* **2006**, *35*, 1182–3.

[82] W. Wu, S. Wieckowski, G. Pastorin, M. Benincasa, C. Klumpp, J.-P. Briand, R. Gennaro, M. Prato, A. Bianco, *Angew. Chem. Int. Ed.* **2005**, *44*, 6358–6362.

[83] B. Dinesh, A. Bianco, C. Ménard-Moyon, *Nanoscale* **2016**, *8*, 18596–18611.

[84] C. A. Dyke, J. M. Tour, *J. Phys. Chem. A* **2004**, *108*, 11151–11159.

[85] L. R. Powell, Y. Piao, Y. Wang, *J. Phys. Chem. Lett.* **2016**, *7*, 3690–3694.

[86] G. Schmidt, S. Gallon, S. Esnouf, J.-P. Bourgoin, P. Chenevier, *Chemistry* **2009**, *15*, 2101–2110.

[87] A. H. Brozena, J. D. Leeds, Y. Zhang, J. T. Fourkas, Y. Wang, *ACS Nano* **2014**, *8*, 4239–4247.

[88] V. C. Moore, M. S. Strano, E. H. Haroz, R. H. Nano, R. E. Smalley, *Nano Lett.* **2003**, *3*, 1379–1382.

[89] B. A. Larsen, P. Deria, J. M. Holt, I. N. Stanton, M. J. Heben, M. J. Therien, J. L. Blackburn, *J. Am. Chem. Soc.* **2012**, *134*, 12485–12491.

[90] Y. Ohno, S. Iwasaki, Y. Murakami, S. Kishimoto, S. Maruyama, T. Mizutani, *Phys. Status Solidi B* **2007**, *244*, 4002–4005.

[91] F. A. Mann, D. Meyer, S. Mischke, S. Kruss, *Bunsenmagazin* **2017**, *19*.

[92] K. Yum, J. H. Ahn, T. P. McNicholas, P. W. Barone, B. Mu, J.-H. Kim, R. M. Jain, M. S. Strano, *ACS Nano* **2012**, *6*, 819–830.

[93] M. Dinarvand, E. Neubert, D. Meyer, G. Selvaggio, F. A. Mann, L. Erpenbeck, S. Kruss, *Nano Lett.* **2019**, *19*, 6604–6611.

[94] H. Wu, R. Nißler, V. Morris, N. Herrmann, P. Hu, S.-J. Jeon, S. Kruss, J. P. Giraldo, *Nano Lett.* **2020**, *20*, 2432–2442.

[95] J. H. Ahn, J.-H. Kim, N. F. Reuel, P. W. Barone, A. A. Boghossian, J. Zhang, H. Yoon, A. C. Chang, A. J. Hilmer, M. S. Strano, *Nano Lett.* **2011**, *11*, 2743–2752.

[96] R. M. Williams, C. Lee, T. V. Galassi, J. D. Harvey, R. Leicher, M. Sirenko, M. A. Dorso, J. Shah, N. Olvera, F. Dao, D. A. Levine, D. A. Heller, *Sci. Adv.* **2018**, *4*.

[97] S. Kruss, D. P. Salem, L. Vuković, B. Lima, E. Vander Ende, E. S. Boyden, M. S. Strano, *Proc. Natl. Acad. Sci.* **2017**, *114*, 1789–1794.

[98] J. Zhang, A. A. Boghossian, P. W. Barone, A. Rwei, J.-H. Kim, D. Lin, D. A. Heller, A. J. Hilmer, N. Nair, N. F. Reuel, M. S. Strano, *J. Am. Chem. Soc.* **2011**, *133*, 567–581.

[99] D. A. Heller, H. Jin, B. M. Martinez, D. Patel, B. M. Miller, T. K. Yeung, P. V. Jena, C. Höbartner, T. Ha, S. K. Silverman, M. S. Strano, *Nat. Nanotechnol.* **2009**, *4*, 114–120.

[100] H. Jin, D. A. Heller, M. Kalbacova, J. H. Kim, J. Zhang, A. A. Boghossian, N. Maheshri, M. S. Strano, *Nature Nanotechnology* **2010**, *5*, 302–309.

[101] E. S. Jeng, A. E. Moll, A. C. Roy, J. B. Gastala, M. S. Strano, *Nano Lett.* **2006**, *6*, 371–375.

[102] E. S. Jeng, P. W. Barone, J. D. Nelson, M. S. Strano, *Small* **2007**, *3*, 1602–1609.

[103] N. F. Reuel, J. H. Ahn, J.-H. Kim, J. Zhang, A. A. Boghossian, L. K. Mahal, M. S. Strano, *J. Am. Chem. Soc.* **2011**, *133*, 17923–17933.

[104] E. S. Jeng, J. D. Nelson, K. L. J. Prather, M. S. Strano, *Small* **2010**, *6*, 40–43.

[105] J.-H. Kim, D. A. Heller, H. Jin, P. W. Barone, C. Song, J. Zhang, L. J. Trudel, G. N. Wogan, S. R. Tannenbaum, M. S. Strano, *nchem* **2009**, *1*, 473–481.

[106] M. Linnemann, M. Kühl, Biochemie für Mediziner: ein Lern-und Arbeitsbuch mit klinischem Bezug, **2006**.

[107] V. du Vigneaud, *Annals of the New York Academy of Sciences* **1960**, *88*, 537–548.

[108] K. H. Altmann, M. Mutter, *Chemie in unserer Zeit* **1993**, *27*, 274–286.

[109] R. B. Merrifield, *J. Am. Chem. Soc.* **1963**, *85*, 2149–2154.

[110] V. Mäde, S. Els-Heindl, A. G. Beck-Sickinger, *Beilstein J. Org. Chem.* **2014**, *10*, 1197–1212.

[111] R. M. Kohli, C. T. Walsh, M. D. Burkart, *Nature* **2002**, *418*, 658–661.

[112] M. Broncel, J. A. Falenski, S. C. Wagner, C. P. R. Hackenberger, B. Koksch, *Chemistry* **2010**, *16*, 7881–7888.

[113] D. N. Woolfson, G. J. Bartlett, M. Bruning, A. R. Thomson, *Curr. Opin. Struct. Biol.* **2012**, *22*, 432–441.

[114] A. R. Thomson, C. W. Wood, A. J. Burton, G. J. Bartlett, R. B. Sessions, R. L. Brady, D. N. Woolfson, *Science* **2014**, *346*, 485–488.

[115] D. N. Woolfson, *Sub-Cellular Biochemistry* **2017**, *82*, 35–61.

[116] M. Gruber, A. N. Lupas, *Trends Biochem. Sci.* **2003**, *28*, 679–685.

[117] A. Lupas, *Trends Biochem. Sci.* **1996**, *21*, 375–382.

[118] N. C. Burgess, T. H. Sharp, F. Thomas, C. W. Wood, A. R. Thomson, N. R. Zaccai, R. L. Brady, L. C. Serpell, D. N. Woolfson, *Journal of the American Chemical Society* **2015**, *137*, 10554–10562.

[119] F. Thomas, N. C. Burgess, A. R. Thomson, D. N. Woolfson, *Angew. Chem. Int. Ed.* **2016**, *55*, 987–991.

[120] G. R. Dieckmann, A. B. Dalton, P. A. Johnson, J. Razal, J. Chen, G. M. Giordano, E. Muñoz, I. H. Musselman, R. H. Baughman, R. K. Draper, *J. Am. Chem. Soc.* **2003**, *125*, 1770–1777.

[121] A. Ortiz-Acevedo, H. Xie, V. Zorbas, W. M. Sampson, A. B. Dalton, R. H. Baughman, R. K. Draper, I. H. Musselman, G. R. Dieckmann, *J. Am. Chem. Soc.* **2005**, *127*, 9512–9517.

[122] G. Grigoryan, Y. H. Kim, R. Acharya, K. Axelrod, R. M. Jain, L. Willis, M. Drndic, J. M. Kikkawa, W. F. DeGrado, *Science* **2011**, *332*, 1071–1076.

[123] J. L. Lau, M. K. Dunn, *Bioorganic & Medicinal Chemistry* **2018**, *26*, 2700–2707.

[124] P. D. Kaiser, J. Maier, B. Traenkle, F. Emele, U. Rothbauer, *Biochimica et Biophysica Acta - Proteins and Proteomics* **2014**, *1844*, 1933–1942.

[125] J. Helma, M. C. Cardoso, S. Muyldermans, H. Leonhardt, *J. Cell Biol.* **2015**, *209*, 633–644.

[126] A. Méndez Ardoy, I. Lostalé-Seijo, J. Montenegro, *ChemBioChem* **2018**, 1–12.

[127] E. H. Hankin, *Nature* **1890**, *43*, 121–123.

[128] D. Behring Stabsarzt, D. Kitasoto, *deutsche* **1890**.

[129] D. Schumacher, C. P. R. Hackenberger, H. Leonhardt, J. Helma, *J. Clin. Immunol.* **2016**, *36 Suppl 1*, 100–107.

[130] J. Tanha, T.-D. Nguyen, A. Ng, S. Ryan, F. Ni, R. MacKenzie, *Protein Eng. Des. Sel.* **2006**, *19*, 503–509.

[131] U. Rothbauer, K. Zolghadr, S. Tillib, D. Nowak, L. Schermelleh, A. Gahl, N. Backmann, K. Conrath, S. Muyldermans, M. C. Cardoso, H. Leonhardt, *Nat. Methods* **2006**, *3*, 887–889.

[132] E. De Genst, K. Silence, K. Decanniere, K. Conrath, R. Loris, J. Kinne, S. Muyldermans, L. Wyns, *Proc. Natl. Acad. Sci.* **2006**, *103*, 4586–4591.

[133] J. Ries, C. Kaplan, E. Platonova, H. Eghlidi, H. Ewers, *Nat. Methods* **2012**, *9*, 582–584.

[134] C. D. Spicer, B. G. Davis, *Nat. Commun.* **2014**, *5*, 1–14.

[135] J. R. Junutula, H. Raab, S. Clark, S. Bhakta, D. D. Leipold, S. Weir, Y. Chen, M. Simpson, S. P. Tsai, M. S. Dennis, Y. Lu, Y. G. Meng, C. Ng, J. Yang, C. C. Lee, E. Duenas, J. Gorrell, V. Katta, A. Kim, K. McDorman, K. Flagella, R. Venook, S. Ross, S. D. Spencer, W. Lee Wong, H. B. Lowman, R. Vandlen, M. X. Sliwkowski, R. H. Scheller, P. Polakis, W. Mallet, *Nat Biotechnol* **2008**, *26*, 925–932.

[136] U. Schnell, F. Dijk, K. A. Sjollema, B. N. G. Giepmans, *Nature Methods* **2012**, *9*, 152–158.

[137] G.-J. Kremers, S. G. Gilbert, P. J. Cranfill, M. W. Davidson, D. W. Piston, *J Cell Sci* **2011**, *124*, 157–160.

[138] G. V. Los, L. P. Encell, M. G. Mcdougall, D. D. Hartzell, N. Karassina, C. Zimprich, M. G. Wood, R. Learish, R. F. Ohana, M. Urh, D. Simpson, J. Mendez, K. Zimmerman, P. Otto, G. Vidugiris, J. Zhu, A. Darzins, D. H. Klaubert, R. F. Bulleit, K. V. Wood, *ACS Chemical Biology* **2008**, *3*, 373–382.

[139] A. Keppler, S. Gendreizig, T. Gronemeyer, H. Pick, H. Vogel, K. Johnsson, *Nat Biotechnol* **2003**, *21*, 86–89.

[140] G. H. Patterson, S. M. Knobel, W. D. Sharif, S. R. Kain, D. W. Piston, *Biophysical Journal* **1997**, *73*, 2782–2790.

[141] D. M. Chudakov, M. V. Matz, S. Lukyanov, K. A. Lukyanov, *Physiological Reviews* **2010**, *90*, 1103–1163.

[142] G. Crivat, J. W. Taraska, *Trends in Biotechnology* **2012**, *30*, 8–16.

[143] E. C. Jensen, *The Anatomical Record: Advances in Integrative Anatomy and Evolutionary Biology* **2012**, *295*, 2031–2036.

[144] S. B. Skube, J. M. Chaverri, H. V. Goodson, *Cytoskeleton* **2010**, *67*, 1–12.

[145] N. Budisa, C. Minks, F. J. Medrano, J. Lutz, R. Huber, L. Moroder, *Proc. Natl. Acad. Sci.* **1998**, *95*, 455–459.

[146] L. Wang, P. G. Schultz, *Angew. Chem. Int. Ed. Engl.* **2005**, *44*, 34–66.

[147] J. Lotze, U. Reinhardt, O. Seitz, A. G. Beck-Sickinger, *Molecular BioSystems* **2016**, *12*, 1731–1745.

[148] H. Mao, S. A. Hart, A. Schink, B. A. Pollok, *J. Am. Chem. Soc.* **2004**, *126*, 2670–2671.

[149] D. Schumacher, J. Helma, F. A. Mann, G. Pichler, F. Natale, E. Krause, M. C. Cardoso, C. P. R. Hackenberger, H. Leonhardt, *Angew. Chem. Int. Ed.* **2015**, *54*, 13787–13791.

[150] T. Dierks, A. Dickmanns, A. Preusser-Kunze, B. Schmidt, M. Mariappan, K. von Figura, R. Ficner, M. G. Rudolph, *Cell* **2005**, *121*, 541–552.

[151] S. F. Mitchell, J. R. Lorsch, *Methods in Enzymology* **2015**, *559*, 111–125.

[152] L. Berrade, J. A. Camarero, *Cell. Mol. Life Sci.* **2009**, *66*, 3909–3922.

[153] R. Borra, J. A. Camarero, *Methods Mol. Biol.* **2017**, *1495*, 111–130.

[154] E. M. M. Sletten, C. R. R. Bertozzi, *Angew. Chem. Int. Ed. Engl.* **2009**, *48*, 6974–6998.

[155] M.-A. Kasper, M. Glanz, A. Stengl, M. Penkert, S. Klenk, T. Sauer, D. Schumacher, J. Helma, E. Krause, M. C. Cardoso, H. Leonhardt, C. P. R. Hackenberger, *Angew. Chem. Int. Ed. Engl.* **2019**, *58*, 11625–11630.

[156] J. M. J. M. Ravasco, H. Faustino, A. Trindade, P. M. P. Gois, *Chem. Eur. J.* **2018**, *25*, 43–59.

[157] S. C. Tsang, J. J. Davis, M. L. H. Green, H. A. O. Hill, Y. C. Leung, P. J. Sadler, *J. Chem. Soc. Chem. Commun.* **1995**, 1803–2.

[158] F. Balavoine, P. Schultz, C. Richard, V. Mallouh, T. W. Ebbesen, C. Mioskowski, *Angew. Chem. Int. Ed. Engl.* **1999**, *38*, 1912–1915.

[159] B. F. Erlanger, B.-X. Chen, M. Zhu, L. Brus, *Nano Lett.* **2001**, *1*, 465–467.

[160] Y.-Z. You, C.-Y. Hong, C.-Y. Pan, *The Journal of Physical Chemistry C* **2007**, *111*, 16161–16166.

[161] H. Yoon, J. H. Ahn, P. W. Barone, K. Yum, R. Sharma, A. A. Boghossian, J. H. Han, M. S. Strano, *Angew. Chem. Int. Ed. Engl.* **2011**, *50*, 1828–1831.

[162] S. F. Oliveira, G. Bisker, N. A. Bakh, S. L. Gibbs, M. P. Landry, M. S. Strano, *Carbon* **2015**, *95*, 767–779.

[163] Z. Liu, S. M. Tabakman, Z. Chen, H. Dai, *Nat. Protoc.* **2009**, *4*, 1372–1381.

[164] E. E. Ferapontova, *Electrochimica Acta* **2017**, 1–25.

[165] M. O. Klein, *Cellular and Molecular Neurobiology* **2018**, *39*, 31–59.

[166] E. S. Bucher, R. M. Wightman, *Annu Rev Anal Chem (Palo Alto Calif)* **2015**, *8*, 239–261.

[167] R. B. Keithley, P. Takmakov, E. S. Bucher, A. M. Belle, C. A. Owesson-White, J. Park, R. M. Wightman, *Anal. Chem.* **2011**, *83*, 3563–3571.

[168] D. L. Robinson, A. Hermans, A. T. Seipel, R. M. Wightman, *Chem. Rev.* **2008**, *108*, 2554–2584.

[169] J. Wang, A. G. Ewing, *Analyst* **2014**, *139*, 3290–3295.

[170] J. Wang, R. Trouillon, Y. Lin, M. I. Svensson, A. G. Ewing, *Anal. Chem.* **2013**, *85*, 5600–5608.

[171] T. Patriarchi, J. R. Cho, K. Merten, M. W. Howe, A. Marley, W. H. Xiong, R. W. Folk, G. J. Broussard, R. Liang, M. J. Jang, H. Zhong, D. Dombeck, M. von Zastrow, A. Nimmerjahn, V. Gradinaru, J. T. Williams, L. Tian, *Science* **2018**, *360*, eaat4422–10.

[172] F. Sun, J. Zeng, M. Jing, J. Zhou, J. Feng, S. F. Owen, Y. Luo, F. Li, H. Wang, T. Yamaguchi, Z. Yong, Y. Gao, W. Peng, L. Wang, S. Zhang, J. Du, D. Lin, M. Xu, A. C. Kreitzer, G. Cui, Y. Li, *Cell* **2018**, *174*, 481–496.e19.

[173] E. Venturelli, C. Fabbro, O. Chaloin, C. Menard-Moyon, C. R. Smulski, T. Da Ros, K. Kostarelos, M. Prato, A. Bianco, *Small* **2011**, *7*, 2179–2187.

[174] M. S. Filipiak, M. Rother, N. M. Andoy, A. C. Knudsen, S. Grimm, C. Bachran, L. K. Swee, J. Zaumseil, A. Tarasov, *Sensors and Actuators B: Chemical* **2018**, *255*, 1507–1516.

[175] C. Li, M. Curreli, H. Lin, B. Lei, F. N. Ishikawa, R. Datar, R. J. Cote, M. E. Thompson, C. Zhou, *J. Am. Chem. Soc.* **2005**, *127*, 12484–12485.

[176] Z. Chen, S. M. Tabakman, A. P. Goodwin, M. G. Kattah, D. Daranciang, X. Wang, G. Zhang, X. Li, Z. Liu, P. J. Utz, K. Jiang, S. Fan, H. Dai, *Nat. Biotechnol.* **2008**, *26*, 1285–1292.

[177] Z. Liu, X. Li, S. M. Tabakman, K. Jiang, S. Fan, H. Dai, *J. Am. Chem. Soc.* **2008**, *130*, 13540–13541.

[178] K. Welsher, Z. Liu, D. Daranciang, H. Dai, *Nano Lett.* **2008**, *8*, 586–590.

[179] V. A. Zamolo, G. Valenti, E. Venturelli, O. Chaloin, M. Marcaccio, S. Boscolo, V. Castagnola, S. Sosa, F. Berti, G. Fontanive, M. Poli, A. Tubaro, A. Bianco, F. Paolucci, M. Prato, *ACS Nano* **2012**, *6*, 7989–7997.

[180] C. Spinato, A. Perez Ruiz de Garibay, M. Kierkowicz, E. Pach, M. Martincic, R. Klippstein, M. Bourgognon, J. T.-W. Wang, C. Ménard-Moyon, K. T. Al-Jamal, B. B. Ballesteros, G. Tobias, A. Bianco, *Nanoscale* **2016**, *8*, 12626–12638.

[181] R. M. Williams, C. Lee, D. A. Heller, *ACS Sensors* **2018**, *3*, 1838–1845.

[182] N. Fakhri, A. D. Wessel, C. Willms, M. Pasquali, D. R. Klopfenstein, F. C. MacKintosh, C. F. Schmidt, *Science* **2014**, *344*, 1031–1035.

[183] S. Courty, C. Luccardini, Y. Bellaiche, G. Cappello, M. Dahan, *Nano Lett.* **2006**, *6*, 1491–1495.

[184] S. Dunn, E. E. Morrison, T. B. Liverpool, C. Molina-Paris, R. A. Cross, M. C. Alonso, M. Peckham, *J Cell Sci* **2008**, *121*, 1085–1095.

[185] S. M. Block, L. S. Goldstein, B. J. Schnapp, *Nature* **1990**, *348*, 348–352.

[186] K. Stamer, R. Vogel, E. Thies, E. Mandelkow, E. M. Mandelkow, *J. Cell Biol.* **2002**, *156*, 1051–1063.

[187] A. Verdel, S. Jia, S. Gerber, T. Sugiyama, S. Gygi, S. I. S. Grewal, D. Moazed, *Science* **2004**, *303*, 672–676.

[188] M. Marczynke, K. Gröger, O. Seitz, *Bioconjug. Chem.* **2017**, *28*, 2384–2392.

[189] D. Nepal, K. E. Geckeler, *Small* **2007**, *3*, 1259–1265.

[190] H. Li, G. Gordeey, O. Garrity, S. Reich, B. S. Flavel, *ACS Nano* **2019**, *13*, 2567–2578.

[191] S. Wang, E. S. Humphreys, S.-Y. Chung, D. F. Delduco, S. R. Lustig, H. Wang, K. N. Parker, N. W. Rizzo, S. Subramoney, Y.-M. Chiang, A. Jagota, *Nat. Mater.* **2003**, *2*, 196–200.

[192] Z. Su, T. Leung, J. F. Honek, *J. Phys. Chem. B* **2006**, *110*, 23623–23627.

[193] Z. Su, K. Mui, E. Daub, T. Leung, J. Honek, *J. Phys. Chem. B* **2007**, *111*, 14411–14417.

[194] C. Gaillard, M. Duval, H. Dumortier, A. Bianco, *J. Peptide Sci.* **2010**, *17*, 139–142.

[195] V. Zorbas, A. Ortiz-Acevedo, A. B. Dalton, M. M. Yoshida, G. R. Dieckmann, R. K. Draper, R. H. Baughman, M. Jose-Yacaman, I. H. Musselman, *J. Am. Chem. Soc.* **2004**, *126*, 7222–7227.

[196] M. S. Arnold, M. O. Guler, M. C. Hersam, S. I. Stupp, *Langmuir* **2005**, *21*, 4705–4709.

[197] A. Bianco, K. Kostarelos, C. D. Partidos, M. Prato, *Chem. Commun.* **2005**, *14*, 571–7.

[198] K. Y. Jiang, L. S. Schadler, R. W. Siegel, X. J. Zhang, H. F. Zhang, M. Terrones, *J. Mater. Chem.* **2004**, *14*, 37–39.

[199] X. Yu, S. N. Kim, F. Papadimitrakopoulos, J. F. Rusling, *Molecular BioSystems* **2005**, *1*, 70–9.

[200] L. Chio, R. L. Pinals, A. Murali, N. S. Goh, M. P. Landry, *Adv. Funct. Mater.* **2020**, 1910556–8.

[201] A. G. Godin, A. Setaro, M. Gandil, R. Haag, M. Adeli, S. Reich, L. Cognet, *Sci. Adv.* **2019**, *5*, eaax1166.

[202] A. G. Beyene, A. A. Alizadehmojarad, G. Dorlhiac, N. Goh, A. M. Streets, P. Král, L. Vuković, M. P. Landry, *Nano Lett.* **2018**, *18*, 6995–7003.

[203] G. Bisker, N. A. Bakh, M. A. Lee, J. Ahn, M. Park, E. B. O'Connell, N. M. Iverson, M. S. Strano, *ACS Sens.* **2018**, *3*, 367–377.

[204] D. A. Heller, G. W. Pratt, J. Zhang, N. Nair, A. J. Hansborough, A. A. Boghossian, N. F. Reuel, P. W. Barone, M. S. Strano, *Proc. Natl. Acad. Sci.* **2011**, *108*, 8544–8549.

[205] J. A. Fagan, *Nanoscale Advances* **2019**, *21*, 845.

[206] A. Hartschuh, *Angew. Chem. Int. Ed. Engl.* **2008**, *47*, 8178–8191.

[207] F. Schöppler, C. Mann, T. C. Hain, F. M. Neubauer, G. Privitera, F. Bonaccorso, D. Chu, A. C. Ferrari, T. Hertel, *J. Phys. Chem. C* **2011**, *115*, 14682–14686.

[208] K. Zhang, X. H. Xu, F. L. Qing, *Eur. J. Org. Chem.* **2016**, *2016*, 5088–5090.

8 | Abbreviations

AcOH	Acetic acid
ADC	Antibody-drug conjugate
AFM	Atomic Force Microscopy
αHB	α-helical coiled-coil peptide barrel
APS	Ammonium persulfate
APTES	(3-Aminopropyl)triethoxysilane
Boc	*Tert*-Butyloxycarbonyl
BSA	Bovine serum albumine
CAR-T	Chimeric antigen receptor T-cell
CC-Hept	Coiled-coil heptamer
CC-Tet	Coiled-coil tetramer
CD	Circular dichroism
CF	Carboxyfluorescein
CoMoCAT	Cobalt-Molybdenum catalyzed process
Cos7	'CV-1 in Origin' cells
CMC	Critical micelle concentration
CVD	Chemical vapor deposition
DCM	Dichloromethane
DMF	Dimethylformamide
DNA	Deoxyribonucleic acid
DOC	Sodium deoxycholate
DOS	Density of states
DWCNT	Double-walled carbon nanotube
EDC	1-Ethyl-3-(3-dimethylaminopropyl)carbodiimide hydrochloride
EGFR	Epidermal growth factor receptor
EPL	Expressed protein ligation
ESI-MS	Electrospray ionization mass spectrometry
Fab	Antigen binding fragment
Fc	Crystallizable fragment
FET	Field-effect transistor

Fmoc	9-Fluorenylmethoxycarbonyl
FP	Fluorescent protein
FSCV	Fast scan cyclic voltammetry
GABA	γ-Aminobutyric acid
GBP	GFP-binding protein
GFP	Green fluorescent protein
HALO-tag	Protein-tag binding haloalkane ligands
HB	Helical barrel
hcAb	Heavy-chain antibody
HE4	Human epididymis protein 4
HiPCO	High-pressure carbon monoxide process
HPLC	High-performance liquid chromatography
IgG	Immunoglobulin G
Kin-5	Kinesin 5
LED	Light emitting diode
LOD	Limit of detection
LUMO	Lowest unoccupied molecular orbital
MALDI-TOF MS	Matrix-assisted laser desorption/ionization - time of flight mass spectrometry
MalPh-Dz	4-(*N*-maleimido)phenyldiazonium tetrafluoroborate
MSD	Mean-squared displacement
mRNA	Messenger ribonucleic acid
MWCNT	Multi-walled carbon nanotube
MWCO	Molecular weight cut-off
NCL	Native chemical ligation
NHS	*N*-hydroxysuccinimid
NIR	Near infrared
NMR	Nuclear magnetic resonance
NP	Nanoparticle
NTA	Nitrilotriacetic acid
PAGE	Polyacrylamide gel electrophoresis
PC12	Cell line derived from a pheochromocytoma of the rat adrenal medulla
PDMS	Polydimethylsiloxane
PEG	Polyethylene glycol
PFO	Poly[9,9-dioctylfluorenyl-2,7-diyl]
PFO-BPy	Poly-[(9,9-dioctylfluorenyl-2,7-diyl)-alt-co-(6,6')-(2,2'-bipyridine)]

PG	Protecting group
PL	Photoluminescence
PLQY	Photoluminescence quantum yield
PNT	Peptide nanotube
POI	Protein of interest
PPI	Protein-protein interactions
PSA	Prostate-specific antigen
PTM	Post-translational modification
RFP	Red fluorescent protein
RNA	Ribonucleic acid
RNS	Reactive nitrogen species
ROS	Reactive oxygen species
SC	Sodium cholate
scFv	Single chain variable fragment
SDBS	Sodium dodecylbenzenesulfonate
SDS	Sodium dodecylsulfate
SET	Single electron transfer
SIMS	Secondary-ion mass spectrometry
SNAP tag	Protein-tag binding benzylguanine derivatives
SPPS	Solid phase peptide synthesis
SPR	Surface plasmon resonance
Sulfo-SMCC	Sulfosuccinimidyl-4-(*N*-maleimidomethyl)cyclohexan-1-carboxylate
SWCNT	Single-walled carbon nanotube
TEM	Transmission electron microscopy
TEMED	Tetramethylethylenediamine
TFA	Trifluoroacetic acid
TGA	Thermogravimetric analysis
THF	Tetrahydrofuran
TIS	Tri*iso*propylsilane
TRIS	Tris(hydroxymethyl)aminomethane
Trt	Triphenylmethyl
UAA	Unnatural amino acid
uPA	Urokinase plasminogen activator
UV	Ultraviolet
VH	Variable region of the antibody's heavy chain
VHH	Variable region of a heavy-chain antibody

Vis	Visible light
VL	Variable region of the antibody's light chain
VP1	Viral envelope protein VP1

Amino acids are abbreviated with the three-letter code. For peptide sequences the one-letter code is used.

9 | List of Figures

List of Figures

A | Publications

First-author publications:

1. F. A. Mann, Z. Lv, J. Grosshans, F. Opazo, S. Kruss, *Angew. Chem. Int. Ed.* **2019**. DOI: 10.1002/anie.201904167.

2. F. A. Mann, J. Horlebein, N. F. Meyer, D. Meyer, F. Thomas, S. Kruss, *Chem. - A Eur. J.* **2018**, 24, 12241-12245. DOI: 10.1002/chem.201800993.

3. F. A. Mann, D. Meyer, S. Mischke, S. Kruss, *Bunsenmagazin* **2017**, 19, 228-237.

4. F. A. Mann, N. Herrmann, D. Meyer, S. Kruss, *Sensors* **2017**, 17, 1521. DOI: 10.3390/s17071521

Co-authored publications:

1. D. Meyer, S. Telele, A. Zelena, A. J. Gillen, A. Antonucci, E. Neubert, R. Nissler, F. A. Mann, L. Erpenbeck, A. Boghossian, S. Köster, S. Kruss, *Nanoscale* **2020**. DOI: 10.1039/D0NR00864H

2. G. Selvaggio, A. Chizhik, R. Nissler, I. Kuhlemann, D. Meyer, L. Vuong, H. Preiss, N. Herrmann, F. A. Mann, Z. Lv, T. A. Oswald, A. Spreinat, L. Erpenbeck, J. Grosshans, V. Karius, A. Janshoff, J. P. Giraldo, S. Kruss , *Nat. Commun.* **2020**. DOI: 10.1038/s41467-020-15299-5

3. M. Dinarvand, E. Neubert, D. Meyer, G. Selvaggio, F. A. Mann, L. Erpenbeck, S. Kruss, *Nano Lett.* **2019**. DOI:10.1021/acs.nanolett.9b02865

4. R. Nissler, F. A. Mann, H. Preiss, G. Selvaggio, N. Herrmann, S. Kruss, *Nanoscale* **2019**. DOI:10.1039/c9nr03258d

5. R. Nissler, F. A. Mann, P. Chaturvedi, J. Horlebein, D. Meyer, L. Vukovic, S. Kruss, *J. Phys. Chem. C* **2019**. DOI:10.1021/acs.jpcc.8b11058

B | Oral talks

1. F. A. Mann, Z. Lv, N. Herrmann, J. Grosshans, F. Opazo, S. Kruss, 3rd Infinity Conference **2020** (Göttingen)
   Nano^2 - Nanotube-nanobody conjugates for near-infrared immunolabeling in vitro and in vivo (Flash talk)

2. F. A. Mann, N. Herrmann, S. Kruss, Bunsentagung **2019** (Jena)
   Nano^2 - Nanotube-nanobody conjugates for near-infrared immunolabeling and sensing

3. F. A. Mann, IMPRS Retreat **2018** (Koblenz)
   Turning carbon nanotubes into sensors

4. F. A. Mann, J. Horlebein, N. Herrmann, D. Meyer, F. Thomas, S. Kruss, Biosensors **2018** (Miami, USA)
   Novel approaches for carbon nanotube based biosensors

5. F. A. Mann, J. Horlebein, F. Thomas, S. Kruss, Bunsentagung **2018** (Hannover)
   Peptide-barrel encapsulated carbon nanotubes

C | Posters

1. F. A. Mann, Z. Lv, N. Herrmann, J. Grosshans, F. Opazo, S. Kruss, 3rd Infinity Conference **2020** (Göttingen)
   Nano^2 - Nanotube-nanobody conjugates for near-infrared immunolabeling in vitro and in vivo

2. F. A. Mann, Z. Lv, N. Herrmann, J. Grosshans, F. Opazo, S. Kruss, NT19 - 20th International Conference on the Science and Application of Nanotubes and Low-Dimensional Materials **2019** (Würzburg)
   Nano^2 - Nanotube-nanobody conjugates for near-infrared immunolabeling in vitro and in vivo

3. F. A. Mann, J. Horlebein, F. Thomas, S. Kruss, NT19 - 20th International Conference on the Science and Application of Nanotubes and Low-Dimensional Materials **2019** (Würzburg)
   Peptide-barrel encapsulated carbon nanotubes

4. F. A. Mann, N. Herrmann, E. Polo, D. Meyer, S. Kruss Quantitative BioImaging Conference **2018** (Göttingen)
   Nanosensor bioconjugates and their application in imaging

5. F. A. Mann, D. Meyer, E. Polo, A. Hagemann, S. Kruss, Bunsentagung **2017** (Kaiserslautern)
   Near-infrared detection of cellular communication using fluorescent nanosensors

6. F. A. Mann, N. Herrmann, E. Polo, S. Kruss, Bunsentagung **2017** (Kaiserslautern)
   Structure and photophysical dynamics of the corona phase around fluorescent nanoparticles

D | Acknowledgements

First of all I would like to thank my supervisor Dr. Sebastian Kruss for giving me the opportunity to work in his group, guiding me throughout the time of my PhD and always supporting me in new ideas and approaches. This was truly helpful and made this time very special and fruitful.
Second, I want to thank Prof. Dr. Martin Suhm and Prof. Dr. Claudia Steinem for being 2nd and 3rd member (and 2nd referee) of my thesis advisory committee as well as for their time, care and helpful remarks during these meetings. These meetings truly helped me to structure my thesis, stay focused and be aware of both open questions and what was already achieved.
I also want to thank all the people I had the possibility to collaborate with during the last years: Jun.-Prof. Dr. Franziska Thomas, Dr. Felipe Opazo, Prof. Dr. Jörg Großhans and Dr. Zhiyi Lv.
Next, I would like to thank all the current and former members of the Kruss group for making these 3.5 years a truly enjoyable time while doing science and also aside it. Here, I especially remember all the great doctoral parties, taking a cold shower in the mountains, smoking cuban cigars, watching Werder Bremen (still the best team in the world!) at the retreat, drinking Tiefseetaucher (and talking like a waterfall) or eating horribly salty pickles at our traditional Mettfrüstück. Thank you: Dr. Elena Polo, Dr. Daniel Meyer, Dr. Elsa Neubert, Robert Nißler, Niklas Herrmann, Jan Horlebein, Sabrina Weber, Gökhan Günay, Seren Hamsici, Meshkat Dinarvand, Gabrielle Selvaggio, Alexander Spreinat, Saba Telele, Larissa Kurth, Maria Dohmen, Frederike Dohrmann, Helen Preiß, Taija Fischer and Sabrina Mischke.
A big thank you also goes also to Prof. Dr. Andreas Janshoff for nice discussions, Petra Lappe for the always funny chats in your offices, Angela Rübeling for keeping the cell lab in such a great condition as well as Dr. Basti Brückner and Dr. Tabea Oswald for all the help with scientific and non-scientific things. Of course also a big thank you to all current and former PhD students of the AKAJ/AKCS. I look back with a lot of joy especially to all these Wednesdays, where we had ONE beer together.
I want to say 'thank you' to my three students I had the opportunity to work with during

their B.Sc./M.Sc. thesis. For me it was always especially rewarding to work, chat and laugh together with you and I learned also a lot from you. I hope that you can say the same about that time. If not, you know, 0.3 degree points worse!!! ;)

Of course I also want to thank my whole family, my brothers Wicky and Chrissi and especially my parents. You made me who I am and I would not have been able to do anything I did without you. You two are the best and I am very proud to have you as my parents.
Finally, my biggest 'Thank you' goes to my wonderful wife Anelia. You are truly the love of my life, the best person I have ever met. I enjoy every moment together with you and I am so thankful for everything. I also want to say 'hello' to our daughter, that will be born in these weeks. I do already love you to the moon and back and this will only get stronger with time. I love you two! <3